Robustness of masonry structures by limit analysis

MSc Thesis in Civil and Architectural Engineering

Aarhus University
Department of Engineering

Students
Anders Juncher Andersen - 201610436
Peter Boye Larsen - 201500389

Supervisors
Giuseppe Abbiati
Lars German Hagsten

June 2022

Abstract

This master's thesis takes a deterministic computational approach to describing structural robustness of masonry structures. A numerical tool is developed based upon lower and upper bound limit analysis and finite elements as first pioneered by S.W. Sloan in [1], [2] and [3]. The tool is experimentally verified by performing a column-loss scenario test on a 3-point supported masonry deep beam.

The computational tool is an upper-and a lower bound model utilizing plane strain triangular strain finite elements and linear shape functions. The upper bound model applies the kinematic theorem by velocity- and plastic multiplier rates degrees of freedom whereas the lower bound model invokes the static theorem by stress state degrees of freedom. The problem is then formulated as a linear programming problem by linearizing a cohesive-frictional Mohr-Coulomb yielding criteria and an optimal solution is then found by using Matlab's linear programming solver and a limit collapse load is found if the two solutions, approaching the exact plastic solution from the upper- and lower side respectively, are within an acceptable threshold of error.

The experiment aims to replicate a modern masonry structure as much as possible and the test object will therefore be constructed as an inner wall would be constructed in modern masonry structures with a load-bearing reinforced concrete beam on top of the masonry resembling the contribution from reinforced concrete slabs resting upon the wall, two areated autoclaved concrete beams between the pillars and the central column, and unreinforced concrete below the masonry pillars to resemble the wall-foundation joint as realistically as possible.

The test object showed decent ductility in failure and the numerical results were in well accordance with the experimental ones as the experimental load was 82.2% of the numerically predicted collapse load, which given the strict assumptions of material behavior done in limit analysis not necessarily obeyed by the multi-level anisotropies of masonry, is taken as an acceptable error.

Preface

This masters thesis has been conducted from February 2022 to June 2022 with a literature study done from September 2021 to February 2022 forming the groundwork for the thesis. The project has been supervised by Giuseppe Abbiati, assistant professor at Aarhus University and Lars German Hagsten, associate professor at Aarhus University.

The experimental campaign has been done as part of a larger project on structural robustness of masonry structures funded by Realdania and we gratefully acknowledge Realdania with the partners; Teknologisk institut, Statens byggeforskningsinstitut, Poul D. rådgivende ingeniører, H+H Danmark and Birch ejendomme, for giving is the opportunity to influence their project.

Notation lists

$\mathbf{A}_b$	Lower bound or upper bound boundary local equality constraint matrix
$\mathbf{A}_{b,global}$	Lower bound or upper bound boundary global equality constraint matrix
$\mathbf{A}_d$	Lower bound discontinuity equilibrium local equality constraint matrix
$\mathbf{A}_{d,global}$	Lower bound discontinuity equilibrium global equality constraint matrix
$\mathbf{A}_i$	Lower bound internal equilibrium local equality constraint matrix
$\mathbf{A}_{i,global}$	Lower bound internal equilibrium global equality constraint matrix
$\mathbf{A}_y$	Lower bound yielding local inequality constraint matrix
$\mathbf{A}_{y,global}$	Lower bound yielding global inequality constraint matrix
$\mathbf{A}_{e,v}$	Upper bound element flow rule velocity components equality constraint matrix
$\mathbf{A}_{e,v,global}$	Upper bound element flow rule velocity components global equality constraint matrix
$\mathbf{A}_{e,\lambda}$	Upper bound element flow rule plastic multiplier components equality constraint matrix
$\mathbf{A}_{e,\lambda,global}$	Upper bound element flow rule plastic multiplier components global equality constraint matrix
$\mathbf{A}_{d,v}$	Upper bound discontinuity flow rule velocity components equality constraint matrix
$\mathbf{A}_{d,v,global}$	Upper bound discontinuity flow rule velocity components global equality constraint matrix
$\mathbf{A}_{d,d}$	Upper bound discontinuity flow rule discontinuity velocity components equality constraint matrix
$\mathbf{A}_{d,d,global}$	Upper bound discontinuity flow rule discontinuity velocity components global equality constraint matrix
A_e	Area of an element
A_k	Yield linearization coefficient with respect to x-directional normal stress σ_x and linearization plane k
B_k	Yield linearization coefficient with respect to y-directional normal stress σ_y and linearization plane k
B	Number of boundary element sides
$\mathbf{b}_i$	Lower bound internal equilibrium local equality vector
$\mathbf{b}_{i,global}$	Lower bound internal equilibrium global equality vector
$\mathbf{b}_d$	Lower bound discontinuity equilibrium local equality vector
$\mathbf{b}_{d,global}$	Lower bound discontinuity equilibrium global equality vector
$\mathbf{b}_b$	Lower bound boundary equilibrium local equality vector
$\mathbf{b}_{b,global}$	Lower bound boundary equilibrium global equality vector
$\mathbf{b}_y$	Lower bound yielding local inequality vector
$\mathbf{b}_{y,global}$	Lower bound yielding global inequality vector
b_x	Body force in x direction
b_y	Body force in y direction
C_k	Yield linearization coefficient with respect to shear stress τ_{xy} and linearization plane k
D_k	Yield linearization strength of linearization plane k
$\mathbf{c}$	Objective coefficient vector in linear programming problem, in the case of the linear fractional program, it is the numerator objective function
c	Cohesive strength of material
$\mathbf{c}_e$	local objective function vector for element e

$\mathbf{c}_d$	local objective function vector for discontinuity d
$\mathbf{c}_{global}$	Global objective function vector for the upper bound problem d
$\mathbf{d}$	Denominator objective coefficient vector in linear fractional program
D	Number of element discontinuities
E	Number of elements
F	generic yield function
$l_{e,i}$	Length of an element e side .
N	generic flow function
N_{1-3}	Generic linear shape functions 1-3, used for element velocity field interpolation for the upper bound and element stress interpolation for the lower bound
P_e	Power dissipation in an element e
P_d	Power dissipation in a discontinuity d
P_{global}	Power dissipation globally by both elements and discontinuities
p	Linearization polygon order
Q_e	Load on element e
Q_{lb}	Lower bound collapse load
Q_{ub}	Upper bound collapse load
R	Radius of mohr stress circle
$\mathbf{T}$	Stress transformation matrix
t	Out-of-plane thickness of elements or linear fractional transformation variable
u_i	Horizontal velocity degree of freedom for node i for the upper bound
v_i	Vertical velocity degree of freedom for node i for the upper bound
$\mathbf{u}_e$	Upper bound velocity vector degree of freedom for element velocities
$\mathbf{u}_d$	Upper bound velocity vector degree of freedom for discontinuity velocities
$\mathbf{u}_p$	Upper bound velocity vector for the loaded points p
W	Work done, either interior or exterior
$\mathbf{x}$	Generic programming design vector
$\mathbf{y}$	Linear fractional transformation design vector

Table 1: Latin notations

α	Linear fractional problem numerator constant
α_k	Angle of linearization plane k
β	Linear fractional problem denominator constant
β	Generic stress vector
β_{global}	Global vector of stress degrees of freedom
β_i	Stress vector for node i
$\beta_{j,i}$	Stress vector for element j, node i
ε	Strain
$\dot{\varepsilon}$	Strain rate
ϕ	Internal angle of friction
γ	Upper bound load multiplier or for the lower bound unit density
λ	Lower bound load multiplier, or upper bound plastic multiplier degree of
λ	Vector of upper bound plastic multiplier degrees of freedom
$\dot{\lambda}$	Upper bound plastic multiplier rate
μ	Yield linearization polygon order constant
ω	Lower bound load proportionality factor
σ_n	Stress normal to plane n

$\sigma_{n,d}$	Stress normal to discontinuity d
σ_x	Horizontal normal stress
σ_y	Vertical normal stress
τ_n	Stress tangential to plane n
$\tau_{n,d}$	Stress tangential to discontinuity d
θ_d	Angle of discontinuity d
θ_b	Angle of boundary b

Table 2: Greek notations

Contents

1 Introduction

In the field of structural robustness, significantly less research has been conducted on masonry structures compared to reinforced concrete and steel structures. In Europe considerations on structural robustness of masonry structures are mainly covered by EN1991-1-7, whereas for structures of materials such as reinforced concrete and steel additional information and requirements are stated in their material specific codes meaning that guidance for the designing engineer in relation to robustness of masonry from the codes is very sparse. This thesis aims to characterize a specific thematic example of robustness experimentally as well as numerically by performing a column-loss scenario on a masonry wall supported by two wide pillars and a central column to be removed.

The experiment is to be done as realistically as possible, and the test object will therefore be constructed as an inner wall would be constructed in modern masonry structures with a load-bearing reinforced concrete beam on top of the masonry resembling the contribution from reinforced concrete slabs resting upon the wall, two areated autoclaved concrete beams between the pillars and the central column and unreinforced concrete below the masonry pillars to resemble the wall-foundation joint as realistically as possible.

Modelling structural robustness mathematically can be approached in several ways where in this thesis, a deterministic alternative load path approach will be taken where the robustness is quantified by the structures ability to form alternative load paths given extreme loading. The deformational capacity and the relative size of the yielding plateau of the force-displacement curve therefore becomes a direct measure of the robustness of the structure. To accommodate this choice, the numerical modelling will be done based on the methodology of limit analysis extremum principles where a lower bound and an upper bound program will be made based within the framework of a discretized stress based finite element formulation, linear shape functions and linear programming.

This makes the predicted loads only predictive in the case that the structure fails in a sufficiently ductile manner, making the experimental study two-fold in the sense that the applicability of limit analysis to masonry is tested by the accordance between the numerically predicted collapse loads and the experimental collapse load, thereby indirectly quantifying the robustness of the specific structural configuration by the ductility required for the limit analysis to be applicable which combines with the ductility as a measure of the structural robustness of the structure.

The aim of this paper is therefore to perform an experimental test testing the behavior of a masonry wall in a sudden column loss scenario to verify alternative load paths as a structural robustness strategy and the applicability of a developed computational tool based upon limit analysis extremum principles.

2 Masonry specific structural robustness

2.1 Definition and overview of structural robustness

An overview and definition of structural robustness exploring four main robustness design methodologies is given in Appendix E. To outline the motivation behind this paper and enhance the readability a summary containing the main points of the structural robustness sections in Appendix E will be provided in this section.

Structural robustness is the ability of a structure to avoid disproportionate collapse as a consequence of an event causing local failure. The interest on the subject escalated in the wake of the collapse incident of Ronan Point in London in 1968, where a large part of the structure failed progressively as consequence of a gas explosion in a flat that removed a bearing facade wall and the total collapse was out of proportion according to the event.

Figure 1: Progressive collapse at Ronan Point in 1968

In the years afterwards many researchers investigated methodologies to design robust structures and which structural characteristics that are of importance. Adam et al. [4] concludes robustness of a structural system depends on the systems strength, ductility, redundancy, continuity, and the type of abnormal loading. The strength of a system depends the design and materials. Ductility is the ability to undergo plastic deformations without rupture and is material specific, where plastic deformations occur when a structural element have reached its yield strength. Redundancy is a structural ability to redistribute load that originally was carried by a failed load bearing component to other components, meaning that a redundant structure has the availability of alternative load paths and thereby limit the spreading of failure. Lastly, continuity is the continuous connectivity between structural elements, such as continuous reinforcement in the case of reinforced concrete members. Obviously, the system characteristics are not distinct from each other, enhancing one or the other is likely to indirectly enhance the remaining. Enhancing continuity and ductility as well as the degree of static indeterminacy of the structural system will increase the redundancy, like a continues sufficiently ductile beam has alternative load paths if a support is lost, as visualized by the deflection curves in figure 2 below.

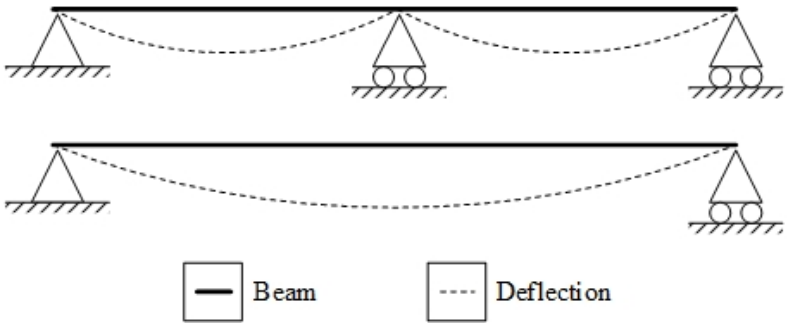

Figure 2: Deflection of redundant continues beam

Designing structures with above mentioned system characteristics can be done in various ways, where four typical approaches is Tie-force based design methods, Key element design, Alternative load path methods, and Risk-based methods.

Tie-force based design methods

Tie-force based design methods indirectly enhance robustness of structures through prescriptive rules describing minimum levels of ductility and continuity. The design methods requires the practicing engineer to detail the structure such that structural members are mechanically tied together in accordance with specified requirements. An example of such prescriptive rules is the minimum tension force requirements for peripheral reinforcement in concrete slabs. In general, Tie-force based design concepts results in robust structures, but the applicability is heavily reliant on material type and structural detail, since providing tension capacities in some materials is troublesome and making prescriptive rules to every structural detail and scenario is unpractical.

Key element design

The key elements are structural elements where local failure is likely to activate progressive collapses disproportionate to action causing the failure. The design method relies on the practicing engineers ability to identify such elements and design the element to resist the action and hereby increase the likelihood of the structure's survival in case of an accidental event. The approach is recommended in many codes and guidelines, but is in some countries seen a method

of last resort, since the method does not enhance redundancy of the structure if the element is removed, regardless of rise in capacity.

Alternative load path methods

The alternative load path method improves the structures redundancy by designing the structure to have adequate ability to form new load transferring mechanisms in case of local failure of a structural element. Intuitive measurements of this ability are continuity of load bearing elements, ductile junctions, as well as designing statically indeterminant systems. Compressive arch action, catenary action, and vierendeel action are also important progressive collapse resisting mechanism being activated if the boundary conditions allow them, but they can be less intuitive to mathematically prove. Though the method is the most direct translation of system characteristics into structural robustness measures, the approach often requires several assumptions and simplifications in practice which can lead to design solutions with different levels of robustness.

Risk-based methods can all the other approaches be risk-informed?

Risk-based methods are based on the principles of consequence and probability of either a hazard happening, damage occurring given a hazard, or extensive global damage given a hazard. Systematic risk assessment may draw upon and implement one or more of the above methods of design methods since they affect the eventual failure probabilities. The structural robustness can then be quantified from the level of risk of the structure. Structural design codes at the present time focus on structures to have safety against local failures, where risk-based methods focus on how potential damages are sustained with an appropriately high level of safety.

2.2 Robustness methodologies within masonry structures

The system characteristics mentioned above are in general properties of any structure and the design methods are applicable to any structure, but the effectiveness is heavily influenced on the type of construction and its structural material. Masonry is a brittle material where little or no plastic deformations occur and rupture occurs almost immediately after the stresses have reached the material yielding strength, and only with little to no tension capacity further complicating application of the four robustness approaches.

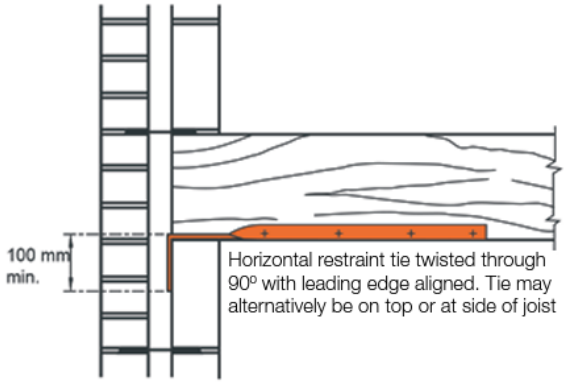

Figure 3: Example of horizontal ties [5]

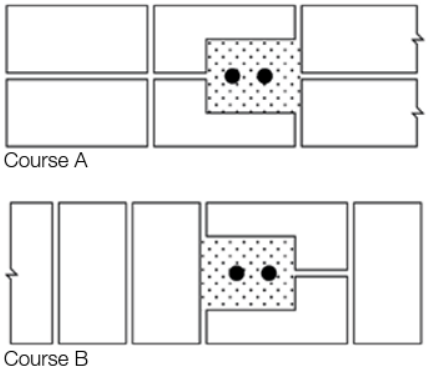

Figure 4: Example of vertical ties [5]

Tie-force based methods within masonry structures is widespread in some parts of the world.

British and American design codes prescribe specific requirements to both vertical and horizontal tie-ing force capacities, and the British code support the requirements with construction details and design solutions, wherefrom two details are shown in figure 3 and 4. With the brittleness and low tension capacity of masonry in mind one can insinuate the problems of anchorage and effectiveness of the ties, since the individual bricks in which the ties is fastened is limited to the friction capacity of the bed joint. Proving the effectiveness of ties on such a small scale not to mention issues such as quality control, workmanship, shrinkage or reduction in bond between floors, mortar and walls makes the method unpractical, why the method is deemed unfit for unreinforced masonry constructions.
Risk-based methods and key element design are both applicable to masonry structures. Designing key elements raises the issue whether it enhances the robustness of a structure since its main focus is to avoid local failure and not prevent progressive collapse given failure, like previously mentioned. Performing risk assessment of a structure relies on loading types and performed robustness measures, and is not a direct measure to be implemented why it, accompanied by key element design, in this paper are evaluated not be appropriate robustness measures in context of masonry structures.
Alternative load paths in unreinforced masonry structures relies on re-mobilisation of internal stresses by compressive arch action or compressive strut action, where the stress field bridges over the failed component in compression. From two separate papers figures of compressive arch action and compressive strut action are recreated below in figure 5a and 5b. Robustness of the structure can be showed by notional element removal method, where a load bearing element or wall piece is hypothetically removed, and the remainder is proved to bridge over the hypothetical hole. For the compressive arch action to be effective and successfully redistribute load adequate abutments capable of providing sufficient resistance against rotation, lateral and axial movements are necessary.

The mentioned methods will all provide a masonry structure with some level of robustness. That being said, the ability of a structure to avoid disproportionate collapse as a consequence of an event causing local failure is not provided or enhanced using the key element methods. Using tie-force based methods will on the other hand provide the structure with such abilities if the tie-ing details are thoroughly made such that local failure of the anchorages are prevented. Generalizing this method is difficult and will be unpractical due to differing scenarios with varying material parameters and geometries. Alternative load paths are arguably the guideline which fits the robustness definition the best. Intuitively, alternative load paths in masonry can be proved through compressive actions, where several authors stress that a great potential of load bearing capacity can be located, why this forms the research area of this paper.

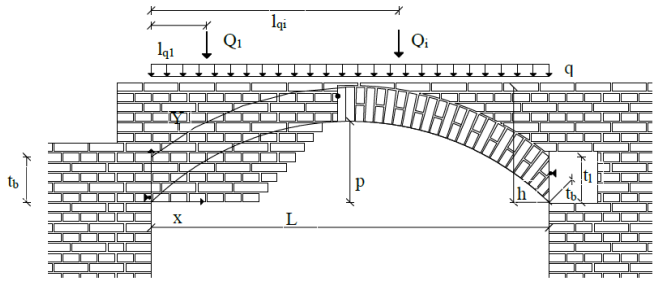

(a) Hidden arch

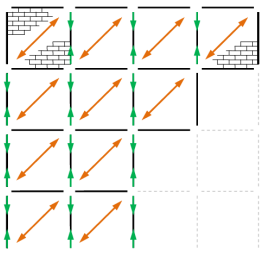

(b) Compressive strut action

Figure 5: Redistribution of load by alternative load paths [6][7]

3 Experimental studies on collapse resisting mechanisms

Appendix E section E.3.2 provides a short introduction to experimental tests of masonry starting by addressing different types of experimental setups according to Adam et al.'s [4] classification method of experimental programs. Since this formed the base of the experiment conducted in this paper the classification method is quickly recapped.
Adam et al. [4] divides experimental campaigns in their research study specifically focusing on structural robustness into four categories distinguishable by geometries and complexities:

a) sub-assemblages usually formed by two beams and one or more columns.
b) frames formed by beams and columns.
c) building structures constructed solely for experimental purposes.
d) actual buildings condemned to demolition.

i do not understand the difference between a, b, c

Each experimental setup has its own benefits. Local robustness with specific resistance mechanisms and capacities of structural details are most likely to be tested in labs as sub-assemblages or frames, since variable control and exact equipment is achievable and accessible in closed environments. Introducing more variables by constructing specimens of a structure solely for experimental purposes is often expensive and requires a large setup, but do supply reliable test results for calibrating numerical models, though effects of specific variables can be difficult to detect. Full scale tests of actual buildings condemned to be demolished are unique opportunities to test global robustness herein prove the actual progressive collapse resistance mechanisms. Test results of this experiment category can rule out or confirm specific mechanisms, but will be difficult to generalize to other structures, since the outcome is a result of the structural characteristics specific to the structure and variables are very hard to control.

In the literature study it is concluded that the rising attention of structural robustness of masonry structures has led to some testing of sub-assemblages of masonry mainly focusing on the behaviour when subjected to impact and blast loads, which in context of structural robustness mostly relates to the key element methods. The majority of robustness related experimental campaigns testing masonry has been focusing on the effects of masonry as a secondary material such as masonry infill walls.
The experimental study made in this paper is an ultimate failure mechanism test of a masonry wall with a concrete slab beam on top. Similar total failure test on masonry is yet unseen with tests on the effects of masonry infill walls and studies of static mechanisms of concrete structures being the nearest relatives.

Experimental studies requires purpose, precise objectives, and professional/strict execution. Expected outcomes and proper experimental equipment fitting the campaign objectives are essential as well as high quality specimens minimizing unwanted variables only blurring the experimental data. To ensure successful execution and data gathering of the experimental study made in this paper experimental campaigns on masonry infill walls and studies of collapse resisting mechanisms of concrete structures are investigated.

3.1 Experimental campaigns on masonry infill walls

The effects of masonry infill walls on load resistance of reinforced concrete frames have recently been given attention. Among the researchers are Kai Qian and Bing Li [8], Li et al. [9], and

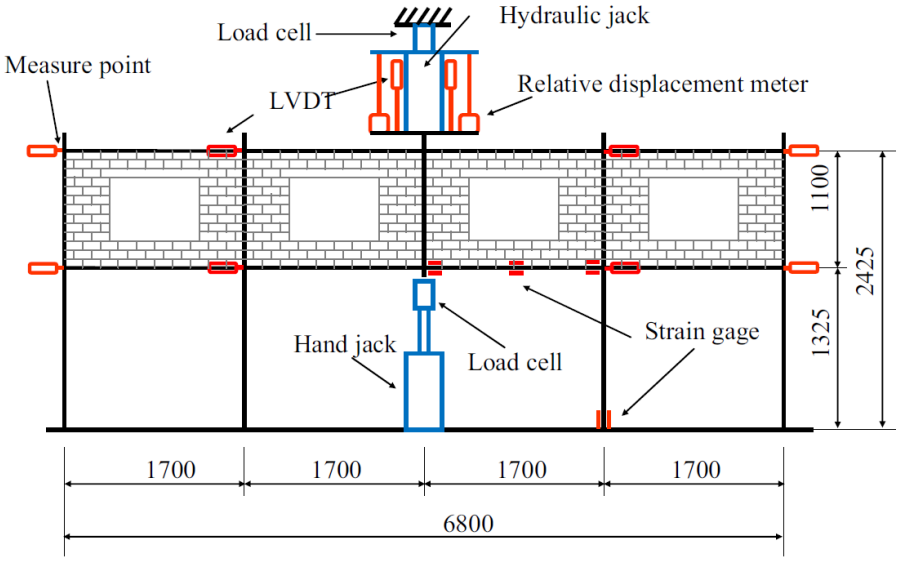

Figure 6: Experimental setups of tests on effects of concrete frame infill walls [10]

Shan et al. [10], who tested the wall type's ability to mitigate progressive collapses. The authors build a two-story reinforced concrete frame with four spans in one-third scale and simulated a column removal as a progressive collapse scenario by applying loading on the center columns of the test units. The load was applied by a hydraulic jack forcing downward displacement controlled with a hand jack underneath by unloading step by step. A schematic of one of the experimental setups showing types and placements of experimental equipment is shown on above figure 6 reproduced from Shan et al. [10]. Tests was performed on structural setups of bare concrete frames, concrete frames with full height infill walls, and concrete frames with infill walls with window sized openings. The findings of Kai Qian and Bing Li [8] is briefly summarized in section E.3.2 in attached Appendix E, but in general all authors find that the infill walls provide a level of resistance against progressive collapse by behaving as equivalent compressive struts.

3.2 Experimental campaigns on reinforced concrete

Tests of structural robustness and the vulnerability of concrete structures to progressive collapse is a well established field of study with many experimental campaigns carried out. Researchers testing mechanisms resisting progressive collapse are Almusallam et al. [11], Pham et al. [12], Qian et al. [13], and Gouverneur et al. [14] to name a few.

Almusallam et al.[11] tests structural robustness of frames made of precast concrete elements a typology especially vulnerable to progressive collapse. In their experimental program failure mechanisms do to large displacements of frames of two beams and three columns are tested. Displacement controlled loading was applied with an actuator to the center column until total failure without experiencing compressive arch action or catenary action. The column loss scenario was simulated by fastening the center column to the actuator, and applying force in a rate loading of 100 $\frac{mm}{s}$. A picture of their test setup is shown below on figure 7.

Pham et al. [12] conducted similar experimental tests on an in-situ reinforced concrete frame setup. The center column was suspended from a supporting H-frame and loaded with steel plates hung underneath. A quick-release device in the suspension was used to suddenly

release the joint by a yanking rope and in this manner simulate a sudden column loss. Linear variable displacement transducers (LVDTs) were arranged along the double-span beam to measure vertical and horizontal deformations and two slow-motion cameras at a frame rate of 240 frames per second were used to capture the in-plane deflections using marked points on the specimens. Doing the tests the authors captured catenary action and confirms that it resists collapse.

Qian et al. [13] simulated a loss of a corner column on an in-situ reinforced concrete frame structure by building one-third scale test models made of two orthogonal beams spanning between three columns as shown in figure 8. The setup was loaded with hanging steel plates placed symmetrically around the center column supported such that it could move freely in the vertical direction, but the rotational and horizontal freedoms were partially restrained. Sudden removal of the corner column was simulated by a developed pin support allowing for rotation when subjected to horizontal force, which they applied with a large hammer. The response of the system was monitored with accelerometers, LVDTs and strain gauges distributed along the beams and corner column.

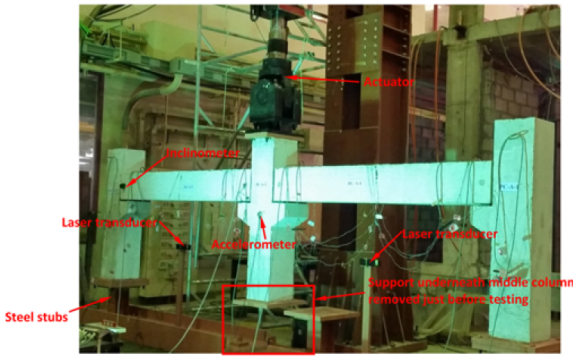

Figure 7: Almusallam et al. test setup [11]

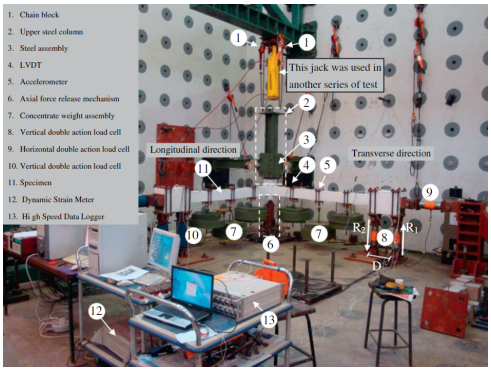

Figure 8: Qian et al. test setup [13]

Lastly, Gouverneur et al. [14] conducted experimental tests on a concrete slab strip with the purpose of testing the load capacity associated with catenary action. As shown in figure 9 the slab strip was spanning as a two-bay beam, where removal of the central support simulated an accidental action. The central support consisted of two concrete spacers and two hydraulic jacks and was removed, initially, by lifting up the slab strip to remove the spacers, and subsequently, by slowly lowering the jacks until clearance occurred and the jacks could be removed. After this stage displacement controlled actuators applied load until total collapse. Multiple LVDTs, strain gauges, potentiometers and dial gauges were located at various points in order to record vertical and horizontal displacements at several locations along the slab length. The measured horizontal compression forces in load-cells at the end support allowed to monitor the tensile catenary forces, which successfully was observed.

3.3 Discussion of experimental setups

The experimental campaigns mentioned above tested progressive collapse resisting mechanisms using different experimental approaches each proving to be effective in their specific setup. Displacement controlled hydraulic jack has proven to be a common way of applying load, though it is not a direct simulation of sudden removal of a supporting element, but it allows effects from unknown variables such as dynamic amplification factors to be at a minimum, while also supplying load-displacement data. Hanging dead weight is a simple but widely used to apply

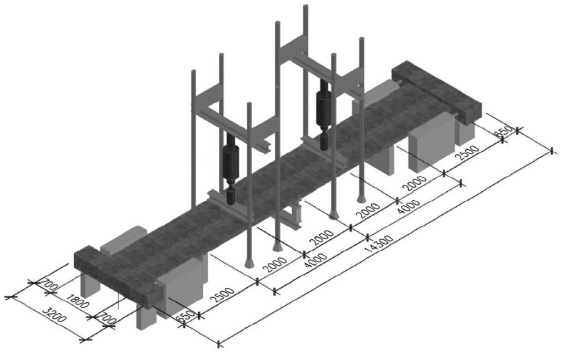

Figure 9: Gouverneur et al. test setup [14]

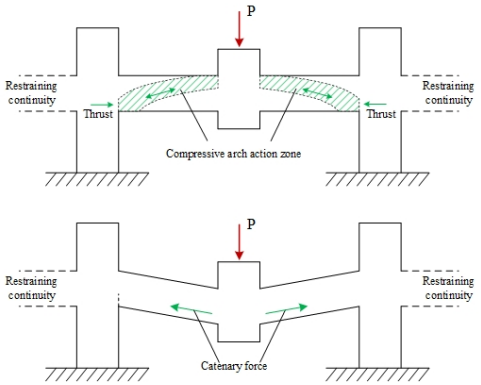

Figure 10: Expected compressive arch and catenary action

load, which neglects the needs of a large steel frame structures and mounted actuators. This type of setup does however require additional monitoring arrangements in forms of accelerometers, LVDTs, and strain gauges or like Pham et al. in [12] with slow motion cameras, since load-displacement data is not directly supplied. Strain gauges however, does not prove to be very useful when it comes to brittle materials such as masonry, since they provide strains based on deformation and does not distinguish between cracks and sliding and elastic elongation.
The experimental campaigns test progressive collapse resisting mechanisms relative to compressive arch action and catenary action sketched on figure 10. Tests on concrete frames with masonry infill walls reveal the infill acting as compressive strut, and tests on in-sito concrete with continues reinforcement shows catenary action when beams undergo large displacement. Catenary action in beams and tensile membrane action in plates are of great importance when assessing the load capacity of concrete structures. Activation requires the structure to undergo large displacements and to have sufficient boundary conditions, which can result in significant increase of structural load carrying capacity and hence the robustness of the structural system [14].

In the experiment conducted in this paper sudden column loss is simulated in a masonry wall with two window sized openings and a concrete slab beam on top to test the mechanisms to mitigate progressive collapse. The setup is shown in below isometric in figure 11. Based on above experimental campaigns the expected mechanisms are compressive arch action in the masonry deep beam and catenary action in the reinforced concrete slab post failure of the masonry. The outcome of the test will be identification of the failure resisting mechanisms, and will be done with a digital image correlation camera system measuring displacements and strains, which Pham et al. did successfully in [12]. Due to the feasible lab facilities, the wall specimen is setup underneath an existing steel frame allowing controlled boundary conditions and a strict environment minimizing unwanted variables.The collapse load will be made with a hydraulic jack mounted on steel frame allowing full visibility for the camera system.

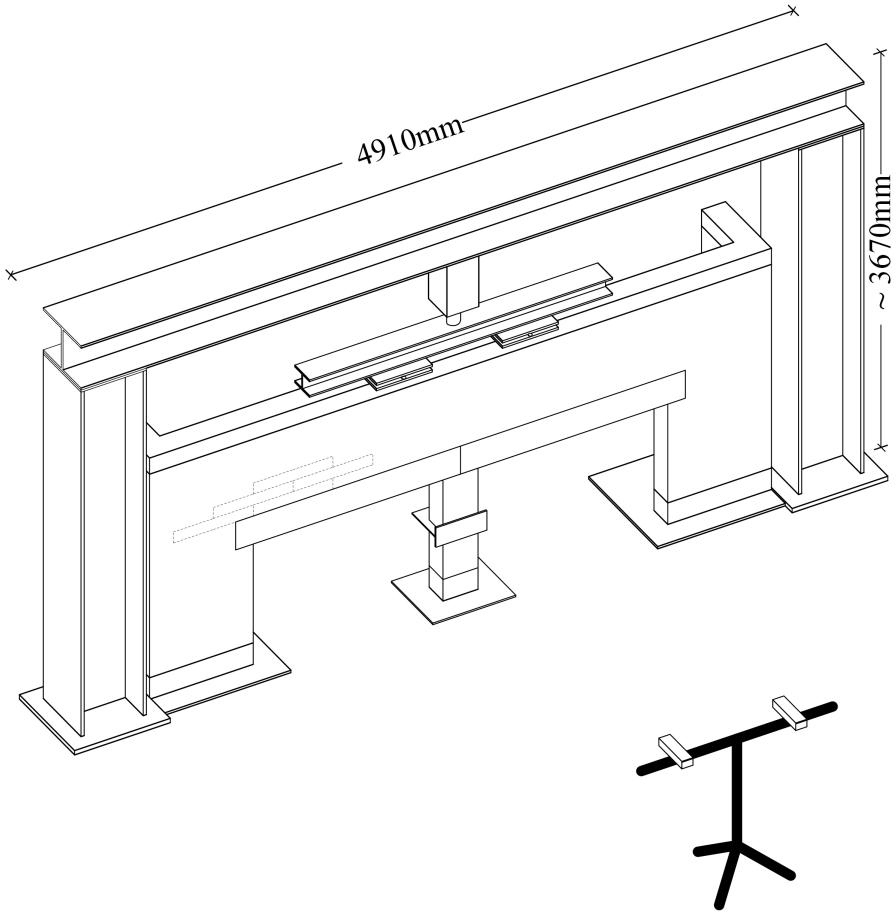

Figure 11: Isometric of experimental setup

from the text is not obvious that this is the experimental setup of the wall

4 Computational modelling of masonry

4.1 Introduction and overview

A comprehensive overview of the mechanical behaviour of masonry and modern approaches to the computational modelling of masonry is given in Appendix E. To keep continuity and readability of this paper, the main points will be we outlined here. The mechanical behavior of masonry is defined by the properties of the blocks and by the mortar as well as the joint interaction of the two. In general, the failure modes of masonry are describable by five different mechanisms as are listed below, and illustrated in figure 12, [15].

(a) Block-mortar interface tensile failure

(b) Block-mortar interface shear sliding failure

(c) Diagonal masonry shear-compression failure

(d) Crushing failure of Masonry blocks

(e) Block and mortar tensile cracking normal to head joints

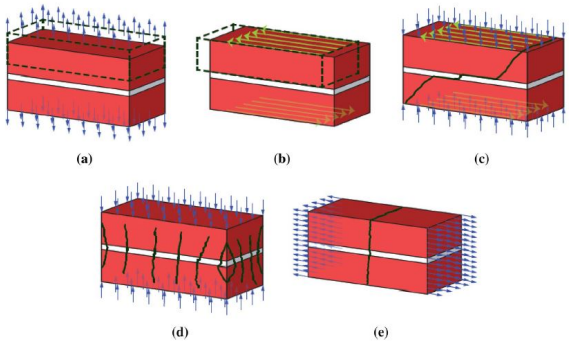

Figure 12: Masonry failure modes [15]

The purpose of a numerical tool is to capture these five yielding phenomena to a sufficient accuracy. The choice of computational tool comes down to the trade off between speed and the complexity required where the authors believe it recommendable to choose the simplest model with sufficient complexity. As outlined in the literature review Appendix E computational modelling of masonry is a fairly demanding task and as the issue at hand is that of structural robustness and by extension failure of large geometries, an efficient and less demanding approach is needed.

Such an approach is developed by Sloan[1] where he models Mohr-Coulomb materials within the framework of stress based finite elements and lower bound limit analysis. Sloan developed the approach for geotechnical problems however it has been applied to masonry by Sutcliffe [16] where he applies it to shear walls and Milani [17] where he applies it to deep beams. This approach will be further extrapolated upon and applied to the test specimen for the robustness test in section 5. An upper bound finite element model will also be applied based on a Mohr-Coulomb criteria also originally developed by Sloan which will be outlined in section 6. The lower and upper bound frameworks works by formulating the general problem mathematically as an optimization problem where the static and kinematic conditions are equality

constraints for the lower and upper bound, respectively and the yielding conditions are inequality constraints. The optimization problem is then formulated as a linear one by linearizing the yielding conditions and the maximum and minimum load multiplier is found for the lower and upper bound solution, respectively.

4.2 General limit analysis

To give some context to the discussion of how to apply limit analysis to masonry structures, a brief overview of the general principles of limit analysis will be given in this section. The theory is mostly based on lecture notes [18] given on plasticity theory during various courses at Aarhus University. When quantifying structural behavior, three types of equations or relations are available, these are the static, kinematic or physical conditions which each describe some mechanical relationship inter-independently of each other. The static conditions is basically describable as inner equilibrium and outer equilibrium of a body and thereby describes the relation between an inner stress field and some outer applied stress or load. If an inner stress field is equilibrated with an outer applied stress it is said to be a statically admissible stress field. This stress field says nothing about the deformational behaviour of the body which is where the kinematic conditions enter. These conditions refer to the relationship between some applied displacement and the strains of the body which must satisfy the kinematic or geometric conditions, which similarly to earlier - says nothing about the inner stresses causing these strains, rotations, deformations or curvatures that arises from the applied displacement only that the strain field is compatible which a bit more descriptively means that the strain field is consistent. These two types of conditions are material independent, that is they are generic relationships to model structural behaviour disregarding material info, which is where the physical conditions apply. These conditions are basically the relationship between the stress state and yielding behavior and the constitutive relationship between stress and strain increments.

Limit analysis is the application of a non-total amount of said conditions for structural analysis thereby creating non-exact solutions. These solutions are based upon the extremum principles(lower and upper) which states that, a solution can be obtained without the fulfillment of all three of the basic conditions required for an exact solution: physical, kinematic, and static but rather, with only two of them which in practice is very convenient. Combining physical and static conditions forms the lower bound solutions and combining the physical and kinematic forms the upper bound solutions. Within each an infinite amount of solutions satisfying the two conditions can be found. As the two different solution types combine a different subset of conditions, if both an upper bound and a lower bound solution returns the same load multiplier, all the three basic types of conditions are met and the solution is exact, this is however rarely achievable.

As mentioned in above paragraph, both extremum principles applies the physical conditions, which as mentioned is the relationship between stress state and yielding behavior. In equative language, this is usually expressed as some function F of the stress tensor σ_{ij} which determines yielding when it equates to zero:

$$F(\sigma_{ij}) = 0 \tag{4.1}$$

Similarly, as mentioned earlier the physical conditions also encompass the constitutive equations for a material meaning the relationship between stresses and strains. For plastic strain increments, this equation is called the flow rule, and is usually written as the plastic strain increment $\Delta\dot{\varepsilon}$ equals the derivative of some flow function $N(\sigma_{ij})$ with respect to the change of the

stress tensor at yielding point multiplied a plastic multiplier rate $\dot{\lambda}$.

$$\Delta\dot{\varepsilon} = \dot{\lambda} \cdot \frac{\partial N(\sigma_{ij})}{\partial \sigma_{ij}} \tag{4.2}$$

Applying the flow rule in conjunction with the basic kinematic equations form the theoretical base of the upper bound solutions, while applying the yield rule to the basic static equations forms the theoretical base for the lower bound solutions. The basic kinematic equations are known as the compatibility equations which state the relationship between inner strains and the geometrical boundary conditions which basically state the relationship between strains and deformations. For the case of plane strain and a deformation field u, v, the relationship between deformation and strains is:

$$\varepsilon_x = \frac{\partial u}{\partial x} \tag{4.3}$$

$$\varepsilon_y = \frac{\partial v}{\partial x} \tag{4.4}$$

$$\gamma_{xy} = \frac{\partial u}{\partial y} + \frac{\partial v}{\partial y} \tag{4.5}$$

Whereas the relationship between the inner strains e.g the compatibility equations which ensure no gaps or overlaps of the strain field are equal to below equation:

$$\frac{\partial^2 \varepsilon_x}{\partial^2 y} + \frac{\partial^2 \varepsilon_y}{\partial^2 x} = \frac{\partial^2 \gamma_{xy}}{\partial y \cdot \partial x} \tag{4.6}$$

Upper bound analysis is now done by finding a mechanism that obeys above kinematic criteria as well as the flow rule.

The static conditions required for the lower bound solutions are as mentioned internal equilibrium and equilibrium with outer traction stresses and the body stresses. Internal equilibrium in tensor format reads:

$$\sigma_{ij,j} + b_i = 0 \tag{4.7}$$

Which in the 2D case of a material with the unit density γ and the y-axis as the gravitational direction translates to:

$$\frac{\partial \sigma_x}{\partial x} + \frac{\partial \tau_{xy}}{\partial y} = 0 \tag{4.8}$$

$$\frac{\partial \sigma_y}{\partial y} + \frac{\partial \tau_{xy}}{\partial x} = \gamma \tag{4.9}$$

$$\tau_{xy} = \tau_{yx} \tag{4.10}$$

Outer equilibrium is similarly satisfied by the stress state at a boundary equaling:

$$\frac{\partial \sigma_x}{\partial x} + \frac{\partial \tau_{xy}}{\partial y} = p_x \tag{4.11}$$

$$\frac{\partial \sigma_y}{\partial y} + \frac{\partial \tau_{xy}}{\partial x} = p_y \tag{4.12}$$

Where p_x is the component of the applied traction vector in the x-direction and p_y is the y-directional component. Lower bound analysis can now be applied by for a loading case finding a stress field that satisfies above equilibrium criteria as well as the yield rule for the given

material.

Having now summed up the equations forming the basics of limit analysis, some requirements are to be met for limit analysis to be applicable. First of all is the small strain requirements which basically requires that the strain field must be sufficiently small for the geometric changes as a result of the strains not to significantly change the geometry of the initial problem. Secondly, the yielding function must be independent of the strain/strain rate and conversely the strain rate should not change the yielding function. This slightly confusing statement means that the material should be perfectly plastic or rigid plastic and thereby no plastic hardening or softening should occur during yielding. For the material, the yielding rule is also required to form a convex surface and the plastic constitutive relationship, that is the yield rule, must be associative meaning the flow function $N(\sigma_{ij})$ must equal the yielding function $F(\sigma_{ij})$.

4.3 Applying limit analysis to masonry

All these principles, conditions and requirements do not necessarily apply smoothly to masonry structures. First of all, there is the issue of anisotropy, as stated in the Appendix E section E.4.1 :

"Masonry is, due to the combination of blocks and mortar and the bond pattern of the two an anisotropic and heterogeneous material. The anisotropic characteristics of masonry exists elastically in the sense that the stress-strain relationship differs with the respect to orientation and in regards to strength as the strength properties also differs with respect to orientation. Similarly, there is a significant difference between tensile and compression strengths complicating even further with compressive strength of the blocks being significantly higher. Furthermore, anisotropy is also observed in the brittleness of the material that is the post peak response differs with respect to load orientation as well. This is illustrated in below figure 13, [19] which shows different failure modes with respect to load inclination".

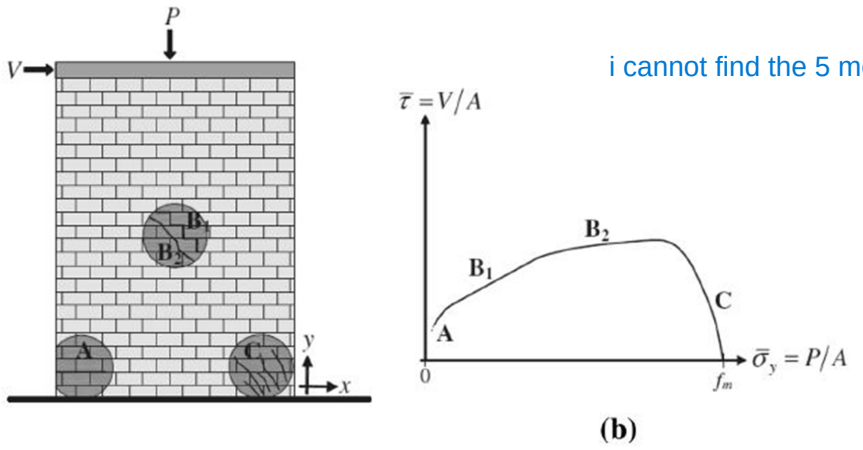

Figure 13: Masonry response with respect to orientation

Several things of the above is interesting. First of all, the anisotropy and heterogeneity requires the physical conditions of the yield rule to either somehow account for the joint-brick interactions or the joints and bricks must be modelled separately. Secondly, the brittle-anisotropy is critical, as the requirement for a no plastic hardening or softening is hard to meet. With respect to figure 12, there are five basic failure modes of masonry with each having different

levels of ductility. Generally speaking, the compression or tensional modes of failure of a, d and e are quasi-brittle [15] whereas the shear related ones of b and c are somewhat ductile. This means, that for a structural element to be rigorously describable by limit analysis the global failure behavior must be generally related to some shear failure. Above point can be generalized into that the ductility of masonry is a function of the stress state imposed on it meaning that this requirement of perfect plasticity can only be met when the masonry in question acts a specific type of structural element. An obvious example here is when masonry acts as a shear wall which is tested in [16] where Sloan's lower bound elements are applied to masonry with the addition of a joint failure criteria, where the experimental results shows good accuracy for the lower bound model when the normal compression stress is at sufficiently high levels and the failure is governed by mode c, in figure 12.

Another type of structural element is that of the deep beam which is the subject of this thesis. The context of interest is that given some local column failure a masonry panel might have to act as a deep beam with the question how much of a load can the element now handle. If one views it at as a Bernoulli beam element the result is likely not to be very much and probably not enough given that it previously where to act as an element in more or less pure compression along the strong axis of the element and not in longitudinal bending. This forms the primary motivation of the experimental campaign for the thesis and the goal is thereby to implement the extremum principled numerical models and to perform a deep beam test with the inclusion of sudden deep beam bending action due to column loss, where the ductility level and the level of confidence of which these limit analysis principles can be applied can be tested. Some other requirements are small deformations, which for masonry is not an issue [16] and a convex yielding surface, which again for masonry is a non issue as it is generally describable by a Mohr-Coulomb yielding criteria.

4.4 Material yielding model

The two models adopted, namely the lower and upper bound limit analysis finite element models revolve around a yield criteria formulation and then static or kinematic relations for the lower or upper bound element respectively. These static and kinematic conditions are formulated within the principles of perfect plasticity and as such are not dependent on the specific material except for the viability of applying perfect plastic behaviour to a material, which for masonry as argued, is not entirely clear when and where this assumption is applicable. The yield rule for the two models are however the same only with differences arising accompanying the linearization of the yield rule as strict upper and lower bound properties must be preserved as the function is linearized.

Masonry is a granular material with the compressive strength massively exceeding the tensile strength and as such can be appropriately characterized as a Mohr-Coulomb material, which in its basic state assume failure to occur in shear with the shear strength linearly proportional by the internal angle of friction to the normal stress applied. Due to the composite and anisotropic nature of masonry no unified failure surface is readily available for use and several possibilities are available with the main being some homogenization process of a representatively sized unit or by micro-modelling the bricks and joints separately with each of the methods having their strengths and weaknesses. In this report, a micro-modelling approach will be taken where failure criteria is created for joints and bricks individually.

The finite elements to be formulated are two-dimensional and operate with stresses as degrees of freedom in the case of the lower bound element and plastic multipliers as degrees of freedom in the case of the upper bound. As the elements are in a plane stress state, a Mohr-Coulomb formulation with respect to two perpendicular normal stresses σ_x and σ_y and a single shear stress τ_{xy} needs to be formulated for the bricks whereas for the joints which due to their geometrical configuration of having much smaller thicknesses than lengths can be modelled with a normal stress with respect to the joints perpendicular plane and a tangential shear stress with respect to the joints tangential plane. The basic equation for yielding by Mohr-Coloumb friction in plane stress can be derived as follows: Letting the normal stress being negative in compression, the shear stress that causes yielding equals:

$$\tau = c - \sigma \cdot \tan(\phi) \tag{4.13}$$

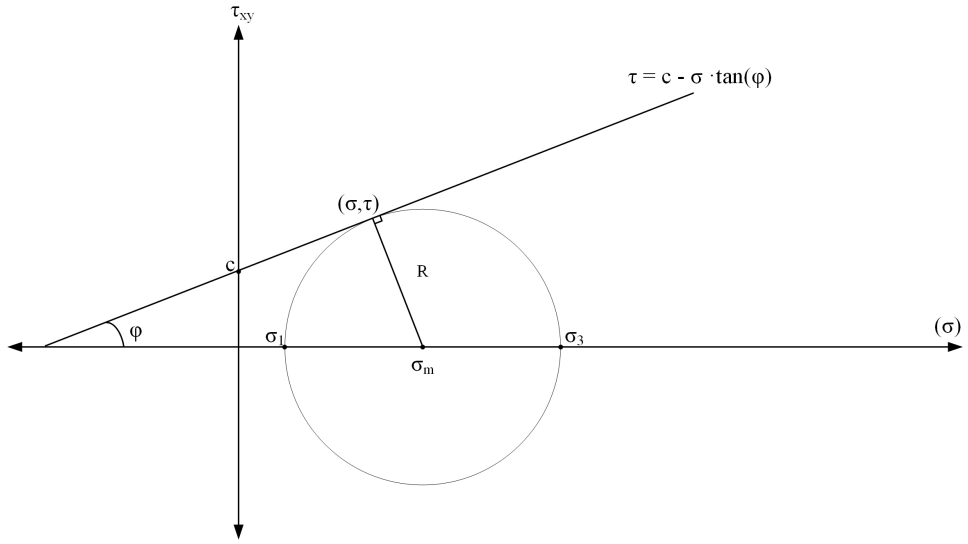

Figure 14: Mohr-Coulomb failure

With τ being the shear stress on the failure plane, c the cohesion, σ the normal stress on the failure plane and ϕ the angle of internal friction. The situation is graphically sketched in figure 14 for a two dimensional stress state in yielding defined by the principal stresses σ_1 and σ_3.

Rephrasing the stresses with respect to the radius R and the center σ_m of the stress state circle yields:

$$\tau = R \cdot \cos(\phi) \qquad \sigma = \sigma_m + R \cdot \sin(\phi) \tag{4.14}$$

Inserting equation 4.14 into 4.13 and multiplying the equation with $\cos(\phi)$ returns:

$$R \cdot \cos^2(\phi) = c \cdot \cos(\phi) - (\sigma_m + R \cdot \sin(\phi)) \cdot \sin(\phi) \tag{4.15}$$

Evaluating the parenthesis, and moving all R's to the left returns:

$$R \cdot \cos^2(\phi) + R \cdot \sin^2(\phi) = c \cdot \cos(\phi) - \sigma_m \cdot \sin(\phi) \tag{4.16}$$

As $\cos^2(\phi) + \sin^2(\phi)$ equates to 1, the expression collapses to:

$$R = c \cdot \cos(\phi) - \sigma_m \cdot \sin(\phi) \tag{4.17}$$

Now, assuming a plane stress state with a stress vector $\beta = [\sigma_x, \sigma_y, \tau_{xy}]$ and applying that for such a stress state the radius of Mohr's circle equals $R = \sqrt{\frac{1}{2} \cdot (\sigma_x - \sigma_y)^2 + \tau_{xy}^2}$, and applying $\sigma_m = \frac{1}{2} \cdot (\sigma_x + \sigma_y)$, equation 4.17 evaluates to equation 4.18 by squaring both sides of the equation and multiplying both sides by two.

$$(\sigma_x - \sigma_y)^2 + 2 \cdot \tau_{xy}^2 = (2 \cdot c \cdot \cos(\phi) - \frac{1}{2} \cdot (\sigma_x + \sigma_y) \cdot \sin(\phi))^2 \tag{4.18}$$

Above equation 4.18 statutes the Mohr-Coloumb yield rule for the plane stress element. Below equation 4.19 formalizes equation 4.18 by formulating it in the canonical form of a yield rule, where yielding occurs when the function F equals zero:

$$F(\sigma_x, \sigma_y, \tau_{xy}) = (\sigma_x - \sigma_y)^2 + 2 \cdot \tau_{xy}^2 - (2 \cdot c \cdot \cos(\phi) + \frac{1}{2} \cdot (\sigma_x + \sigma_y) \cdot \sin(\phi))^2 = 0 \tag{4.19}$$

equation 4.19 equates to the equation of a circle on the form $x^2 + y^2 = R^2$ with:

$$x = (\sigma_x - \sigma_y), \quad y = 2 \cdot \tau_{xy}, \quad R = (2 \cdot c \cdot \cos(\phi) + \frac{1}{2} \cdot (\sigma_x + \sigma_y) \cdot \sin(\phi). \tag{4.20}$$

The above equation 4.19 is nonlinear and as the problem is to be formulated as a linear programming problem, the circle formulated by said equation is to be linearized. The linearization is done somewhat differently for the lower and upper bound solutions as they are to be strict bounds and the area defined by the linearized polygon can in the case of the lower bound not protrude the circle and in the case of the upper bound cannot extrude the circle area. These specific linearizations will be discussed in the sections regarding the formulation of the upper and lower bound elements. A graphical example of the linearization of equation 4.20 with 12 vertices is shown in figure 15.

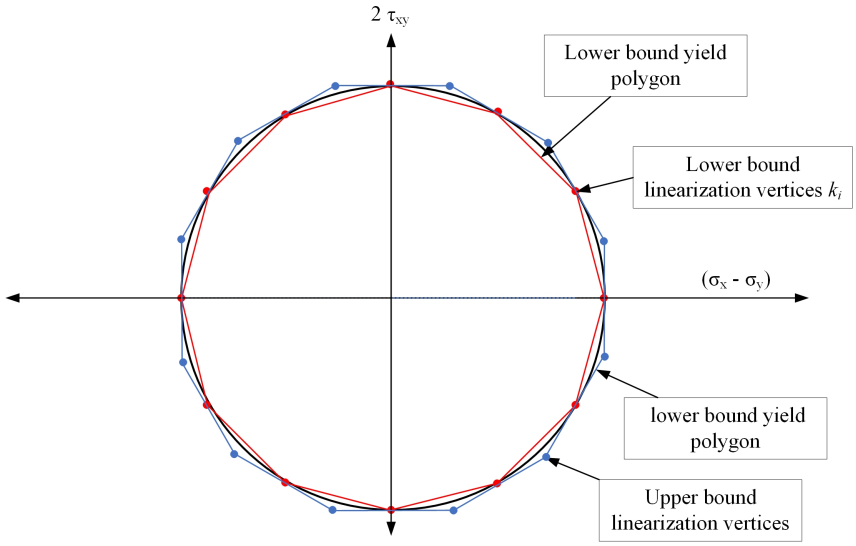

Figure 15: Linearization example

Due to their plane nature, joints are modelled as zero thickness elements and as such does not require linearization as they can be described by equation 4.13, where the generetic stress variables τ and σ are the replaced by the stress in the specific plane n of the joint τ_n and σ_n by projecting the stress state into the plane of the specific joint with an angle θ by the transformation as graphically shown in figure 16:

$$\sigma_n = sin^2(\theta) \cdot \sigma_x + \cos^2(\theta) \cdot \sigma_y - \sin(2 \cdot \theta) \cdot \tau_{xy} \tag{4.21}$$

$$\tau_n = -\frac{1}{2}\sin(2 \cdot \theta) \cdot \sigma_x + \frac{1}{2}\sin(2 \cdot \theta) \cdot \sigma_y + \cos(2 \cdot \theta) \cdot \tau_{xy} \tag{4.22}$$

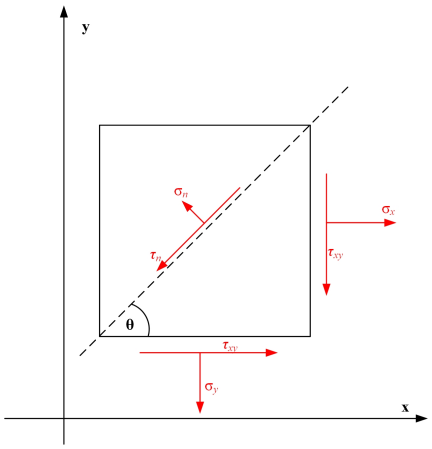

Figure 16: Plane stress rectangle

The failure surface of the joints can thereby be mathematically formulated as in equation 4.23 where the index j represents the properties of joint j and index n the stress state in the plane defined by joint j. The formulation is graphically shown in figure 17.

$$\tau_n = c_j - \sigma_n \cdot \tan(\phi_j) \tag{4.23}$$

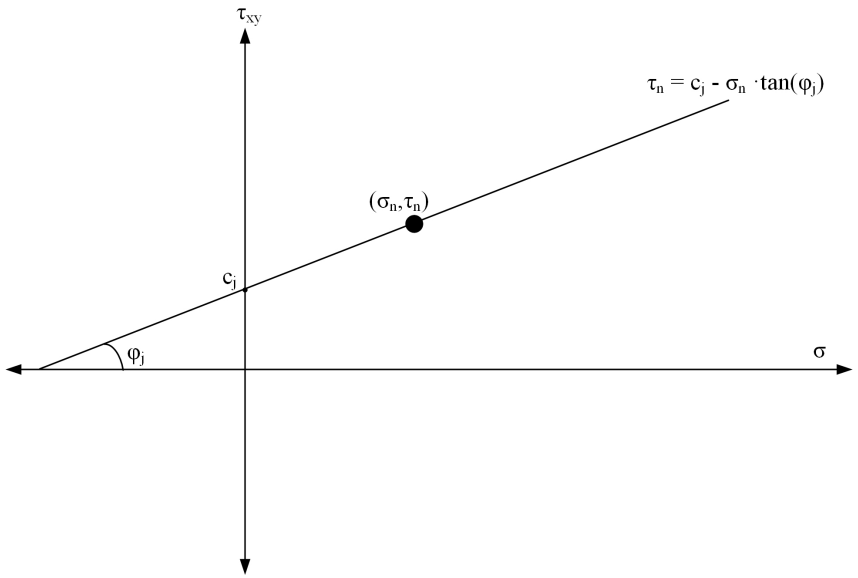

Figure 17: Mohr-Coulomb yield line for a planar joint

Having now described the general concepts of limit analysis, the general adopted yielding behavior of the chosen material, the numerical formulation of the static conditions and kinematic conditions as well as the numerical implementation of the physical conditions will now described in the next two sections.

5 The lower bound finite element

For the lower bound elements the requirements, as previously stated, for a viable solution are:

(a) Static conditions, equilibrium most hold within the entire element for any arbitrary part of the body and boundary stresses must be in equilibrium with external loads and reactions, that is they must be equal to each other.

(b) Physical conditions, the yielding rule is obeyed continuously throughout the body.

To satisfy the static conditions in a manner suitable for numerical formulation Sloan [1] suggests a discretization of a body into triangular plane strain elements with the stress state as the degrees of freedom. Stresses are linearly interpolated within the elements thereby satisfying equilibrium continuously by satisfying it in all nodes. The elements differentiates from traditional finite elements in the sense that each node is unique to its parent element meaning that several triangles sharing a nodal coordinate will each have its own unique node associated with that pair of coordinates. The basic geometrical layout of these finite elements is illustrated in below figure:

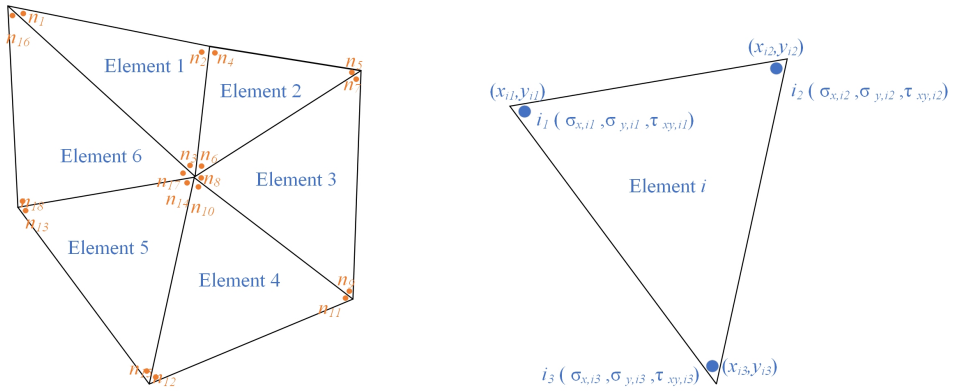

Figure 18: Sloan finite elements

As can be seen in figure 18 each finite element has three nodes each containing three stress degrees of freedom. Thereby for a discretization of E number of elements, there will be $9 \cdot E$ degrees of freedom.

Equilibrium is then satisfied by enforcing three types of equilibrium equations:

(a) Internal equilibrium, nodal stresses are linearly interpolated into the centroid of the individual triangular elements and equated the body forces acting upon the individual element.

(b) discontinuity equilibrium, equilibrium is satisfied continuously in the discontinuities of the elements or one can say the interfaces between two elements, by enforcing it discretely in the two nodal pairs defining the interface and by the linear stress interpolation equilibrium is satisfied throughout the entire interface.

(c) Boundary equilibrium, equilibrium equations are created for all boundaries with respect to static loads applying force to the individual discretized boundary. Also, the boundaries which are subject to load optimization are equated the product of the load multiplier degree of freedom and the local load proportionality factor and supported degrees

of freedom are removed from the boundary system of equations as they need not be in equilibrium with some exterior load.

The physical conditions are to be enforced by requiring every unique node to obey a Mohr-Couloub yielding model $f(\sigma) \leq 0$, this will be further expanded upon in section 5.6. Having a set of equilibrium equations to be satisfied and a set of yielding equations to be obeyed allows the lower bound stress state problem to be formulated as an optimization problem. As the equilibrium equations are linear, and the yielding criteria can be linearized, the lower bound problem can be formulated as a linear programming problem with the equilibrium equations acting as equality constraints and the yielding inequalities acting as inequality constraints. Denoting λ as the load multiplier and β as the global stress state vector, the optimization problem can be formulated as in equation 5.1 where the **A** matrices are the linear coefficient constraint matrices, β is the stress vector for the system and λ is the load multiplier:

Max λ subject to:

$$\mathbf{A}_d \cdot \beta = 0 \quad \mathbf{A}_i \cdot \beta = \mathbf{b}_i \quad \mathbf{A}_b \cdot [\beta, \lambda] = \mathbf{b}_b \quad \mathbf{A}_y \cdot \beta \leq \mathbf{b}_y \tag{5.1}$$

where the subscript d refers to discontinuities, i internal, b boundary and y yielding.

The formulation of the individual equalities and inequalities will be outlined in below sections:

5.1 Internal equilibrium

To satisfy the internal equilibrium, the following two basic equilibrium equations for respectively x-directional equilibrium and y-directional equilibrium must be continuously satisfied within the domain of the elements.

$$\frac{\partial \sigma_x}{\partial x} + \frac{\partial \tau_{xy}}{\partial y} = b_x \quad \frac{\partial \sigma_y}{\partial y} + \frac{\partial \tau_{xy}}{\partial x} = b_y \tag{5.2}$$

The stress state in the element varies linearly according to:

$$\sigma_x(x,y) = \sum_{i=1}^{3} N_i(x,y) \cdot \sigma_{x,i} \quad \sigma_y(x,y) = \sum_{i=1}^{3} N_i(x,y) \cdot \sigma_{y,i} \quad \tau_{xy}(x,y) = \sum_{i=1}^{3} N_i(x,y) \cdot \tau_{xy,i} \tag{5.3}$$

Where N_i refers to the linear shape function related to local node i. The shape functions are:

$$N_1(x,y) = \frac{1}{2 \cdot A_e} \cdot ((x_2 \cdot y_3 - x_3 \cdot y_2) + y_{23} \cdot x + x_{32} \cdot y) \tag{5.4}$$

$$N_2(x,y) = \frac{1}{2 \cdot A_e} \cdot ((x_3 \cdot y_1 - x_1 \cdot y_3) + y_{31} \cdot x + x_{13} \cdot y) \tag{5.5}$$

$$N_3(x,y) = \frac{1}{2 \cdot A_e} \cdot ((x_1 \cdot y_2 - x_2 \cdot y_1) + y_{12} \cdot x + x_{21} \cdot y) \tag{5.6}$$

Where A_e is the element area, x_i and y_i is the i'th nodes x and y-coordinate, respectively and the x_{ij}'s and y_{ij}'s equal $x_i - y_j$ and $y_i - y_j$:

$$y_{12} = y_1 - y_2 \qquad y_{23} = y_2 - y_3 \qquad y_{31} = y_3 - y_1$$

$$x_{21} = y_2 - y_1 \qquad x_{32} = x_3 - x_2 \qquad x_{13} = x_1 - x_3$$

Applying above equation 5.3 and equations 5.4 - 5.6 to equation 5.2, denoting the i'th nodes stress vector $\begin{bmatrix}\sigma_{ix} & \sigma_{iy} & \tau_{ixy}\end{bmatrix}$ as β_i such that:
$\begin{bmatrix}\beta_1 & \beta_2 & \beta_3\end{bmatrix} = \begin{bmatrix}\sigma_{1x} & \sigma_{1y} & \tau_{1xy} & \sigma_{1x} & \sigma_{2y} & \tau_{2xy} & \sigma_{3x} & \sigma_{3y} & \tau_{3xy}\end{bmatrix}$ and vectorizing yields:

$$\frac{1}{2 \cdot A_e} \cdot \begin{bmatrix} y_{23} & 0 & x_{32} & y_{31} & 0 & x_{13} & y_{12} & 0 & x_{21} \\ 0 & x_{32} & y_{32} & 0 & x_{13} & y_{31} & 0 & x_{21} & y_{12} \end{bmatrix} \cdot \begin{bmatrix} \beta_1 \\ \beta_2 \\ \beta_3 \end{bmatrix} = \begin{bmatrix} b_x \\ b_y \end{bmatrix} \tag{5.7}$$

Thereby, two equilibrium constraints are created for each finite element, with the first row in equation 5.7 representing x-direction equilibrium and the second row y- directional equilibrium. Above equation 5.7 shows that the equilibrium constraint matrix **A** for element i and the vector containing the equalities **b** equals:

$$\mathbf{A}_i = \frac{1}{2 \cdot A_e} \cdot \begin{bmatrix} y_{23} & 0 & x_{32} & y_{31} & 0 & x_{13} & y_{12} & 0 & x_{21} \\ 0 & x_{32} & y_{32} & 0 & x_{13} & y_{31} & 0 & x_{21} & y_{12} \end{bmatrix} \qquad \mathbf{b}_i = \begin{bmatrix} b_x \\ b_y \end{bmatrix} \tag{5.8}$$

5.2 Finite element discontinuity equilibrium

In the element interfaces, the stress field is statically admissible if there exists equilibrium between the shear and normal stresses from the parent elements acting on the plane.

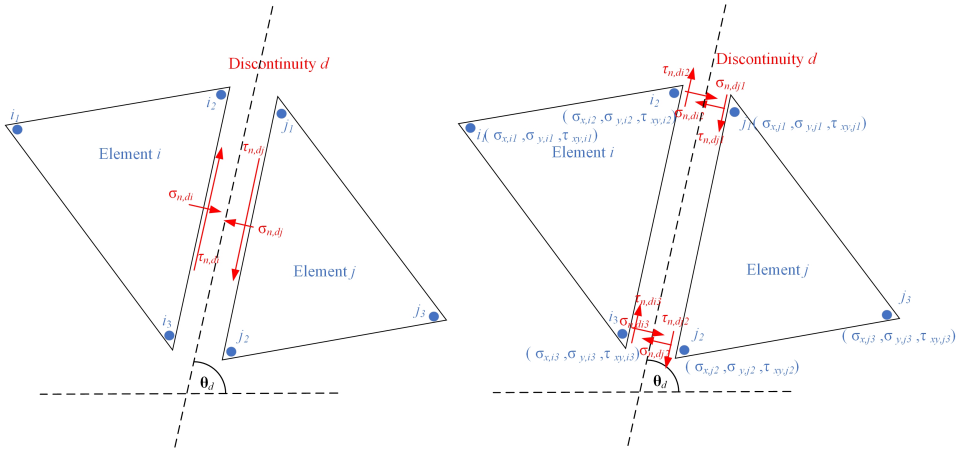

Figure 19: Interface equilibrium (left, general equilibrium (right, discretized equilibrium

Above figure 19 shows to the left the continuous equilibrium to be satisfied and to the right the equilibrium to be discretely satisfied as allowed by the linear stress field distribution. The equilibrium is enforced by satisfying equilibrium between the nodal pairs defining the discontinuity from elements i and j, that is equilibrium between the nodes sharing the same coordinates from two elements. For the example sketched in figure 19 the following four relations have to be enforced:

$$\sigma_{n,i,3} = \sigma_{n,j,2} \qquad \tau_{n,i,3} = \tau_{n,j,2} \qquad \sigma_{n,i,2} = \sigma_{n,j,1} \qquad \tau_{n,i,2} = \tau_{n,j,1} \tag{5.9}$$

To satisfy these equations the general stress coordinates of $(\sigma_x, \sigma_y, \tau_{xy})$ have to be rotated into the plane defined by the discontinuity d. This is done by trigonometric relations with the angle θ_d of the inclined plane d. For a stress rectangle in plane stress state, the normal and shear stress on any given plane as illustrated in figure 16 and is formulated as shown in equation 4.21 4.22 and :

Vectorizing equation 4.21 and 4.22 constructs the following stress transformation matrix $\mathbf{T}$ from node i with respect to interface d:

$$\begin{bmatrix} \sin^2(\theta_d) & \cos^2(\theta_d) & -\sin(2\cdot\theta_d) \\ -\frac{1}{2}\sin(2\cdot\theta_d) & \frac{1}{2}\sin(2\cdot\theta_d) & \cos(2\cdot\theta_d) \end{bmatrix} \cdot \begin{bmatrix} \sigma_{x,i} \\ \sigma_{y,i} \\ \tau_{xy,i} \end{bmatrix} = \begin{bmatrix} \sigma_{n,d} \\ \tau_{n,d} \end{bmatrix} \tag{5.10}$$

$$\mathbf{T}(\theta_d) = \begin{bmatrix} \sin^2(\theta_d) & \cos^2(\theta_d) & -\sin(2\cdot\theta_d) \\ -\frac{1}{2}\sin(2\cdot\theta_d) & \frac{1}{2}\sin(2\cdot\theta_d) & \cos(2\cdot\theta_d) \end{bmatrix} \tag{5.11}$$

Applying above equation 5.11 to equation 5.9 and denoting the nodal stress vectors as $\beta_{u,v}$ where u represents the element index e.g. i or j and v represents the local node ID e.g 1, 2 or 3 -returns the following vectorial expression for equilibrium at interface d, for the example illustrated in figure 19:

$$\begin{bmatrix} \mathbf{T}(\theta_d) & -\mathbf{T}(\theta_d) & 0 & 0 \\ 0 & 0 & \mathbf{T}(\theta_d) & -\mathbf{T}(\theta_d) \end{bmatrix} \cdot \begin{bmatrix} \beta_{i,2} \\ \beta_{j,1} \\ \beta_{i,3} \\ \beta_{j,2} \end{bmatrix} = \begin{bmatrix} 0 \\ 0 \\ 0 \\ 0 \end{bmatrix} \tag{5.12}$$

Above equation 5.12 shows that the constraint matrix $\mathbf{A}_d$ for discontinuity d and the vector containing the equalities equals:

$$\mathbf{A}_d = \begin{bmatrix} \mathbf{T}(\theta_d) & -\mathbf{T}(\theta_d) & 0 & 0 \\ 0 & 0 & \mathbf{T}(\theta_d) & -\mathbf{T}(\theta_d) \end{bmatrix} \quad \mathbf{b}_d = \begin{bmatrix} 0 \\ 0 \\ 0 \\ 0 \end{bmatrix} \tag{5.13}$$

5.3 Boundary equilibrium

The boundary equilibrium works similar to the discontinuity equilibrium in the sense that the nodal stress vectors are transformed by transformation matrix $T(\theta)$ into the plane b of the boundary. These nodal stresses must equal the nodal outer forces affecting said nodes, and by the previous argument of linear stress interpolation - equilibrium is satisfied continuously by satisfying it discretely in the corner nodes. The situation is sketched in below figure 20:

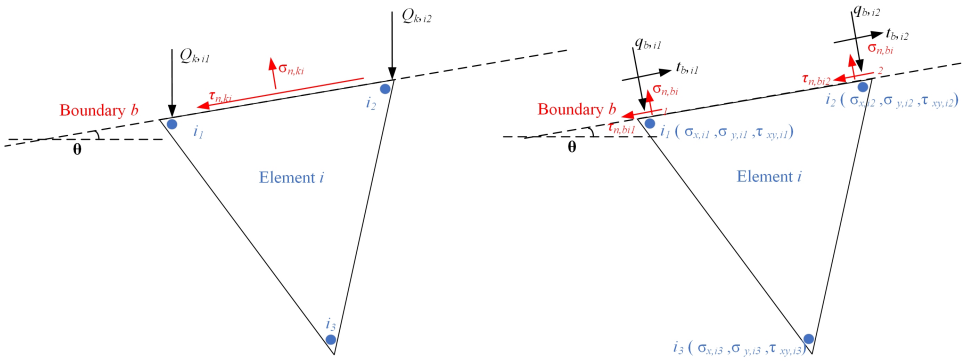

Figure 20: Boundary equilibrium

Like the implementation of equation 5.10 to equation 5.9 in above section, the local constraint matrix for boundary b is expressible by below equation 5.14 with β_{ij} being the i'th

elements j'th nodes stress vector and with the addition of the load multiplier λ. This makes the local boundary systems of equation with respect to the angle of the boundary θ_b as in equation 5.14, where ω describes the load proportionality of the applied load to be optimized on boundary b.

$$\begin{bmatrix} \mathbf{T}(\theta_b) & 0 & -\omega \\ 0 & \mathbf{T}(\theta_b) & -\omega \end{bmatrix} \cdot \begin{bmatrix} \beta_{i,1} \\ \beta_{i,2} \\ \lambda \end{bmatrix} = \begin{bmatrix} q_{b,i,1} \\ t_{b,i,1} \\ q_{b,i,2} \\ t_{b,i,2} \end{bmatrix} \tag{5.14}$$

$$\mathbf{A}_b = \begin{bmatrix} \mathbf{T}(\theta_b) & 0 & -\omega \\ 0 & \mathbf{T}(\theta_b) & -\omega \end{bmatrix} \quad \mathbf{b}_b = \begin{bmatrix} q_{b,i,1} \\ t_{b,i,1} \\ q_{b,i,2} \\ t_{b,i,2} \end{bmatrix} \tag{5.15}$$

The inclusion of the load multiplier λ directly in the boundary constraint matrix is where this implementation diverges from the original Sloan implementation. Here the load multiplier is implemented directly into the boundary constraint matrices whereas in the original formulation, a separate objective function vector was defined for optimizing the non-static load. This new approach has several advantages, it allows the possibility of optimizing both shear and normal loads simultaneously as well as allowing the user to force the stress acting on the loaded sides to stay in a predefined proportional pattern whereas for the original implementation, the linear program was at its own will in the sense that it was allowed to highly stress some areas and not others on a loaded boundary. This Sloan boundary formulation is good for a single local load however, for more practical problems this is rarely the case and therefore the methodology has been slightly expanded. The situation is sketched in below figure 21 and stated in equation 5.16 where ω are vectors controlling the load orientation and proportionality.

$$\begin{bmatrix} \mathbf{T}(\theta_b) & 0 & -\omega \\ 0 & \mathbf{T}(\theta_b) & -\omega \end{bmatrix} \cdot \begin{bmatrix} \beta_{i,1} \\ \beta_{i,2} \\ \lambda \end{bmatrix} = \begin{bmatrix} 0 \\ 0 \\ 0 \\ 0 \end{bmatrix} \tag{5.16}$$

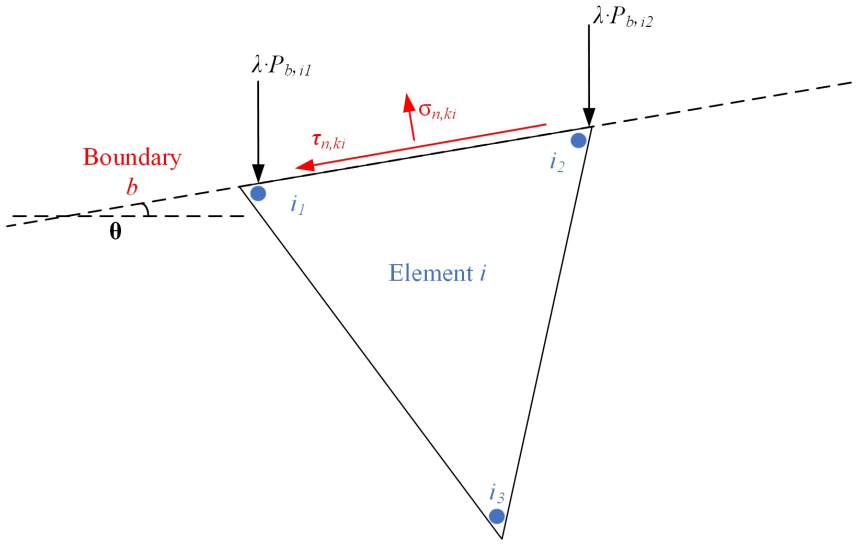

Figure 21: Load multiplier on boundary

5.4 Assembling the equality constraint matrices

Having described the formulation of the three individual types of local constraint matrices and equality vectors, all that is left for the formulation of the global constraint matrix is to calculate all the local ones by looping over all the elements for the element constraint matrices, all the finite element interfaces for the discontinuity equilibrium matrices and all the boundaries for the boundary equilibrium matrices. The local degrees of freedom have to have assigned global ones and all the equilibrium equations are concatenated. This can be formulated as in below equation 5.17 to 5.21 where E denotes the amount of elements, D the amount of interfaces, and B the amount of boundaries. For the global concatenation a zero vector is added vertically to the interface and elements constraint matrices as they do not refer to λ they have one less degree of freedom than the global boundary matrix:

$$\mathbf{A}_{d,global} = \sum_{d=1}^{D} \mathbf{A}_d \tag{5.17}$$

$$\mathbf{A}_{i,global} = \sum_{i=1}^{E} \mathbf{A}_i \tag{5.18}$$

$$\mathbf{A}_{b,global} = \sum_{b=1}^{B} \mathbf{A}_b \tag{5.19}$$

The global equality constraint matrix is now constructed by vertically concatenating the above three mentioned matrices.

$$\mathbf{A}_{global} = \begin{bmatrix} A_{d,global} \\ \mathbf{A}_{i,global} \\ \mathbf{A}_{b,global} \end{bmatrix} \tag{5.20}$$

The vector of equalities is assembled similarly:

$$\mathbf{b}_{d,global} = \sum_{d=1}^{D} \mathbf{b}_d \tag{5.21}$$

$$\mathbf{b}_{i,global} = \sum_{i=1}^{E} \mathbf{b}_i \tag{5.22}$$

$$\mathbf{b}_{b,global} = \sum_{b=1}^{B} \mathbf{b}_b \tag{5.23}$$

$$\mathbf{b}_{global} = \begin{bmatrix} \mathbf{b}_{d,global} \\ \mathbf{b}_{i,global} \\ \mathbf{b}_{b,global} \end{bmatrix} \tag{5.24}$$

The global system of equality constraint equations now read, where β_{global} is the vector containing all the global stress variables and λ is the load multiplier:

$$\mathbf{A}_{global} \cdot \begin{bmatrix} \beta_{global} \\ \lambda \end{bmatrix} = \mathbf{b}_{global} \tag{5.25}$$

5.5 Constraint matrix example

To demonstrate the lower bound stress finite element framework, a simple example is introduced. Below figure 22 shows the discretization. A rectangle is divided into four elements, twelve nodes and with three internal interfaces and six outer boundaries. The system is loaded at one global point shown by a red arrow and supported at three points shown by blue arrows. The system has the following amount of linear equalities:

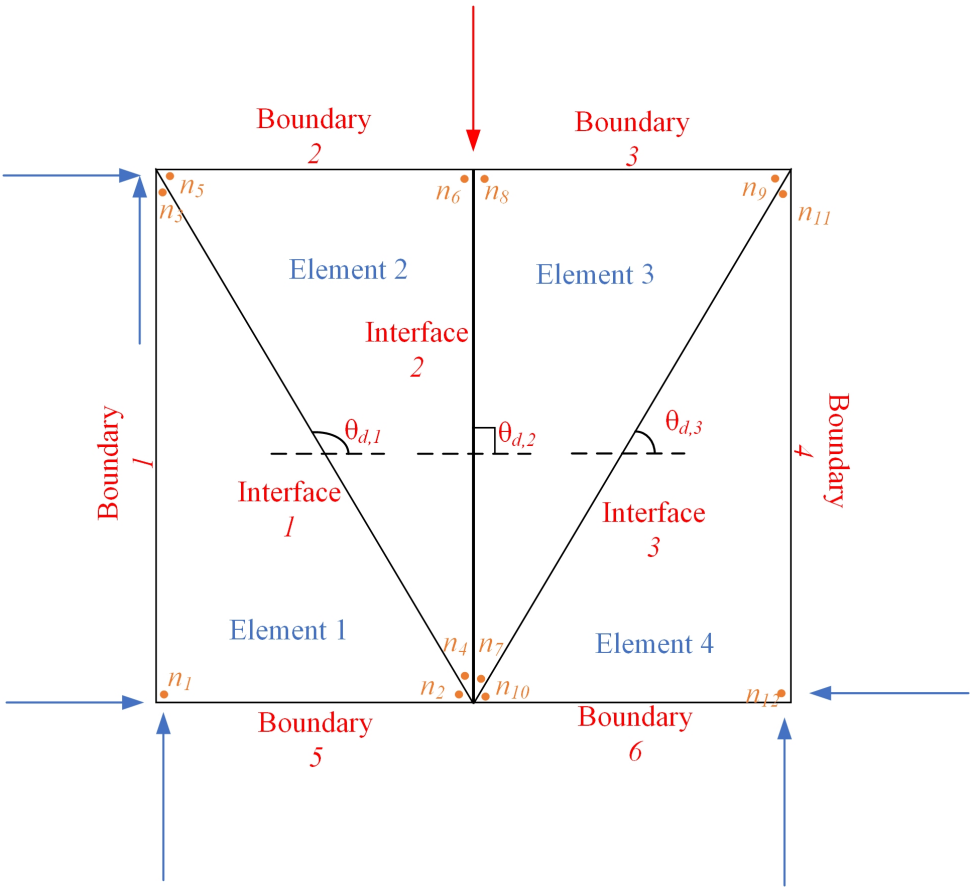

Figure 22: Lower bound example illustration

1. internal equilibrium equations: 8, each element imposes two equilibrium constraints
2. internal interface equilibrium equations: 12, each interface imposes four equilibrium constraints
3. boundary equilibrium equations: 18, each boundary imposes four equilibrium constraints, however the supported nodes are not to be in equilibrium with some prescribed exterior force and as such do not impose a constraint. For illustrative purposes, all the stress degrees of freedom of the supported nodes are restrained whereas in reality only one normal stress component and the tangential stress will be supported. This configuration is also possible in the model and makes the equilibrium equations not to be removed but the influence of the restrained degrees of freedom removed. As there are three supported nodes, the amount of constraints are 18 due to 6 boundaries · 4 constraints - 3 nodes · 2 constraints.

The interface constraint matrix is created as shown in below equation 5.26. To compress the system of equation, each zero entry is of the same size of $\mathbf{T}(\theta_{d,i})$ that is a two by three, meaning each row in the below matrix in fact represents two constraints.

$$\mathbf{A}_{d,global} =$$

$$\begin{bmatrix}
0 & \mathbf{T}(\theta_{d,1}) & 0 & -\mathbf{T}(\theta_{d,1}) & 0 & 0 & 0 & 0 & 0 & 0 & 0 & 0 \\
0 & 0 & \mathbf{T}(\theta_{d,1}) & 0 & -\mathbf{T}(\theta_{d,1}) & 0 & 0 & 0 & 0 & 0 & 0 & 0 \\
0 & 0 & 0 & \mathbf{T}(\theta_{d,2}) & 0 & 0 & -\mathbf{T}(\theta_{d,2}) & 0 & 0 & 0 & 0 & 0 \\
0 & 0 & 0 & 0 & 0 & \mathbf{T}(\theta_{d,2}) & 0 & \mathbf{T}(\theta_{d,2}) & 0 & 0 & 0 & 0 \\
0 & 0 & 0 & 0 & 0 & 0 & \mathbf{T}(\theta_{d,3}) & 0 & 0 & -\mathbf{T}(\theta_{d,3}) & 0 & 0 \\
0 & 0 & 0 & 0 & 0 & 0 & 0 & \mathbf{T}(\theta_{d,3}) & 0 & 0 & -\mathbf{T}(\theta_{d,3}) & 0 & 0
\end{bmatrix} \tag{5.26}$$

The above matrix $\mathbf{A}_{d,global}$ satisfies below equation where β_i is the i'th nodes stress vector: $\beta_i = \begin{bmatrix}\sigma_{x,i} & \sigma_{y,i} & \tau_{xy,i}\end{bmatrix}$:

$$\mathbf{A}_{d,global} \cdot \begin{vmatrix}\beta_1 & \beta_2 & \beta_3 & \beta_4 & \beta_5 & \beta_6 & \beta_7 & \beta_8 & \beta_9 & \beta_{10} & \beta_{11} & \beta_{12} & \lambda\end{vmatrix}^T = \mathbf{b}_{d,global} \tag{5.27}$$

The boundary constraint matrix is created as shown in below equation 5.28 . For each local node in a boundary that is not being supported, a constraint is created equaling the local nodes stress vector with respect to the boundary angle to the outer load applied. For the two nodes in contact with the load to be optimized (node 6 and 8) there is added a ω at the end column associated with the load multiplier degree of freedom. As the load is the same on both nodes, $\omega = \begin{bmatrix}1 & 0\end{bmatrix}^T$ To compress the system of equations, each zero entry is of the same size of $\mathbf{T}(\theta_{b,i})$ that is a two by three, meaning each row in the below matrix in fact represents two constraints.

$$\mathbf{A}_{boundary,global} =$$

$$\begin{bmatrix}
0 & \mathbf{T}(\theta_{b,5}) & 0 & 0 & 0 & 0 & 0 & 0 & 0 & 0 & 0 & 0 & 0 \\
0 & 0 & 0 & 0 & \mathbf{T}(\theta_{b,2}) & 0 & 0 & 0 & 0 & 0 & 0 & 0 & 0 \\
0 & 0 & 0 & 0 & 0 & \mathbf{T}(\theta_{b,2}) & 0 & 0 & 0 & 0 & 0 & 0 & -\omega \\
0 & 0 & 0 & 0 & 0 & 0 & 0 & \mathbf{T}(\theta_{b,3}) & 0 & 0 & 0 & 0 & -\omega \\
0 & 0 & 0 & 0 & 0 & 0 & 0 & 0 & \mathbf{T}(\theta_{b,3}) & 0 & 0 & 0 & 0 \\
0 & 0 & 0 & 0 & 0 & 0 & 0 & 0 & 0 & \mathbf{T}(\theta_{b,4}) & 0 & 0 & 0 \\
0 & 0 & 0 & 0 & 0 & 0 & 0 & 0 & 0 & 0 & \mathbf{T}(\theta_{b,6}) & 0 & 0
\end{bmatrix} \tag{5.28}$$

The above matrix $\mathbf{A}_{b,global}$ satisfies below equation where β_i is the i'th nodes stress vector: $\beta_i = \begin{bmatrix}\sigma_{x,i} & \sigma_{y,i} & \tau_{xy,i}\end{bmatrix}$:

$$\mathbf{A}_{b,global} \cdot \begin{bmatrix}\beta_1 & \beta_2 & \beta_3 & \beta_4 & \beta_5 & \beta_6 & \beta_7 & \beta_8 & \beta_9 & \beta_{10} & \beta_{11} & \beta_{12} & \lambda\end{bmatrix}^T = \mathbf{b}_{b,global} \tag{5.29}$$

as there are no exterior loads besides the one to be optimized, both the boundary and interface vector of equalities is zero.

$$\mathbf{b}_{b,global} = \mathbf{0} \qquad \mathbf{b}_{d,global} = \mathbf{0} \tag{5.30}$$

The global element constraint matrix is just a diagonal matrix of the local individual matrix. The vector of equalities has the values of the gravitational load of the material with t being the thickness of the media and γ the density of the media.

$$\mathbf{A}_{i,global} = \begin{bmatrix} \mathbf{A}_{i,1} & 0 & 0 & 0 \\ 0 & \mathbf{A}_{i,2}0 & 0 & 0 \\ 0 & 0 & \mathbf{A}_{i,3} & 0 \\ 0 & 0 & 0 & \mathbf{A}_{i,4} \end{bmatrix} \qquad \mathbf{b}_{i,global} = \begin{bmatrix} 0 \\ \gamma \cdot t \\ 0 \\ \gamma \cdot t \\ 0 \\ \gamma \cdot t \\ 0 \\ \gamma \cdot t \end{bmatrix} \tag{5.31}$$

The global sub matrices outlined above can now be assembled as done in equation 5.17 and 5.21 and put into equation 5.25. This concludes the equality constraints, the inequality constraints will be described in the following section.

5.6 Yielding constraints

The goal of the yielding constraints is to form a set of linear inequality constraints that disallows the stress state to violate the yielding conditions. As earlier stated in section 4.4, for the yielding of the bricks the nonlinear inequality 4.19 is to be linearized and as such made into a set of linear functions of σ_x, σ_y and τ_{xy} in the form of: $A_k \cdot \sigma_x + B_k \cdot \sigma_y + \tau_{xy} \cdot C_k \leq D_k$ where A_k, B_k, C_k and D_k represents constants associated with the k'th linearization plane thereby transforming the nonlinear inequality of equation 4.19 into a set of p linear inequalities were p is the number of linearization planes.

The linearization planes are created by drawing a regular polygon within the circle defined by equation 4.19 with p vertices. The equation for whether a point (x,y) lies within a line defined by the two points (x_1,y_1) and (x_2,y_2) is:

$$y - y_2 = \frac{y_2 - y_1}{x_2 - x_1} \cdot (x - x_2) \tag{5.32}$$

Rearranging the equation by moving quotients of the variables (x,y) and non-variable products on the right side yields:

$$y \cdot (x_2 - x_1) - x \cdot (y_2 - y_1) = x_2 \cdot y_1 - y_2 \cdot x_1 \tag{5.33}$$

The set coordinates of the two points defining a yield polygon line (x_1,y_1), (x_2,y_2) are equal to:

$$x_1 = R \cdot \cos(\alpha_k - \mu), \quad y_1 = R \cdot \sin(\alpha_k - \mu) \quad x_2 = R \cdot \cos(\alpha_k + \mu), \quad y_2 = R \cdot \sin(\alpha_k + \mu) \tag{5.34}$$

Where $\alpha_k = \frac{2 \cdot \pi \cdot k}{p}$ and $\mu = \frac{\pi}{p}$. This is now inserted in equation 5.33 together with the relationships from equation 4.20, restated below for clarity:

$$x = (\sigma_x - \sigma_y), \quad y = 2 \cdot \tau_{xy}, \quad R = (2 \cdot c \cdot \cos(\phi) + \frac{1}{2} \cdot (\sigma_x + \sigma_y) \cdot \sin(\phi). \tag{5.35}$$

Inserting above returns:

$$\begin{aligned} &2 \cdot \tau_{xy} \cdot (R \cdot \cos(\alpha_k + \mu) - R \cdot \cos(\alpha_k - \mu)) - (\sigma_x - \sigma_y) \cdot (R \cdot \sin(\alpha_k + \mu) - R \cdot \sin(\alpha_k - \mu)) \\ &\quad = R \cdot \cos(\alpha_k + \mu) \cdot R \cdot \sin(\alpha_k - \mu) - (R \cdot \sin(\alpha_k + \mu) \cdot R \cdot \cos(\alpha_k - \mu)) \end{aligned} \tag{5.36}$$

Above equation 5.36 expands even further by substituting R for $2\cdot c\cdot\cos(\phi)+\frac{1}{2}\cdot(\sigma_x+\sigma_y)\cdot\sin(\phi)$ as shown possible in section 4 but for the sake of readability, this is not shown. Said equation now becomes an exercise of trigonometric relations and identities where the equation collapses nicely into below equation 5.37 as seen in [1].

$$\sigma_x\cdot(\cos(\alpha_k)+\sin(\phi)\cdot\cos(\mu))+\sigma_y\cdot(\sin(\phi)\cdot(\cos(\mu)-\cos(\alpha_k))+\tau_{xy}\cdot 2\cdot\sin(\alpha_k)=2\cdot c\cdot\cos(\phi)\cdot\cos(\mu) \tag{5.37}$$

Above equation is the foundation for the yield criteria for a node for the linearization plane k of the yield surface with the stress degrees of freedom: $[\sigma_x,\quad \sigma_y,\quad \tau_{xy}]$. As the stress state for this node is within the linearized yield polygon and thereby admissible if the left-hand side of equation 5.37 is equal to or less than the right-hand side. By equation 5.37, the yield inequality for the node i is defined by:

$$[A_k\quad B_k\quad C_k]\cdot[\sigma_{x,i}\quad \sigma_{y,i}\quad \tau_{xy,i}]^T\leq D_k;\qquad k=1,2,.....p \tag{5.38}$$

with: $A_k=\cos(\alpha_k)+\sin(\phi)\cdot\cos(\mu)$, $B_k=\sin(\phi)\cdot(\cos(\mu)-\cos(\alpha_k))$, $C_k=2\cdot\sin(\alpha_k)$, $D_k=2\cdot c\cdot\cos(\phi)\cdot\cos(\mu)$ and p denoting the total number of linearization planes.

Above means that for each node p inequality constraints are made where the local inequality constraint matrix for node i: $\mathbf{A}_{y,i}$ together with the vector containing the inequalities $\mathbf{b}_{y,i}$ can be more formally expressed as stated in equation 5.39 and graphically be illustrated by that the stress state in node i lying within the linearized circle as show in figure 23:

$$\mathbf{A}_{yield,i}=\begin{bmatrix}A_1 & B_1 & C_1\\ A_2 & B_2 & C_2\\ . & . & .\\ A_k & B_k & C_k\\ . & . & .\\ A_p & B_p & C_p\end{bmatrix}\qquad \mathbf{b}_{yield,i}=\begin{bmatrix}D_1\\ D_2\\ .\\ D_k\\ .\\ D_p\end{bmatrix} \tag{5.39}$$

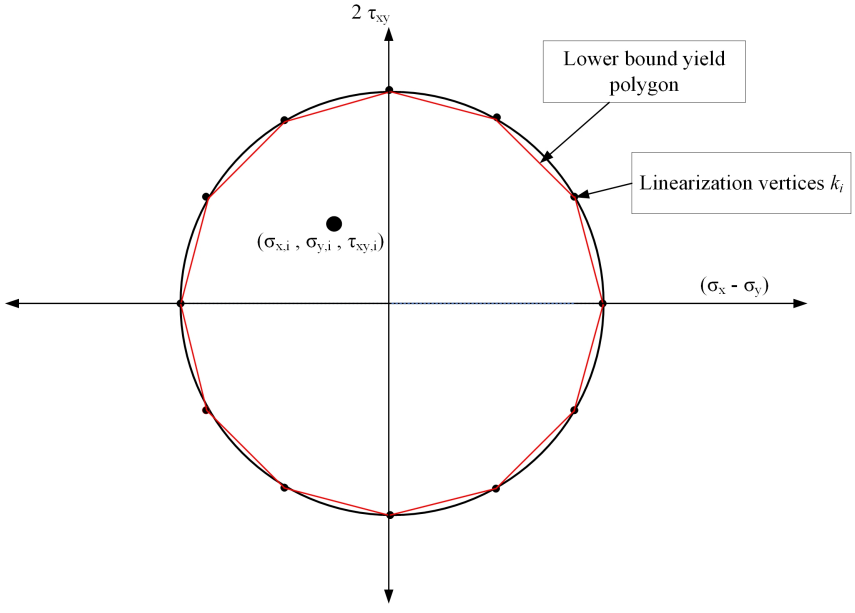

Figure 23: Lower bound stress state

This thereby concludes the yielding constraints for the individual nodes related to brick yielding. By summing over all the nodes with respect to their individual global degrees of freedom, the global yielding matrix for the bricks is created.

As masonry also contains joints, a yielding criteria for these also needs to be created. This is especially important as these joints often are the planes of weakness within the masonry structure and thereby prone to yielding before the bricks. As stated earlier in section 4 the yielding criteria for a joint is simpler than the brick as their physical dimensionality make their stress state describable by a single normal stress and a tangential stress as stated in equation 4.23, restated and slightly rephrased below:

$$F_j = |\tau_n| - c_j + \sigma_n \cdot \tan(\phi_j) = 0 \tag{5.40}$$

The tangential and normal stress in the joint plane can be generalized with respect to the brick pattern inclination as seen in [16], by the same principle as done just before for the bricks, but with the difference of applying the stress rotation equations of equation 4.21 and 4.22. Very similar to the previous stress transformations with respect to the global stress coordinates, the stress state in joint j with respect to the adjacent node i equals as in below equation 5.41 where θ_j is the inclination angle of the joint:

$$\sigma_{n,j} = \sin^2(\theta_j) \cdot \sigma_{x,i} + \cos^2(\theta_j) \cdot \sigma_{y,i} - \sin(2\theta_j) \cdot \tau_{xy,i} \tag{5.41}$$

$$\tau_{n,j} = -\frac{1}{2}\sin(2\theta_j) \cdot \sigma_{x,i} + \frac{1}{2}\sin(2\theta_j \sigma_{y,i} + \cos(2\theta_j) \cdot \tau_{xy,i} \tag{5.42}$$

Inserting equations 5.41 and 5.42 into equation 5.40, returns the following expression for the failure of a node in a joint plane:

$$F_j = -\frac{1}{2}|\sin(2\theta_j)\cdot(\sigma_{y,i}-\sigma_{x,i})+2\cdot\cos(\theta_j)\cdot\tau_{xy,i}| + (\sin^2(\theta_j)\cdot\sigma_{x,i}+\cos^2(\theta_j)\cdot\sigma_{y,i}-\sin(2\theta_j))\cdot\tan(\phi_j) = 0 \tag{5.43}$$

The absolute sign can be removed by making two constraints instead of one and having the first constraint have the coefficients that are within the absolute value sign change sign for the two respective constraints, e.g for each node placed at a joint, to not violate the yielding criteria for this joint, two constraints are made by vectorizing equation 5.43 as done in below equations 5.44;

$$\mathbf{A}_{y,j} \cdot \beta_i \leq \mathbf{b}_{y,j} \tag{5.44}$$

With $\beta_i = \begin{bmatrix}\sigma_{x,i} & \sigma_{y,i}\tau_{xy,i}\end{bmatrix}$ being the i'th nodes stress vector of joint j and:

$$\mathbf{A}_{y,j} = \begin{bmatrix} \sin^2\cdot\tan(\phi) - \frac{1}{2}\sin(\theta_j) & \frac{1}{2}\sin(\theta_j) + \cos^2\cdot\tan(\phi) & \cos(2\theta_j) - \sin(2\theta_j)\cdot\tan(\phi_j) \\ \sin^2\cdot\tan(\phi) + \frac{1}{2}\sin(\theta_j) & -\frac{1}{2}\sin(\theta_j) + \cos^2\cdot\tan(\phi) & -\cos(2\theta_j) - \sin(2\theta_j)\cdot\tan(\phi_j) \end{bmatrix} \tag{5.45}$$

$$\mathbf{b}_{y,j} = c_j \tag{5.46}$$

The local inequality constraint matrices are assembled to global matrices similar to done earlier in equation 5.20:

$$\mathbf{A}_{y,solids} = \sum_{i=1}^{N} \mathbf{A}_{y,i} \tag{5.47}$$

$$\mathbf{A}_{y,joints} = \sum_{j=1}^{J} \mathbf{A}_{y,j} \tag{5.48}$$

Where N is the number of nodes, J is the number of nodes associated with a joint as well as a solid object.

All the constraints for the lower bound optimization problem has now been accounted for and the problem can be assembled globally. Assembling the problem basically means restating equation 5.1 with the terminology used for the individual global sub matrices, for clarity the global inequality and equality matrices have not been concatenated:

Max λ subject to:

$\mathbf{A}_{d,global} \cdot \beta_{global} = \mathbf{b}_{d,global}$

$\mathbf{A}_{i,global} \cdot \beta_{global} = \mathbf{b}_{i,global}$

$\mathbf{A}_{b,global} \cdot \begin{bmatrix} \beta_{global} & \lambda \end{bmatrix}^T = \mathbf{b}_{b,global}$

$\mathbf{A}_{y,solids} \cdot \beta_{global} \leq \mathbf{b}_{y,solids}$

$\mathbf{A}_{y,joints} \cdot \beta_{global} \leq \mathbf{b}_{y,joints}$

This thereby concludes the lower bound element, the total collapse load from the lower bound solution Q_{lb} is obtained by summing the total forces acting on the individual loaded elements $Q_{i,e}$ found by integrating the loaded boundary stresses $\sigma_{i,e}$ as maximized by above optimization problem over the loaded areas.

$$Q_{i,e} = \frac{1}{2}(\sigma_{1,e} + \sigma_{2,e}) \cdot l_e \cdot t \qquad Q_{lb} = \sum_{i=1}^{e_{load}} Q_{i,e} \tag{5.49}$$

6 The upper bound finite element

For the upper bound elements, the requirements for a rigorous upper solution are:

(a) Kinematic conditions, the velocity field must be compatible, that is, there must be consistency in the velocity field of the solution, this is solved by assuming a linear velocity variation within the elements and constant strain. The velocity field must also be in compliance with the boundary conditions.

(b) Physical conditions, the plastic flow must obey an associative flow rule:

$$\dot{\varepsilon_{ij}} = \dot{\lambda} \cdot \frac{dF}{d\sigma_{ij}} \tag{6.1}$$

and with $F(\sigma_{ij}) = 0$ and $\dot{\lambda} \geq 0$

The upper bound element is based on a kinematically admissible velocity field in compatibility with the boundary conditions. A kinematically admissible velocity field must also satisfy an associated flow rule continuously throughout the body and the objective of the formulation is therefore to articulate an expression for the flow rule in compatibility with a velocity field, that is equation 6.1 for plastic flow within the elements under the condition of constant strain and equations for plastic flow within possible discontinuities - that is separation- of the elements. Crudely speaking, these conditions together with the boundary conditions act as the constraints for the problem while an expression for the energy dissipated by the kinematically admissible mechanism will act as the objective function to be minimized. The optimization problem is in contrast to the lower bound problem a minimization one, which in canonical form, as formulated by Sloan [2], reads:

$$\begin{aligned} &\min \mathbf{c}^T \cdot x \\ &\text{subject to } \mathbf{A}_{equality} \cdot x = \mathbf{b}_{eq}, \quad \mathbf{A}_{inequality} \cdot x \leq \mathbf{b}_{inequality} \end{aligned}$$

Sloan made an upper bound framework in 1989 that allowed discontinuities of the velocity field, however with the disadvantage that the user had to specify the sign direction a priori for each discontinuity as the velocity jump normal to the discontinuity is governed by the dilatation that occurs irrespective of the sign of the tangential velocity jump. As such the dilatational motion is a function of the absolute value of the difference in tangential velocities between the two elements, thereby creating a non-linear constraint if the direction of the tangential velocity jump is not specified a priori. Specifying the direction of a possible velocity jump is however very impractical except for very simple geometries, why Sloan [3] some years later created an updated formulation where by basically creating slack variables for the velocity discontinuity jumps, making it possible to specify as many discontinuities as the user wishes without specifying the sign a priori. This is done by formulating the flow rule non-rigorously locally for the discontinuities, while retaining the upper bounding properties.

6.1 Upper bound element formulation

To formulate the flow rule in a discretized manner, constant strain rate linear velocity elements are used. These upper bound elements utilize linear shape functions and nodes unique to every element akin to the lower bound elements, but whereas the stresses are the degrees of freedom

for the lower bound elements, the nodal velocities and element plastic multipliers are the degrees of freedom for the upper bound elements under the assumption of constant strain rates throughout each element [2]. Reusing the generic degree of freedom vector β, the degrees of freedom for element e are, where u_i's are the horizontal velocities and v_i's are the vertical velocities :

$$\beta_e = \begin{bmatrix} u_{i,1} & v_{i,1} & u_{i,2} & v_{i,2} & u_{i,3} & v_{i,3} & \lambda_{i,1} & \lambda_{i,2} & . & . & \lambda_{i,k} & . & . & \lambda_{i,p} \end{bmatrix}, \quad k = 1,2,..p \tag{6.2}$$

These degrees of freedom for the element are displayed in below figure 24, where each element has $6+p$ amount of degrees of freedom where p is the polygon order of the linearization.

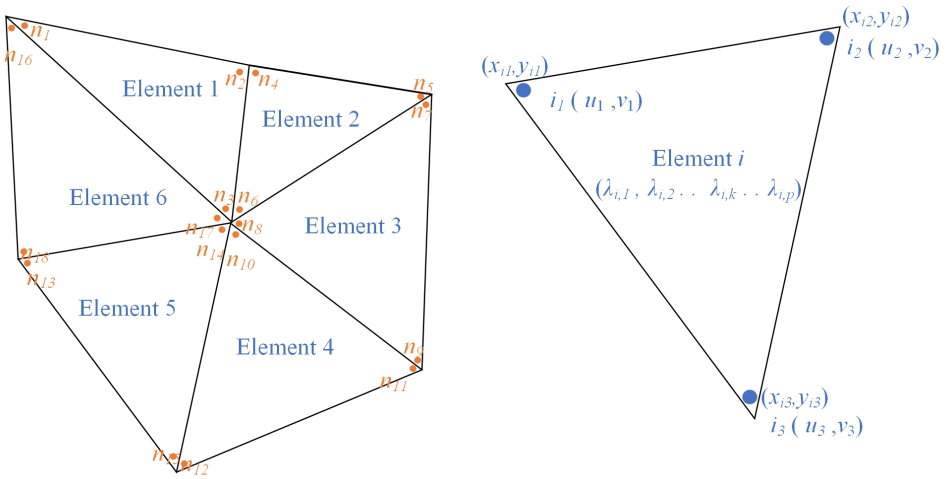

Figure 24: Upper bound element degrees of freedom

The same linear shape functions as used the lower bound elements are used, here they dictate the velocity field within the elements instead of the stress field. As the shape functions are linear, the compatibility condition of equation 4.6 are inherently satisfied. The element velocity field with respect to these shape functions and the discrete nodal velocities $\begin{bmatrix} u_{i,1} & v_{i,1} & u_{i,2} & v_{i,2} & u_{i,3} & v_{i,3} \end{bmatrix}$ are:

$$u(x,y) = \sum_{i=1}^{3} N_j(x,y) \cdot u_j \qquad v(x,y) = \sum_{i=1}^{3} N_j(x,y) \cdot v_j \tag{6.3}$$

Where the shape functions N_1, N_2 and N_3 are:

$$N_1(x,y) = \frac{1}{2 \cdot A_e} \cdot ((x_2 \cdot y_3 - x_3 \cdot y_2) + y_{23} \cdot x + x_{32} \cdot y) \tag{6.4}$$

$$N_2(x,y) = \frac{1}{2 \cdot A_e} \cdot ((x_3 \cdot y_1 - x_1 \cdot y_3) + y_{31} \cdot x + x_{13} \cdot y) \tag{6.5}$$

$$N_3(x,y) = \frac{1}{2 \cdot A_e} \cdot ((x_1 \cdot y_2 - x_2 \cdot y_1) + y_{12} \cdot x + x_{21} \cdot y) \tag{6.6}$$

Where A_e is the element area and the x_{ij}'s and y_{ij}'s equal $x_i - y_j$ and $y_i - y_j$:

$$y_{12} = y_1 - y_2 \qquad y_{23} = y_2 - y_3 \qquad y_{31} = y_3 - y_1$$

$$x_{21} = y_2 - y_1 \qquad x_{32} = x_3 - x_2 \qquad x_{13} = x_1 - x_3$$

To discretize the flow rule with respect to the constant strain rate field the left hand side of the flow rule equation 6.1 is equated to the change in the velocity field with respect to coordinates thereby creating the equations below by first specifying the generic strain field as a constant strain field with equation 6.7 and thereafter substituting equations 6.4 - 6.6 into below equation 6.7 returns:

$$\dot{\varepsilon_{ij}} = \dot{\varepsilon_x} + \dot{\varepsilon_y} + \dot{\varepsilon_{xy}} \tag{6.7}$$

with: $\dot{\varepsilon_x} = \frac{du}{dx}, \quad \dot{\varepsilon_y} = \frac{dv}{dy}, \quad \dot{\varepsilon_{xy}} = (\frac{du}{dy} + \frac{dv}{dx})$

$$\dot{\varepsilon_{ij}} = \sum_{j=1}^{3} \frac{dN_j(x,y) \cdot u_j}{dx} + \sum_{j=1}^{3} \frac{dN_j(x,y) \cdot v_j}{dy} + \sum_{i=1}^{3} \frac{dN_j(x,y) \cdot u_j}{dy} + \sum_{j=1}^{3} \frac{dN_j(x,y) \cdot v_j}{dx}) \tag{6.8}$$

To accommodate the right hand side of the flow rule equation while maintaining a linear set of equations leads to yet another linearization of the yield surface. As mentioned in section 4, to retain the upper bounding properties, the linearized surface must always either align or protrude the convex yield surface and therefore the linearization process is principally the same as in previous section 5 in equations 5.34 to 5.38 but where the vertex coordinates are slightly different. The vertex coordinates are:

$$x_1 = R \cdot \frac{\cos(\alpha_k - \mu)}{\cos(\mu)}, \quad y_1 = R \cdot \frac{\sin(\alpha_k - \mu)}{\cos(\mu)} \quad x_2 = R \cdot \frac{\cos(\alpha_k + \mu)}{\cos(\mu)}, \quad y_2 = R \cdot \frac{\sin(\alpha_k + \mu)}{\cos(\mu)} \tag{6.9}$$

With $\alpha_k = \frac{2 \cdot \pi \cdot k}{p}$ and $\mu = \frac{\pi}{p}$. Analogously to the lower bound solution, the above is inserted into equation 5.33 and applied to equation 4.20 which returns an expression for a single yield line k on the form in below equation 6.10 for the yield rule not to be violated:

$$F_k = [A_k \quad B_k \quad C_k] \cdot [\sigma_{x,i} \quad \sigma_{y,i} \quad \tau_{xy,i}]^T \leq D_k; \qquad k = 1, 2, ...p \tag{6.10}$$

with: $A_k = cos(\alpha_k) + sin(\phi), \quad B_k = sin(\phi) - cos(\alpha_k), \quad C_k = 2 \cdot sin(\alpha_k), \quad D_k = 2 \cdot c \cdot cos(\phi)$. The entire yield surface in a node equals:

$$F = \sum_{k=1}^{p} (A_k \cdot \sigma_x + B_k \cdot \sigma_y + C_k \cdot \tau_{xy} - D_k) \leq 0 \tag{6.11}$$

Applying this to the flow rule equation returns equation 6.12 by differentiating with respect to the unknown stresses and summing over the order of the yield polygon:

$$\dot{\varepsilon_{ij}} = \dot{\lambda} \cdot \frac{dF}{d\sigma_{ij}} = \dot{\lambda} \cdot \frac{dF}{d\sigma_x} + \dot{\lambda} \cdot \frac{dF}{d\sigma_y} + \dot{\lambda} \cdot \frac{dF}{d\tau_{xy}} = \sum_{k=1}^{p} (\lambda_k \cdot (A_k + B_k + C_k)) \tag{6.12}$$

By conjoining above equation 6.12 with equation 6.8 and differentiating the shape functions with respect to the coordinates articulates the flow rule formulation for the plastic flow within the upper bound element e as seen in below equation 6.13:

$$\mathbf{A}_{e,v} \cdot \begin{bmatrix} u_1 & v_1 & u_2 & v_2 & u_3 & v_3 \end{bmatrix}^T - \mathbf{A}_{e,\lambda} \cdot \begin{bmatrix} \lambda_1 & \lambda_2 & . & . & \lambda_k & . & . & \lambda_p \end{bmatrix}^T = 0 \tag{6.13}$$

with $\begin{bmatrix}\lambda_1 & \lambda_2 & . & . & \lambda_k & . & . & \lambda_p\end{bmatrix}^T \geq 0$

Where $\mathbf{A}_{e,v}$ is a matrix gathering the linear coefficients associated with the linearly interpolated velocities and $\mathbf{A}_{E,\lambda}$ is a matrix gathering the linear coefficients associated with the linearized yielding function. These matrices equal:

$$\mathbf{A}_{e,v} = \frac{1}{2 \cdot A_e} \begin{bmatrix} y_{23} & 0 & y_{31} & 0 & y_{12} & 0 \\ 0 & x_{32} & 0 & x_{13} & 0 & x_{21} \\ x_{32} & y_{23} & x_{13} & y_{31} & x_{21} & y_{12} \end{bmatrix} \tag{6.14}$$

$$\mathbf{A}_{e,\lambda} = \begin{bmatrix} A_1 & A_2 & . & . & A_k & . & . & A_p \\ B_1 & B_2 & . & . & B_k & . & . & B_p \\ C_1 & C_2 & . & . & C_k & . & . & C_p \end{bmatrix} \tag{6.15}$$

Above equations 6.13, 6.14 and 6.15 constitutes the constraints associated with kinematic admissibility for plastic flow within the local finite elements.

The global constraint matrices are created by summing over all the local ones with respect to global coordinates. This is shown in below equations 6.16 and 6.17, where D is the total amount of discontinuities and E is the total amount of elements:

$$\mathbf{A}_{e,v,global} = \sum_{e=1}^{E} \mathbf{A}_{e,v} \tag{6.16}$$

$$\mathbf{A}_{e,\lambda,global} = \sum_{e=1}^{E} \mathbf{A}_{\mathbf{e}}, \lambda \tag{6.17}$$

Above equations 6.16, and 6.17 thereby concludes the constraints that forces inter-element velocity jumps to be kinematically admissible.

6.2 Upper bound discontinuity formulation

The primary aim of the discontinuity formulation is to allow kinematically admissible jumps of velocity between the finite elements meaning, differences in velocities between the finite elements that satisfies the flow rule. A phenomena that occurs when plastic yielding occurs is plastic volume increase which, in contrary to the elastic Poisson effect, always is a volume increase regardless of the sign of the plastic deformation. The relationship between the tangential deformation of a discontinuity and the associated dilatational perpendicular deformation is governed by a material property called the dilatation angle, which for the assumption of associated flow equals the internal angle of friction. The basic schematic of the behavior is illustrated in below figure 25.

As the dilation arises from plastic volume increase due to yielding which only expands and not contracts, the relationship between Δv_{ij} and Δu_{ij} can be deducted from the flow rule in equation 6.1, which for a stress state in a single plane can be written as:

$$\dot{\varepsilon} = \dot{\lambda} \cdot \frac{dF}{d\sigma} \iff \begin{bmatrix} \Delta\dot{u}_{ij} = \dot{\lambda} \cdot \frac{dF}{d\tau_n} \\ \Delta\dot{v}_{ij} = \dot{\lambda} \cdot \frac{dF}{d\sigma_n} \end{bmatrix} \tag{6.18}$$

By completing the differentials and using the Mohr-Coulomb equation for a single plane stress state, that is $F(\sigma_n, \tau_n) = |\tau| + \sigma_n \cdot \tan(\phi) - c = 0$, above equation 6.18 becomes:

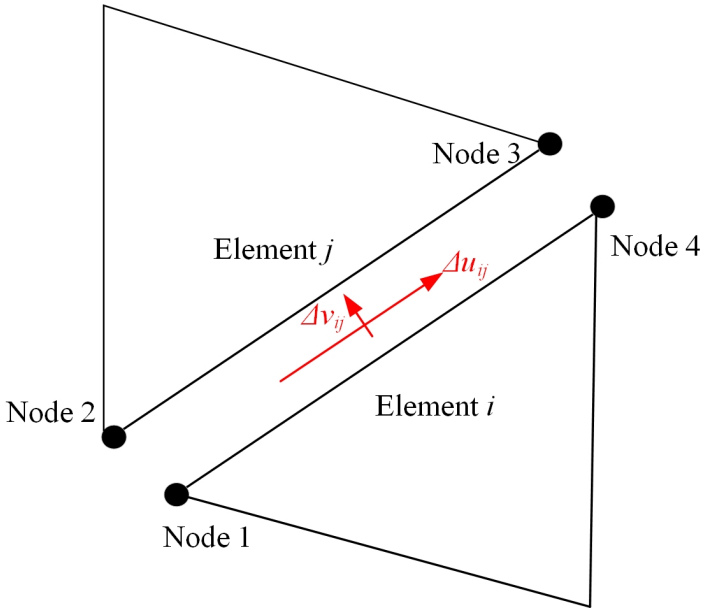

Figure 25: Illustration of discontinuity velocity jump

$$\begin{bmatrix} \Delta\dot{u}_{ij} = \dot{\lambda} \\ \Delta\dot{v}_{ij} = \dot{\lambda} \cdot \tan(\phi) \end{bmatrix} \tag{6.19}$$

By exchanging $\dot{\lambda}$ with Δu_{ij} the relationship between Δv_{ij} and Δu_{ij} becomes as in below equation where the absolute sign is included as the volume expansions occurs no matter the sign on the tangential displacement:

$$\Delta v_{ij} = |\Delta u_{ij}| \cdot \tan(\phi) \tag{6.20}$$

The absolute sign makes above equation non-linear which is an issue. This issue is in [3] solved by adding non-negative velocity degrees of freedom for the discontinuities, where two degrees of freedom are added for each nodal pair. The tangential velocity jump at each pair is then definable as the difference of the two degrees of freedom defined for that specific nodal velocity jump, for instance for the velocity for nodal pair 1,2:

$$\Delta u_{12} = u_{12}^{+} - u_{12}^{-}, \qquad u_{12}^{+} \geq 0, \quad u_{12}^{-} \geq 0 \tag{6.21}$$

The absolute sign in equation 6.20 can now be circumvented by letting the perpendicular velocity jump be a function of the sum of these two variables instead of the difference, that is $\Delta v_{12} = (u_{12}^{+} + u_{12}^{-}) \cdot \tan(\phi)$. This approach is not intuitively sound as for positive values for both degrees of freedom, the velocity jump will be wrong, however it is argued in [3] that in practical instances, this is almost never the case and given the case that both velocities are positive, the material will numerically behave stronger than in reality thereby maintaining a rigorous upper bound solution.

typo?

Continuing with the formulation, the tangential velocity jumps at the nodal pairs 1,2 and 3,4 equals, with respect to the element nodal velocity global degrees of freedom and the inclination of the discontinuity θ_d in cartesian coordinates:

$$u_{12} = (u_2 - u_1) \cdot \cos(\theta_d) + (v_2 - v_1) \cdot \sin(\theta_d) \quad u_{34} = (u_4 - u_3) \cdot \cos(\theta_d) + (v_4 - v_3) \cdot \sin(\theta_d) \tag{6.22}$$

Similarly, the perpendicular velocity jump is:

$$v_{12} = (u_1 - u_2) \cdot \sin(\theta_d) + (v_1 - v_2) \cdot \cos(\theta_d) \quad v_{34} = (u_1 - u_2) \cdot \sin(\theta_d) + (v_3 - v_4) \cdot \cos(\theta_d) \tag{6.23}$$

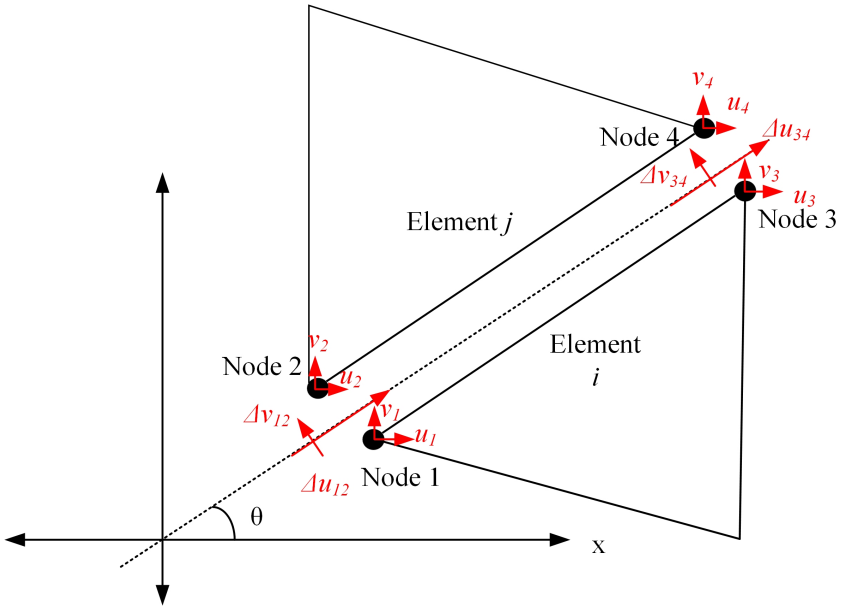

Figure 26: Illustration of discretized discontinuity velocity jump

Equating above equations 6.22 and 6.23 with equations 6.20 and 6.21 returns below equations 6.24, 6.25, 6.26 and 6.27:

$$(u_2 - u_1) \cdot \cos(\theta_d) + (v_2 - v_1) \cdot \sin(\theta_d) = u_{12}^+ - u_{12}^-, \qquad u_{12}^+ \geq 0, \quad u_{12}^- \geq 0 \tag{6.24}$$

$$(u_4 - u_3) \cdot \cos(\theta_d) + (v_4 - v_3) \cdot \sin(\theta_d) = u_{34}^+ - u_{34}^-, \qquad u_{34}^+ \geq 0, \quad u_{34}^- \geq 0 \tag{6.25}$$

$$(u_1 - u_2) \cdot \sin(\theta_d) + (v_1 - v_2) \cdot \cos(\theta_d) = (u_{12}^+ - u_{12}^-) \cdot \tan(\phi), \qquad u_{34}^+ \geq 0, \quad u_{34}^- \geq 0 \tag{6.26}$$

$$(u_1 - u_2) \cdot \sin(\theta_d) + (v_3 - v_4) \cdot \cos(\theta_d) = (u_{34}^+ - u_{34}^-) \cdot \tan(\phi), \qquad u_{34}^+ \geq 0, \quad u_{34}^- \geq 0 \tag{6.27}$$

Vectorizing above equations 6.24, 6.25, 6.26 and 6.27 returns the flow rule formulation for kinematically admissible velocity jumps between the finite elements. This vectorization is in shown below equation 6.28 for a discontinuity defined by the nodal pairs 1,2 and 3,4:

$$\mathbf{A}_{d,e} \cdot \begin{bmatrix} u_1 & v_1 & u_2 & v_2 & u_3 & v_3 & u_4 & v_4 \end{bmatrix}^T - \mathbf{A}_{d,d} \cdot \begin{bmatrix} u_{12}^+ & u_{12}^- & u_{34}^+ & u_{34}^- \end{bmatrix}^T = 0 \tag{6.28}$$

with $\begin{bmatrix} u_{12}^+ & u_{12}^- & u_{34}^+ & u_{34}^- \end{bmatrix} \geq 0$

Where $\mathbf{A}_{d,e}$ is the constraint coefficient matrix containing all the linear coefficients associated with the element velocity degrees of freedom and equals:

$$\mathbf{A}_{d,e} = \begin{bmatrix} -\cos(\theta_d) & -\sin(\theta_d) & \cos(\theta_d) & \sin(\theta_d) & 0 & 0 & 0 & 0 \\ \sin(\theta_d) & -\cos(\theta_d) & -\sin(\theta_d) & \cos(\theta_d) & 0 & 0 & 0 & 0 \\ 0 & 0 & 0 & 0 & -\cos(\theta_d) & -\sin(\theta_d) & \cos(\theta_d) & \sin(\theta_d) \\ 0 & 0 & 0 & 0 & \sin(\theta_d) & -\cos(\theta_d) & -\sin(\theta_d) & \cos(\theta_d) \end{bmatrix} \tag{6.29}$$

Similarly, the coefficient matrix containing the linear coefficients associated with the discontinuity velocity degrees of freedom equals:

$$\mathbf{A}_{d,d} = \begin{bmatrix} 1 & -1 & 0 & 0 \\ \tan(\phi) & \tan(\phi) & 0 & 0 \\ 0 & 0 & 1 & -1 \\ 0 & 0 & \tan(\phi) & \tan(\phi) \end{bmatrix} \tag{6.30}$$

The global constraint matrices are again created by summing over all the local ones with respect to global coordinates. This is shown in below equation 6.31 and 6.32, where D is the total amount of discontinuities and E is the total amount of elements:

$$\mathbf{A}_{d,e,global} = \sum_{d=1}^{D} \mathbf{A}_{d,e} \tag{6.31}$$

$$\mathbf{A}_{d,d,global} = \sum_{d=1}^{D} \mathbf{A}_{d,d} \tag{6.32}$$

Above equations 6.31 and 6.32 thereby concludes the constraints that forces inter-element velocity jumps to be kinematically admissible.

6.3 Upper bound boundary conditions

The upper bound boundary conditions are somewhat simpler to implement than the lower bound boundary conditions. The free edge boundaries requires no constraints and the supported boundaries can be modelled by forcing the velocities at those degrees of freedom to be zero. The loading is however tricky to implement in the case of more complex loading than a single point load. There is not as direct a connection between the upper bound boundary conditions and the applied load as in the lower bound, as in the case of the upper bound one models loading by forcing certain velocity degrees of freedom to be nonzero. This has the fallacy that it is not guaranteed that these imposed velocities corresponds to the velocities of the mechanism produced by the loading. In the case of a single point load, the correct velocity field can very accurately be assumed to be produced by forcing the velocity degree of freedom in the direction of the load and at the location of the load to be nonzero, however in the case of multiple point loads and distributed loads, the loading velocity boundary conditions are not obvious. Concluding this, the constraints coming from the boundaries are concatenated from the supported sides and the forced movement of the loaded degrees of freedom. The boundary constraint matrix therefore reads as in below equation 6.33:

$$\mathbf{A}_b = \begin{bmatrix} \mathbf{A}_{support} \\ \mathbf{A}_{load} \end{bmatrix} \cdot \mathbf{u}_e = \mathbf{b}_b \tag{6.33}$$

Where fore the case of a single point load, $b_b = \begin{bmatrix} 0 \\ 1 \end{bmatrix}$.

6.4 Objective function and energy dissipation

As mentioned previously, the aim of the upper bound formulation is to formulate an expression for the energy dissipated given a certain velocity field and plastic multiplier rates while being kinematically admissible. This subsection will describe how this energy dissipation is formulated and subsequently discretized to fit the linear velocity constant strain elements.

Power can be dissipated both by plastic flow in continuum meaning power dissipated by plastic flow within the elements and by plastic shearing in discontinuities. The power dissipated by plastic flow in a continua element e is equal to below integral 6.34:

$$P_e = \int_A (\sigma_x \cdot \dot{\varepsilon}_x + \sigma_y \cdot \dot{\varepsilon}_y + \tau_{xy} \cdot \dot{\gamma}_{xy}) dA \tag{6.34}$$

Reformulating above equation with respect to the linearization polygon as defined in equations 6.11, 6.10 and 6.12 returns:

$$P_c = \int_A \sum_{k=1}^{p} \dot{\lambda}_k \cdot (A_k + B_k + C_k) dA \tag{6.35}$$

If plastic flow occurs then $F(\sigma_{ij}) = 0$ and thereby: $\sum_{k=1}^{p} (\dot{\lambda}_k \cdot (A_k + B_k + C_k)) = D_k = 2 \cdot c \cdot \cos(\phi)$, with c being the material cohesion and ϕ being the angle of internal friction, allows the following rewriting of equation 6.35:

$$P_e = \int_A \sum_{k=1}^{p} \dot{\lambda}_k \cdot D_k dA \tag{6.36}$$

Now, applying the assumption of constant strain within the element, the integral is replaceable by the element area and the power dissipation on the triangle elements is formulated as:

$$P_c = 2 \cdot c \cdot \cos(\phi) \cdot A_e \cdot \sum_{k=1}^{p} \dot{\lambda}_k \tag{6.37}$$

The objective function for element e, $\mathbf{c_e}$ is a vector which multiplied by the design vector returns some scalar to be minimized. By vectorizing equation 6.37 with respect to the degrees of freedom of the plastic multiplier rates: $\mathbf{P}_{c,e} = \mathbf{c}_e^T \cdot \dot{\lambda}_e$, the contribution to the objective function from power dissipated by plastic flow within the elements is equal to below equation 6.38:

$$\mathbf{c}_e = \begin{bmatrix} 2 \cdot c \cdot \cos(\phi) \cdot A_e & 2 \cdot c \cdot \cos(\phi) \cdot A_e & . & . & 2 \cdot c \cdot \cos(\phi) \cdot A_e \end{bmatrix} \tag{6.38}$$

$$, \begin{bmatrix} \dot{\lambda}_{e,1} & \dot{\lambda}_{e,2} & . & . & \dot{\lambda}_{e,p} \end{bmatrix}$$

The power dissipated by plastic flow in discontinuities is equal to the product of the area of plastic shearing and the shear strength e.g in the discontinuity expressible by below integral:

$$P_d = \int_L c \cdot |\Delta u| dL \tag{6.39}$$

As we previously defined $|\Delta u| = (u^+ + u^-)$ to eliminate the non-linearity, the integral becomes:

$$P_d = c \cdot (u^+ + u^-) dL \tag{6.40}$$

Now vectorizing with respect to the nodal pairs (1,2), (3,4) defining the discontinuity and evaluating the integral with the assumption of linear variation of velocity, above equation 6.40 can be discretized into:

$$P_d = \begin{bmatrix} \frac{c}{2} & \frac{c}{2} & \frac{c}{2} & \frac{c}{2} \end{bmatrix} \cdot \begin{bmatrix} u_{12}^+ & u_{12}^- & u_{34}^+ & u_{34}^- \end{bmatrix}^T \tag{6.41}$$

The objective function contribution from power dissipated in discontinuities is thereby equal to:

$$\mathbf{c}_d = \begin{bmatrix} \frac{c}{2} & \frac{c}{2} & \frac{c}{2} & \frac{c}{2} \end{bmatrix} \tag{6.42}$$

The global objective function vector for the discontinuities and the continua elements are made by summing up equations 6.42 and 6.38 with respect to the global degrees of freedom: $\lambda_{e,global}, \mathbf{u}_{d,global}$ where E denotes the amount of elements and D denotes the amount of discontinuities:

$$\mathbf{c}_{e,global} = \sum_{e=1}^{E} \mathbf{c}_e \tag{6.43}$$

$$\mathbf{c}_{d,global} = \sum_{d=1}^{D} \mathbf{c}_d \tag{6.44}$$

These two contributions thereby conclude the objective function. Formulating it with respect to all the degrees of freedom $\beta_{global} = \begin{bmatrix} \mathbf{u}_{e,global} & \dot{\lambda}_{e,global} & \mathbf{u}_{d,global} \end{bmatrix}$ the global objective function $\mathbf{c}_{global}$ equals:

$$\mathbf{c}_{global} = \begin{bmatrix} \mathbf{0} & \mathbf{c}_{e,global} & \mathbf{c}_{d,global} \end{bmatrix} \tag{6.45}$$

And the power dissipated equals:

$$P_{global} = \begin{bmatrix} \mathbf{0} & \mathbf{c}_{e,global} & \mathbf{c}_{d,global} \end{bmatrix}^T \cdot \begin{bmatrix} \mathbf{u}_{e,global} & \dot{\lambda}_{global} & \mathbf{u}_{d,global} \end{bmatrix} \tag{6.46}$$

6.5 Recasting into a linear fractional program

So far we have limited the derivations to constituent parts of the optimization problem, which as formulated by Sloan [3] is formulated as:

Minimize $\mathbf{c}^T \cdot x$
Subject to:
$\mathbf{A}_{eq} \cdot x = \mathbf{b}_{eq}, \quad [\lambda_e, u_d] \geq 0$
Above can be clarified by inferring the notation used in this section to below equation:

Minimize $\begin{bmatrix} \mathbf{0} & \mathbf{c}_{e,global} & \mathbf{c}_{d,global} \end{bmatrix}^T \cdot \begin{bmatrix} \mathbf{u}_{e,global} & \dot{\lambda}_{e,global} & \mathbf{u}_{d,global} \end{bmatrix}$
Subject to:

$$\begin{bmatrix} \mathbf{A}_{e,v,global} & -\mathbf{A}_{e,\lambda,global} & 0 \\ \mathbf{A}_{d,e,global} & 0 & -\mathbf{A}_{d,d,global} \\ \mathbf{A}_b & 0 & 0 \end{bmatrix} \cdot \begin{bmatrix} \mathbf{u}_{e,global} \\ \dot{\lambda}_{e,global} \\ \mathbf{u}_{d,global} \end{bmatrix} = \begin{bmatrix} 0 \\ 0 \\ \mathbf{b}_b \end{bmatrix}$$
$$[\lambda_{e,global}, u_{d,global}] \geq 0 \tag{6.47}$$

The issue here, as stated earlier is that as the problem is phrased now, there is no direct correlation between the loading pattern and the minimized mechanism, meaning that only if the user is able to accurately predict the proportionality of the velocity field with respect to the loading pattern will the solution be correct. This is not an issue if for instance, an object is loaded with a single local load then an obvious velocity boundary condition to impose is that the velocity in the direction of the load at the point of the load will be non-zero. However given multiple loads it is not given that the correct mechanism is directly proportional with said pattern.

The issue arises once the internal power dissipated is equated to the external power applied:

$$W_{ext} = W_{int} \tag{6.48}$$

Which expands to:

$$\gamma \cdot \mathbf{p}^T \cdot \mathbf{u}_p = \mathbf{c}_{global}^T \cdot \begin{bmatrix} \mathbf{u}_{e,global} & \dot{\lambda}_{global} & \mathbf{u}_{d,global} \end{bmatrix} \tag{6.49}$$

Where $\mathbf{p}$ is the vector controlling the proportionality of the applied loads, γ is the load multiplier and lastly $\mathbf{u}_p$ is the vector of displacements at the load locations. Rearranging the equation and isolating the load multiplier γ returns:

$$\gamma = \frac{\mathbf{c}_{global}^T \cdot \begin{bmatrix} \mathbf{u}_{e,global} & \dot{\lambda}_{global} & \mathbf{u}_{d,global} \end{bmatrix}}{p^T \cdot \mathbf{u_p}} \tag{6.50}$$

Above equation 6.50 is non-linear as both the denominator and the numerator of the fraction is dependent of the velocity field. To include this coupling between the loading and the mechanism the program therefore has to be moved outside the bounds of regular linear programming. There exists however, a technique called linear fractional programming where a programming problem of a fraction of linearly linear objective functions, thereby being non-linear, is recasted into a linear programming problem by a Charnes-Cooper transformation where basically, a transformation of the independent variables is made and the denominator is forced to equal a scalar, that is the norm of the solution is forced. What is meant here is, that since the programming problem contains the velocity field both in the numerator and the denominator, the problem can be infinitely scaled, so one has to force the problem to have a certain length which in conjunction with the change of variable allows a solution. Why this transformation is allowable will not be explained here, it is however explained in [20], but it recasts a fractional problem on the canonical form:

Minimize $\frac{\mathbf{c}_{global}^T \cdot \mathbf{x} + \alpha}{\mathbf{d}^T \cdot \mathbf{x} + \beta}$
Subject to: $\mathbf{A} \cdot \mathbf{x} \leq \mathbf{b}$
Where $\mathbf{c}$ and $\mathbf{d}$ are vectors, and α and β are scalars, and rephrases into a regular linear programming problem on the form:

Minimize $\mathbf{c}^T \cdot \mathbf{y} + \alpha \cdot t$
Subject to: $\mathbf{A} \cdot \mathbf{y} \leq \mathbf{b} \cdot t$

$$\begin{aligned}&\mathbf{d}^T \cdot \mathbf{x} + \beta \cdot t = 1\\ &[t] \geq 0\end{aligned} \tag{6.51}$$

The original design vector $\mathbf{x}$ has been transformed into $\mathbf{y}$ and an independent variable t has been added to the original design vector which is restrained to be non-negative. The transformation equals:

$$\mathbf{y} = \frac{\mathbf{x}}{\mathbf{d}^T \cdot \mathbf{x} + \beta}, \quad t = \frac{1}{\mathbf{d}^T \cdot \mathbf{x} + \beta} \tag{6.52}$$

Where it follows that once a solution to the problem in equation 6.5 is found, then the solution to the original problem is obtained by:

$$\mathbf{x} = \frac{\mathbf{y}}{t} \tag{6.53}$$

Adapting the upper bound minimization problem in equation 6.47 with the change of objective function from $\mathbf{c}_{global}^T \cdot \mathbf{x}$ to $\lambda = \frac{\mathbf{c}^T \cdot \begin{bmatrix}\mathbf{u}_{e,global} & \dot{\lambda}_{global} & \mathbf{u}_{d,global}\end{bmatrix}}{p^T \cdot \mathbf{u_p}}$ requires some reformulation of the problem, as the canonical linear fractional problem is without equality constraints, holding only the fractional objective function and inequalities. The equality constraints $\mathbf{A}_{eq} \cdot \mathbf{x} = \mathbf{b}_{eq}$ are recast into inequalities by:

$$\mathbf{A}_{eq} \cdot \mathbf{x} \geq \mathbf{b}_{eq}, \quad \mathbf{A}_{eq} \cdot \mathbf{x} \leq \mathbf{b}_{eq} \tag{6.54}$$

Which is further made into a constraint on the form $\mathbf{A} \cdot \mathbf{x} \leq \mathbf{b}$ by:

$$\begin{bmatrix}\mathbf{A}_{eq}\\ -\mathbf{A}_{eq}\end{bmatrix} \cdot \mathbf{x} \leq \begin{bmatrix}\mathbf{b}_{eq}\\ -\mathbf{b}_{eq}\end{bmatrix} \tag{6.55}$$

The scalars α and β in the canonical linear fractional problem are zero, and the vector $\mathbf{c}$ is the power dissipation coefficients $\begin{bmatrix}\mathbf{0} & \mathbf{c}_{elements,global} & \mathbf{c}_{discontinuities,global}\end{bmatrix}^T$ and the vector $\mathbf{d}^T$ is the vector $\mathbf{p}$ controlling load proportionality e.g for equal loading, it will be a unity vector for the loaded degrees of freedom. The upper bound linear fractional programming problem is thereby equal to:

Minimize $\lambda = \mathbf{c_global}^T \cdot \begin{bmatrix}\mathbf{u}_{e,global} & \dot{\lambda}_{e,global} & \mathbf{u}_{d,global}\end{bmatrix}$
Subject to:

$$\begin{bmatrix}
\mathbf{A}_{e,v,global} & -\mathbf{A}_{e,\lambda,global} & 0 \\
\mathbf{A}_{d,v,global} & 0 & -\mathbf{A}_{d,d,global} \quad 0 \\
\mathbf{A}_{boundary} & 0 & 0 \\
-\mathbf{A}_{e,v,global} & \mathbf{A}_{e,\lambda,global} & 0 \\
-\mathbf{A}_{d,v,global} & 0 & \mathbf{A}_{d,d,global} \quad 0 \\
-\mathbf{A}_{b,global} & 0 & 0
\end{bmatrix} \cdot \begin{bmatrix}\mathbf{u}_{e,global}\\ \dot{\lambda}_{e,global}\\ \mathbf{u}_{d,global}\end{bmatrix} \leq \begin{bmatrix}0\\0\\0\end{bmatrix}$$

$$\mathbf{p}^T \cdot \begin{bmatrix}\mathbf{u}_{e,global} & \dot{\lambda}_{e,global} & \mathbf{u}_{d,global}\end{bmatrix} = 1$$

$$[\lambda_{e,global}, u_{d,global}] \geq 0 \tag{6.56}$$

What is noticeable in above expression, is that the equality of $\mathbf{p}^T \cdot \begin{bmatrix}\mathbf{u}_{e,global} & \dot{\lambda}_{e,global} & \mathbf{u}_{d,global}\end{bmatrix} = 1$ forces movement in the system and therefore one can omit to force movement in the boundary condition constraints, where the only boundary constraints left are supports where movement is forced to be zero which makes the entire constraint matrix homogeneous resulting in the model

very being cheap to evaluate in the Matlab linear programming solver. This homogeneity of the constraint matrix also means that the added variable t in the transformation can be omitted as there are no constraints controlling it and it can therefore assume any positive value without influencing the final result. This thereby concludes the upper bound formulation and given the equality $\mathbf{p}^T \cdot \begin{bmatrix} \mathbf{u}_{e,global} & \dot{\lambda}_{e,global} & \mathbf{u}_{d,global} \end{bmatrix} = 1$ which forces the denominator in equation 6.50 to 1, then the applied load multiplier and exterior work done is obtained by:

$$\gamma = \mathbf{c}_{global}^T \cdot \begin{bmatrix} \mathbf{u}_{e,global} & \dot{\lambda}_{e,global} & \mathbf{u}_{d,global} \end{bmatrix} \tag{6.57}$$

The total upper bound collapse load Q_{ub} is then determined by summing the forces $Q_{e,i}$ acting on each element:

$$Q_{e,i} = \frac{1}{2} \cdot \gamma \cdot p_i \cdot t \cdot l_e (u_{1,e} + u_{2,e}) \qquad Q_{ub} = \sum_{i=1}^{e_{load}} Q_{i,e} \tag{6.58}$$

Where l_e is the length of the loaded element side, t the out of plane thickness, $p_{e,i}$ is the relative load factor for the specific element, $u_{1,e}$ is the velocity of the first loaded degree of freedom of the loaded side in the direction of the load and $u_{2,e}$ is the second.

7 Experimental program

The experimental program tests a progressive collapse scenario of calcium silicate masonry wall with cement based thin layer masonry mortar. The collapse scenario was simulated by an instant removal of a center column in a two-span unreinforced masonry frame leaving the beam element to act as a deep beam. The sudden column loss was made by pulling a build-in T-profile simulating instant removal. Preparatory to the column removal the wall was loaded with a hydraulic jack as previously shown in figure 11 simulating the effects of an evenly distributed gravity load from hypothetical above storeys and floors schematised in below figure 27.

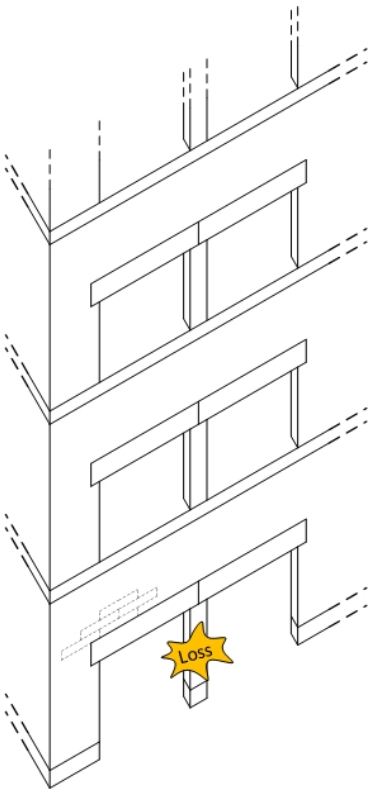

Figure 27: Isometric of simulated collapse scenario

7.1 Purpose of experimental program

The experimental program was intended to either verify or deny compressive arch action as load bearing mechanism within unreinforced masonry structures experiencing local failure, where the presence of this assumed load bearing mechanism is argued for in Appendix E section E.3.1 and was summarized in section 2.
Referring to the classification method in Adam et al. [4] the experimental setup was a mix between a sub-assemblage and a specimen of a masonry structure. The specimen was made as accurately to new-build calcium silicate masonry structures as the lab facilities allowed, hereby making the test of mechanisms resisting progressive collapse tested within a realistic environment of modern masonry construction allowing for reliable results. The justification of the experimental investigations is argued for in Appendix E in section E.3.2 and summarized in section 3, but a brief summary is that similar experimental test in masonry is unseen and that it is a necessity to learn of the mechanics of masonry structures experiencing local failure to be

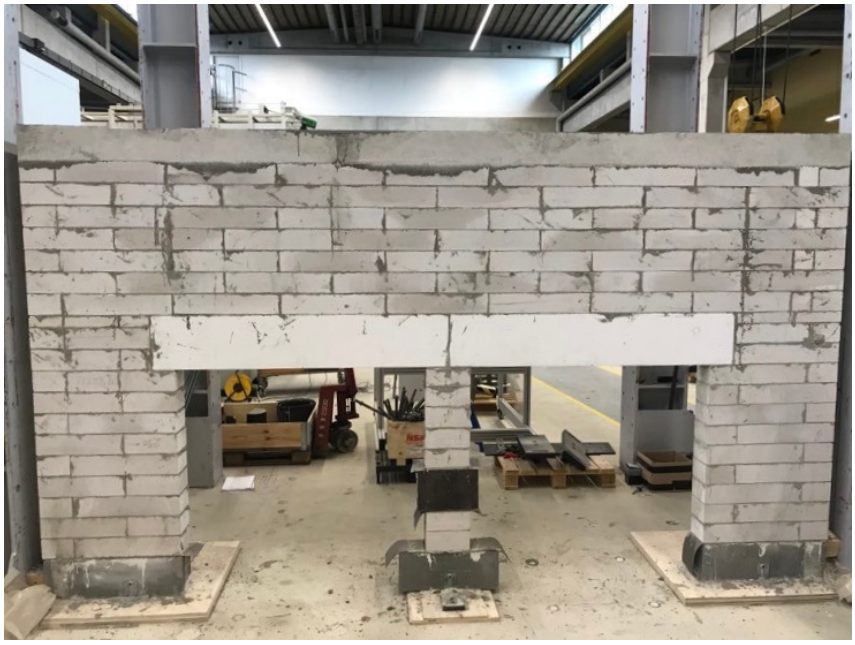

Figure 28: Picture of the experimental specimen

able to improve the knowledge of robustness related issues of masonry structures.
Compressive arch action in masonry panels and catenary action in concrete slab beams when a structure undergo large deformations are commonly expected collapse resisting mechanisms within masonry constructions, but are yet to be shown under conditions of sudden loss of load bearing structural elements.
Large scale tests of the effects of local failures within masonry structures are concluded in Appendix E section E.3.2 as objective of future research, but the opportunity of testing a building condemned to be demolished was not present, why the current priority was given to the investigation of compressive arch action in a two dimensional purpose build lab size wall piece.
To summarize the main purpose from a numerical point of view as described in section 4.3 the acquired test results were intended to validate the numerical modelling framework established in section 5 and 6 as suitable frameworks to perform a deep beam predictions with the inclusion of sudden deep bending action due to column loss, and hereby solve issues of robustness of masonry structures by being able to predict alternative load paths.

7.2 Test setup and procedure

The test specimen was designed as a segment of a facade elevation with two window sized openings and was supported out-of-plane with two intersecting pillars. The construction drawings of the experimental test object in Appendix A shows the intended design and contain details on specific boundary solutions.

The masonry wall was build on unreinforced concrete foundations mounted with angle brackets on a plywood plate fastened to strong floor. In this way foundation was restrained against movement both in and out of plane, hereby simulating the conditions of a continues foundation beam. Vapour seal was placed between the concrete and the calcium silicate blocks as in new build masonry structures to replicate the friction properties of the interface. Figure 29 shows pictures of foundation doing the construction process. In sub-figure 29a it can be seen that the concrete blocks where placed against the steel frame preventing movement in this di-

(a) In-plane movement restraining

(b) Casting of concrete foundation

(c) Out-of-plane movement restraining

Figure 29: Foundation of masonry wall specimen

rection, where the angle brackets shown in sub-figure 29c prevent movement in the orthogonal direction. In sub-figure 29c the vapour seal in the interface between the masonry blocks and concrete foundation is also visible and sub-figure 29b pictures the casting process.
The masonry part of the wall specimen as made with H+H calcium silicate 1900 K10 adaptation bricks as calcium silicate units are frequently used as load bearing elements in modern masonry construction. Though the elements normally used have larger dimensions than what was used to construct the test specimen, the smaller K10 adaptation bricks was chosen so that the test object would have additional bed joints. The bed joints were assumed as the planes of weakness of the masonry and with additional bed joints the compressive force in the arch action would have to pass more interfaces and with different angles. This allows the test results to be more generalizable and to be less dependent of the individual brick strengths. Figure 30 sketches the differing angles between the compressive arch force and the bed joints.
Above the openings were placed autoclaved aerated concrete beams as in typical masonry construction both with minimum 100mm bearings on the pillars as recommended by the manufacturer H+H, who supplied the 15M26-141 beams. The height of the remainder of wall segment, and so the height of the masonry deep beam, was based on a typical story height to be about 700mm equal to 7 courses. The autoclaved aerated concrete beams and the 7 course high deep beam is depicted in figure 31.
On top of the masonry panel a slab beam was casted to imitate the effects of peripheral rein-

forcement in concrete slabs. Normally, peripheral ties is placed eccentric to the wall plane, due to the slab bearings on top of the wall why the slab beam is eccentric to wall plane. To avoid any out-of-plane moments from loading the test specimen directly on the slab beam the width was casted the same as the masonry wall and two Y10 reinforcement bars was placed in plane with the wall. To ensure full anchorage of the reinforcement at the end of the wall and simulate a continues peripheral stringer 4 rods were casted in and bolted at the end of the intersecting pillars and tied together with the two Y10 steel bars with L-bars. Figure 32 shows the used reinforcement before the concrete was casted.
The central column which was to be removed doing the test, was constructed with a steel T-profile build in between two bricks as shown in figure 33a. The profile acted as pulling device where a tension cable was fastened and pulled to provide the necessary tension force needed to remove the column. In the surrounding courses two layers of vapour seal was placed instead of the thin layer mortar to create two friction-less interfaces easing the collapse.

The test specimen was deigned with two intersecting walls to support the wall segment against out-of-plane movements, but additional measures was taken to accommodate a possible scenario where the pulling force from the column removal would introduce out-of-plane rotation, which could provoke another collapse than of a compressive arch passing its limits. Below figures of wooden elements installed a few millimeters from the wall, such that theirs support

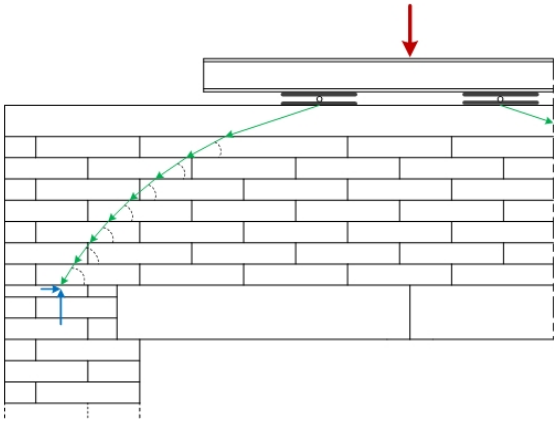

Figure 30: Arch action compressive force passing interfaces with different angles

Figure 31: Autoclaved aerated concrete beams and K10 bricks

(a) Peripheral reinforcement

(b) Anchorage of reinforcement

(c) In-sito rods

Figure 32: Reinforcements of slab beam

(a) Front of collapse setup

(b) Back of collapse setup

(c) Mounted tension cable

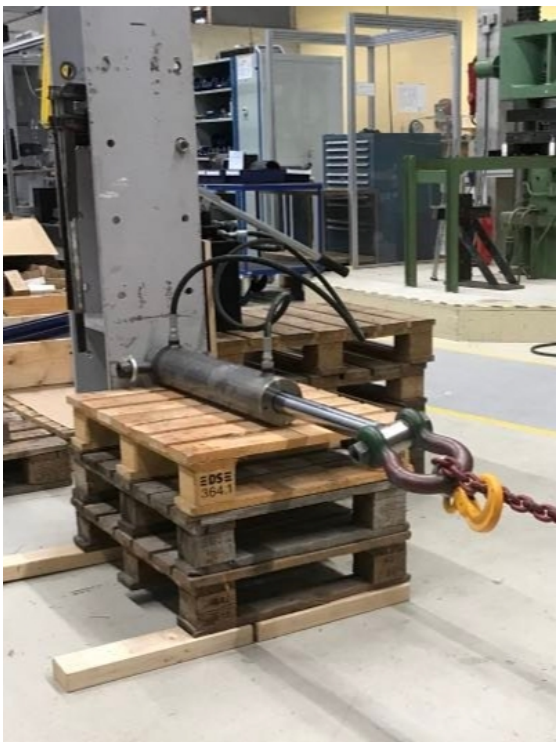

(d) Manual hand jack

Figure 33: Steel T-profile collapse mechanism

function only were activated if necessary and any vertical effects was avoided.

The experimental test consist of three main procedures as schematized on below figure 35, firstly, loading of the wall, secondly, removal of the center column, and thirdly, loading until total collapse.

(a) Front of collapse setup (b) Back of collapse setup

Figure 34: Additional out-of-plane supports

In the first step the wall is loaded with 50kN, hereby simulating a serviceability stress state in the wall due to gravity loads from floors supported by the wall and gravity loads from hypothetical storeys above. The supports of the load distributing beam are placed at the central plane off the aerated concrete beams to simulate a distributed load the best, thereby ensuring the best conditions for a compressive arch to be developed when the central column is removed.
The second step proceeds from the first step by initiating the column removal and is a very crucial step, where the preparatory loading forms the basis for testing the masonry walls vulnerability to sudden column loss. The removal will show whether the wall instantly will collapse progressively or have sufficient displacement capacity to redistribute and withstand a sudden step load and the dynamic effects hereof, which will make the third step possible.
In the third step the wall is brought to total collapse by raising the applied load. If this step is reached a progressive collapse resisting mechanism has taken action and forcing total collapse will reveal the type of mechanism and its load capacity.

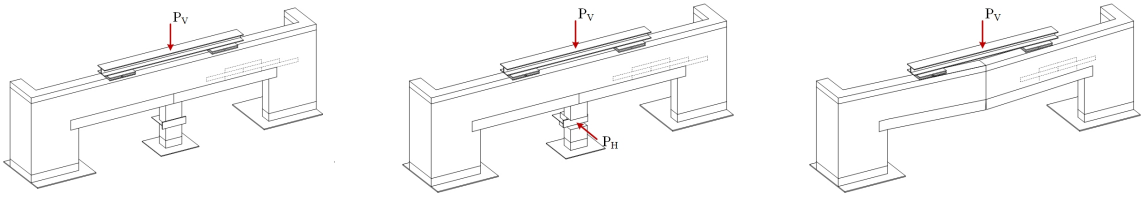

(a) Loading of the wall (b) Removal of the center column (c) Load until total collapse

Figure 35: Main procedures of experimental test

7.3 Experimental equipment

The test specimen was loaded with a hydraulic jack that applied load to a load cell mounted on a HEB200 steel beam distributing the load to two supports free to rotate in the walls direction, hereby accommodating for large deformations of the specimen. The load sought to imitate gravity loads from hypothetical storeys and floors above which in reality are constant doing a collapse, but due to the load being applied with a hydraulic jack, the applied pressure decreased when the test object deformed, why the pressure was constantly reapplied doing the test. If the experimental facilities had allowed it, this issue could have been avoided by applying load with a hydraulic actuator under load-control while it at the same time would supply load-displacement data.
The pulling force used to remove the central column was provided by a manual hand jack slowly pulling the T-profile through the column hereby making the collapse more controlled and less instant.

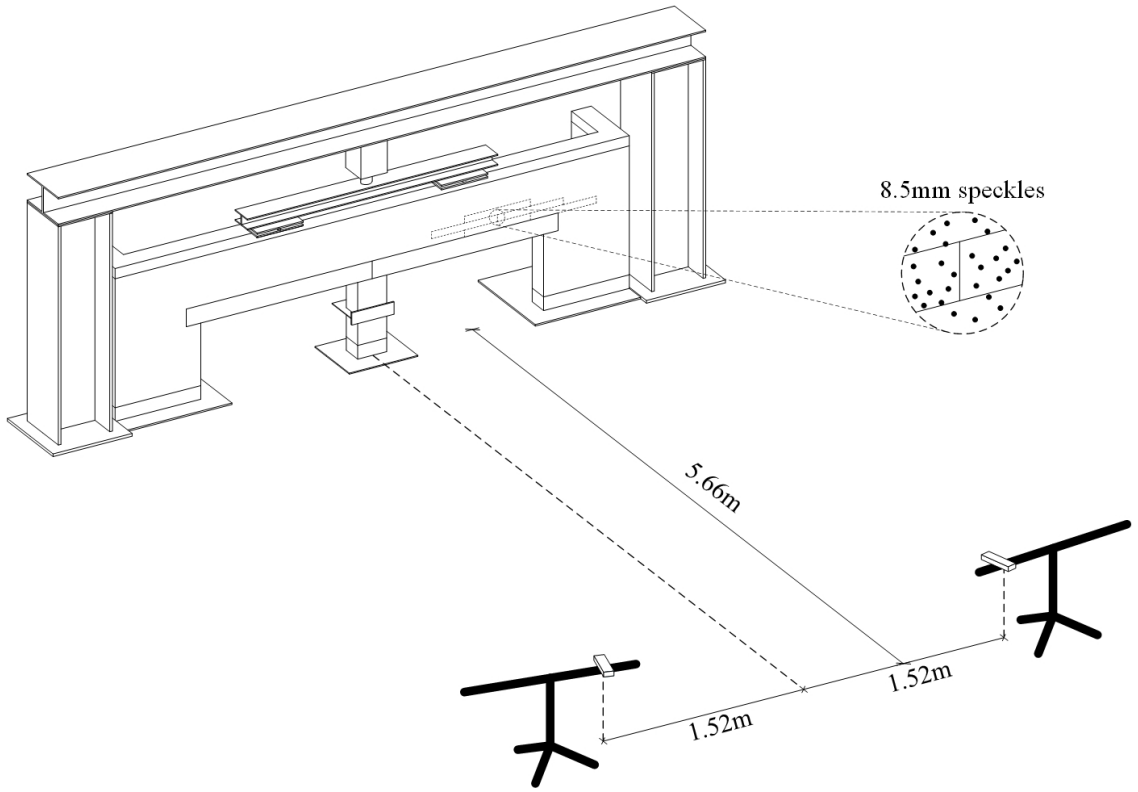

Figure 36: Setup of DIC system

Digital Image Correlation(DIC) was used to monitor the wall doing the collapse test. DIC is an optical method which measures deformation on an object's surface. This is done by comparing unique speckles from reference picture before deformation has occurred and a picture where the object has deformed. VIC-3D systems from Correlated Solutions was utilized to post-process the pictures taken with two Basler acA1920-155um cameras. As shown in figure 36, the cameras was calibrated at a distance of 5.66m to test specimen and with an internal distance 3.04m, and lighted up with two 85Watt LED spots lights placed in between the cameras as close to wall as possible with entering the camera view. The camera view was cropped to a view showing from the slab beam to middle of the masonry pillars such that the cameras could capture 200 frames per second.
The wall was carefully painted with a non-reflecting white color in a very thin layer to ensure

optimal contrast with the black speckles that had a diameter of 8.5mm. Painting the background color in too thick a layer could have the consequence that the crack pattern visible on the painted surface is different from the actual crack pattern behind the painted surface, why paint job was performed with utmost concerns.

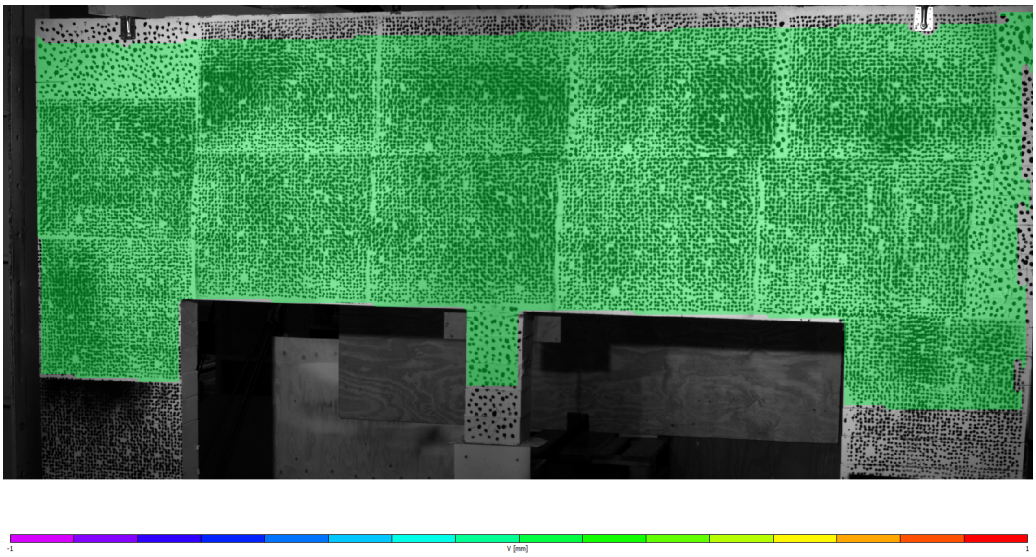

(a) Still picture 1

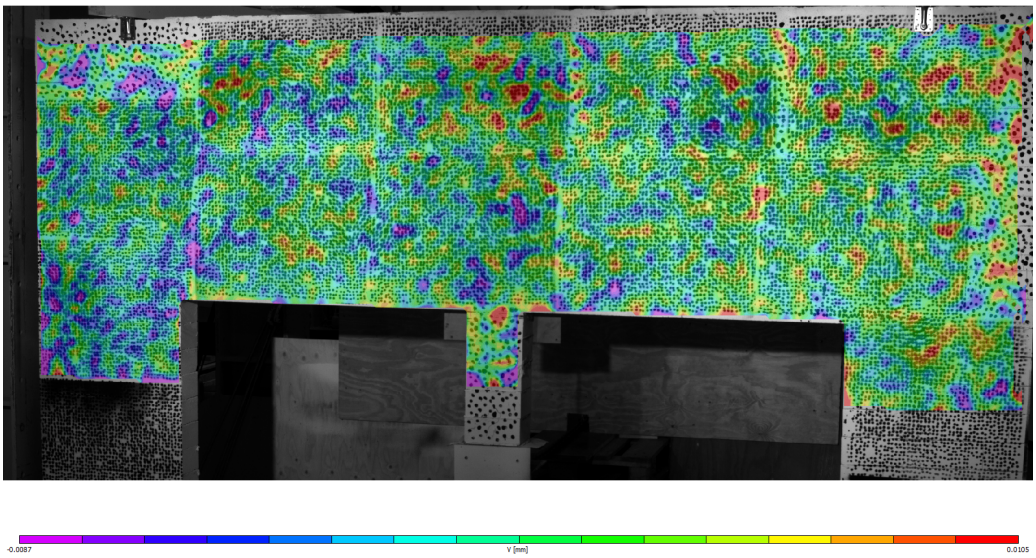

(b) Still picture 2

Figure 37: Speckle noise test

The speckle pattern was generated with Correlated Solutions speckle generator program, where a pattern with 8.5mm speckles with a density of 75% and a variation 60% has been tested before hand and was proven a sufficient speckle pattern at the required distance. A noise test was performed as shown on figure 37, where two still picture of the test object with contour plots of vertical displacements were investigated. Figure 37a was the picture first taken and the reference picture, why the displacements plotted are zero and the wall was undeformed. Figure 37b was another picture of the unloaded wall taken a split second later, where the specimen seemed to have deformed about 0.03mm, though it had not been subjected to any new loads and should have been zero as well. This noise could be due to speckle pattern errors and poor light

conditions and could blurry the test results. VIC-3D can perform likewise noise tests on a series of pictures, finding the the 1-standard deviation confidence in the match in pixels. Comparing figure 38a showing the speckles and figure 38b showing a contour plot of the standard deviation confidence, it can be interpreted that the noise and uncertainty of the results tend to cluster and raise where the speckles are more blurred and the contrast between background color and the speckles was bad. As 0 indicates a perfect match a standard deviation confidence interval of 0.013 pixels was considered sufficient for this large displacement test, or in other words, a maximum noise of 0.01mm as depicted on figure 37b, was considered to be enough precision to describe deformation field of a large displacement test.

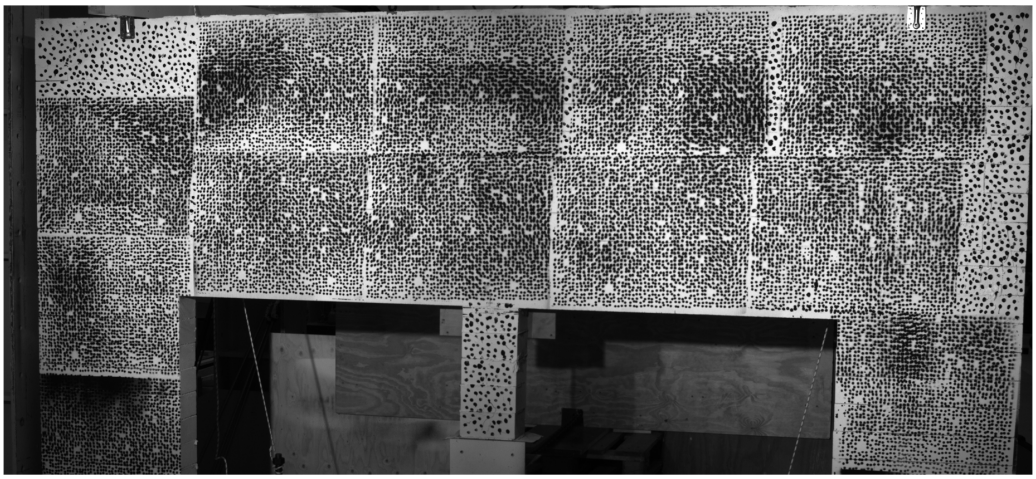

(a) Speckles on the specimen

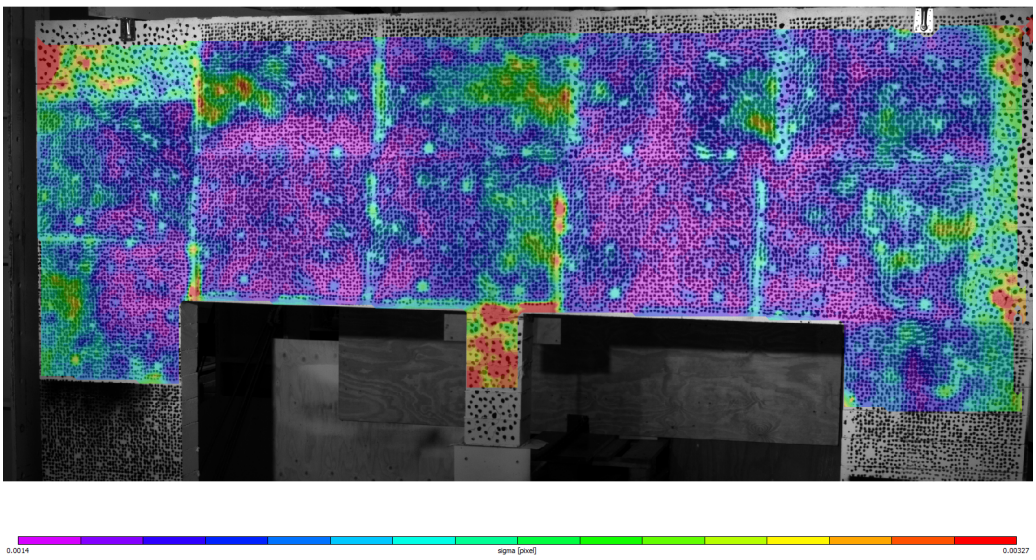

(b) Standard deviation confidence of the test results

Figure 38: Confidence speckle noise test

7.3.1 Material tests

Experimental tests of the concrete compressive strength and cohesion and internal angle of friction of masonry specimens were performed two days prior to collapse test of masonry wall performed the 25th of May. The tests were performed as close to the execution date of the collapse test as possible and were used to calibrate the numerical prediction framework with as

accurate material parameters as possible. The material tests are reported in Appendix B, but the essentials of the studies will be outlined below.

Concrete cylinder compressive strength test

Compressive strength tests were performed on three concrete cylinders in accordance with EN 12390-3 Testing hardened concrete - Part 3: Compressive strength of test specimens[21]. The three cylinders had hardened in 21 days, which is 7 days less than the recognized 28 days of hardening for concrete to have its full strength. The specimens had a diameter of 100mm and a height of 200mm, wherefrom two of three cylinders were not compacted probably doing the casting process, which resulted in a reduced cross section area at the top. The concrete cylinders were tested on at a time in a uni axial test setup with a loading rate of 1.71 $^{kN}/_{s}$, where the compressive strengths obtained are tabulated in below table 3 recreated from Appendix B. Though the number of samples is few, the compressive strength of second concrete cylinder is seen as an outlier due to its very low compressive strength compared with the other two, why it is disregarded. The average compressive strength equals 25.04MPa, which in conclusion is the compressive strength of the concrete used in the top slab beam. The test setup shown on below figure 39 along with the failure type of cylinder one in figure 40.

Figure 39: Concrete cylinder test setup

Figure 40: Failure of cylinder 1

Table 3: Measurements and observation of concrete cylinders

Sample	Cross section area	Compressive strength	Failure type
[-]	$[mm^2]$	$[MPa]$	[-]
1	7854.0	24.82	Figure 68.4
2	7854.0	18.76	Unsatisfactory
3	7854.0	25.25	Figure 68.4

Initial shear strength test of calcium silicate masonry

Initial shear strength tests on four calcium silicate masonry samples with KS Blokfix thin layer masonry mortar were conducted in accordance with EN 1052-3 Methods of test of masonry - Part 3: Determination of initial shear strength[22]. The masonry samples were made the same day the masonry wall was build with the same calcium silicate units and mortar batch, allowing them to have hardened in 24 days when they were tested the 23rd of May.
With a clamp like setup like shown on below figure 41 the samples was precompressed to four different compressive stress states of 0.2MPa, 0.6MPa, 0.8MPa, and 1.0MPa, before vertical load was applied to the center brick with an actuator speed of $0.1\frac{mm}{min}$ ensuring a slow fracture and a good depiction of the plastic domain of calcium silicate mortar interfaces. All four samples failed in the mortar leaving the mortar-brick interface intact as the failure of sample 2 visualize in figure 42. The similar types of failure is a good indication that the thin layer mortar is the weak link in calcium silicate masonry, but obviously more tests are needed to conclude this for sure.

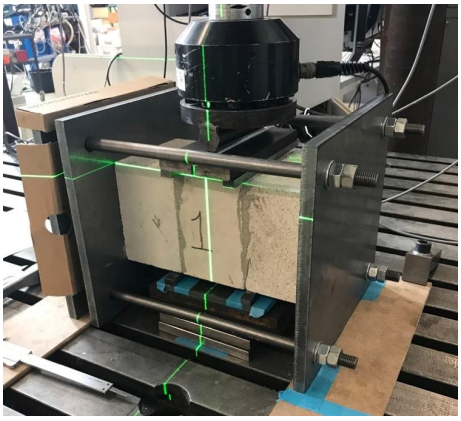

Figure 41: Shear strength test setup

Figure 42: Failure in mortar sample 2

Table 4 below is a recreated table reported in Appendix B, which contains sample data of cross section areas, precompression loads, maximum vertical loads, resulting initial shear strengths, and failure types. The individual shear strengths are plotted against their individual normal compressive stresses on subsequent figure 43, where from their relationship is determined from linear regression as EN 1052-3 prescribes[22]. The internal friction angle was recorded as the slope of the line and cohesion the intersection of the line with the vertical axis to be 26.11° and 0.25MPa, respectively.

Table 4: Measurements and observation of masonry samples

Sample [-]	Cross section area $[mm^2]$	Precompression load $[MPa]$	Vertical load $[kN]$	Initial shear strength $[MPa]$	Failure type [-]
1	22657.8	0.2	16.37	0.36	Figure 73c
2	22454.6	0.6	25.52	0.57	Figure 73c
3	22574.8	0.8	24.32	0.54	Figure 73c
4	22447.5	1.0	36.13	0.8	Figure 73c

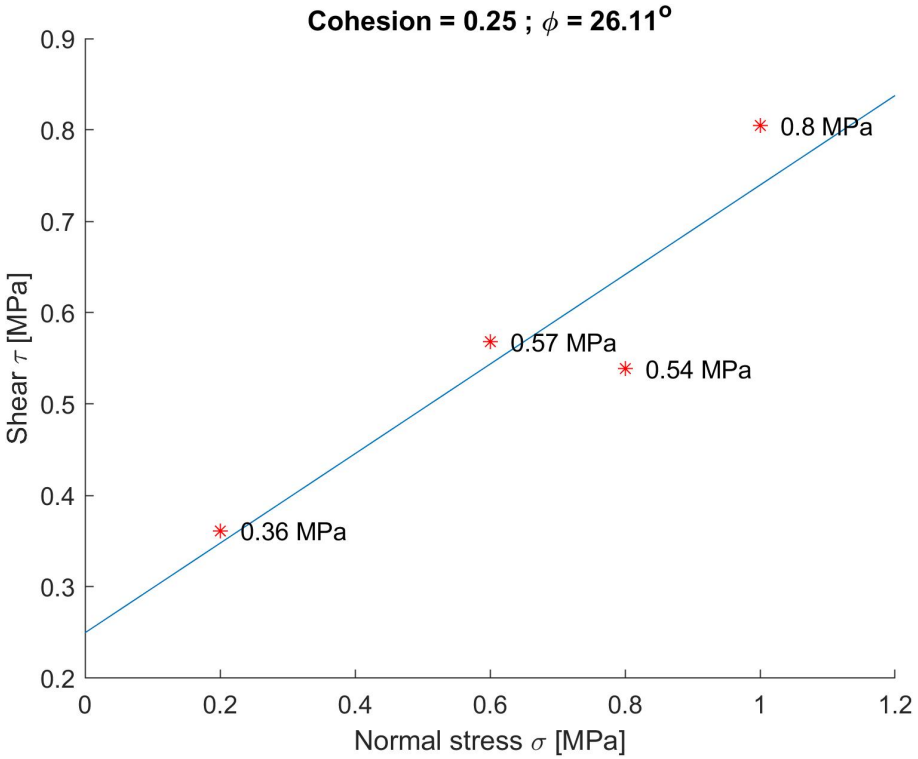

Figure 43: Relationship between shear and normal compressive stresses

8 Numerical predictions

8.1 Meshing and material parameters

To numerically characterize the experimental setup the meshing of the geometry must accurately allow the the five failure modes described in section 4, figure 12 to be non-restricted by the specific mesh-configuration. The general meshing layout is therefore done as conceptually shown in figure 44. The Mohr-Coulomb yielding model is made without a compression cap and therefore failure in compression is already disallowed from happening. This is justified by the purpose of the program being to model deep beam behavior and therefore failure in compression is unlikely to occur before a tension or shear failure occurs. Below figure 44 shows the nodal layout of a full brick-two half brick ensemble. The meshing is shown with blue lines while the joint layout of the ensemble is sketched with yellow lines. As no joint specific nodes are created, the local nodes located adjacent to a joint line are created as such to obey the yielding criteria for both the brick/solid material and that of the joint of which it is adjacent to with respect to the inclination plane of this specific joint.

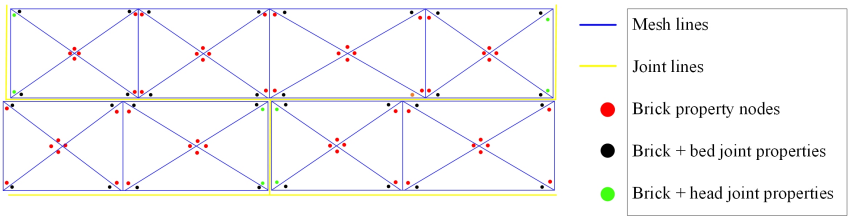

Figure 44: Micro-scale meshing

Similarly, each individual full-size brick is discretized into at least four quadrants of four triangles each which allows failure to occur as shown in below figure 45, where the four basic failure modes of vertical brick joint tensile failure, diagonal shear-compression failure, horizontal joint tensile failure and horizontal joint shear failure is all non-prohibited by the meshing.

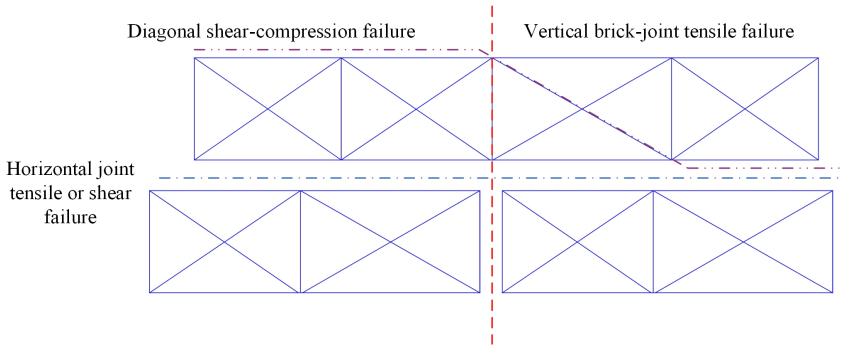

Figure 45: Failure types allowable by meshing

The global meshing is done by the principles outlined above. As the areas with concrete and aerated autoclaved concrete are materially more continuous the meshing can be done a bit more freely in these areas. Around the corners of the aerated autoclaved concrete beams and in the area of the applied loading were the stress field is expected to change in the case of the lower bound, and the velocity field expected to rotate in the case of the upper bound, the meshing needs to be quite fine in order to let this happen. The meshing layout is done in the open-source software GMSH and the meshing is shown in below figure 46 with a characteristic element length of 0.12m .

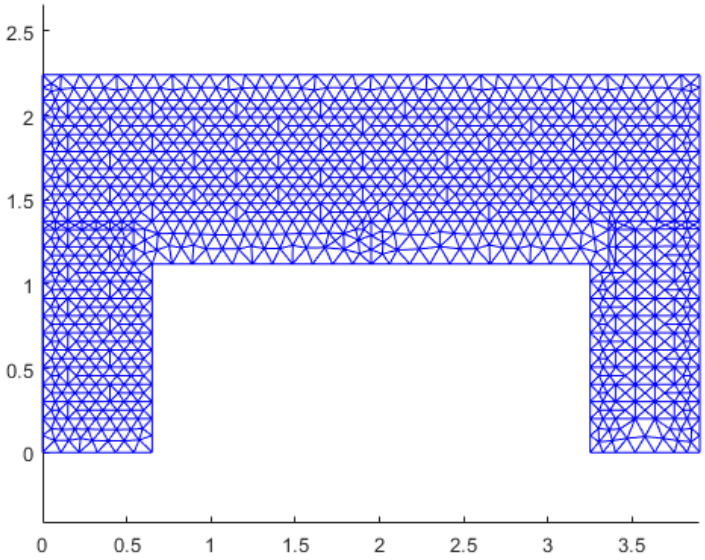

Figure 46: Basic meshing of experimental setup

The applied material properties are displayed in below figure 47, where the different solid materials are displayed with red-brown colour for the CSU-bricks, gray for the concrete, light blue for the aerated autoclaved concrete and the joints are outlined with yellow lines. The red lines are loaded vertically, and the green lines are supported vertically and horizontally, where for the lower bound model the vertical normal stresses and shear stresses are non-restricted with respect to equilibrium, meaning the vertical normal stress and the shear stress is supported, but not the horizontal normal stress, as in reality any horizontal forces must be transferred at the bottom in shear.

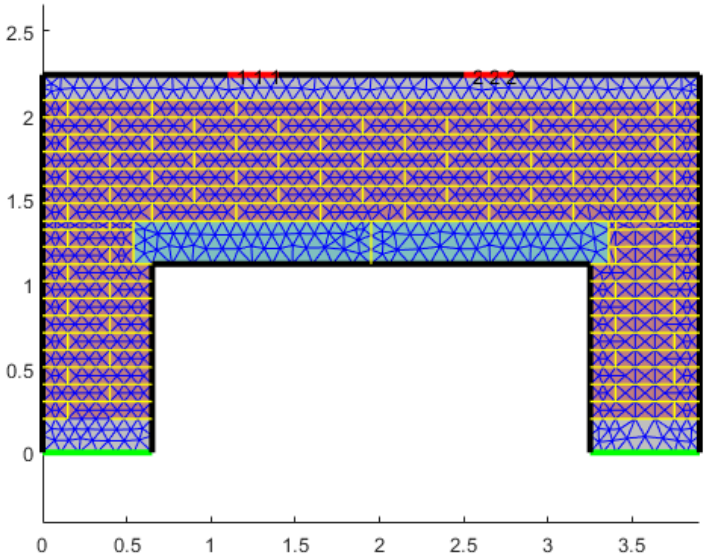

Figure 47: Meshed setup with applied properties

Above figures show the meshing with a characteristic length of 0.12m. Calculations has

been run with other mesh sizes as shown in tables 6, 8, 7 and 9, illustrations of these meshes are shown in Appendix D.

The applied material parameters are as follows in table 5 table, the reasoning behind the parameters are explained afterwards:

Table 5: Applied material property table

which one are measured with material testing?

Parameter	Denotation	Value
CSU-brick cohesion	c_{brick}	2.127 MPa
CSU-brick angle of internal friction	ϕ_{brick}	45°
Unreinforced concrete cohesion	c_{URC}	4.085 MPa
Unreinforced concrete angle of internal friction	ϕ_{URC}	51.8°
AAR concrete cohesion	c_{AAR}	0.13 MPa
AAR concrete angle of internal friction	ϕ_{AAR}	25.6°
Joint cohesion	c_{joint}	0.25[MPa]
Joint angle of internal friction	ϕ_{joint}	26.1°

The only material parameters known with good accuracy are the ones for the joints as they have been tested. The other material parameters are based on experiments conducted by others, that fits the materials in the experiment conducted the best.

The first parameters are that of the calcium silicate bricks. Finding experiments done on cohesive strength and internal angle of friction for these as a stand-alone material has been tricky, as shear tests on masonry usually is done as an assemblage of bricks and joints. However, Hulse and Ambrose [23] has conducted a series of tests on regular clay bricks where they test the initial shear strength, $f_{v,0}$, which practically equals the cohesion, in relation to the bricks compressive strength f_c. They infer the relationship as in equation 8.1, with all units in MPa:

$$f_{v,0} = \frac{f_c}{31} + 1.45 \tag{8.1}$$

Applying this to the H+H calcium silicate bricks with a declared mean compressive strength of 24.4 MPa returns:

$$c_{brick} = \frac{24.4MPa}{31} + 1.45MPa = 2.127MPa \tag{8.2}$$

The internal angle of friction has not been tested for the single brick case however, Sutcliffe [16] applies an angle of 45 degrees for regular clay bricks and the same is adopted here.

The parameters of concrete is a bit trickier as the top beam is reinforced with longitudinal rebars however, whether these will yield before total collapse of the wall assemblage is unclear and it is therefore difficult to characterize the specific contribution of these in the collapse scenario. As the reinforcement is only expected to work by catenary action at extreme deformation levels and due to the expected global deep beam behavior where the concrete is expected to be in compression, the defacto strength gain from the reinforcement is deemed negligible and is therefore omitted. The initial strength e.g the cohesion will therefore be calculated as for unreinforced concrete as done in [24] by the following equations 8.3 and 8.4:

$$c = \frac{f_c \cdot f_t}{2\sqrt{f_t \cdot (f_c - 2 \cdot f_t}} \tag{8.3}$$

$$\phi = \sin^{-}1(\frac{f_c - 4 \cdot f_t}{f_c - 2 \cdot f_t}) \tag{8.4}$$

The cylinder tests shows a compressive strength of $f_c = 25$ MPa which by applying the Eurocode formula f_{tm} evaluates to:

$$c = \frac{f_c \cdot f_t}{2\sqrt{f_t \cdot (f_c - 2 \cdot f_t}} = 4.085MPa \tag{8.5}$$

$$\phi = \sin^{-} 1(\frac{f_c - 4 \cdot f_t}{f_c - 2 \cdot f_t}) = 51.8^{\circ} \tag{8.6}$$

This now leaves the aereated autoclaved concrete. For this, applicable shear tests are sparse as well. This report will for the cohesion be based on a series of tests done on longitudinally reinforced AAC single-spanning slabs in [25] where the shear tests for similarly reinforced slabs with similar densities show a shear strength of approximately 0.13 MPa, which corresponds with the Portland Cement Association estimations with ranges the shear strength of AAC in the range of 0.05-0.14 MPa. The internal angle of friction was not tested, here the numerical simulation will be based on tests done on lightweight cellular concrete in [26] which estimates the internal angle of friction of lightweight concrete with the same density as the AAC-beams to be 25.6 degrees.

8.2 Lower bound results

Running the lower bound program returns a statically admissible internal stress field and thereby a collapse load. Graphically, this is expressed by the following figures, figure 48 shows the σ_x stress field, figure 49 shows the σ_y stress field, figure 50 shows the shear stress field τ_{xy} and lastly figure 51 shows a plot of which nodes are have an inequality constraint active, that is a point where yielding occurs. The stress plots have a contour bar for reference with units in Pascal and the yielding plot shows which type of yielding occurs, that is whether a solid yield inequality is active or either a head- or bedjoint inequality is active. The lower bound result is a collapse load of: $Q_{lb} = 190.1$kN. A discussion of the chosen calculated collapse load of the system with respect to different mesh configurations and number of linearization planes is shown in section 8.4.

Below figure 48 shows the x-directional stress distribution, with x being the horizontal axis. The illustration shows a clear compression strut in the concrete beam between the two applied loads. As the strength field of the wall is highly anisotropic, and the concrete is significantly stronger than especially the joints but also the bricks, the subsequent stress field is a bit unclear however, stress concentrations around the upper corners of the aereated autoclaved concrete beams is present and slight concentrations at the pillar bottoms as well at the supported boundaries. What can be interpreted from the above is that given the concretes high strength, stresses can be pushed quite wide horizontally within the concrete beam allowing for less horizontal distance the vertical load has to travel within the brick wall, thereby causing much less of a tilt of the general compressive struts angle of attack on the joints which activates much more frictional strength with respect to the low cohesive strength.

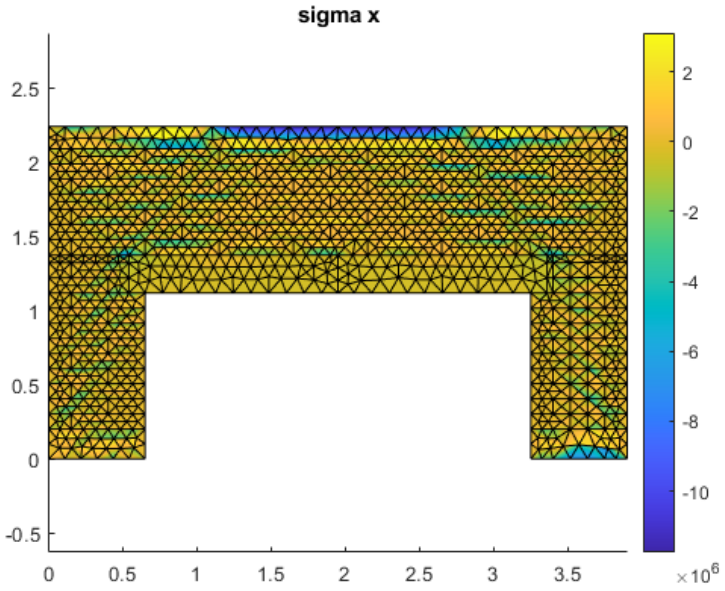

Figure 48: X-directional normal stress

Below figure 49 shows the y-directional stress distribution, with y being the vertical axis. The plot shows a field of compression from the load areas to the supported areas resembling an inclined compressive strut from the load areas to the supported areas with the stresses concentrated at the aereated autoclaved concrete beam corners where the angle of attack of the strut changes. The inclination changes at the areas around the aereated autoclaved concrete beams where due to their weakness, the stresses in ultimate collapse state has to curl around these corners and then move to the supported edges. A note here is that the program has no compressive cap, and therefore one should be attentive to that the compressive stresses do not reach the compressive strength of the bricks and mortar assemblages. As the compressive strength caps out at around $\approx$ 11 MPa this is considerably less than the compressive strength of the bricks at 24.4 MPa.

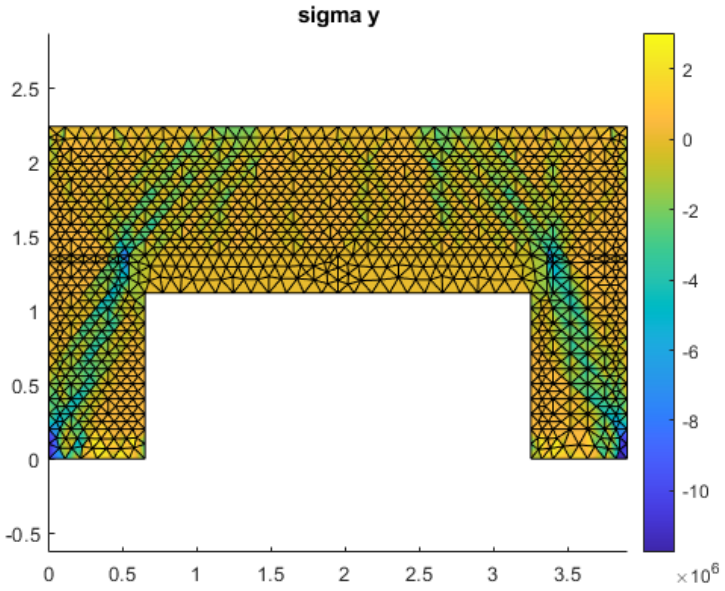

Figure 49: Y-directional normal stress

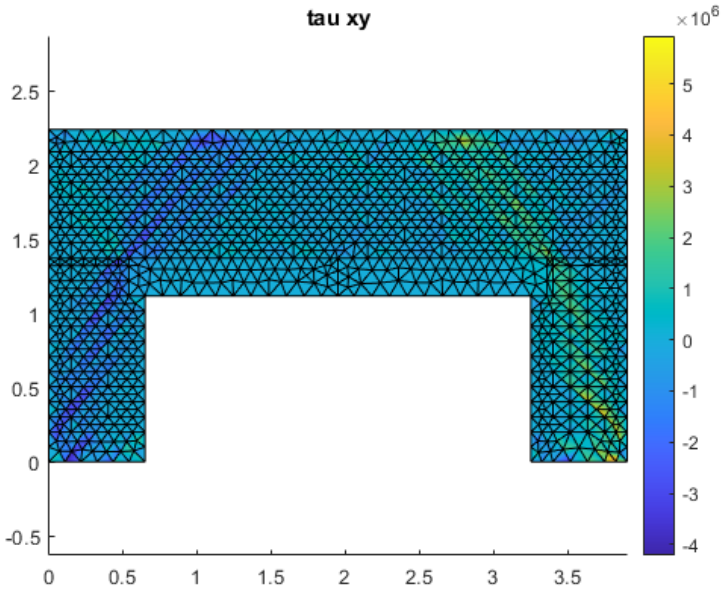

Figure 50: Shear stress

Above figure 50 shows the shear stress distribution at the lower bound collapse stress state. The plot shows that the stress field follows the vertical normal stress field in the sense that forces are transferred in vertical stress and shear to move the forces from the load points to above the pillars and subsequently to the supports.

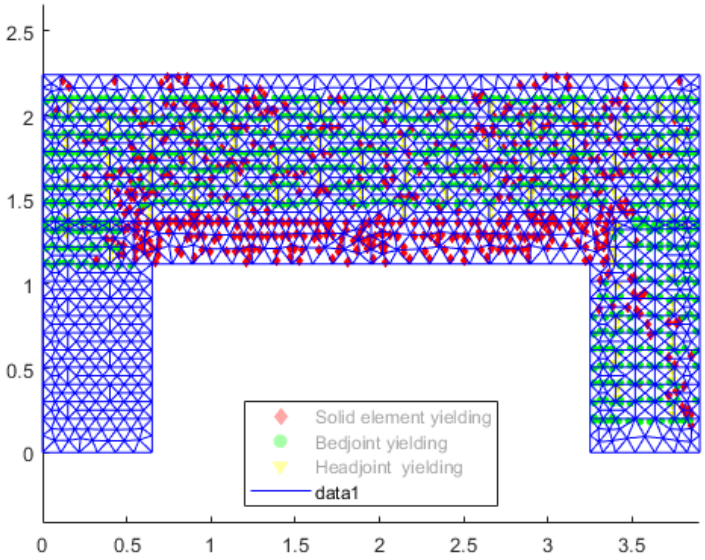

Figure 51: Yield plot

8.3 Upper bound results

Running the upper bound program returns a kinematically admissible velocity field and a collapse load by equating internal power dissipated as evaluated by the objective function design vector product with external power applied. The graphical illustration of this is a plot of nodal velocities with direction and size as shown in figure 52.

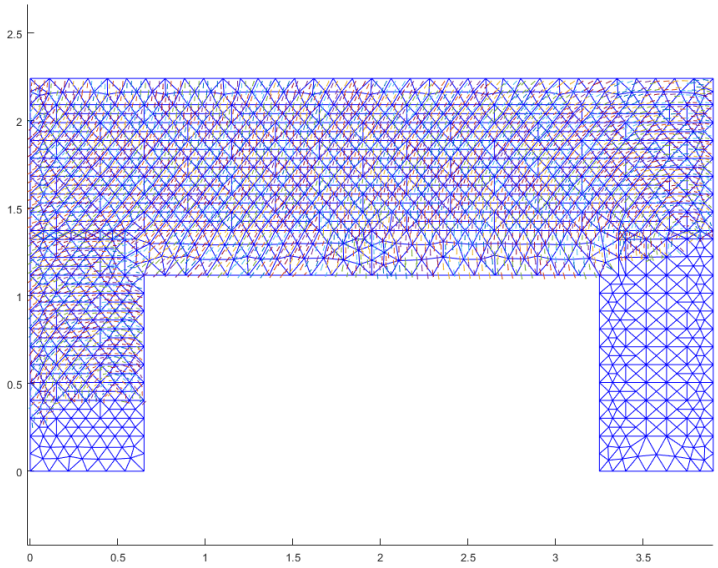

Figure 52: Velocity plot

The velocity plot crudely translates to rigid body movements as illustrated in below figure 53, where there is separation above the pillars with rotation of the left pillar bot not the right

one, and a diagonal separation on the deep beam part where the left side rotates clockwise and the right side counter-clockwise.

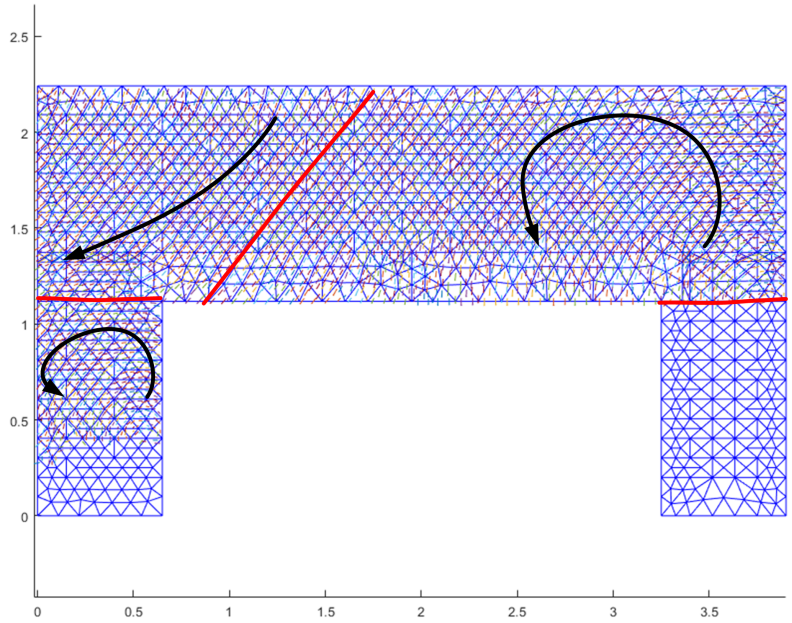

Figure 53: Mechanism illustration

8.4 Discussion of numerical predictions

Below tables 6 to 9 shows some comparisons of the two models at different mesh sizes, two different yield function linearization polygon orders and the associated number of degrees of freedom and constraint equations:

Table 6: Lower bound, p = 16

Characteristic length	Number of elements	Number of DoFs	Number of equalities	Number of inequalities	Computational time [s]	Total load [kN]
0.20	1506	13555	12260	78520	230	143
0.15	1596	14365	13012	83036	287	144
0.1350	1889	17002	15378	97908	378	180
0.12	2477	22294	20094	128128	781	185
0.10	3040	27217	24600	156100	1242	189

Table 7: Upper bound, p = 16

Characteristic length	Number of elements	Number of DoFs	Number of equalities	Number of inequalities	Computational time [s]	Total load [kN]
0.20	1506	41956	20978	32390	9.55	217
0.15	1596	44444	22222	34868	11.0	201
0.1350	1889	52626	26313	41292	11.4	191
0.12	2477	69078	34539	54216	28.7	193
0.10	3040	84264	42312	66120	47.6	197

Table 8: Lower bound, p = 30

Characteristic length	Number of elements	Number of DoFs	Number of equalities	Number of inequalities	Computational time [s]	Total load [kN]
0.20	1506	13555	12260	141772	411	145
0.15	1596	14365	13012	150068	491	145,00
0.1350	1889	17002	15378	177246	664	181
0.12	2477	22294	20094	232252	1780	186
0.10	3040	27361	24728	284480	2850	190

Table 9: Upper bound, p = 30

Characteristic length	Number of elements	Number of DoFs	Number of equalities	Number of inequalities	Computational time [s]	Total load [kN]
0.20	1506	63040	31520	54004	9.10	216
0.15	1596	66788	33394	57212	9.60	199
0.1350	1889	79072	39536	67738	15.9	190
0.12	2477	103756	51878	88894	42.0	192
0.10	3040	127272	63636	109032	85.0	191

Below figures 54a and 54b show computational time for the upper and lower bound solutions with respect to the mesh characteristic length at yield linearization polygon orders 16 and 30. First of all, the lower bound models are a lot more expensive to evaluate and this increases quite rapidly with respect to mesh characteristic length with run times ranging from 230 - 1242 seconds for p = 16 and 411 - 2850 seconds for p = 30. It is interesting to note that even though the amount of constraints scale linearly with the number of elements and polygon order and thereby the characteristic mesh length, the computational effort required most certainly do not. The upper bound solutions are quite a lot faster to run even though the amount of equalities, inequalities and degrees of freedom are quite larger. This comes down to two things as mentioned previously, the homogeneity of the equality constraints, and then the diagonality of the inequality matrix. As the inequalities basically state that the plastic multipliers and discontinuity velocities must be larger or equal zero, the inequality matrix is basically one large homogeneous diagonal matrix of ones.

Below figure 55 shows total collapse for the upper and lower bound solutions with respect to the mesh characteristic length at yield linearization polygon orders 16 and 30. One would expect the solutions to asymptotically approach an exact solution as the mesh refines where the lower bound solutions will reach this asymptote from below and the upper bound from above. The solutions appear to converge to a collapse load around 190kN, making this the principally

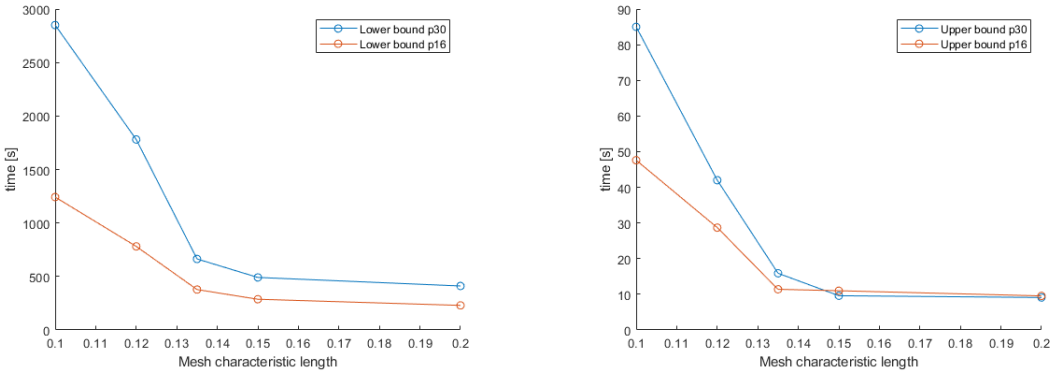

(a) Lower bound run times for different mesh sizes(b) Upper bound run times for different mesh sizes

predicted collapse load. However, as stated earlier masonry does not obey every assumption required for applying the extremum principles of limit analysis and this prediction is therefore very likely to overestimate the capacity of the test specimen.

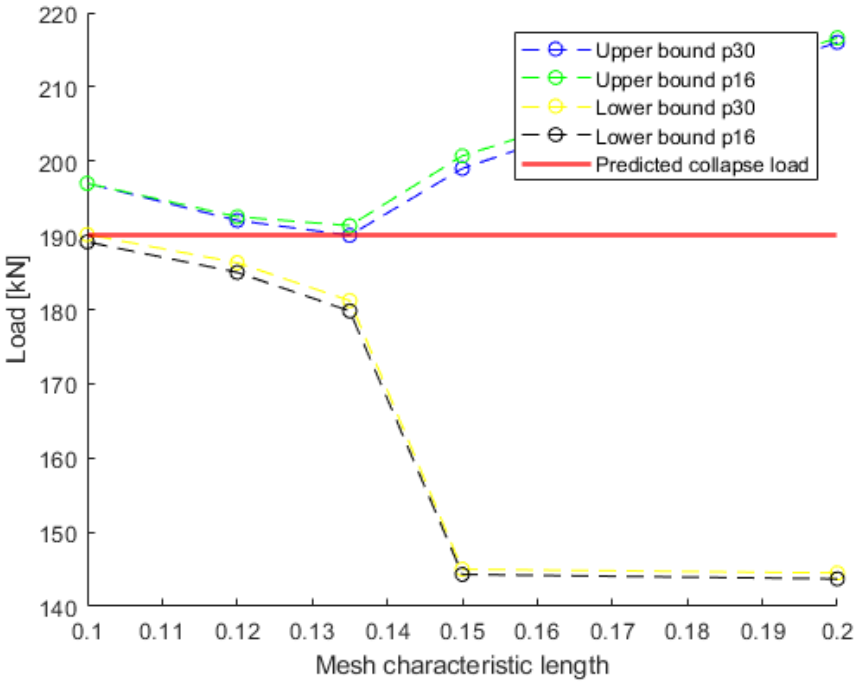

Figure 55: Collapse loads for different mesh sizes

How ductile the collapse will be is the primary unknown and is in essence the purpose of the experimental test. If the collapse shows good ductility, the collapse load should be able to reach around 80-90% of the predicted perfectly plastic load multiplier. The reasoning for this prediction not being 100 % is that the numerical tool still takes strength contributions from all joints yielding in tension, whereas in reality at collapse point they will be separated and the strength comes from purely the compressive strut action within the wall. This issue is illustrated on the yielding plot in figure 51, where it can be seen that almost all nodes in the active areas are yielding and contributing strength where the nodes that are yielding in tension should provide zero tensile strength.

What figure 55 also shows is that unexpectedly, the upper bound solutions diverges off the predicted collapse load asymptote as the mesh refines. This is unfortunate and can be due to a few reasons. First, some mesh configurations appear to allow the model to find a non-global mechanism which ruins the results when set in comparison with the lower bound results as these are always global failure modes. Therefore, a few additional constraints for the velocity field of the loaded elements has been implemented to help facilitate activation of more triangles however, these additional constraints might skew the individual mesh configurations results slightly differently. Secondly, the upper bound model is quite prone to differing the failure mechanism around the pillars. The finest mesh k = 0.1 translates at the left pillar bottom, where k = 0.12 and k = 0.135 rotates at the left pillar, and k = 0.15 and k = 0.20 does not activate movement in the pillars but rotates the beam part above the right pillar and translates above the left. This is all shown in Appendix D, where the illustrations from running different meshing configurations are shown. Similarly to the upper bound, the lower bound is also prone to differing the final failure yield layout of the structure which is shown by the yielding plots for different mesh configurations in Appendix D, as meshes k = 0.2 and k = 0.15 yield in the left pillar, k = 0.135 yield in both pillars and k = 0.12 and k = 0.1 yield in the right pillar. A take-away from this inconsistency of failure modes for both upper- and lower bound models is that due to the near symmetrical geometrical configuration, whether the left or right pillar will fail is very close and small changes in the equations such as different meshing can change the calculated failure mode.

Summarizing above points regarding the upper bound solution, then it evaluates very fast however, it is slightly unstable with respect to the collapse load and for practical use, one should try different mesh configurations and verify by running the lower bound as well. The lower bound solution is more intuitive to interpret as the link between stress distribution and collapse load is clear and it is easier to intuitively verify the veracity of the solution, in contrary to the upper bound where the link between kinematics and loading is more complicated especially for complicated geometries and material anisotropies as is the case of masonry. The intuitive failure mechanisms are also somewhat unclear due to the large inherent multi-scale anisotropies. In the case of the experimental specimen these failure mechanisms can differ dramatically with even small meshing changes. These points all argue the lower bound model superior to the upper bound one however, it runs very slowly in relation to the upper bound. Finally, the collapse load predicted from an assessment of the different meshing configurations for both upper and lower bound solutions is approximately 190 kN.

8.5 Verification

A hand calculation is made to verify and provide context to the numerical predictions. Two calculations are made concurrently of two similar collapse scenarios, where load barring capacity of the compressive struts are limited of the shear strength in the bed joints at the supporting pillars. The scenarios and their specific geometrical conditions are visualized in figure 56 that shows two compressive struts having different heights of the deep beam and different support lengths, which results in different angles with the vertical axis. In the first collapse scenario the autoclaved aerated concrete beams are imagined to fall down doing the collapse and leave the length bed joint without the support length of the beams, where in the second collapse scenario the compressive struts are able to press through the aerated concrete beams, leaving the length bed joint the same as the width of the supporting pillars.

Figure 57 zooms in on the area just above the pillars. As it can be seen, there is no additional lateral restraints leaving the shear strength of the bed joint just above the pillar as the only lateral

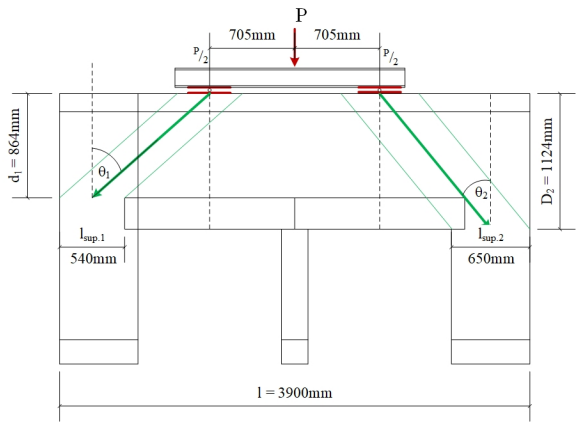

Figure 56: Expected collapse scenarios

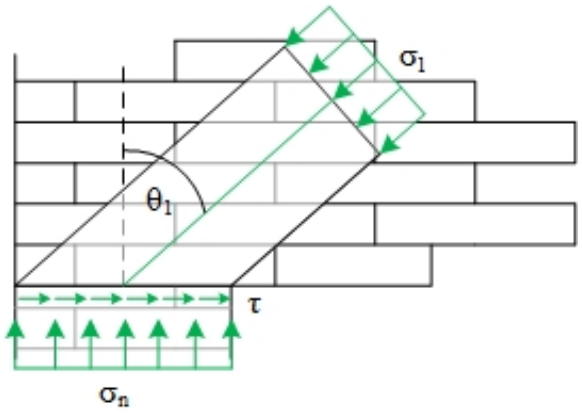

Figure 57: Bed joint stresses

support, why the length of this sets the boundaries of the width of the compressive strut σ_1. The shear strength is given by the initial shear strength and the contribution from friction as is written in below equation.

$$\tau = \mu \cdot \sigma_n + f_{v0} \tag{8.7}$$

with simple trigonometry τ and σ_n can be described by σ_1:

$$\begin{aligned} l_{sup} \cdot \sigma_n &= cos(\theta) \cdot l_{sup} \cdot cos(\theta) \cdot \sigma_1 \quad &\Rightarrow \quad \sigma_n &= \sigma_1 \cdot cos^2(\theta) \\ l_{sup} \cdot \tau &= cos(\theta) \cdot l_{sup} \cdot sin(\theta) \cdot \sigma_1 \quad &\Rightarrow \quad \tau &= \sigma_1 \cdot cos(\theta) \cdot sin(\theta) \end{aligned}$$

Replacing τ and σ_n in bed joint failure criteria in equation 8.7 and isolating σ_1 returns:

$$\sigma_1 \cdot cos(\theta) \cdot sin(\theta) = \mu \cdot \sigma_1 \cdot cos^2(\theta) + f_{v0} \quad \Rightarrow \quad \sigma_1 = \frac{f_{v0}}{sin(\theta) \cdot cos(\theta) - \mu \cdot cos^2(\theta)}$$

With σ_1 determined σ_n can be described and hence the applied load as the double of σ_n multiplied with the length of the support and thickness of the wall.
The calculations is made in below table 10 for both collapse scenario 1 and 2, which results in load capacities of 63.3kN and 134.1kN.

Table 10: Calculation inputs and result

Input	Scenario 1	Scenario 2
Wall thickness [t]	150mm	150mm
Wall length [l]	3900mm	3900mm
Support length [l_{sup}]	540mm	650mm
Deep beam height [d]	864mm	1124mm
Point load placings from center [l_{load}]	705mm	705mm
Angle of compression strut w. vertical axis [θ] $\theta = atan(\frac{0.5(l-l_{sup})-l_{load}}{d})$	48.5°	39.3°
Material properties		
Initial shear strength [f_{vk0}]	0.28MPa	0.28MPa
Internal angle of friction [θ_{fric}]	25.0°	25.0°
Friction coefficient [μ] $\mu = atan(\theta_{fric})$	0.411	0.411
Load capacity		
Compressive strut stress [σ_1] $\sigma_1 = \frac{f_{vk0}}{sin(\theta)\cdot cos(\theta)-\mu\cdot cos^2(\theta)}$	0.888MPa	1.149MPa
Support normal stress [σ_n] $\sigma_n = \sigma_1 \cdot cos^2(\theta)$	0.390MPa	0.688MPa
Applied load		
Load [P] $P = 2 \cdot \sigma_n \cdot l_{sup} \cdot t$	63.3kN	134.1kN

The 134.1kN is 70.5% of the collapse load predicted by the computational approach which is assessed as a very reasonable relation as the anisotropy and material complexity of the structure only allows very crude hand calculations as the one above whereas the numerical programs should be able to calculate considerably higher collapse loads however, still within the same order of magnitude of a hand calculation, which conveniently it is.

9 Experimental results

9.1 Test observations

The collapse test of the calcium silicate masonry wall was conducted the 25th of May and went according to plan as described in section 7.2. The wall was loaded with 50kN whereafter the central column was removed with out collapsing such that the load bearing mechanism could be revealed by increasing the load until total collapse, which is was. The collapsed test specimen is shown on below figure 58.

Figure 58: Collapsed test object

The wall was loaded to 50kN without developing any visible cracks. When the column removal was initiated the out-of-plane force was observed to drag the wall out of plane until the horizontal support was activated, which especially effected the left pillar here introducing some sliding in the bed joint in the level where the aerated concrete beam was supported. Doing the removal the masonry deep beam was lifted due to tilting of the masonry bricks in center column, before the intended sliding mechanism with the 4 vapours seal layers was initiated. As the central column collapsed the remainder of the test object did only undergo minor displacements with a small crack between the two aerated concrete beams, and so progressive collapse did not initiate. Seemingly, the wall immediately redistributed the applied load to the outer pillars. The specimen was then loaded until collapse, which happened at a load level of 156.2kN, where the concrete slab beam failed. Up until this point, individual bricks slid and cracks developed in the middle of the masonry deep beam and the areas above the supports lifted, as a compressive arch is expected to collapse fracturing into in four rigid parts. Figures 59a to 59f shows the test specimen after collapse, where the large crack in the center of the deep beam on figure 59a and 59b splits the beam in two elements rotating inwards. The rotation leads to the uplift at the supports depicted on figure 59c and 59d. The two pillars reacted differently with the left pillar

tilting outwards as shown in figure 59e and the pillar to the right failing sliding in a bed joint near the foundation as shown in 59f. The difference can be due to poor workmanship of the bricklayer or the angle brackets mounted on the plywood supplying different levels of vertical support, though it should not provide any support in this direction.

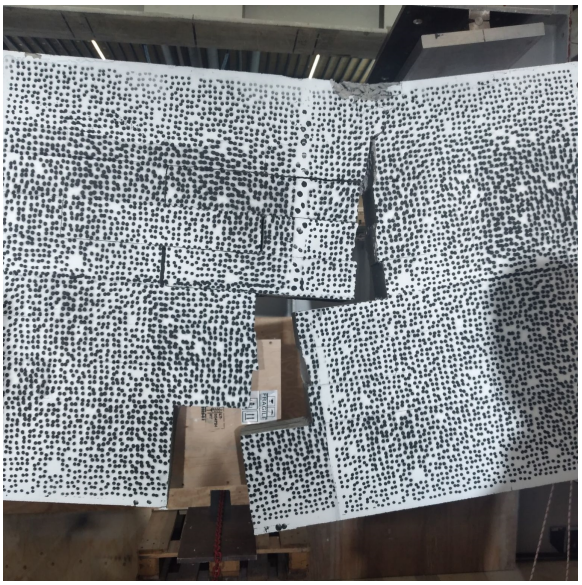

(a) Central crack from the front

(b) Central crack from the back

(c) Uplift left pillar

(d) Uplift right pillar

(e) Foundation failure left pillar (f) Foundation failure right pillar

Figure 59: Failure observations of experimental test

9.2 Test results

The experiment was monitored with DIC-Camera system capturing 34704 pictures of the test, wherefrom displacements and strains are calculated by the VIC software, while a load cell provided the load data. Both data sets are aligned according to time in below plot in figure 60 and plotted against each other in a force-displacement plot in subsequent figure 62, with the displacements at the red point marked in figure 61.

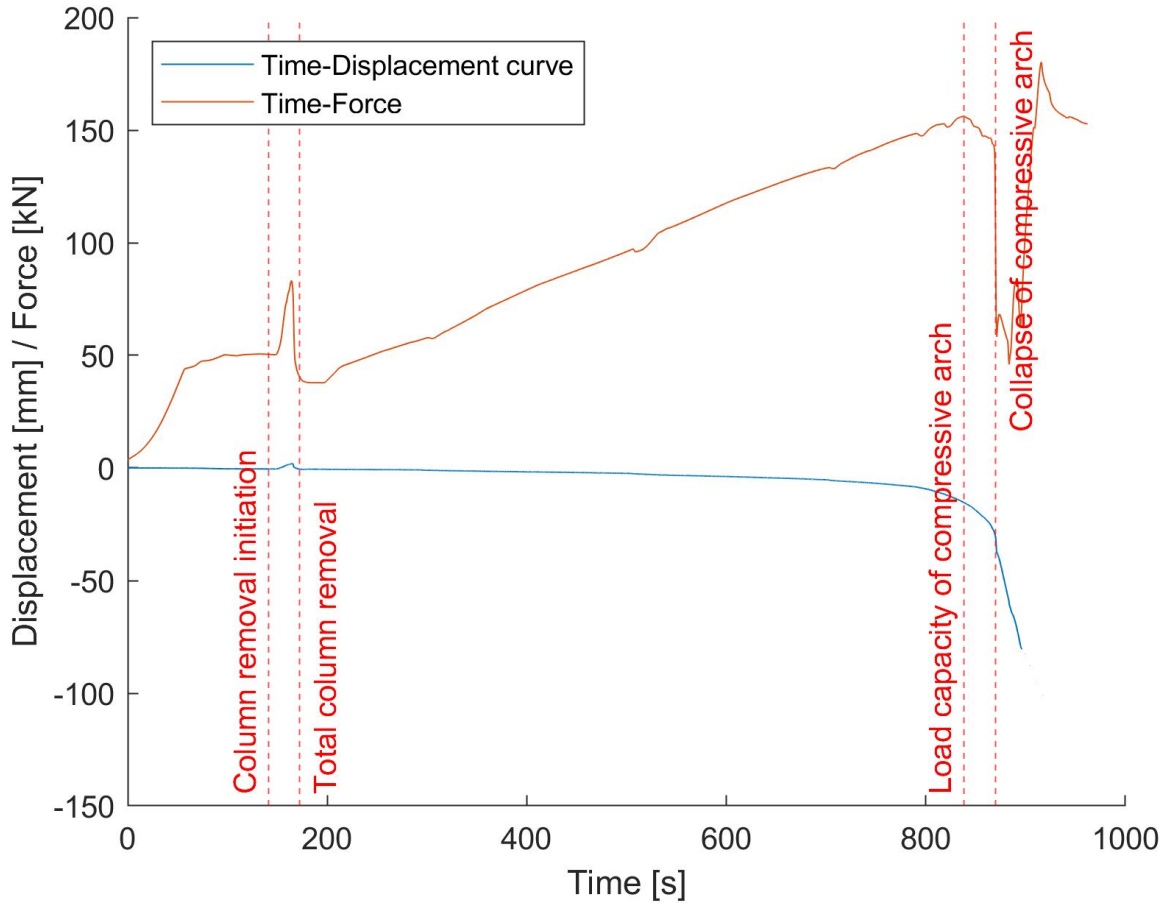

Figure 60: Time- & Force-displacement curve of central point marked in figure 61

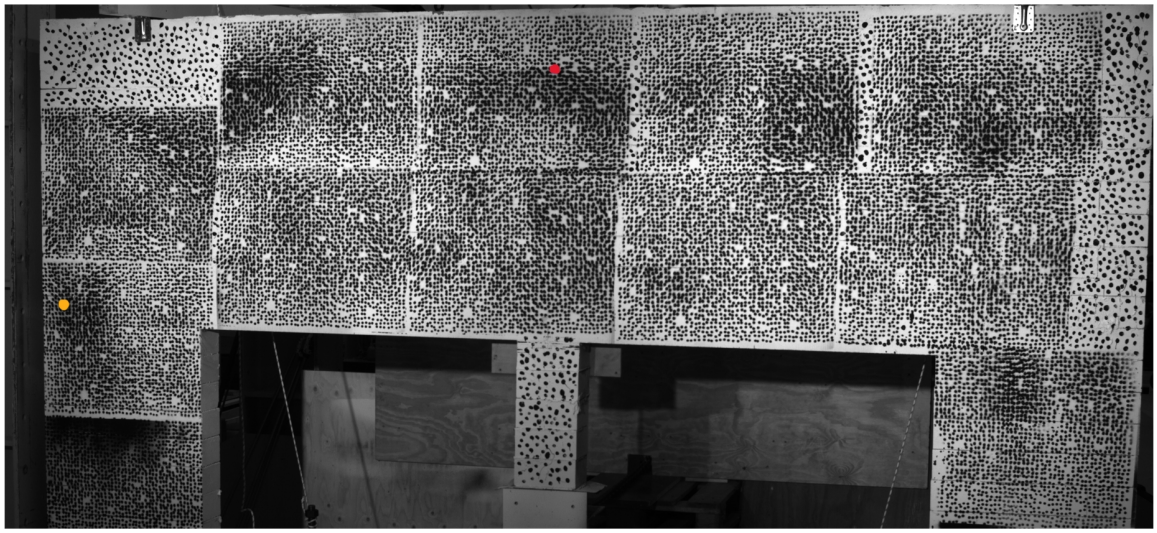

Figure 61: Force-displacement data point

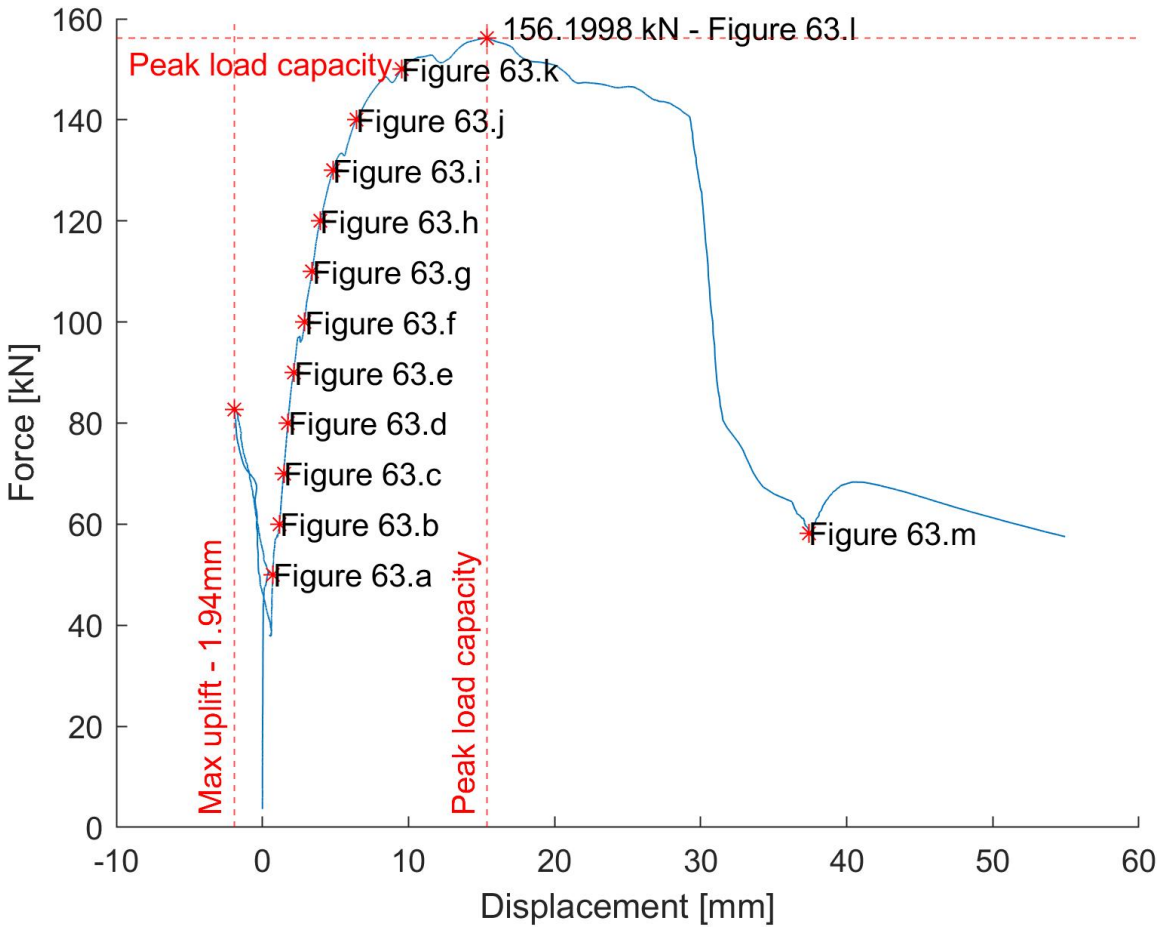

Figure 62: Force-displacement curve of data point

The force-displacements curve displays a maximum uplift of 1.94mm before right before the removal of the central column, whereafter the force drops after the removal. The peak load capacity of the test specimen was found to be 156.2kN at a deflection of about 16mm. Between 10mm and 30mm the curve shows a plateau like area insinuating that the global failure is somewhat quasi-ductile.

At every 10kN of the loading, a point is plotted referring to below subfigures in figure 63 showing the specimen at the load steps and the developments of the principle strains on a contour plot. The contour plots are a bit skewed in the area by the left pillar due to spalling of the beam early doing the test, why the values in this area are wrong. The principle strains reveals the developments of the center crack and the uplift at the support and compressive struts. The cracks and uplift happens quite early in the loading process, where figure 63c at 70kN detects the earliest uplift at the pillar to the right. Figure 63f at 100kN depicts the presence of a compressive strut going from where the load is applied til the left part of the pillar to the right. Subsequently to the strain figures the vertical displacements at maximum load capacity is shown in figure 64 depicting a fairly symmetrical displacement, though the center crack develops towards the right load point a split second later.

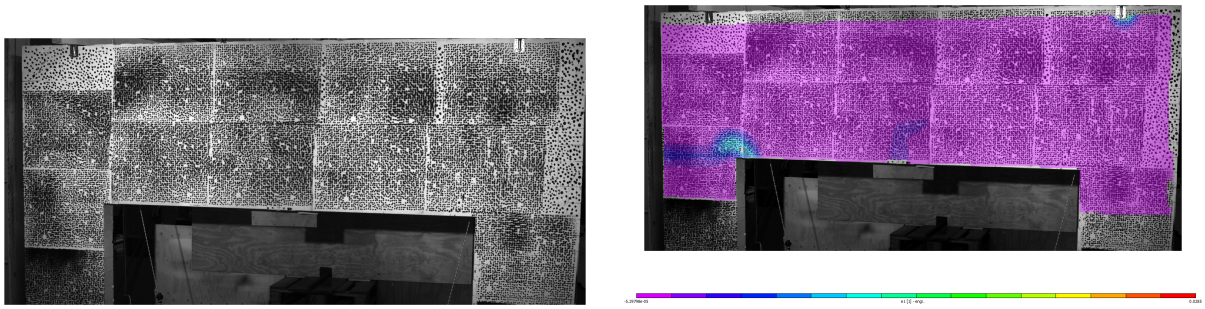

(a) Test object and principle strains at 50kN load level

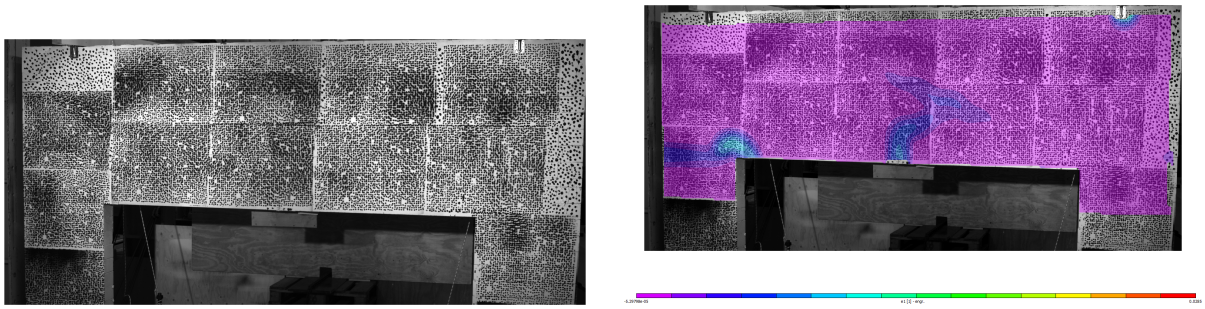

(b) Test object and principle strains at 60kN load level

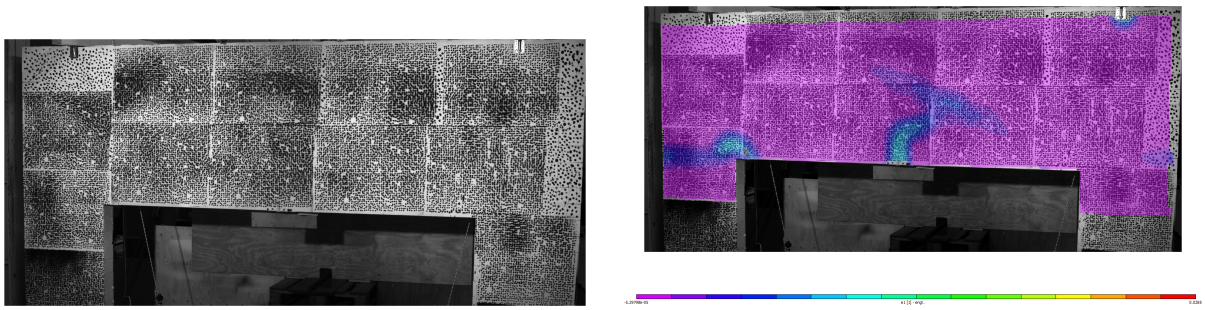

(c) Test object and principle strains at load level

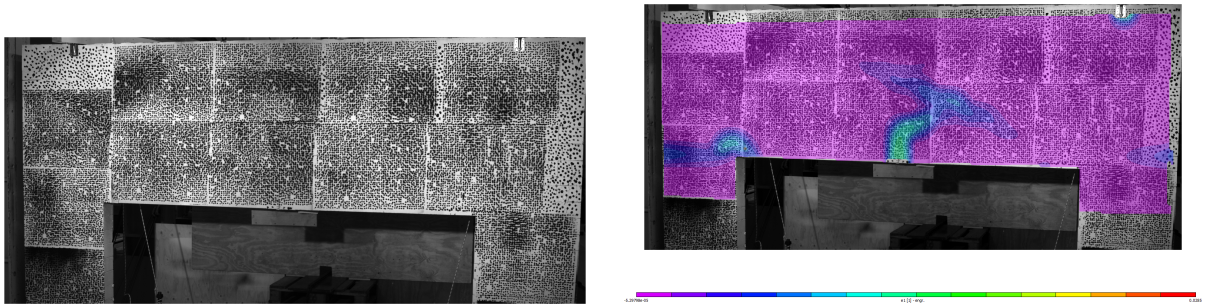

(d) Test object and principle strains at load level

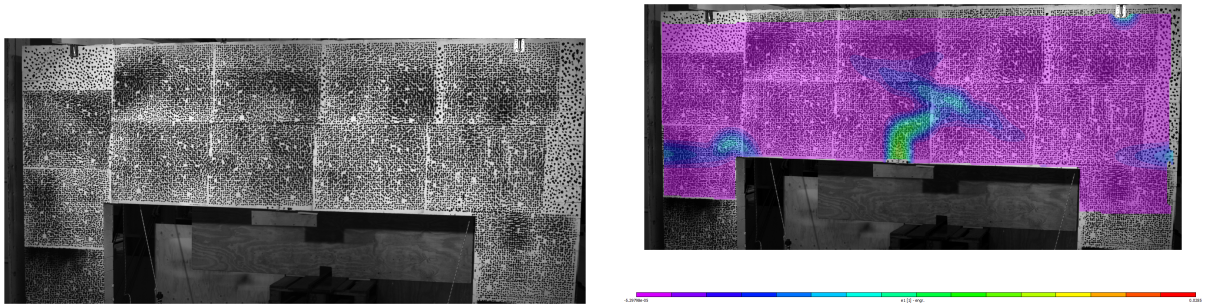

(e) Test object and principle strains at 90kN load level

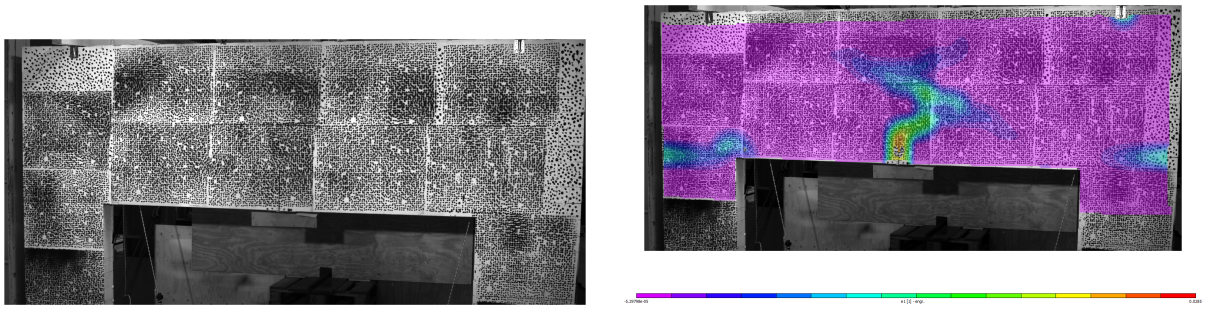

(f) Test object and principle strains at 100kN load level

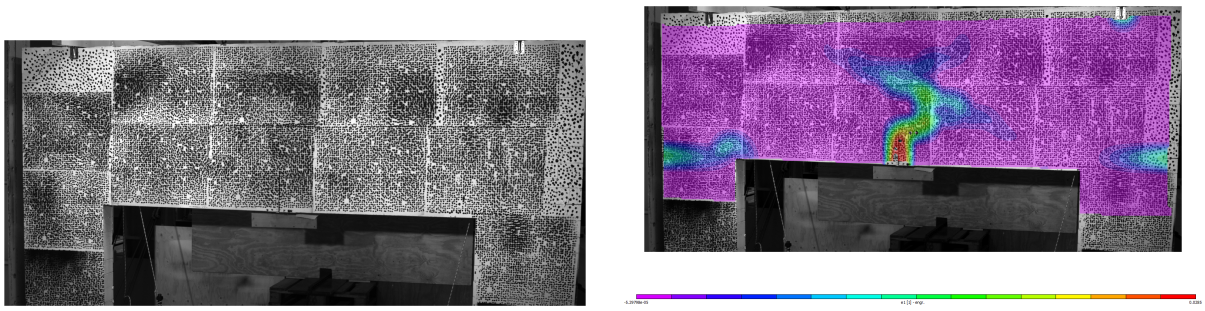

(g) Test object and principle strains at 110kN load level

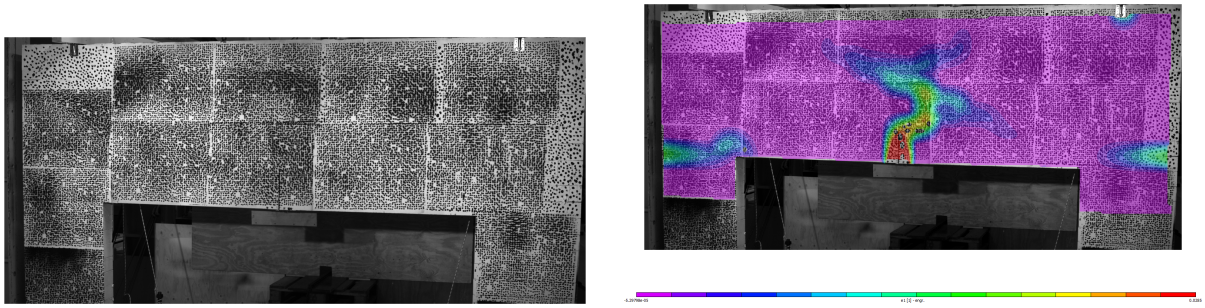

(h) Test object and principle strains at 120kN load level

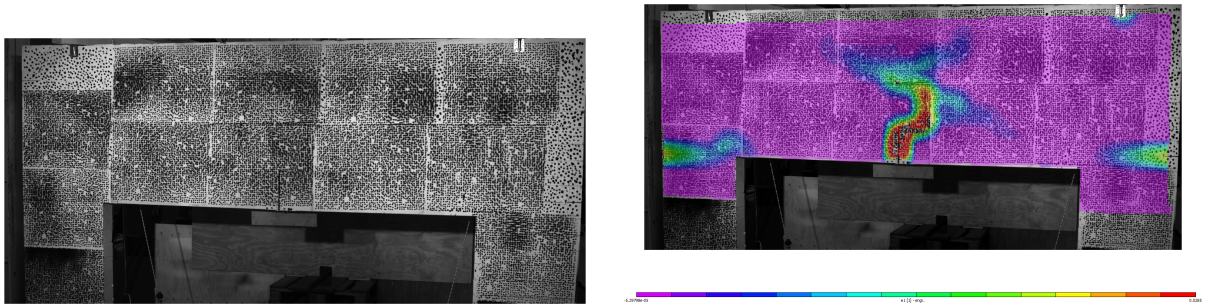

(i) Test object and principle strains at 130kN load level

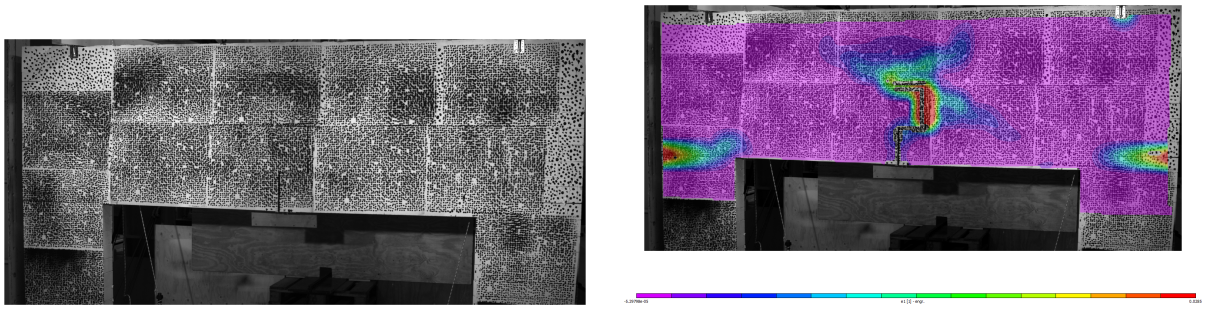

(j) Test object and principle strains at 140kN load level

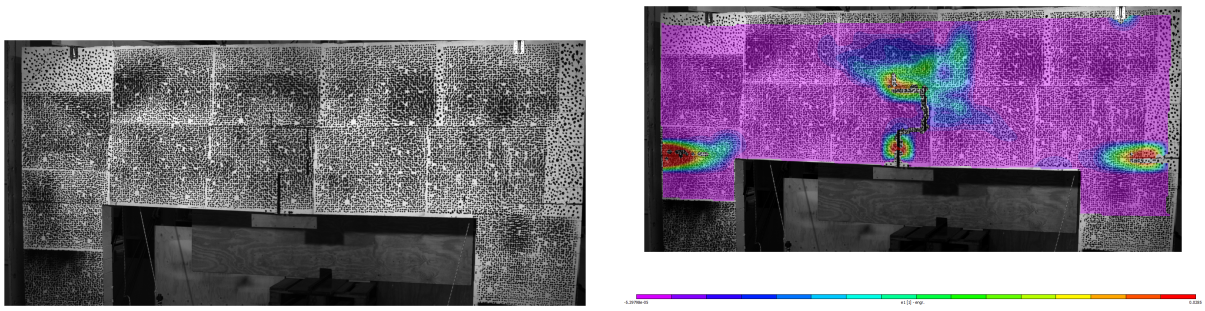

(k) Test object and principle strains at 150kN load level

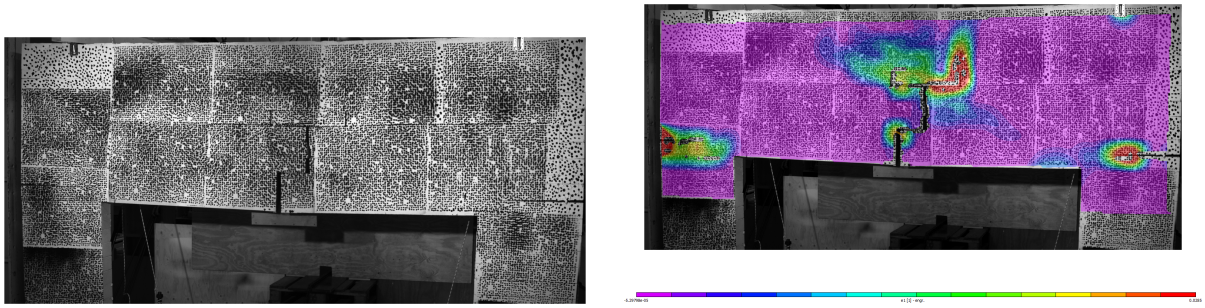

(l) Test object and principle strains at 156.2kN load level

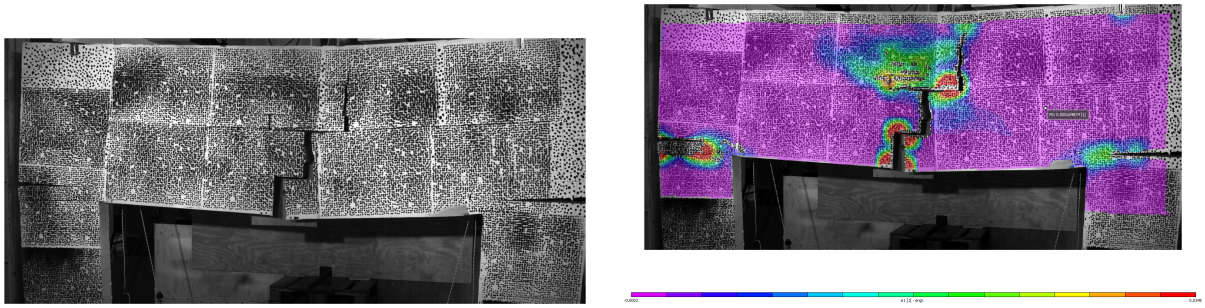

(m) Test object and principle strains at at 58.2kN load level post-peak

Figure 63: Progression of principle strain doing the test.

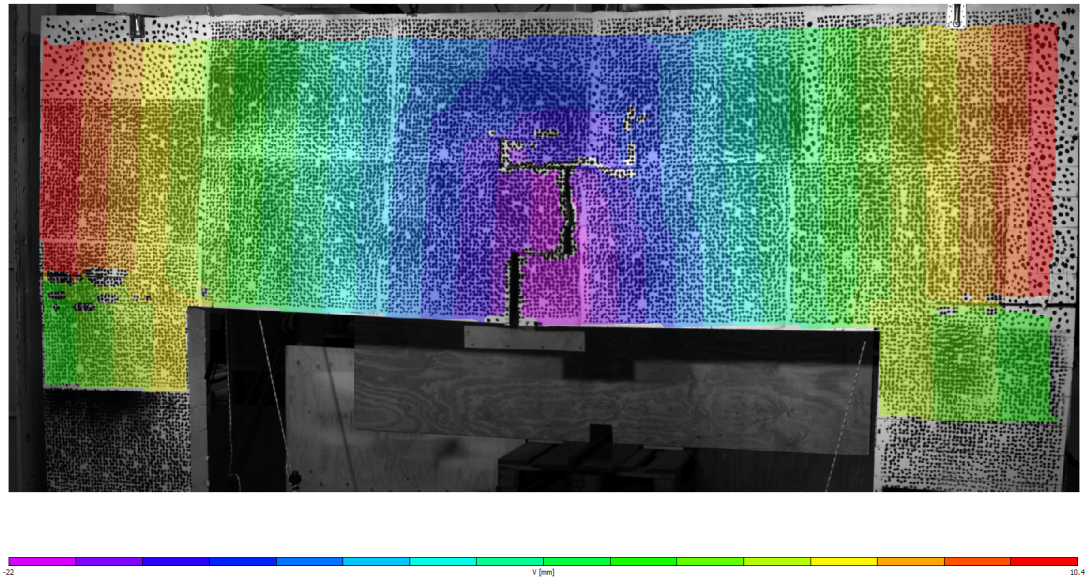

Figure 64: Vertical displacements at maximum load capacity

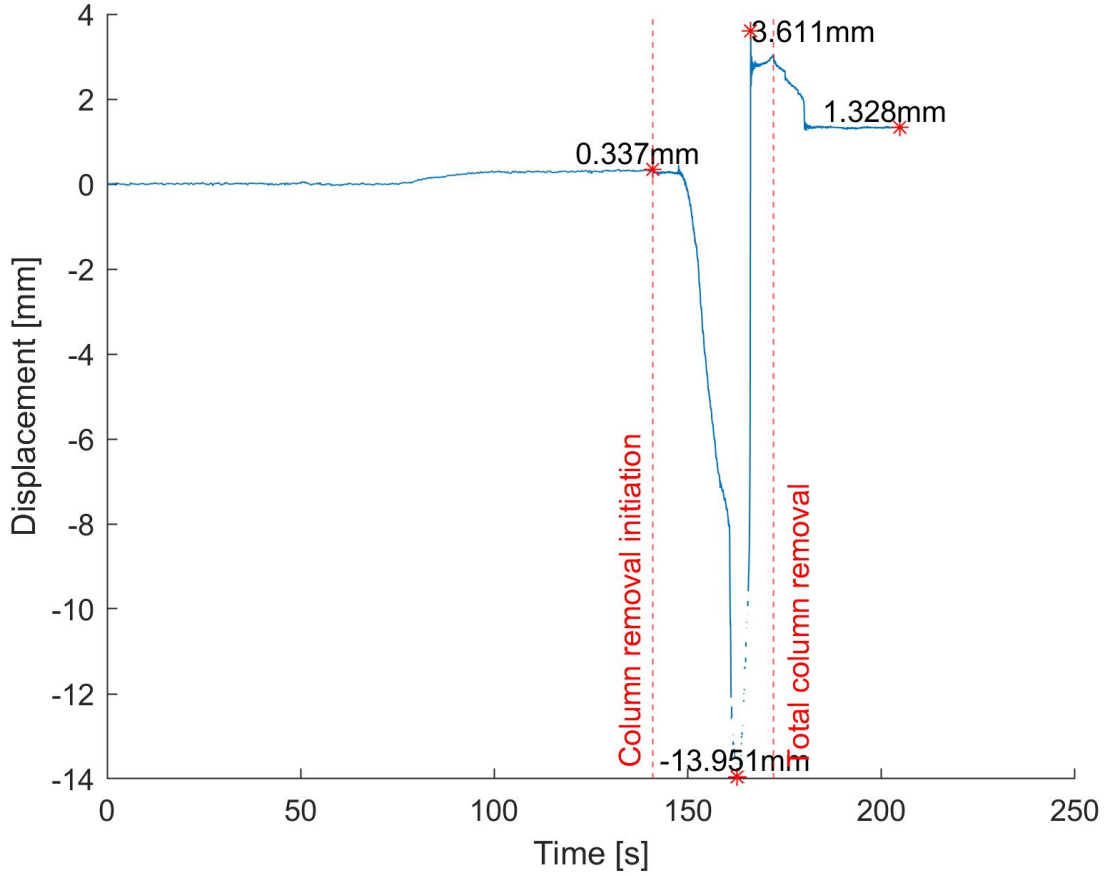

Figure 65: Time-displacement of the top left pillar

The effects of the column removal on the left pillar is shown in figure 65, where the out-of-plane displacements in the orange point on figure 61 is displayed doing the removal. The plot shows that the pillar has moved 14mm before the sliding mechanism in the central column is taken action and the wall almost falls back into its original position ending with permanent displacement in the bed joint of 1mm. Up until 150kN it was in this weakened bed joint the uplift was observed, but at maximum load capacity the uplift was observed in the bed joint in above course as can be seen in figure 63l. The behavior is difficult to explain, but is most likely due to the connectivity with the intersecting wall.

9.3 Experimental collapse load in relation to limit analysis collapse load

The experimental collapse load was: $P_{experimental} = 156.2$ kN while the numerical limit analysis collapse load is: $P_{numerical} = 190$kN. This amounts to the experimental collapse being 82.2% of the numerical one. As stated earlier, the experimental collapse load was expected to be in the 80% - 90% range of the numerical one given a somewhat ductile failure. The failure was quasi-ductile as evidenced by the force displacement curve on figure 62, and the assessed collapse load of 80%-90% of the numerical one is therefore in decent accordance with the experimental one. Another element of inherent uncertainty is that of the material properties which for masonry is an inherent major issue when it comes to predicting collapse loads.

The predicted stress distribution from the lower bound corresponds well with the wall strain field imminently before failure as shown in figure 84w, where there is a clear compressive strut

from the loaded points to the pillars which quite narrowly pushes through the pillar-beam joint as the outer beam parts lifts quite massively. The lift is unpredictable by the lower bound but the same narrow compression strut at this conjunction is evident. In regards to the upper bound, none of the mesh configurations predicted the experimental failure mechanism, which is quite unfortunate. A remark here is that as shown on pictures 59e and 59f then the left pillar rotates in failure while the right one translates alluring to the deduction that the possible failure modes are very close in comparison to each other making the discrepancies less concerning.

It is however difficult to generalize the veracity of this quasi-ductile failure mode for all masonry, meaning that it would be untrue to extrapolate that since this specific deep beam frame test showed quasi-ductile failure that all masonry deep beams will behave similarly. The reinforced concrete beam is a major contributor to the global deformation capacity as even though brittle tensile failure occurs within the masonry as evidenced by figure 63. The stiffness of the concrete beam allows equilibrium to be maintained even though the masonry starts rotating somewhat rigidly. As joint tensile failures starts occurring quite early in the collapse phase, if one was to apply the method to real-life structures, then one should be able to argue the ductility of the failure mode with good certainty.

10 Conclusions

Structural robustness of masonry structures has been investigated in the perspective of a specific example of a central column loss scenario of a 3-point supported CSU-brick wall with a concrete beam on top resembling the defacto concrete beam behavior of a reinforced concrete slab resting upon the wall. The experiment has been done in the spirit of showing the ductility level of the failure mode of such a structure thereby trying to verify the applicability of limit analysis to such a structure. Due to the multi-level of anisotropic behavior including the brittleness of the failure modes, this applicability is not intuitively verifiable without experimental studies. The experimental study however, showed decent ductility in failure and the numerical results were in well accordance with the experimental ones as the experimental load was 82.2% of the numerically predicted collapse load. The column-loss scenario was forced at around a third of the total collapse load and seemed to not effect the final outcome of the experiment however, it is hard to generalize this as the wall at the extraction point was restrained laterally therefore not reproducing out of plane effects of the column loss scenario, but the in-plane acceleration of the wall from the column sudden loss did not effect the walls in-plane load capacity nor cause some progressive collapse mechanism.

One of the primary arguments of applying limit analysis in the perspective of structural robustness is that it requires relatively few mechanical parameters to characterize and is fast to evaluate. A conventional stiffness based formulation would need a lot more parameters to characterize the non-linear regime and it would be very computationally expensive to evaluate however, it would be able to account for the non-linear damage and hardening phenomena. The limit analysis model however, does run very fast which makes it practical to use and apply to geometries on a structural scale. Summarizing the points regarding computational limit analysis, the methodology and the programs are practical and efficient in the sense that they are fast and it is practical to have two solutions to the same problem that one knows should be in the very same vicinity of each other for mutual verification, however they build on a set of principles and assumptions which generally must be obeyed as they generally were in the conducted experiment.

It is however difficult to generalize the applicability of the limit analysis method to all masonry as it is builds on a set of certain assumptions of failure behaviour that if disobeyed will wildly overestimate the load. Another point in relation to this is that the manual hand calculated strut-and-tie model predicted quite a lot lower than the numerical one at 70,5% of the load calculated by the numerical programs meaning that the programs can find the very extremum loads quite precisely as also evidenced by the near equality of the lower and upper bound solutions. This means that for practical uses, one should use the methodology at extreme care as a non-ductile failure will render the programs useless and directly dangerous as they will be likely to overestimate the failure loads quite massively.

Summarizing, it has been shown by the quasi-ductile failure that the alternative load path method is likely to be an applicable robustness strategy within masonry structures and can be numerically characterized with limit analysis.

References

[1] S. W. Sloan, "Lower bound limit analysis using finite elements and linear programming," *International Journal for Numerical and Analytical Methods in Geomechanics*, vol. 12, 1988.

[2] S. W. Sloan, "Upper bound limit analysis using finite elements and linear programming," *International Journal for Numerical and Analytical Methods in Geomechanics*, vol. 13, pp. 263–282, 1989.

[3] S. W. Sloan, "Upper bound limit analysis using discontinous velocity field," *Computational methods applied mechanical engineering*, vol. 127, pp. 293–314, 1995.

[4] J. M. Adam, F. Parisi, J. Sagaseta, and X. Lu, "Research and practice on progressive collapse and robustness of building structures in the 21st century," *Engineering Structures*, vol. 173, pp. 122–149, 2018.

[5] B. S. I. (BSI), *BS 5628-1: code of practice for the use of masonry; part 1: structural use of unreinforced masonry*. BSI, 2009.

[6] A. G. Ltd, *Review of international research on structural robustness and disproportionate collapse*. Department for Communities and Local Government, 2011.

[7] T. Institut, *Lærebog: Part 2; Husets totale stabilitet*. Teknologisk Institut, 2015.

[8] K. Qian and B. Li, "Effects of masonry infill wall on the performance of rc frames to resist progressive collapse," *Journal of Structural Engineering (United States)*, vol. 143, no. 9, 2017.

[9] S. Li, S. Shan, C. Zhai, and L. Xie, "Experimental and numerical study on progressive collapse process of rc frames with full-height infill walls," *Engineering Failure Analysis*, vol. 59, pp. 57–68, 2016.

[10] S. Shan, S. Li, S. Xu, and L. Xie, "Experimental study on the progressive collapse performance of rc frames with infill walls," *Engineering Structures*, vol. 111, pp. 80–92, 2016.

[11] T. H. Almusallam, H. M. Elsanadedy, Y. A. Al-Salloum, N. A. Siddiqui, and R. A. Iqbal, "Experimental investigation on vulnerability of precast rc beam-column joints to progressive collapse," *KSCE Journal of Civil Engineering*, vol. 22, no. 10, pp. 3995–4010, 2018.

[12] A. Pham and k. Tan, "Experimental study on dynamic responses of reinforced concrete frames under sudden column removal applying concentrated loading," *Engineering Structures*, vol. 139, pp. 31–45, 2017.

[13] K. Qian and B. Li, "Dynamic performance of rc beam-column substructures under the scenario of the loss of a corner column—experimental results," *Engineering Structures*, vol. 42, pp. 154–167, 2012.

[14] D. Gouverneur, R. Caspeele, and L. Taerwe, "Experimental investigation of the load-displacement behaviour under catenary action in a restrained reinforced concrete slab strip," *Engineering Structures*, vol. 49, pp. 1007–1016, 2013.

[15] A. M. D'Altri, V. Sarhosis, G. Milani, J. Rots, S. Cattari, S. Lagomarsino, E. Sacco, A. Tralli, G. Castellazzi, and S. de Miranda, "Modeling strategies for the computational analysis of unreinforced masonry structures: Review and classification," *Archives of Computational Methods in Engineering*, vol. 27, no. 4, pp. 1153–1185, 2020.

[16] D. Sutcliffe, H. Yu, and A. Page, "Lower bound limit analysis of unreinforced masonry shear walls," *Computers and Structures*, vol. 79, 2001.

[17] G. Milani, P. Lourenço, and A. Tralli, "Homogenised limit analysis of masonry walls, part i: Failure surfaces," *Computers and Structures*, vol. 84 Issues 3–4. Pages 166-180, 2006.

[18] L. G. H. et al, *Theory of plasticity,lecture notes*. Unpublished, 2022.

[19] C. Calderini, S. Cattari, and S. Lagomarsino, "In-plane strength of unreinforced masonry piers," *Earthquake Engineering and Structural Dynamics*, vol. 38, no. 2, pp. 243–267, 2009.

[20] W. W. Charnes, A. Cooper, "Programming with linear fractional functionals," *Naval Research Logistics Quarterly*, vol. 9, pp. 181–186, 1962.

[21] C. C. E. de Normalisation, *EN 12390-3: Testing hardened concrete - Part 3: Compressive strength of test specimens*. Brussels (Belgium):CEN, 2019.

[22] C. C. E. de Normalisation, *EN 1052-3: Methods of test for masonry - Part 3: Determination of initial shear strength*. Brussels (Belgium):CEN, 2002.

[23] R. A. R. HULSE, "The shear strength of bricks and brickworks," 1982.

[24] J. Piratheepan, "Determination of c and phi from idt and unconfined compression testing and numerical analysis," *Journal of Materials in Civil Engineering*, vol. 24, 2012.

[25] S. Aroni, "Shear strength of reinforced aerated concrete slabs," *Materials and Structures*, vol. 22, pp. 443–449, 1989.

[26] e. A. Tiwari. B, "Mechanical properties of lightweight cellular concrete for geotechnical applications," *Journal of Materials in Civil Engineering*, vol. 29, 2017.

[27] B. R. Ellingwood, R. Smilowitz, D. Dusenberry, D. Duthinh, H. lew, and N. Carino, *Best Practices for Reducing the Potential for Progressive Collapse in Buildings*. NIST Interagency/Internal Report (NISTIR), 2007.

[28] C. C. E. de Normalisation, *EN 1996-1-1: Eurocode 6 – Design of masonry structures – part 1–1: General rules for reinforced and unreinforced masonry structures*. Brussels (Belgium):CEN, 2005.

[29] D. of Defence (DoD), *Design of buildings to resist progressive collapse (UFC 4-023-03)*. Washington, DC: Unified Facilities Criteria, 2016.

[30] G. S. A. (GSA), *Alternative path analysis and design guidelines for progressive collapse resistance*. Washington, DC: Office of Chief Architects, 2013.

[31] J. Morton, *Accidental damage robustness and stability: BS 5628: Structural use of masonry: part 1: unreinforced masonry*. BDA, 1985.

[32] H. Jacques, *The Stone Skeleton: Structural Engineering of Masonry Architecture*. Cambridge University Press, 1995.

[33] G. Maier and A. Nappi, "A theory of no-tension discretized structural systems," *Engineering Structures,Volume 12, Issue 4,Pages 227-234,*, 1990.

[34] M. Daniele, P. Rui, and P. Andrea., "Using the applied element method for modelling calcium silicate brick masonry subjected to in-plane cyclic loading," *Earthquake Engineering and Structural Dynamics. 47*, 2018.

[35] S. Pietruszczak and X. Niu, "A mathematical description of macroscopic behaviour of brick masonry," *International Journal of Solids and Structures*, vol. 29 Issue 5 Pages 531-546, 1992.

[36] L. Macorini and B. Izzuddin, "A non-linear interface element for 3d mesoscale analysis of brick-masonry structures," *International Journal for Numerical Methods in Engineering*, vol. 85, issue 12, 2011.

[37] M. Petracca, L. Pelà, R. Rossi, Z. S., G. Camata, and E. Spacone, "Micro-scale continuous and discrete numerical models for nonlinear analysis of masonry shear walls," *Construction and Building Materials*, vol. 149, Pages 296-314, 2017.

[38] V. Sarhosis, K. Bagi, J. Lemos, and G. Milani, *Computational Modeling of Masonry Structures Using the Discrete Element Method*. IGI Global, 2016.

[39] M. Gilbert, C. Smith, and T. Pritchard, "Masonry arch analysis using discontinuity layout optimisation," *CE-Engineering and Computational Mechanics*, vol. 163, pp. 167–178, 2010.

A Drawings of experimental setup

A.1 Experimental setup

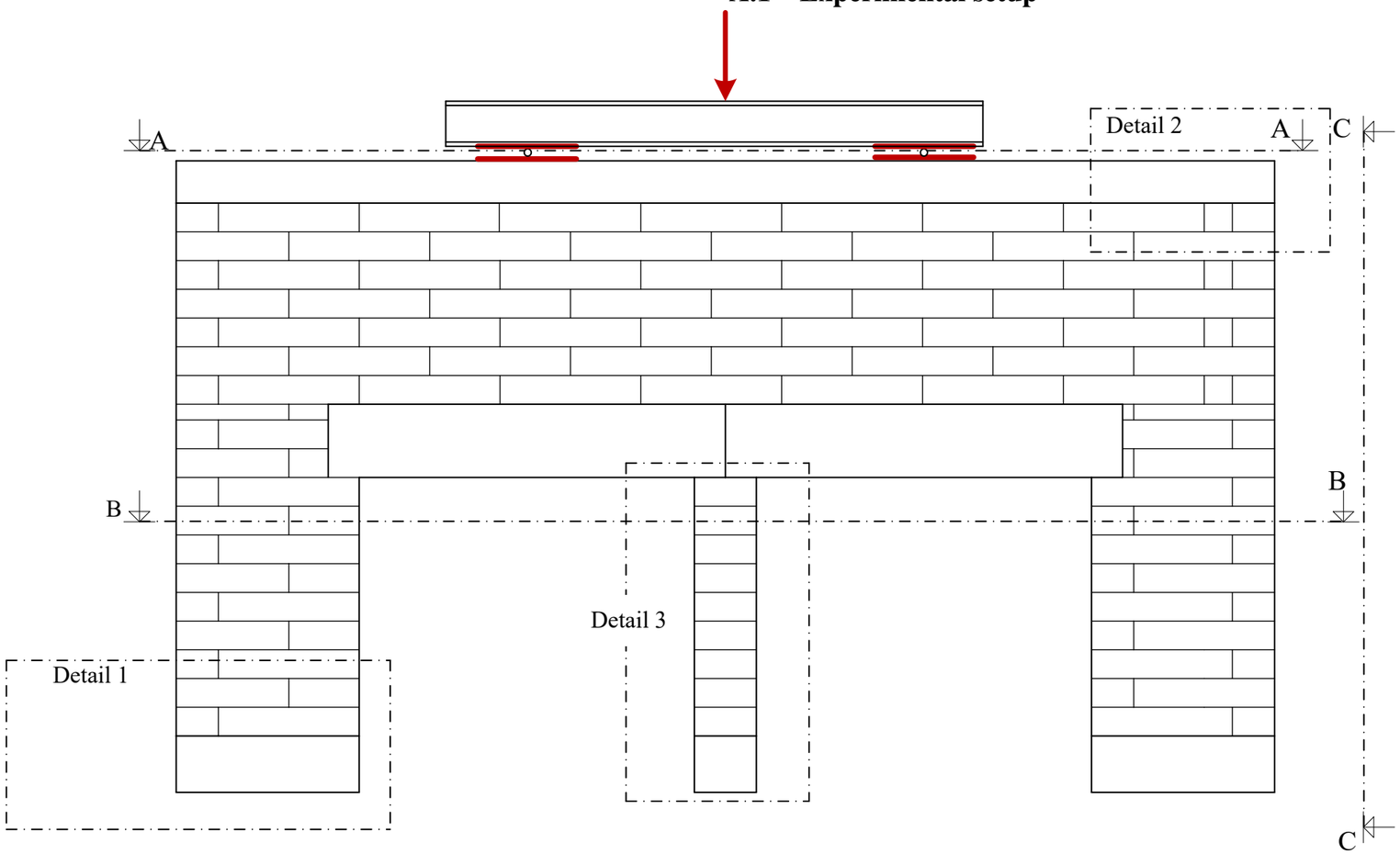

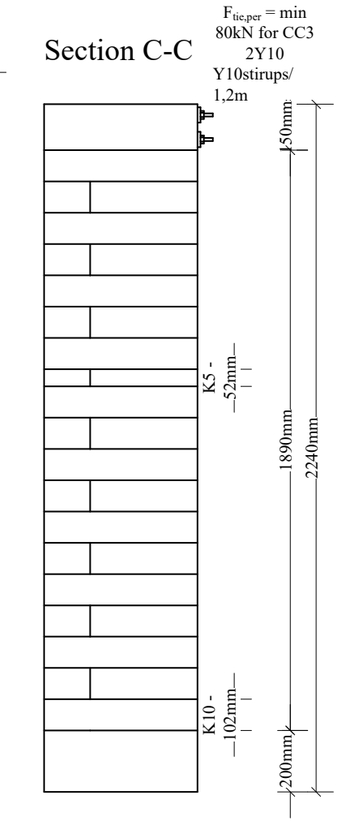

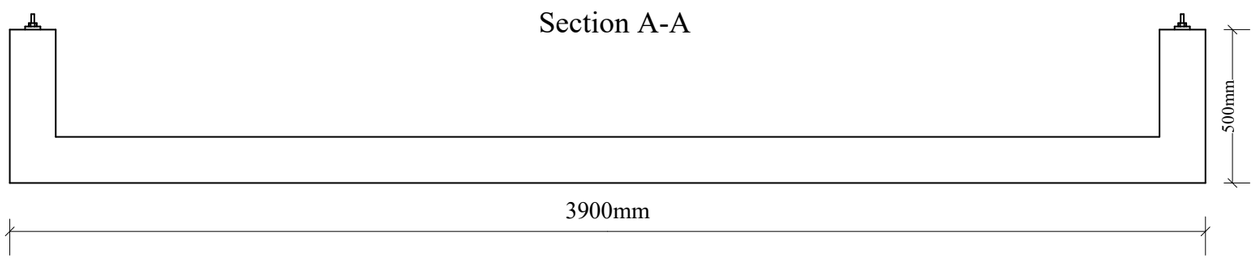

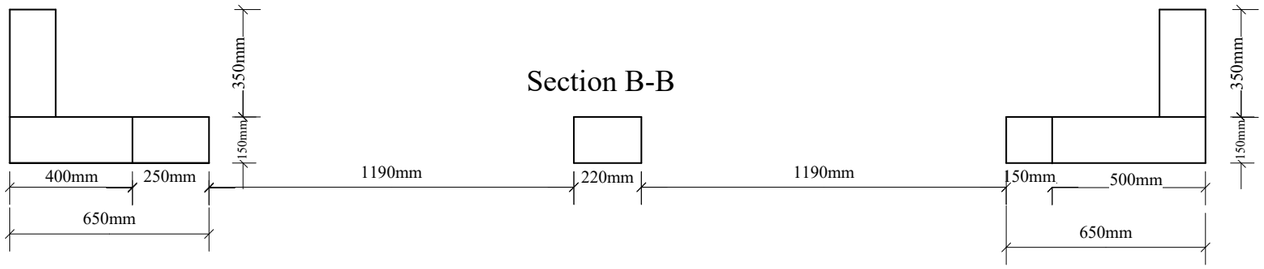

Experimental setup	
Date:	18.03.22
Scale:	1:20
Name:	Anders & Peter

A.2 Foundation

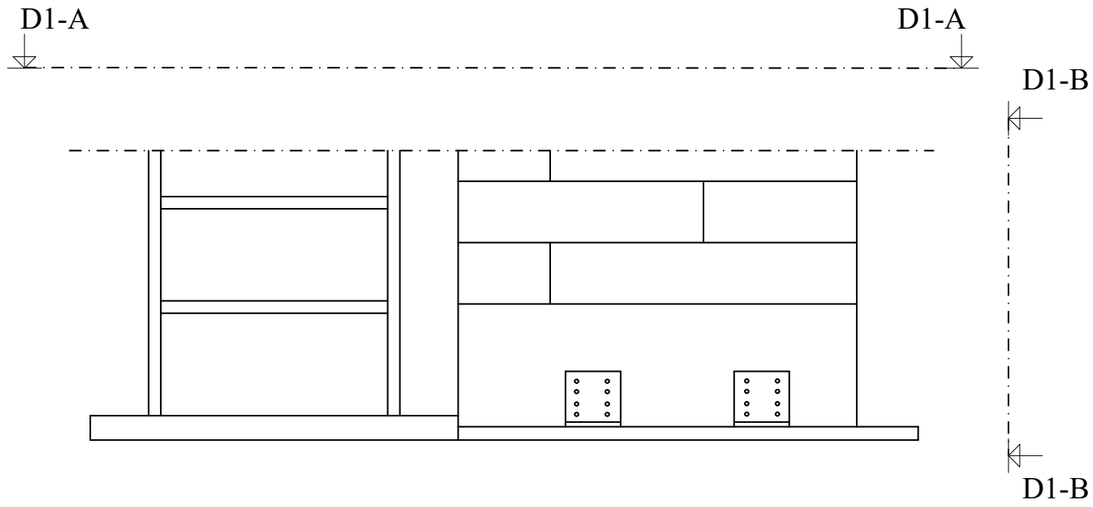

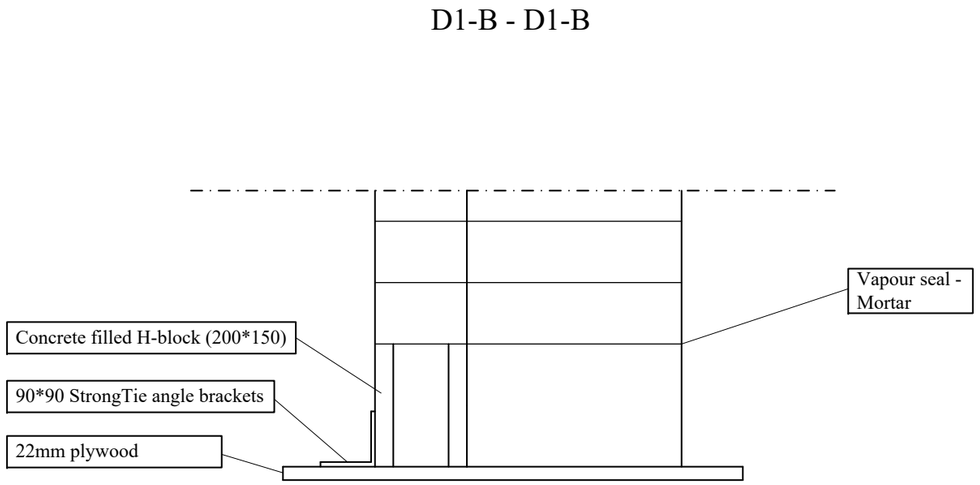

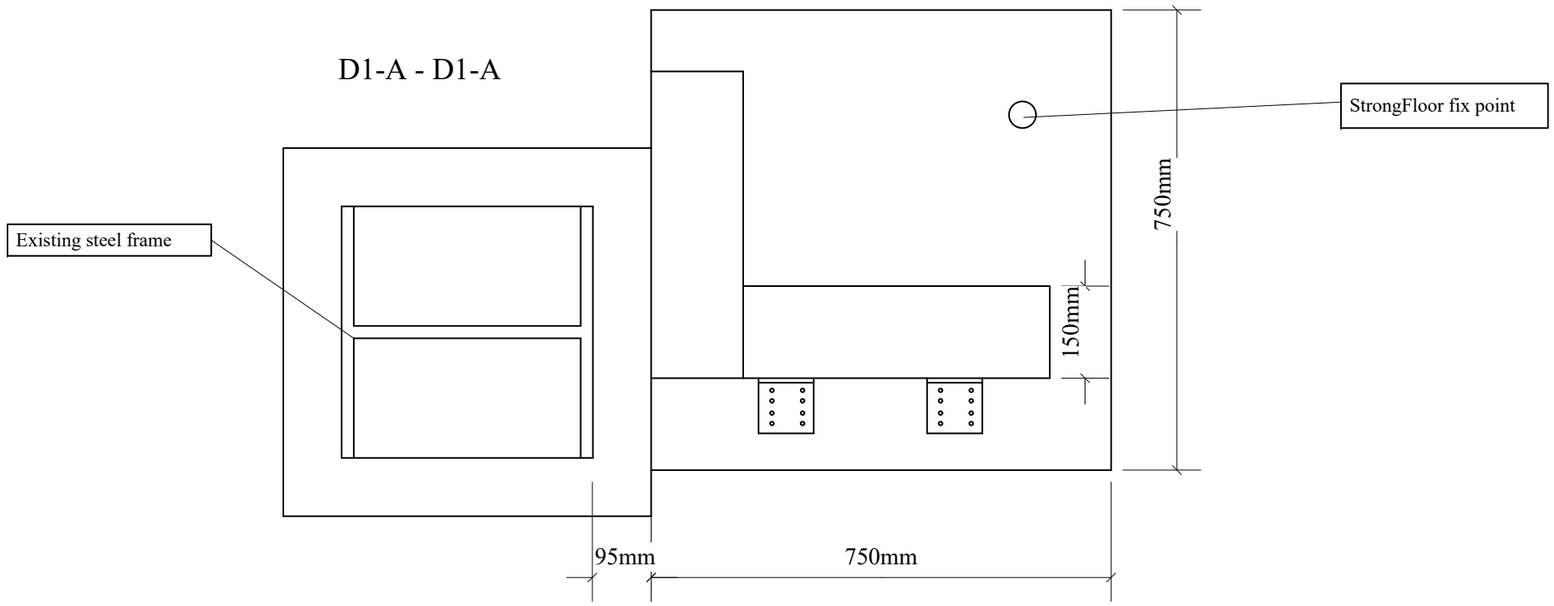

Detail 1 - Foundation	
Date:	18.03.22
Scale:	1:10
Name:	Anders & Peter

A.3 Slab beam reinforcement

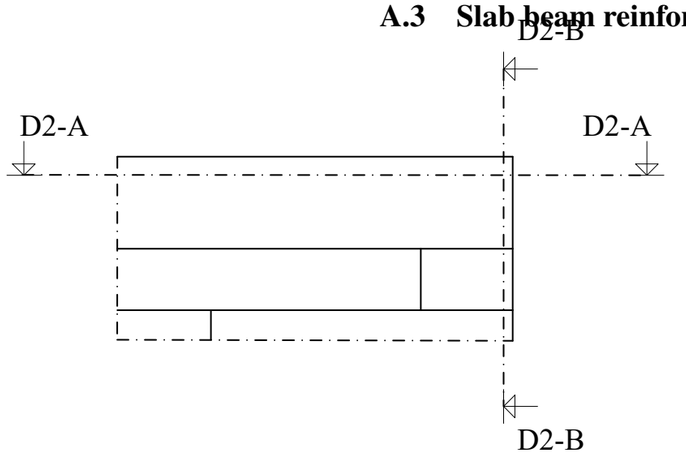

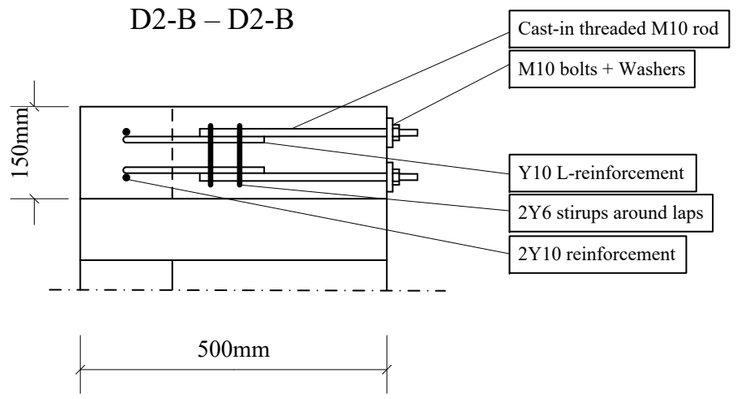

D2-A – D2-A

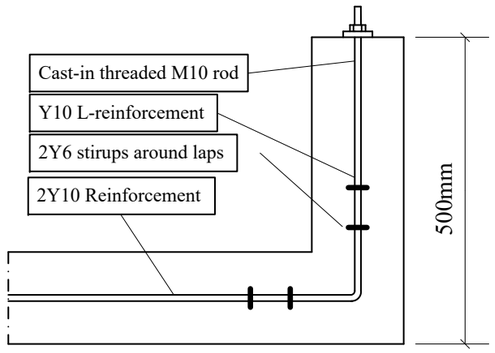

Detail 2 – Slap beam reinforcement	
Date:	18.03.22
Scale:	1:10
Name:	Anders & Peter

A.4 Column removal

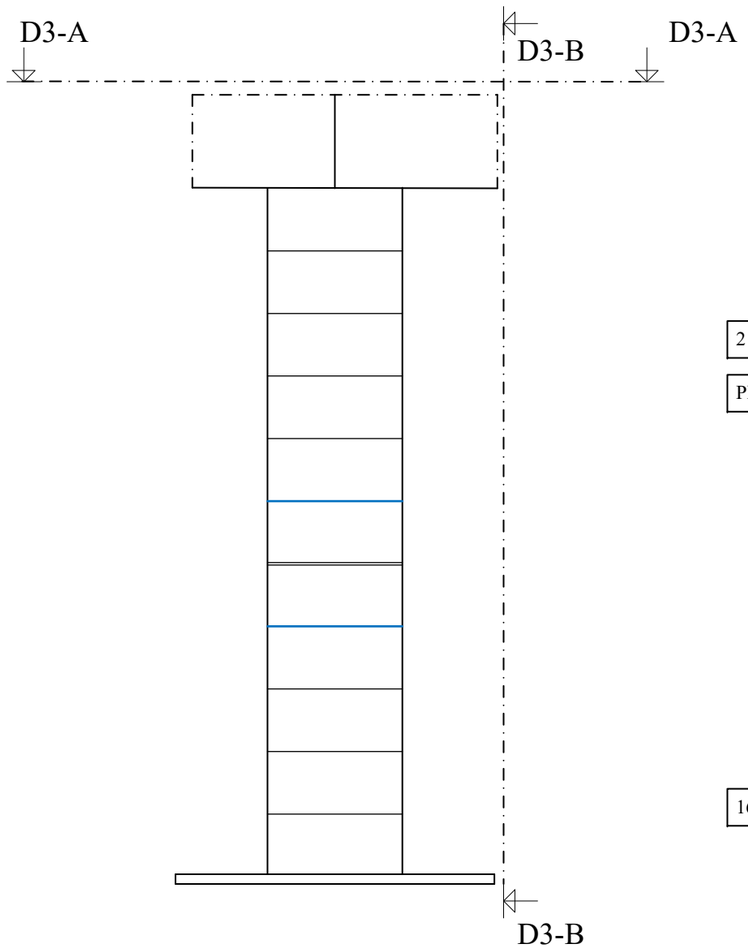

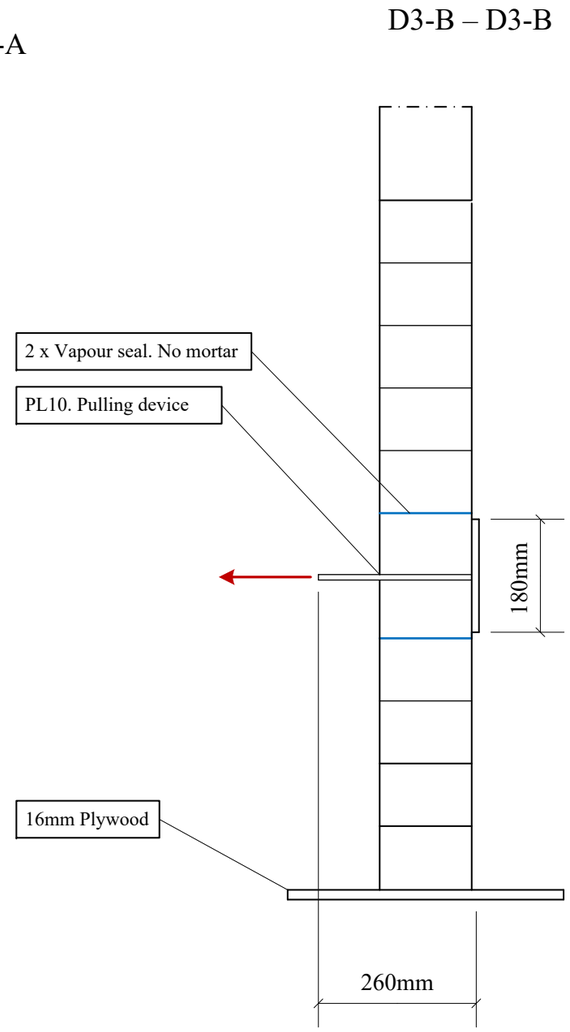

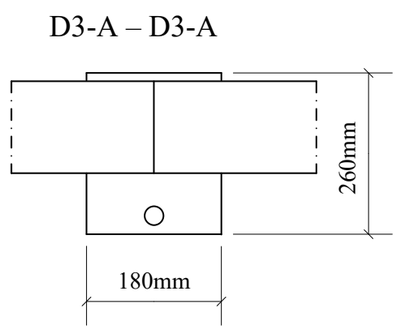

Detail 3 – Column removal	
Date:	18.03.22
Scale:	1:10
Name:	Anders & Peter

B Determination of concrete strength and Mohr-Coulomb parameters of CSUs

B.1 Scope

Present experimental tests have the purpose of determining the compressive strength of the top slab beam and the internal friction angle and cohesion of the calcium silicate units forming, which in combination forms the specimen being tested in the main experimental test of progressive collapse resisting mechanisms within unreinforced masonry. The material properties are used in the numerical model described in section 5 and 6 where they form the yield criterions used as inequality constraints in the optimization formulation.

B.2 Concrete cylinder compressive strength test

The compressive strength of the hardened concrete cylinders are tested in accordance with EN 12390-3 Testing hardened concrete - Part 3: Compressive strength of test specimens[21].

The tested specimens were hardened concrete cylinders made from the same concrete batch used in the top slab beam of the main experimental test made the 2nd of May, wherefrom 3 cylinders are casted with a diameter of 100mm and a height of 200mm. All cylinders was carefully vibrated until large air bobbles are not occurring as shown on below figure 66 and compressed with the mold lit.

Figure 66: Concrete filled cylinder molds

Figure 67: Hardened concrete cylinders

The cylinders were placed laterally to ensure that possible air bobbles were formed at the side of concrete cylinder and not on the top, hereby ensuring the largest possible cross section area on the surface and a satisfactory failure of the cylinder specimen. After two days of hardening the cylinders were removed from the molds and kept in airtight plastic bag until the 23rd of May, where they where tested. As depicted on figure 67 the cross section area of two cylinders were not intact when they were removed from the molds, which could blurry the test results of these. It is likely that the mold lits were not fastened probably and air was let in doing the process.

The conrete cylinders were tested one at a time in a uni axial test setup, where they were tested with a loading rate of 1.71 $^{kN}/_{s}$. The peak compressive strength of samples are reported in below table 11.

Table 11: Measurements and observation of concrete cylinders

Sample	Cross section area	Compressive strength	Failure type
[-]	$[mm^2]$	$[MPa]$	[-]
1	7854.0	24.82	Figure 68.4
2	7854.0	18.76	Unsatisfactory
3	7854.0	25.25	Figure 68.4

The failures of the concrete cylinders are compared with the satisfactory failures from EN12390-3 to verify the validity of the experimental results. Failures of cylinders one and three shown on figure 69, shows great resemblance with the satisfactory failure farthest to the right on the figure 68. The failure type of cylinder two did not resemble very well with any of the satisfactory failures nor the unsatisfactory failures from EN12390-3[21], but the very low compressive strength does indicate that the cylinder was flawed and unsatisfactory. The compressive strength of this cylinder is therefore discarded and the compressive strength of the concrete used is taken as the average of the strength of cylinder one and three, which equals 25.04MPa.

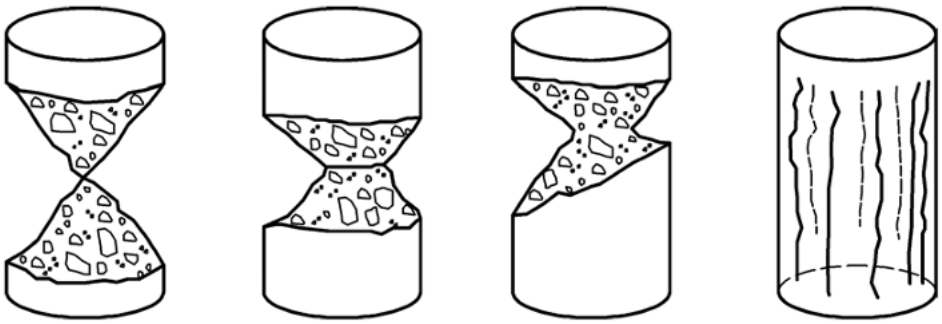

Figure 68: Satisfactory failure of cylinder specimen acc. EN12390-3

(a) Failure of cylinder 1 (b) Failure of cylinder 2 (c) Failure of cylinder 3

Figure 69: Failures of cylinder specimens

B.3 Initial shear strength of calcium silicate units

Determination of initial shear strength of calcium silicate masonry is tested in accordance with EN 1052-3 Methods of test of masonry - Part 3: Determination of initial shear strength[22].
The tested calcium silicate masonry samples was made of leftover bricks and KS Blokfix mortar used when the wall specimen was made the 29th of April. The samples measured 150x150x300mm resulting in an approximate cross-sectional area of the specimens parallel to the shear force of $2 \cdot (150 \cdot 150) mm^2$. The dimensions of the test samples are shown below figure 70.

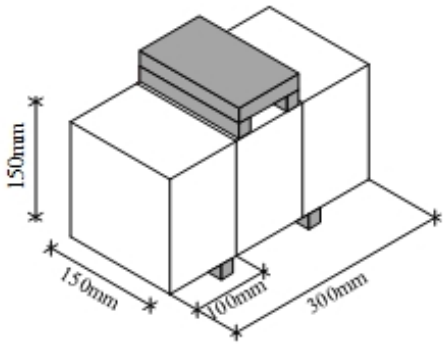

Figure 70: Dimensions of masonry sample

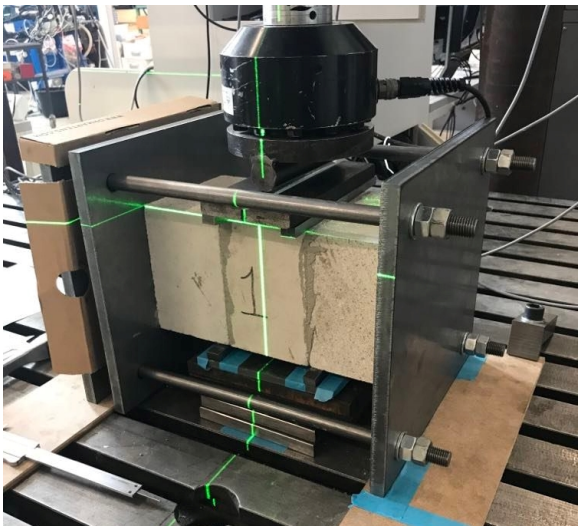

Figure 71: Steel clamp

The shear force was a result of the vertical load only applied to the center brick as near to the mortar interface as possible, as implied in figure 70. The load was applied with actuator with a speed of $0.1 \frac{mm}{min}$ ensuring a slow fracture and a good depiction of the plastic domain of calcium silicate mortar interfaces. Precompression of the samples were made with the clamp setup shown in figure 71 with four steel rods, three steel plates and a load cell measuring the applied force provided by tightening the bolts uniformly, which was ensured by measuring the distance between the plates surrounding the load cell with a vernier caliper. The cardboard made sure that the load cell was fixed to center of the steel plates and masonry sample and did not introduce any additional force to the load cell.
On the 23rd of May the initial shear strength of the four masonry specimens was tested with four different compressive stress states, 0.2MPa, 0.6MPa, 0.8MPa, and 1.0MPa. Figure 72 below shows the numbering of the four masonry samples before they were tested and the following table 12 reports the cross section area, precompression load, maximum vertical load, initial shear strength, and type of failure according to figure 73. The stress-strain curves of the four samples are reported in figures 74 - 80.

Figure 72: Masonry samples

Table 12: Measurements and observation of masonry samples

Sample [-]	Cross section area $[mm^2]$	Precompression load $[MPa]$	Vertical load $[kN]$	Initial shear strength $[MPa]$	Failure type [-]
1	22657.8	0.2	16.37	0.36	Figure 73c
2	22454.6	0.6	25.52	0.57	Figure 73c
3	22574.8	0.8	24.32	0.54	Figure 73c
4	22447.5	1.0	36.13	0.8	Figure 73c

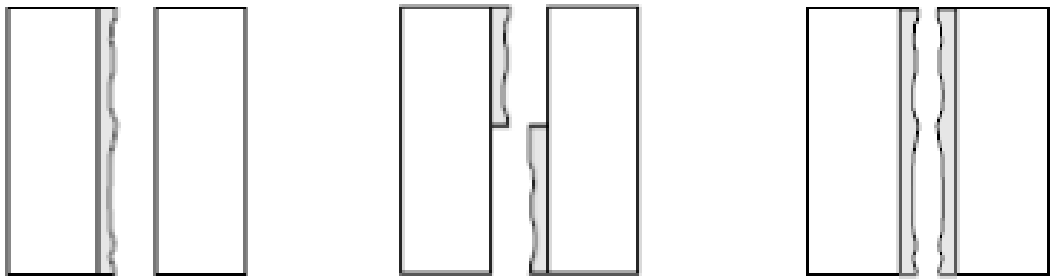

(a) Satisfactory failure type 1 (b) Satisfactory failure type 2 (c) Satisfactory failure type 3

Figure 73: Satisfactory failure types of masonry samples acc. EN 1052-3

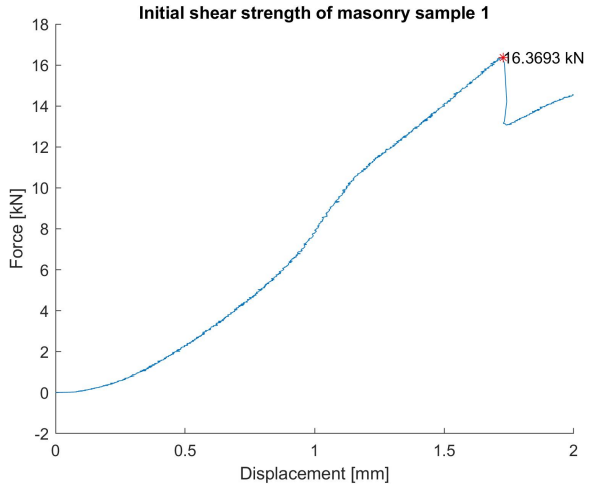

Figure 74: Stress-strain curve of sample 1

Figure 75: Failure type of sample 1

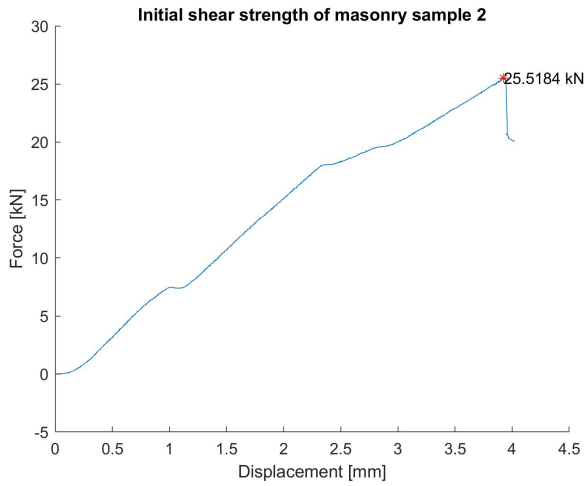

Figure 76: Stress-strain curve of sample 2

Figure 77: Failure type of sample 2

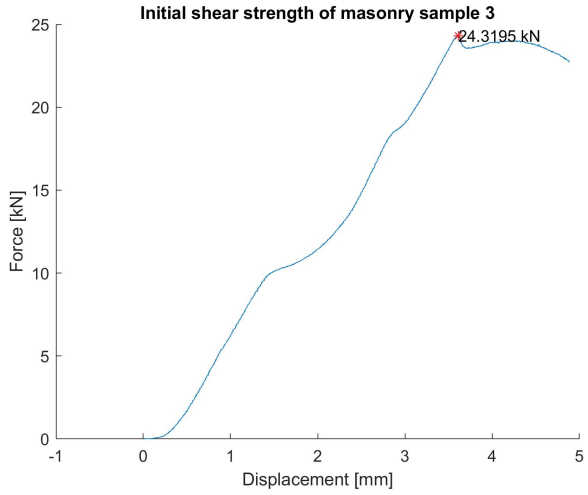

Figure 78: Stress-strain curve of sample 3

Figure 79: Failure type of sample 3

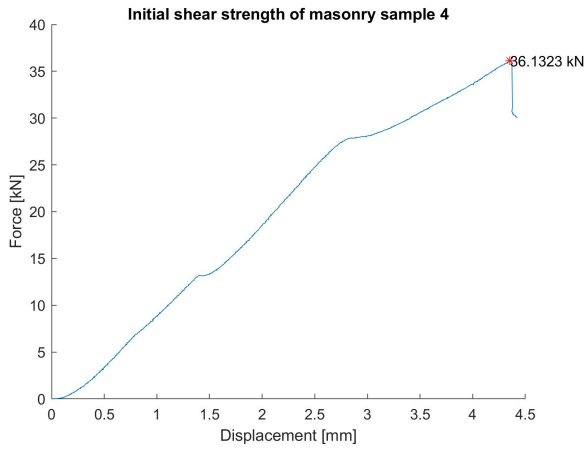

Figure 80: Stress-strain curve of sample 4

Figure 81: Failure type of sample 4

C Progress of experiment in pictures

C.1 Step 1: Loading the wall

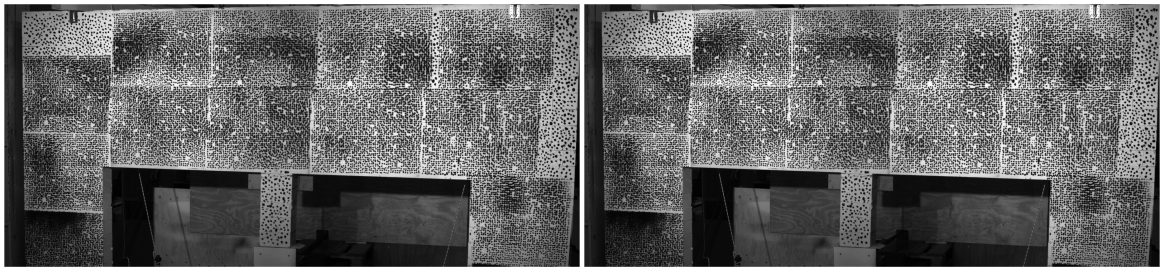

(a) Loading of the wall 0kN (b) Loading of the wall 50kN

Figure 82: Loading of the wall

C.2 Step 2: Column removal

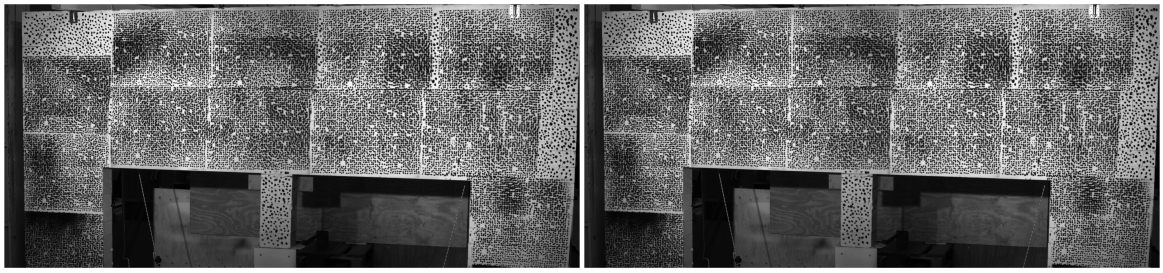

(a) Column removal second 10 (b) Column removal second 20

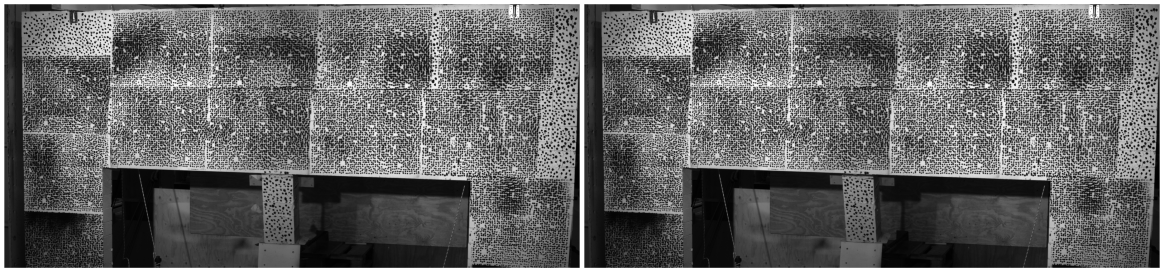

(c) Column removal second 30 (d) Column removal second 35

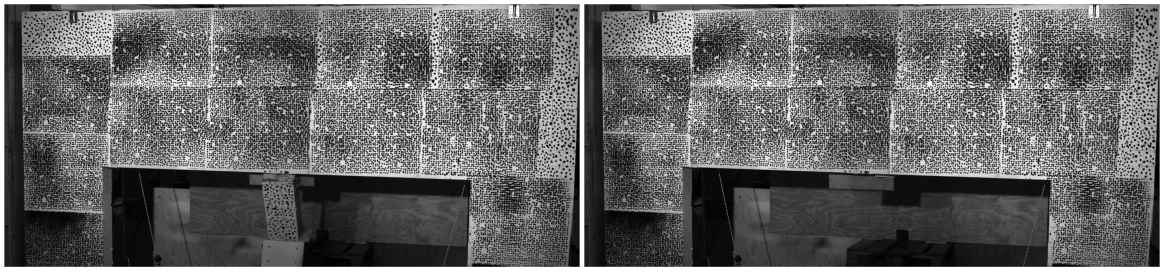

(e) Column removal second 39 (f) Column removal second 40

Figure 83: Column removal

C.3 Step 3: Load until total collapse

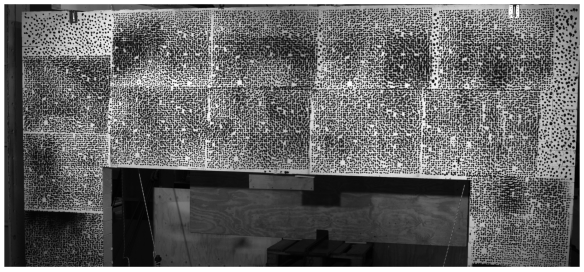

(a) 50kN Load

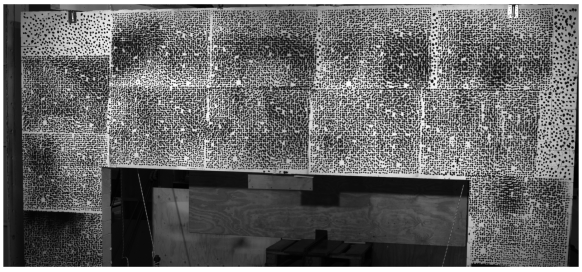

(b) 55kN Load

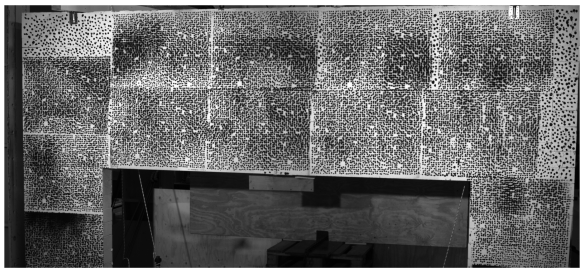

(c) 60kN Load

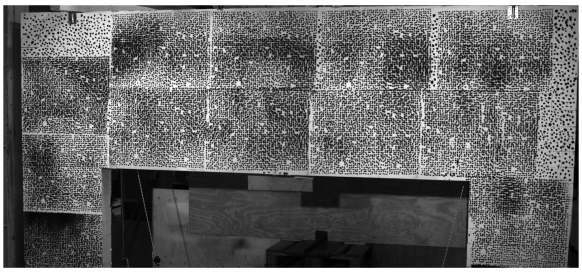

(d) 65kN Load

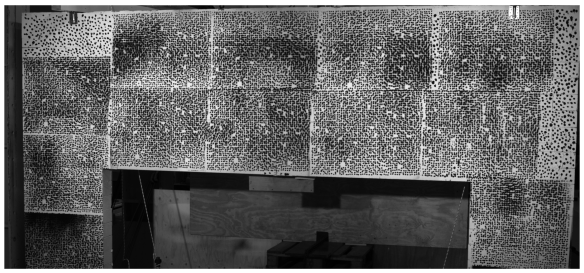

(e) 70kN Load

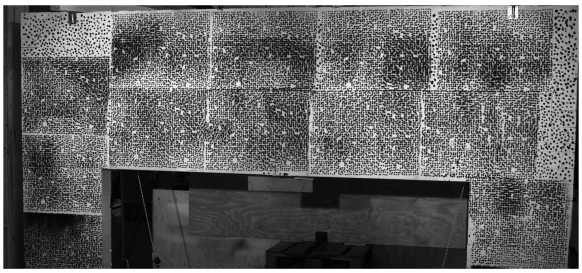

(f) 75kN Load

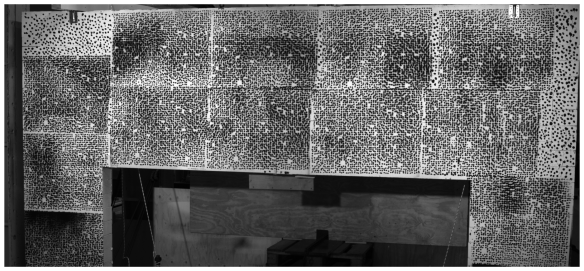

(g) 80kN Load

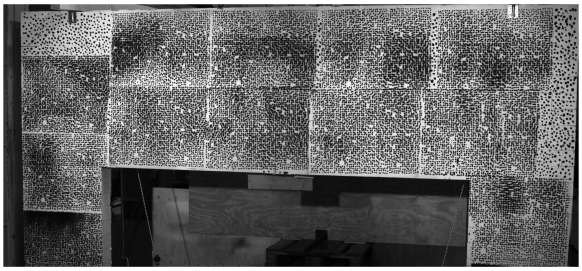

(h) 85kN Load

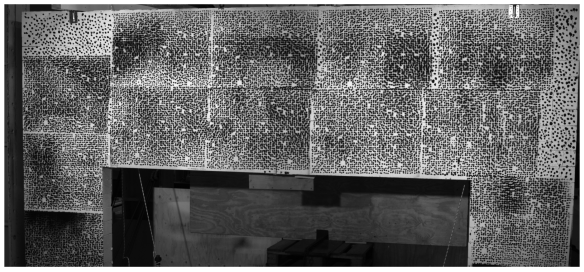

(i) 90kN Load

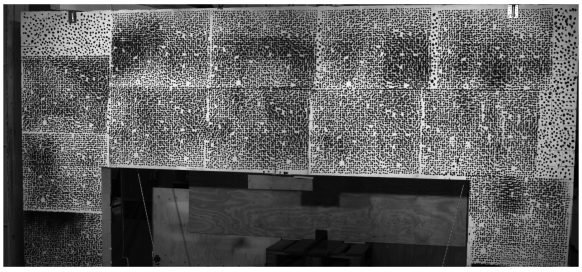

(j) 95kN Load

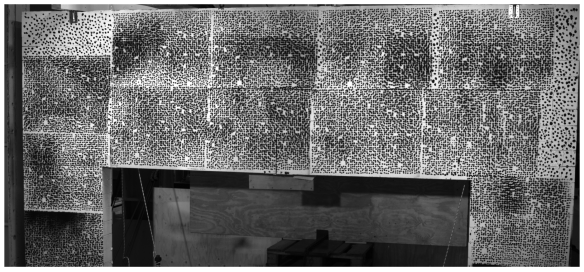

(k) 100kN Load

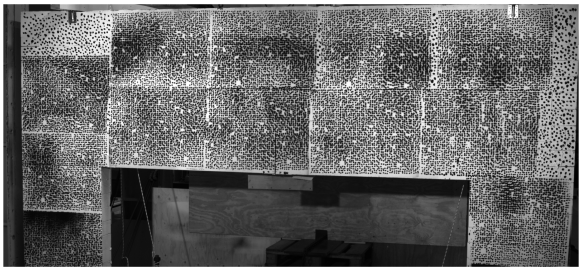

(l) 105kN Load

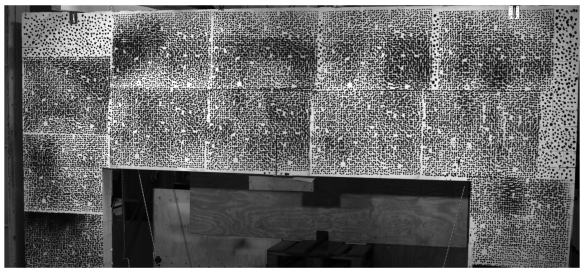

(m) 110kN Load

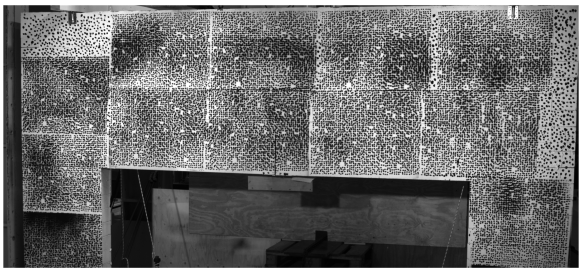

(n) 115kN Load

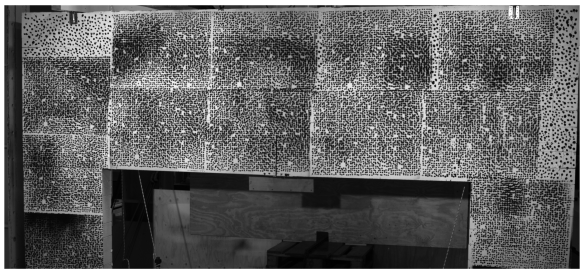

(o) 120kN Load

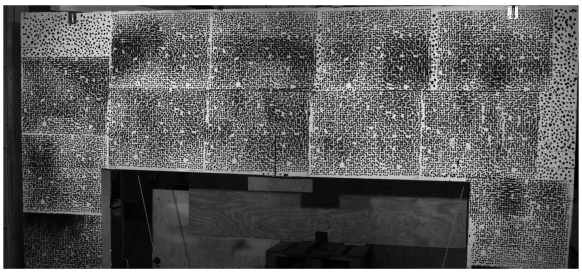

(p) 125kN Load

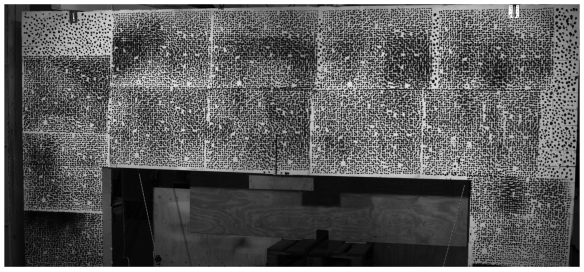

(q) 130kN Load

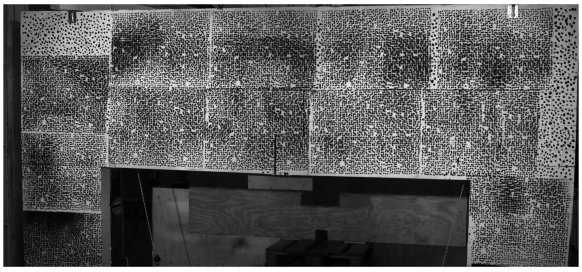

(r) 135kN Load

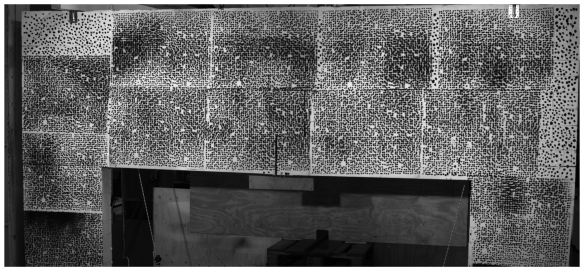

(s) 140kN Load

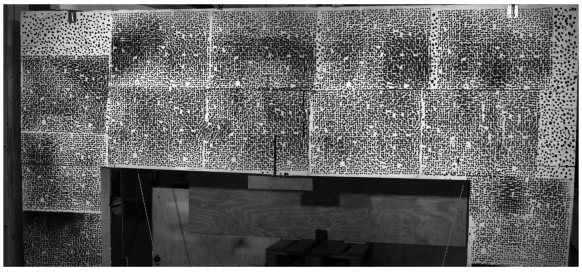

(t) 145kN Load

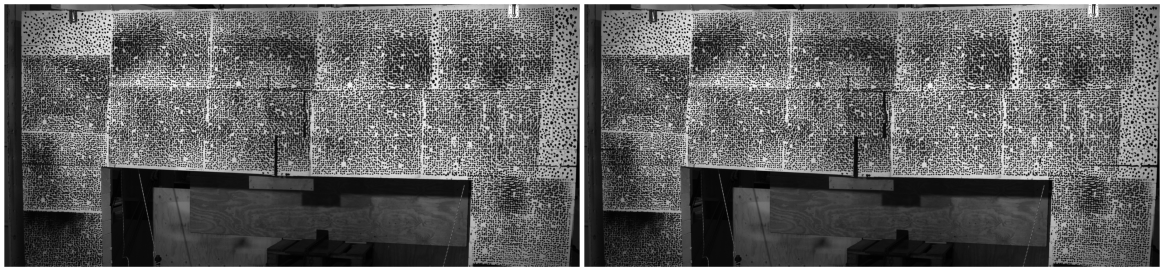

(u) 150kN Load (v) 155kN Load

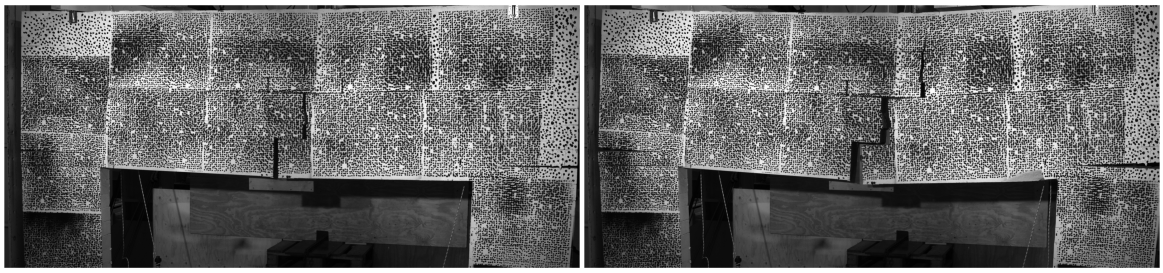

(w) 156.2kN Load (x) 58.2kN Load

Figure 84: Progress until collapse

D Numerical results from different meshing configurations

D.1 Mesh k = 0.1

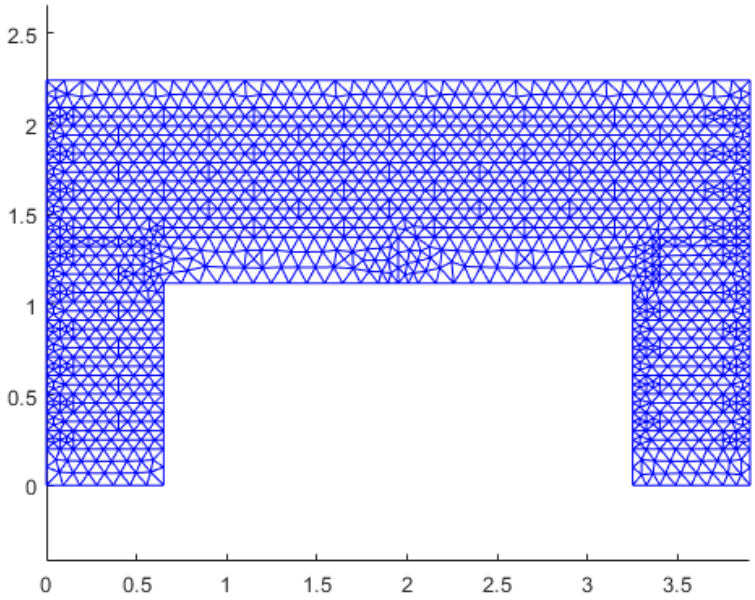

Figure 85: k01 meshing illustration

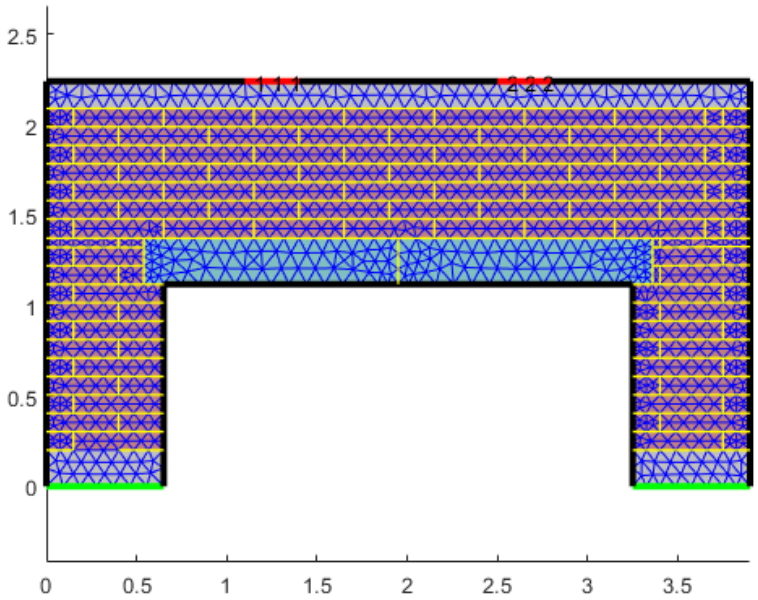

Figure 86: k01 material

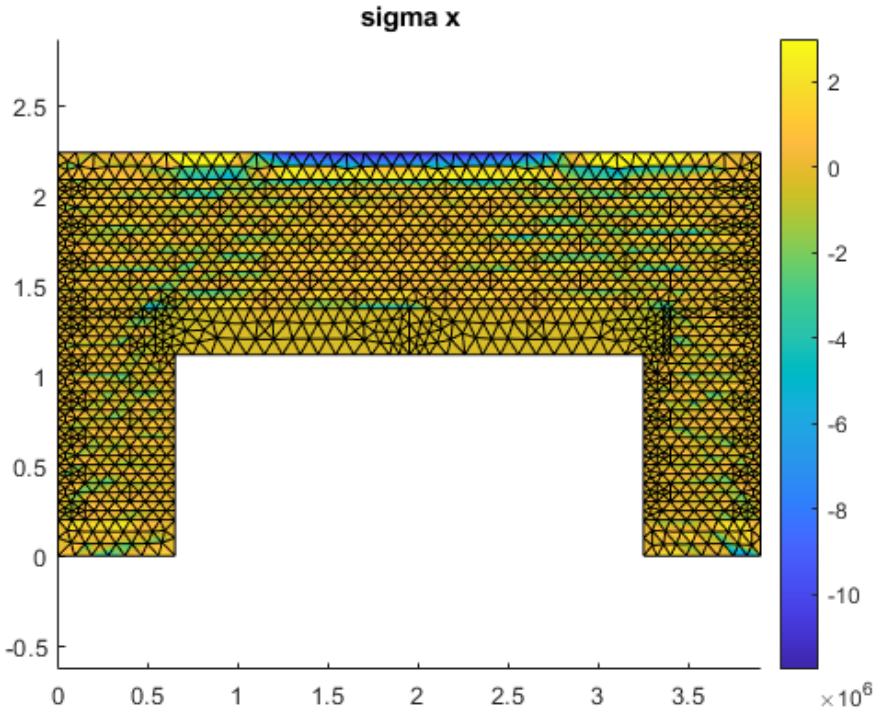

Figure 87: k01 sigma x stress field

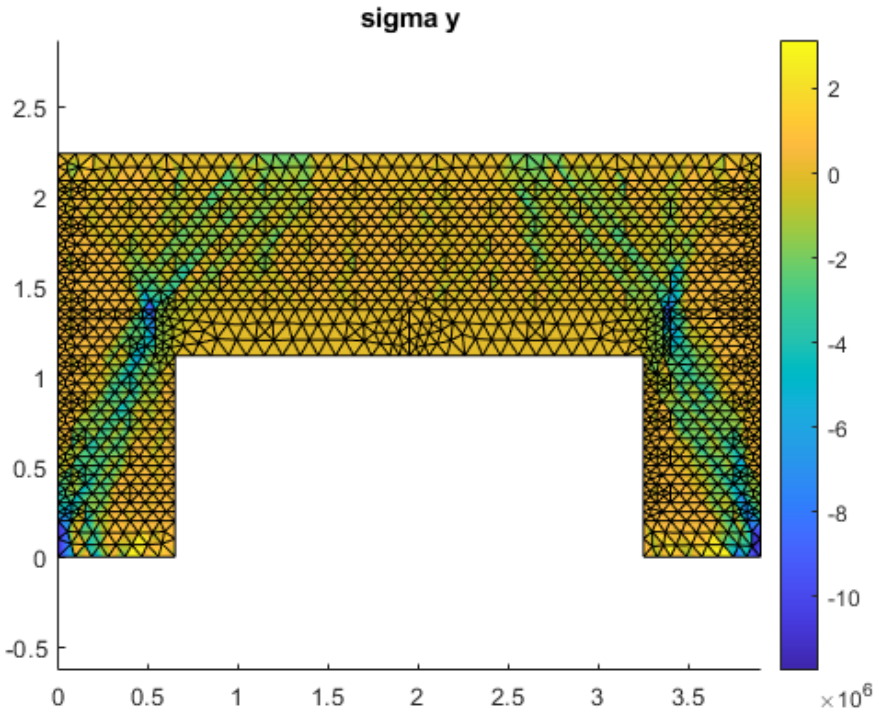

Figure 88: k01 sigma y stress field

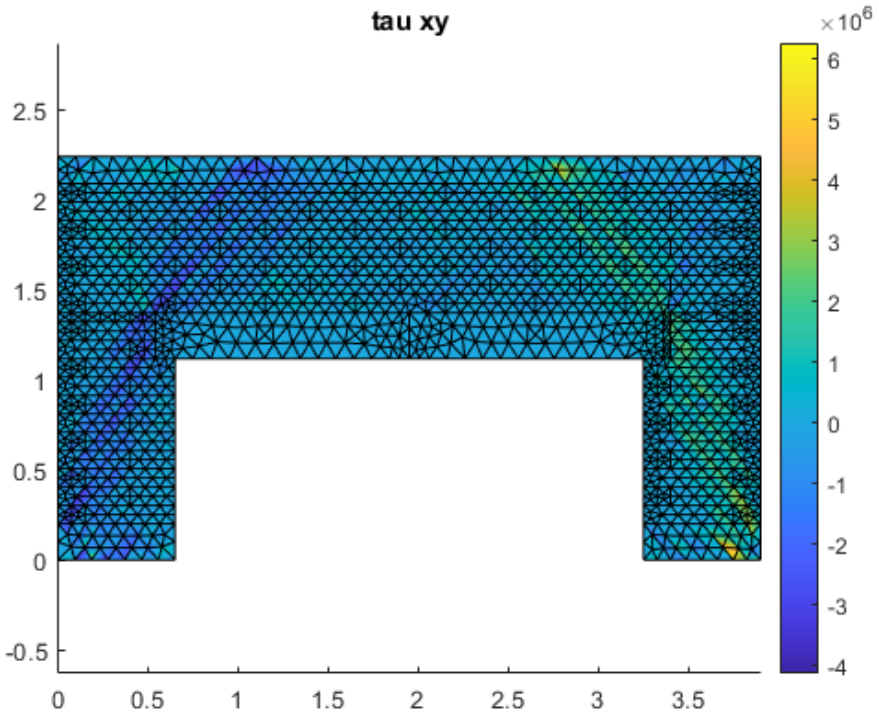

Figure 89: k01 shear stress field

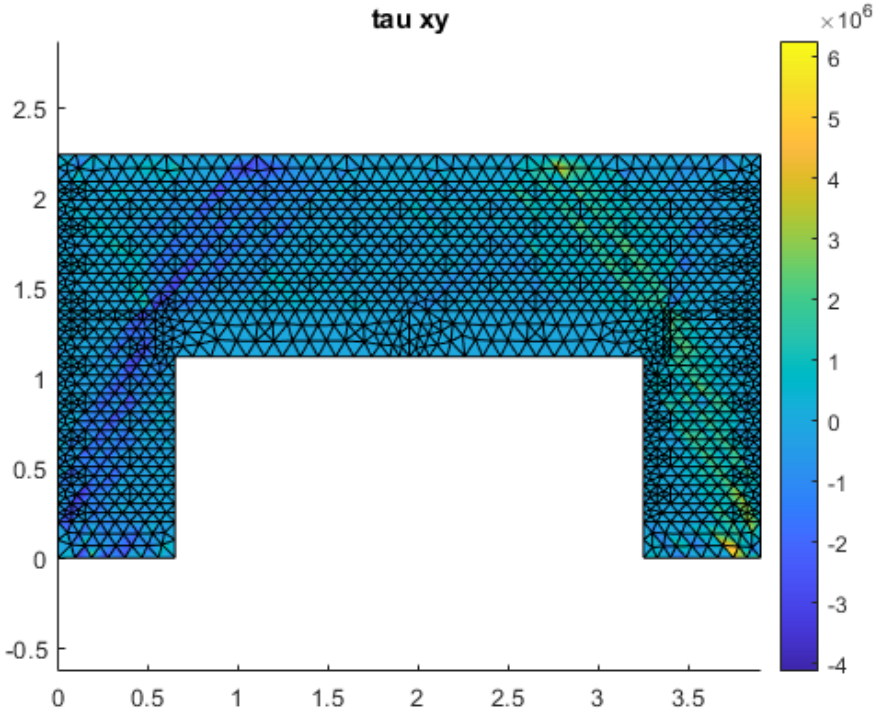

Figure 90: k01 shear stress field

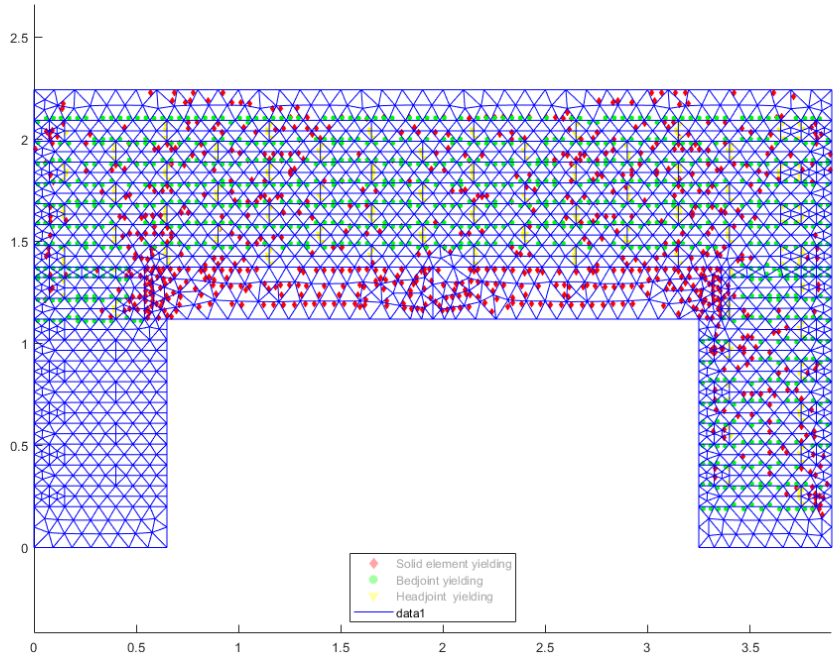

Figure 91: k01 nodal yielding plot

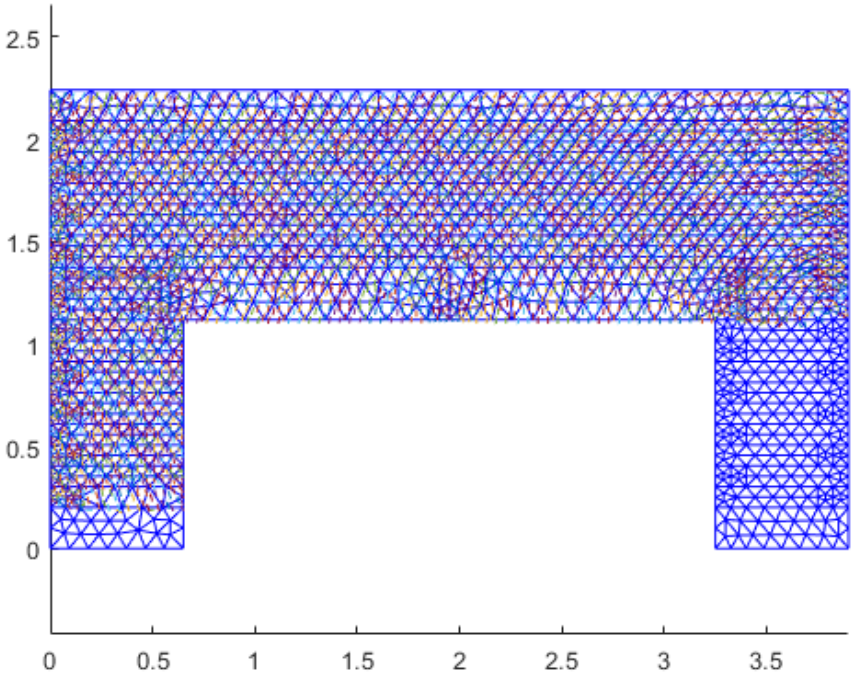

Figure 92: k01 velocity plot

D.2 Mesh k = 0.12

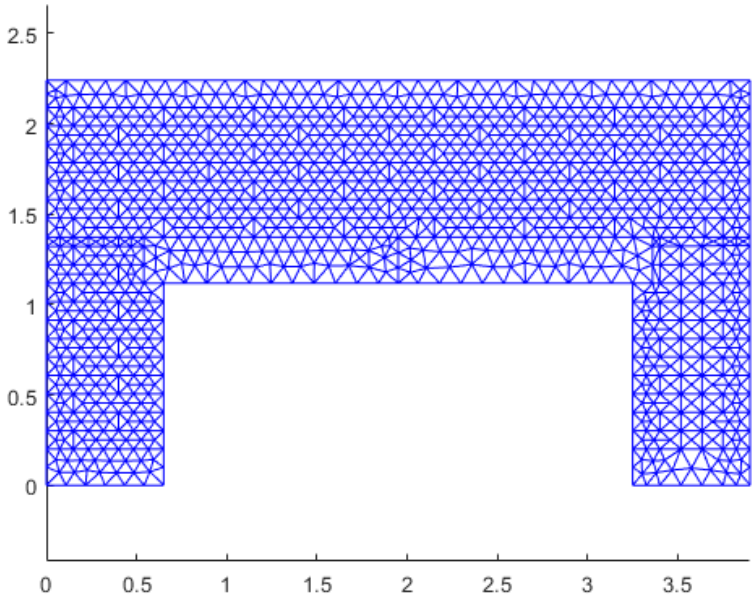

Figure 93: k012 meshing illustration

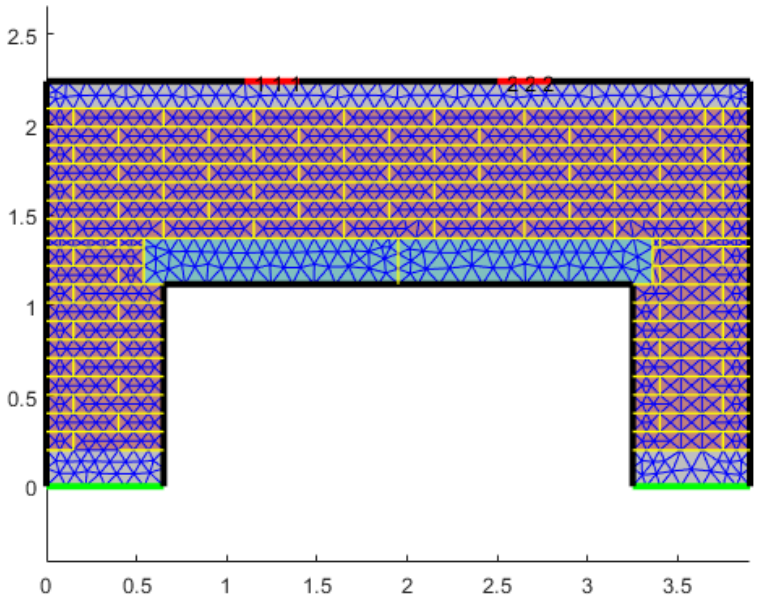

Figure 94: k012 material

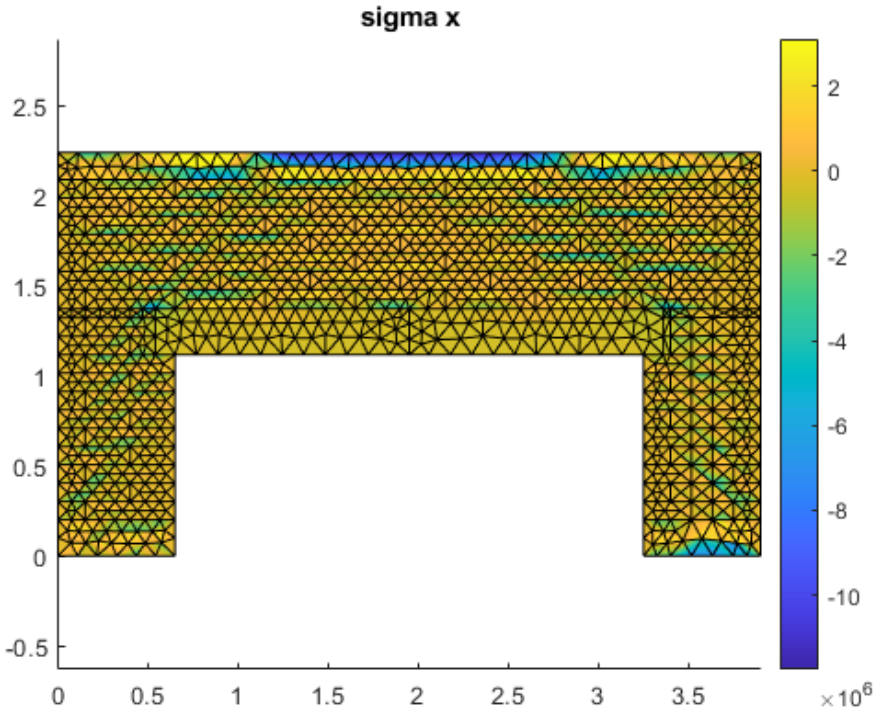

Figure 95: k012 sigma x stress field

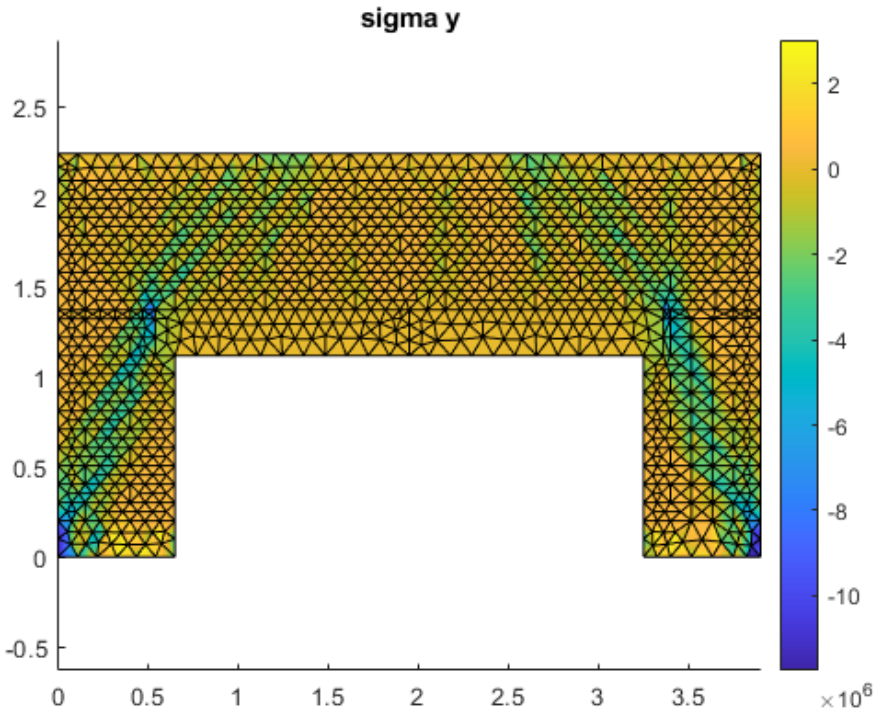

Figure 96: k012 sigma y stress field

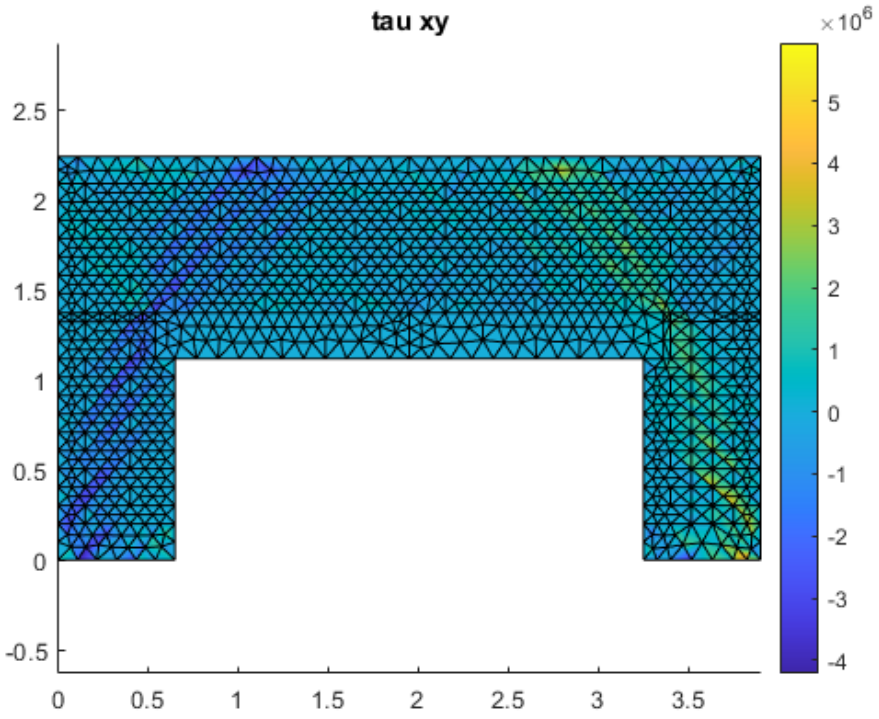

Figure 97: k012 shear stress field

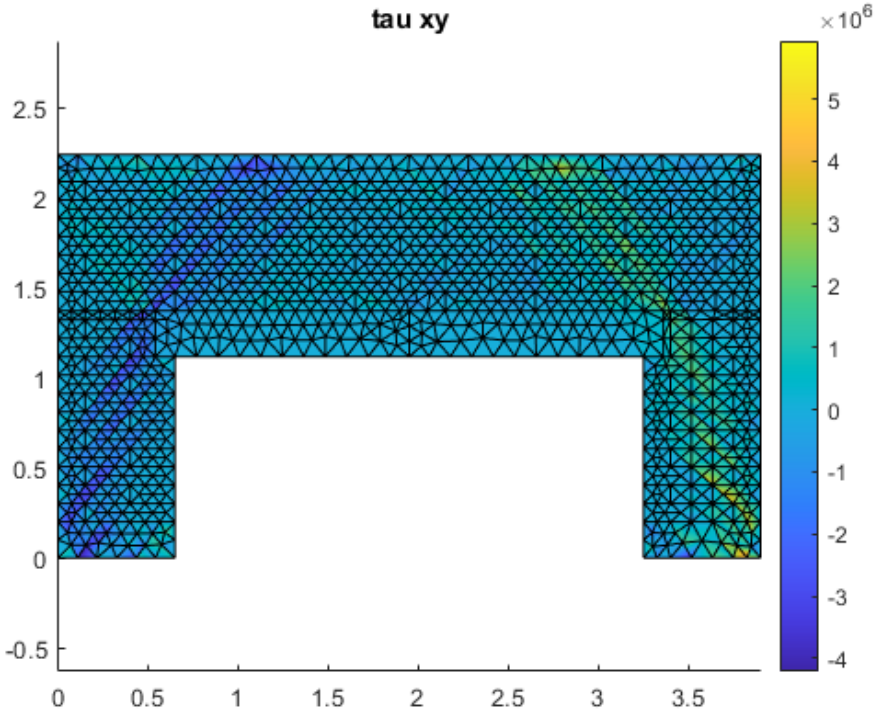

Figure 98: k012 shear stress field

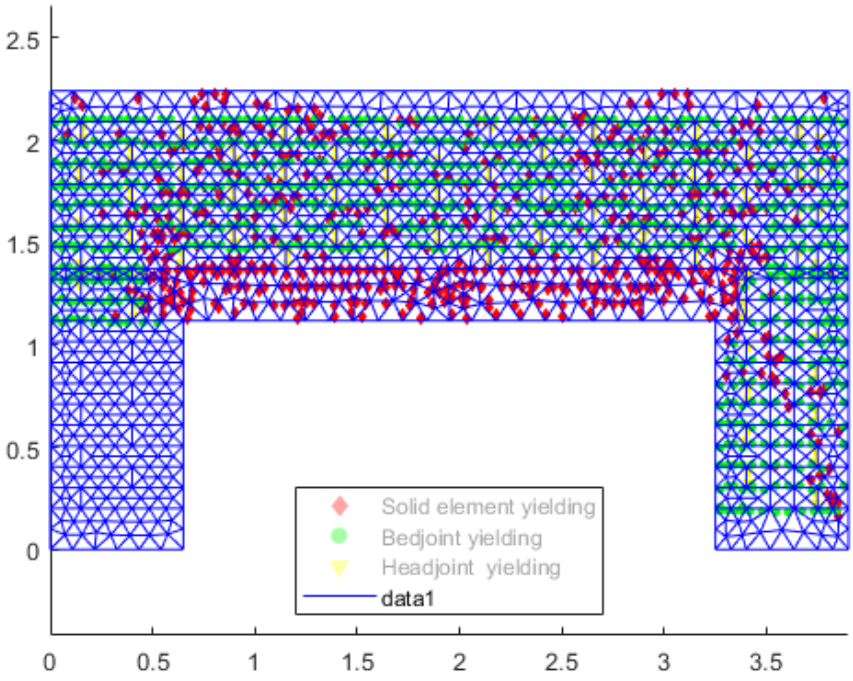

Figure 99: k012 nodal yielding plot

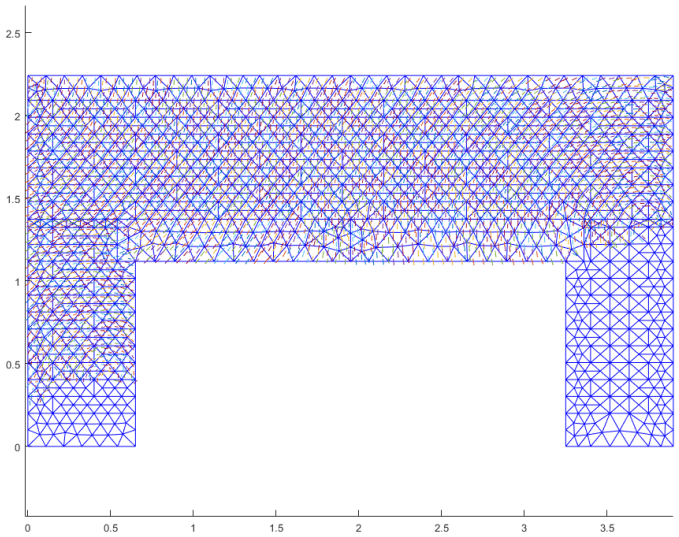

Figure 100: k012 velocity plot

D.3 Mesh k = 0.135

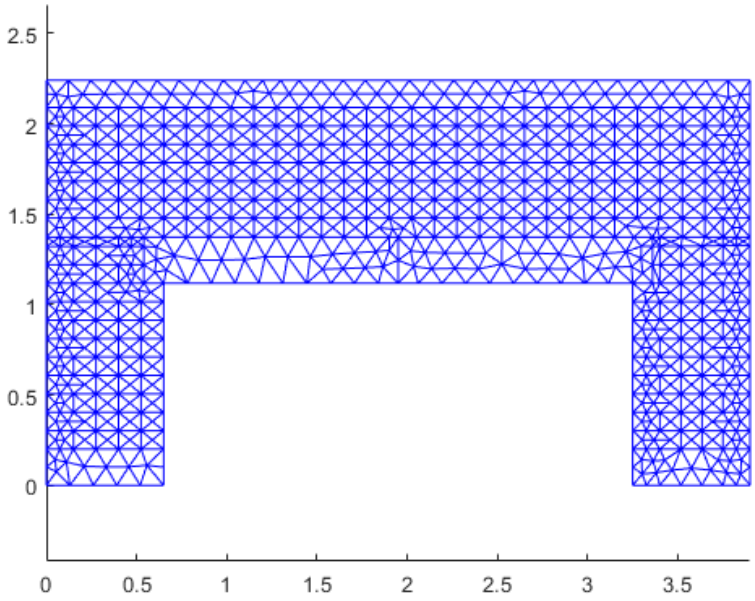

Figure 101: k0135 meshing illustration

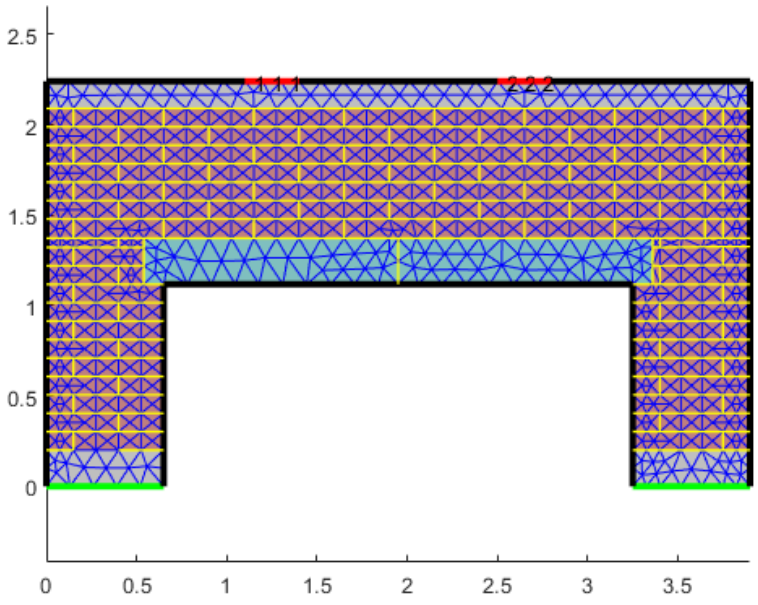

Figure 102: k0135 material

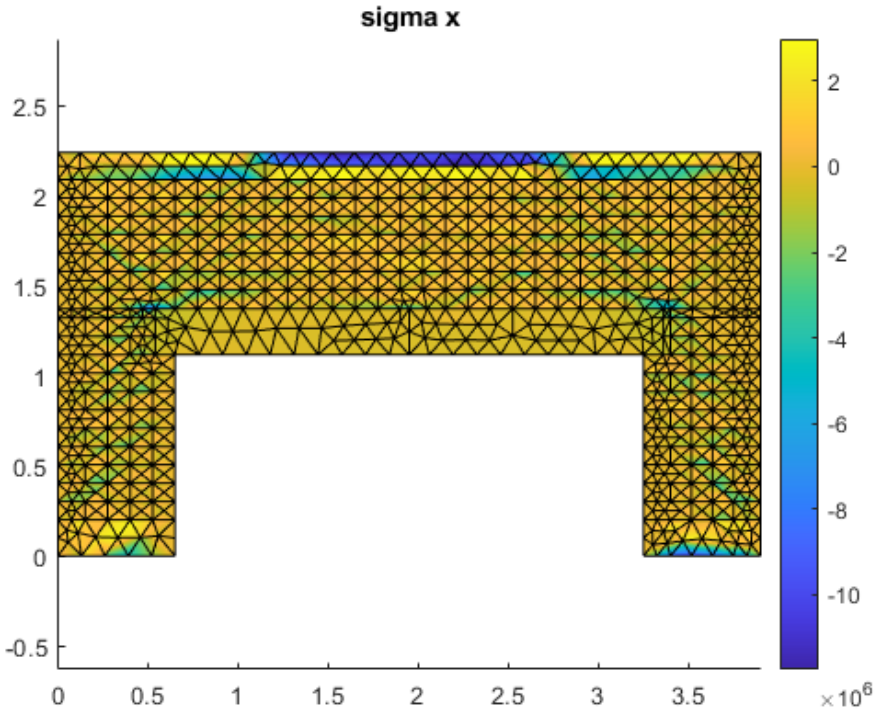

Figure 103: k0135 sigma x stress field

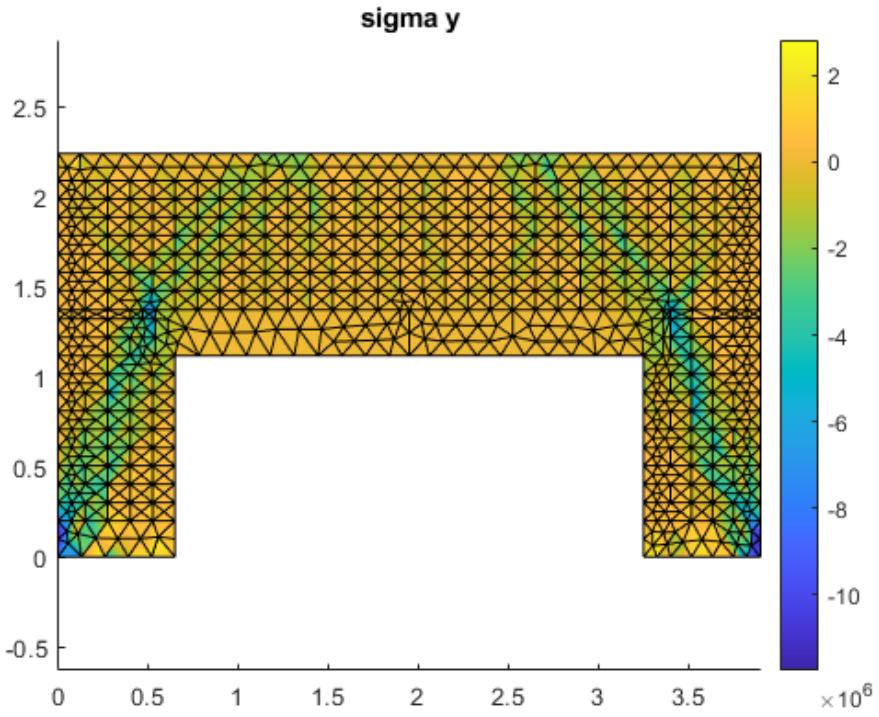

Figure 104: k0135sigma y stress field

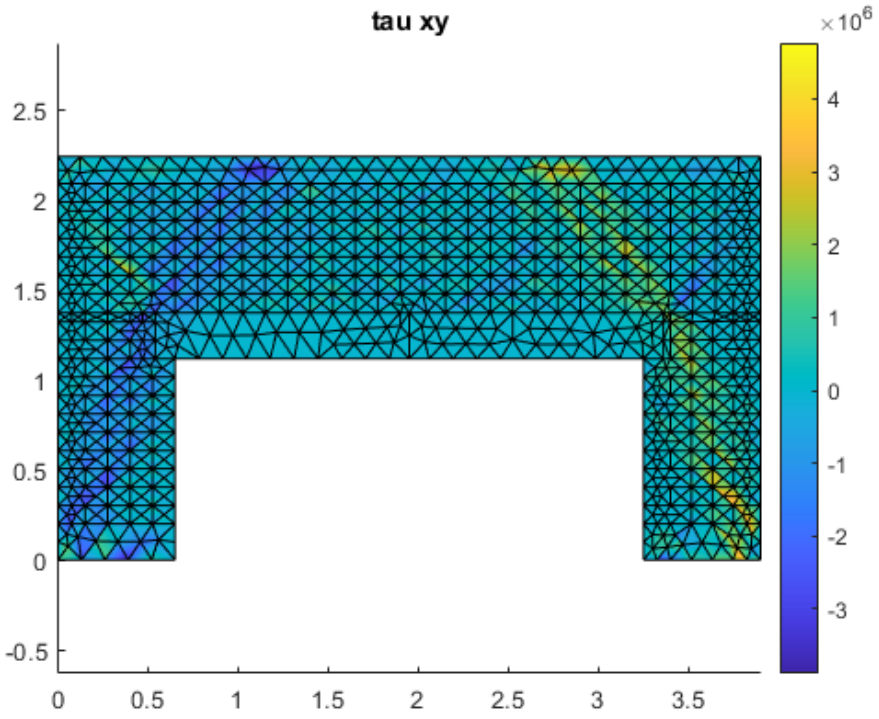

Figure 105: k0135 shear stress field

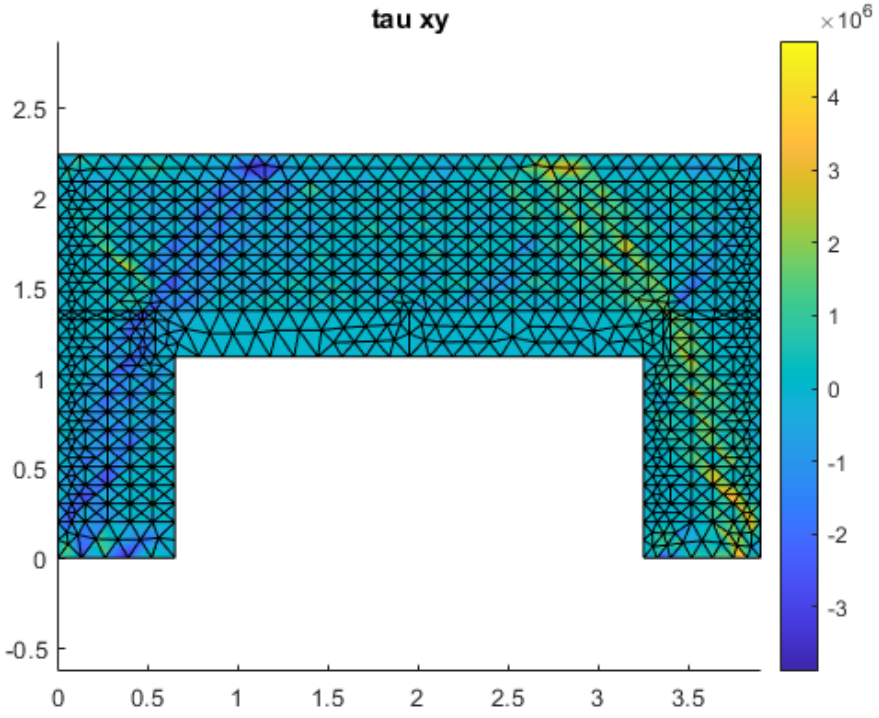

Figure 106: k0135shear stress field

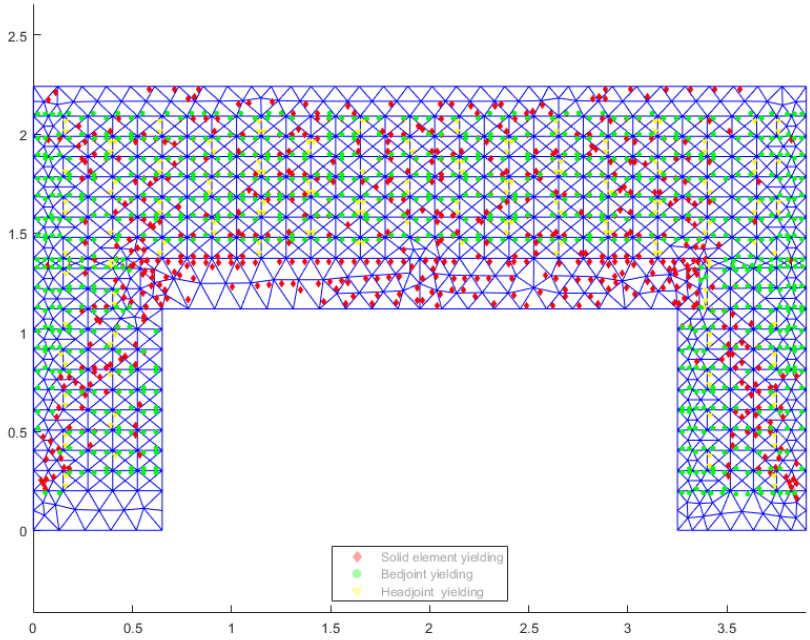

Figure 107: k0135 nodal yielding plot

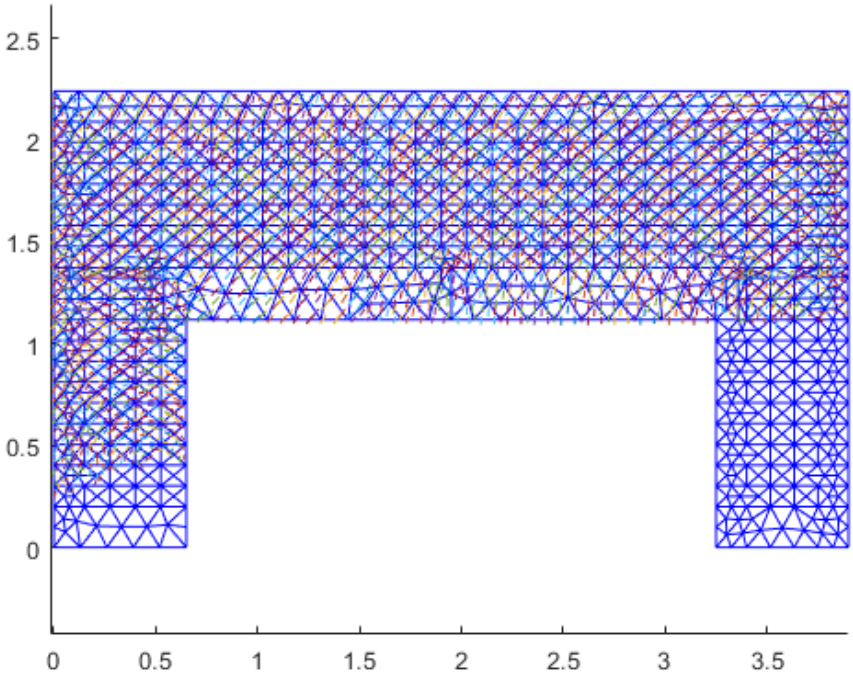

Figure 108: k0135 velocity plot

D.4 Mesh k = 0.15

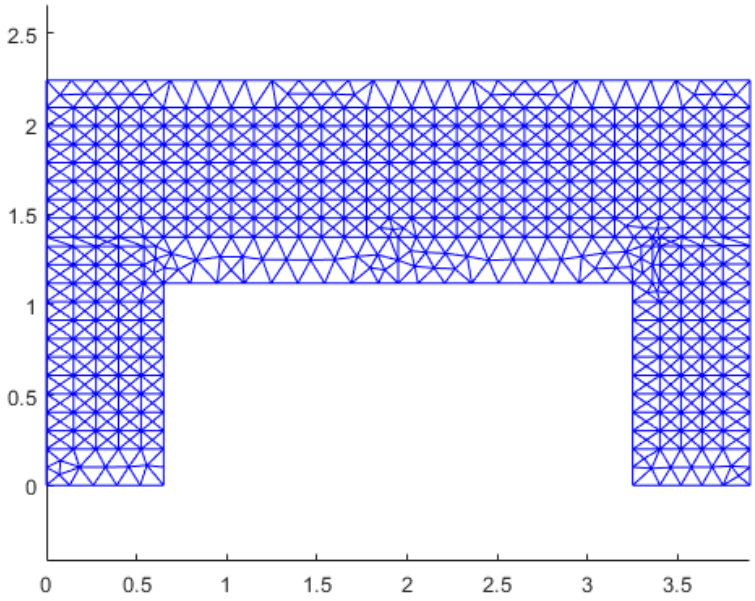

Figure 109: k015 meshing illustration

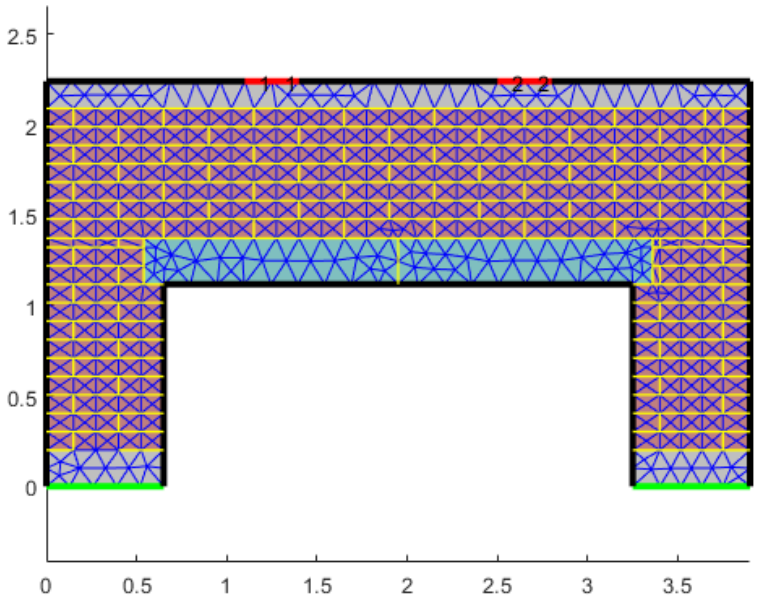

Figure 110: k015 material

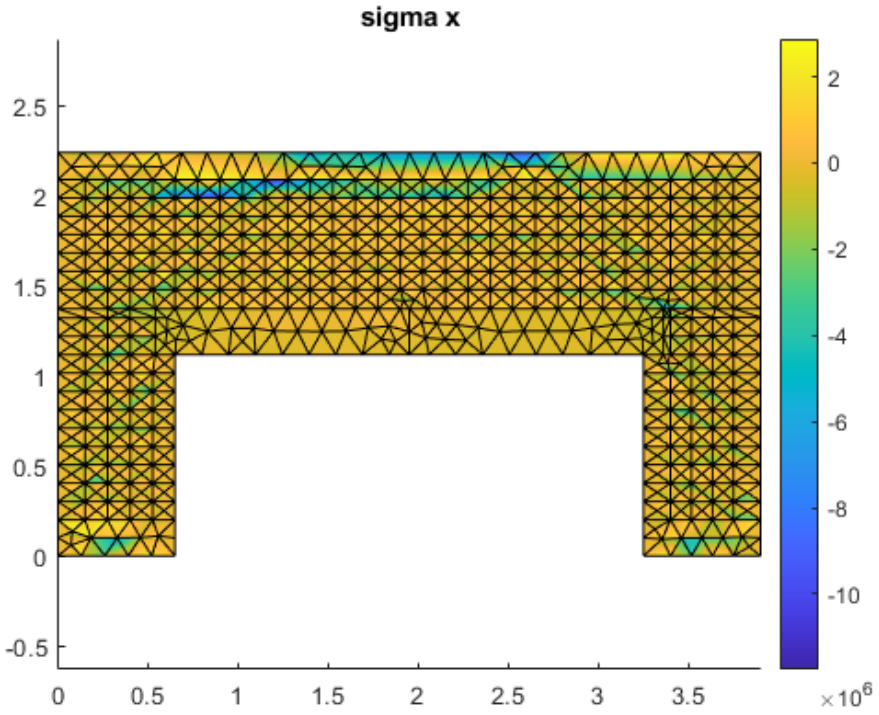

Figure 111: k015 sigma x stress field

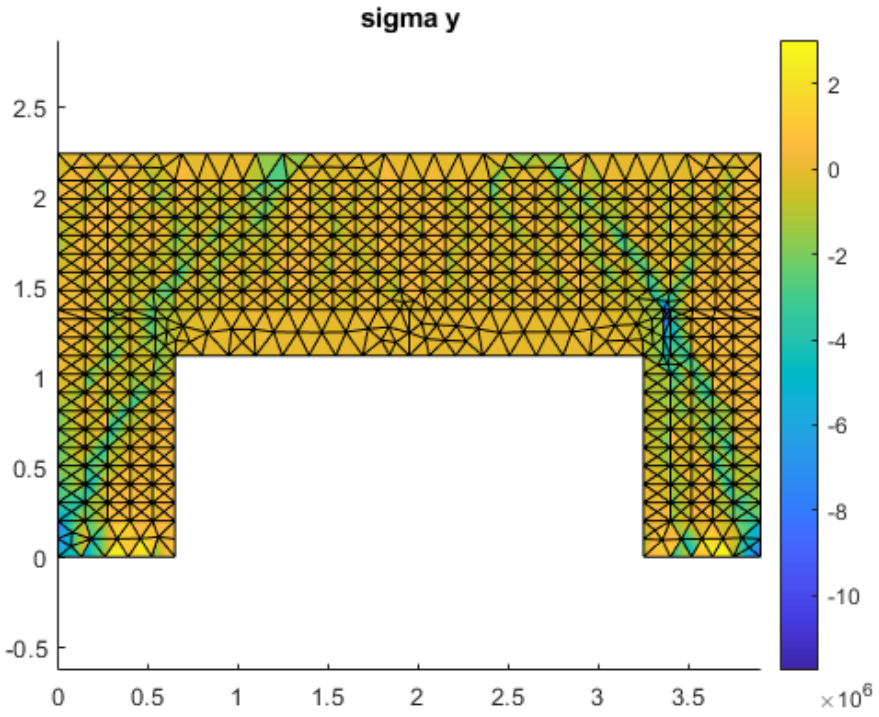

Figure 112: k015 sigma y stress field

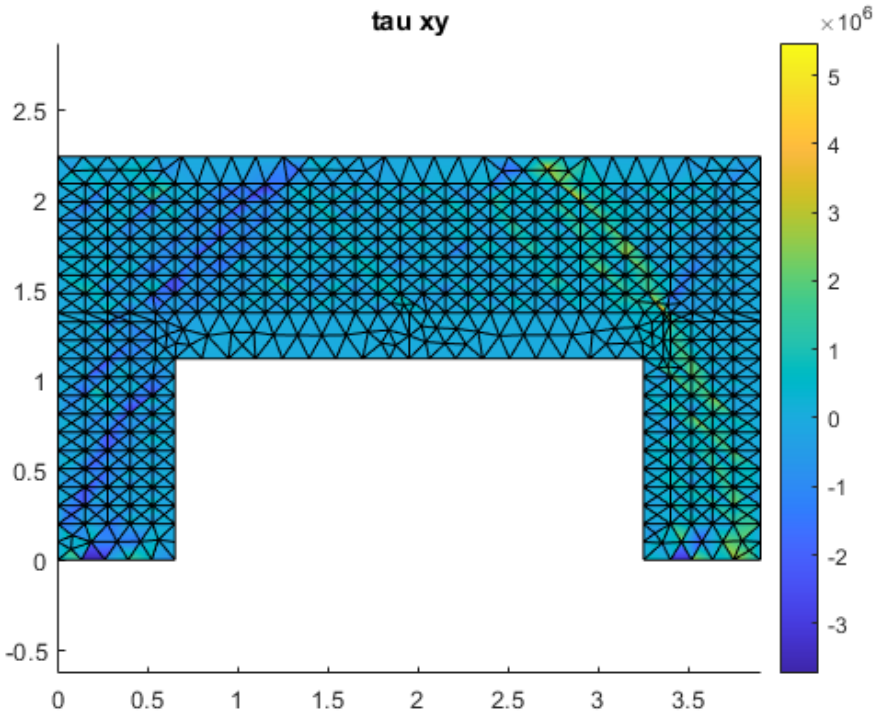

Figure 113: k015 shear stress field

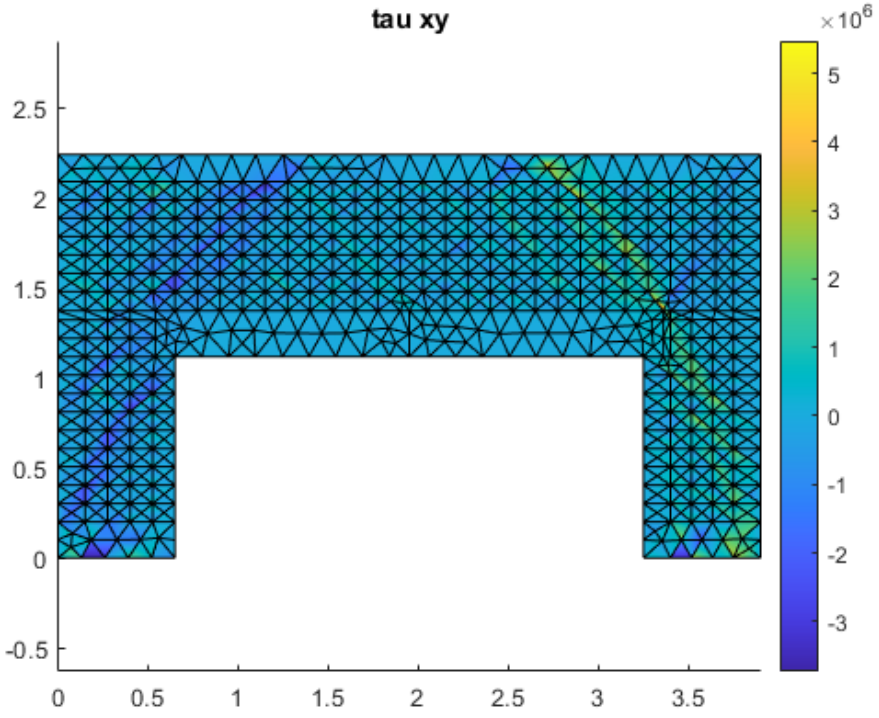

Figure 114: k015 shear stress field

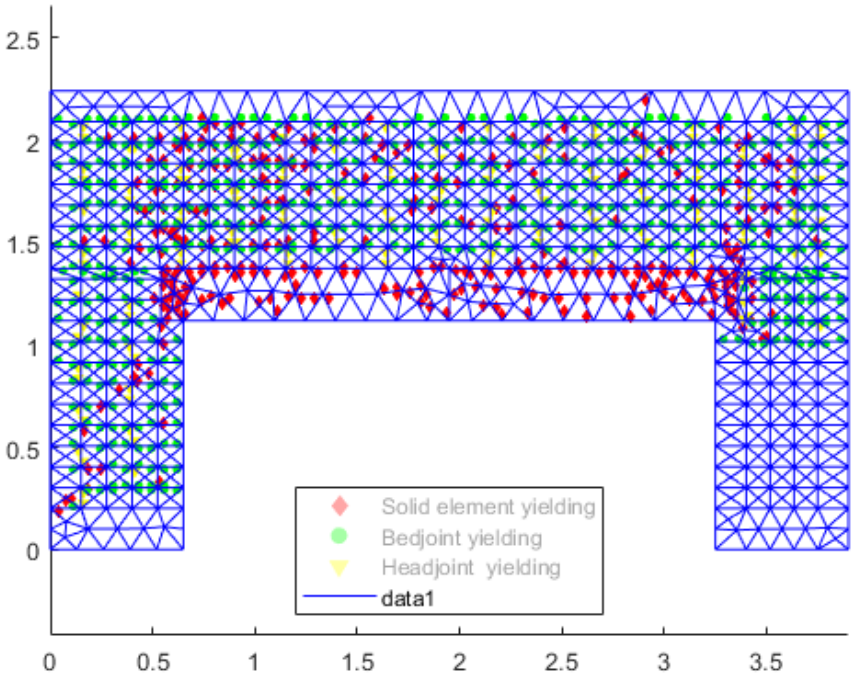

Figure 115: k015 nodal yielding plot

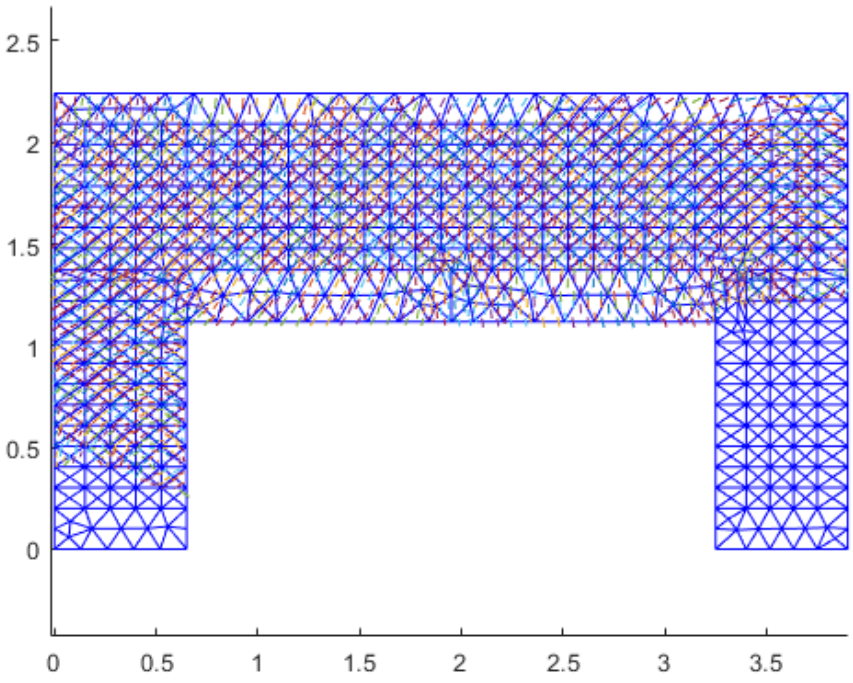

Figure 116: k015 velocity plot

D.5 Mesh k = 0.2

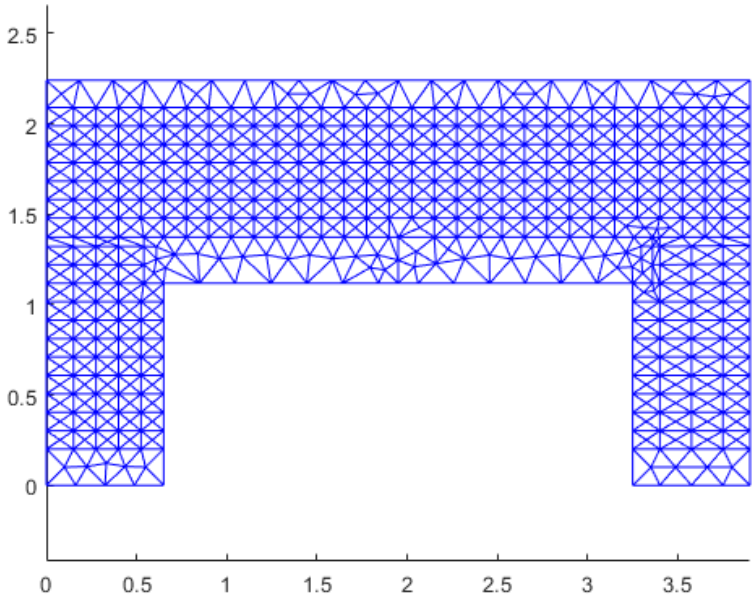

Figure 117: k02 meshing illustration

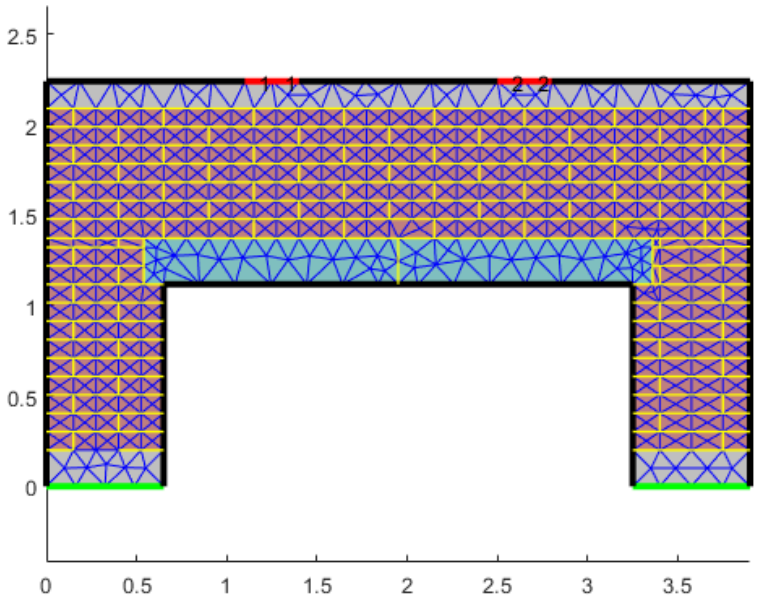

Figure 118: k02 material

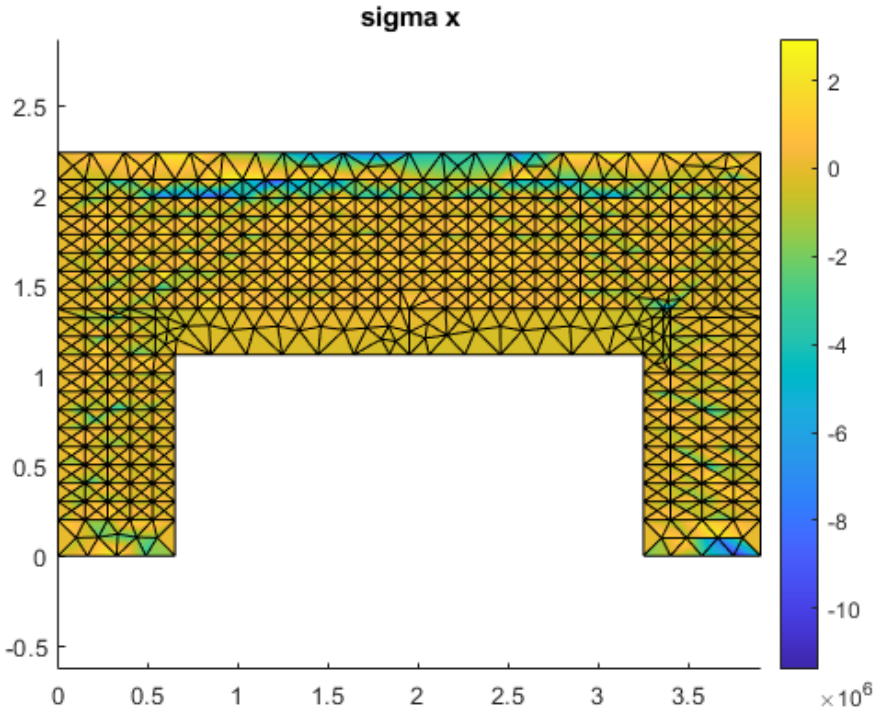

Figure 119: k02 sigma x stress field

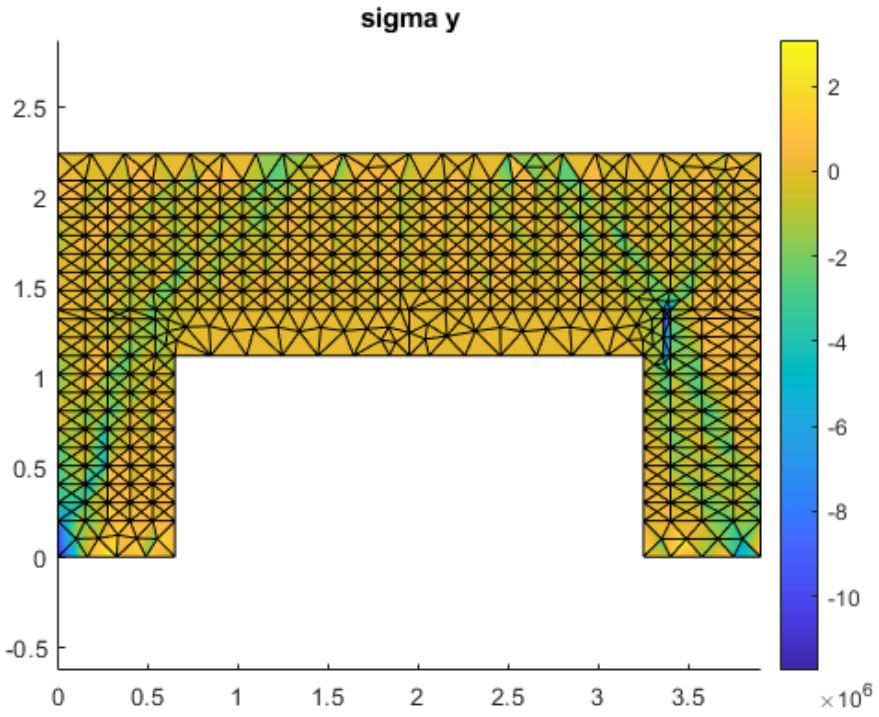

Figure 120: k02 sigma y stress field

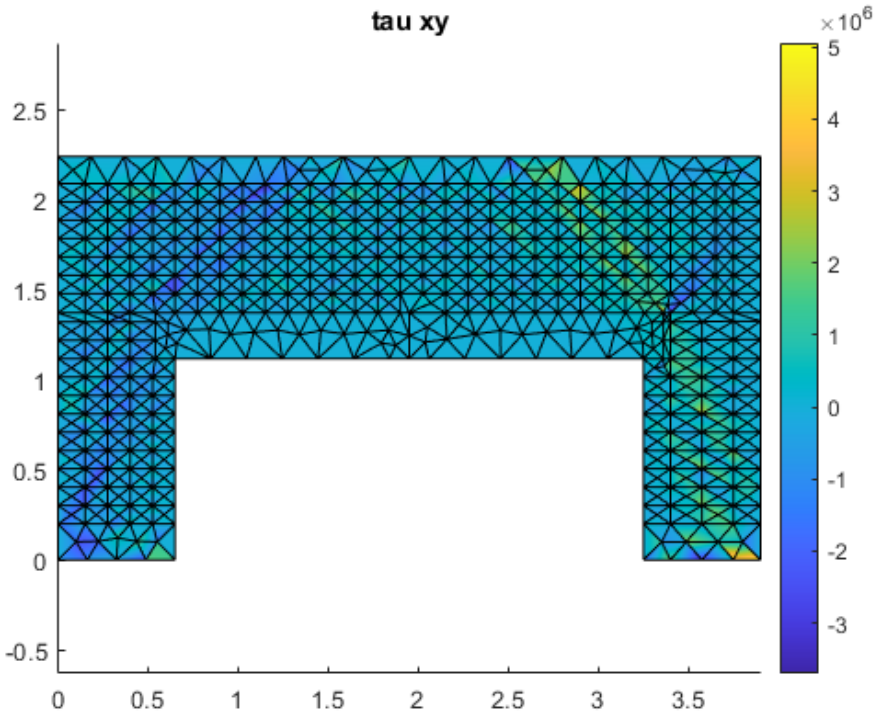

Figure 121: k02 shear stress field

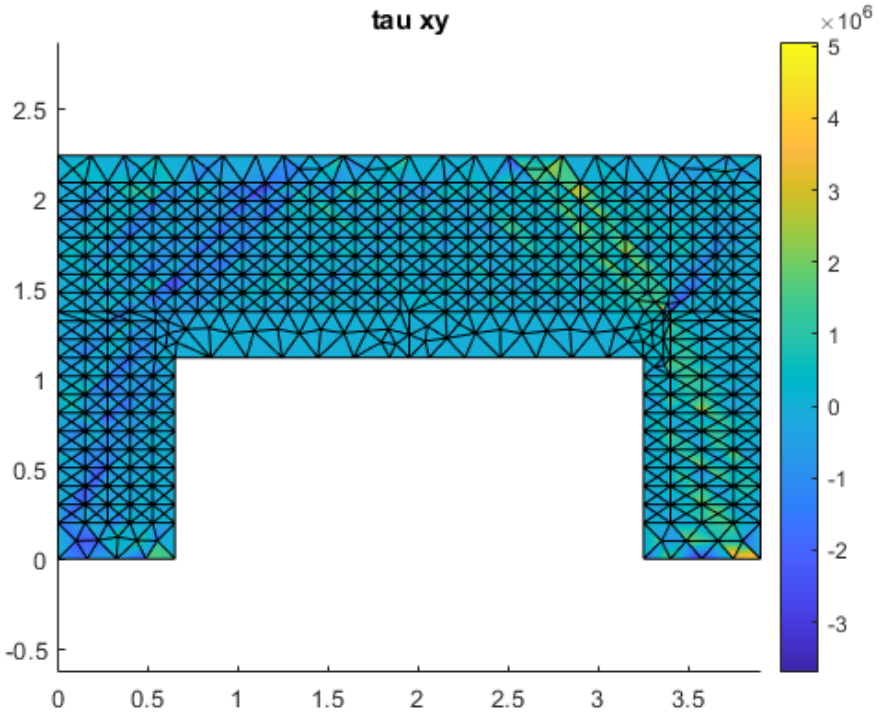

Figure 122: k02 shear stress field

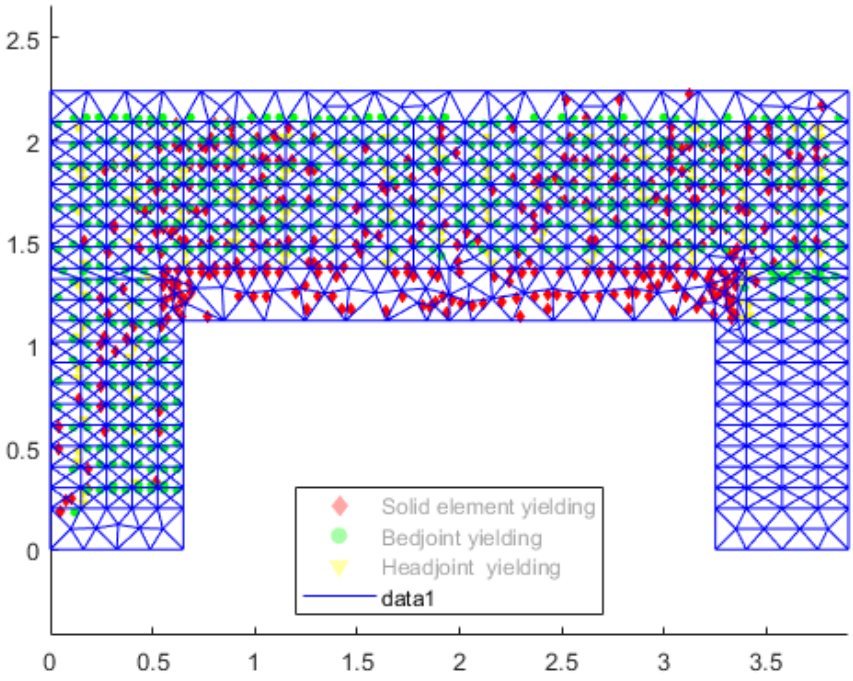

Figure 123: k02 nodal yielding plot

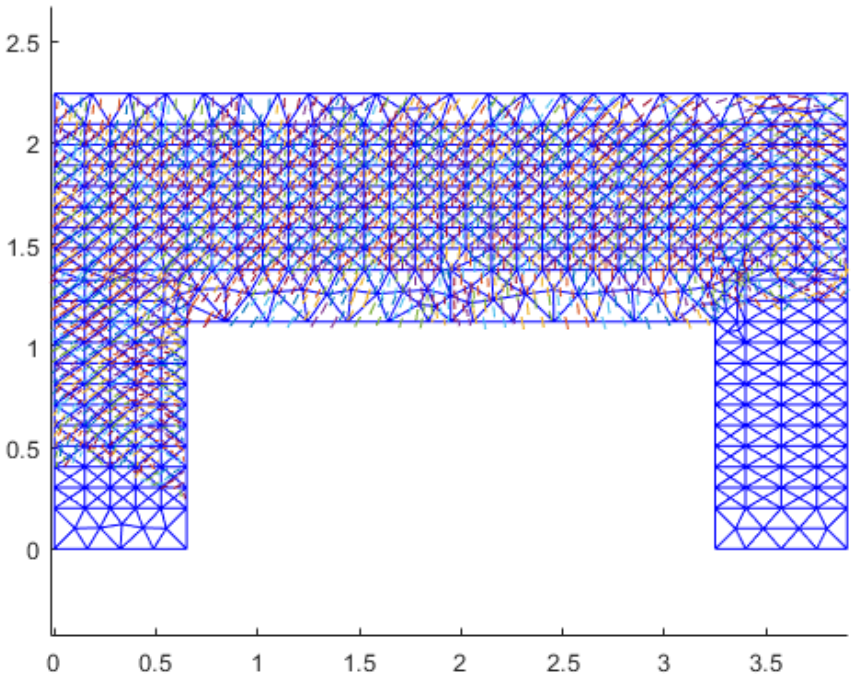

Figure 124: k02 velocity plot

E Literature study: Robustness of masonry structures

E.1 Introduction

In the field of structural robustness significantly less information is available on masonry structures compared to concrete and steel structures. In Europe considerations on structural robustness of masonry structures are mainly covered by EN1991-1-7, whereas for structures of materials such as reinforced concrete and steel additional information and requirements are stated in their material specific codes.

Authors Adam et al. and Ellingwood et al. both addresses this knowledge gap in their own papers on progressive collapse and robustness of structures. They argue that masonry walls both in situ-build and pre-engineered are inherently more vulnerable than walls of other materials due to of difficulties in providing continuity and ductility, but are fairly redundant by having a large number of bearing walls and shorter spans, which to some extent compensate for the reduced ductility. Prolonging the issue the authors comment that pre-engineered buildings are designed tightly with respect to the design envelope as a result of competition, and are sensitive to even moderate deviations from the design envelope caused by unforeseen events or change in live loads, which further confirms that comprehensive studies on masonry buildings need to be made on how a local failure in any part could propagate elsewhere and how alternative load paths can be formed to avoid progressive collapse [4, 27].
Forming alternative load paths in masonry is difficult and even harder to prove. Even though the scientific community have devoted a consistent effort to the computational analysis of masonry structures in order to develop tools for the prediction of the structural behavior, the computational analysis of masonry structures is still a challenging task. D'altri et al. highligt in their literature study on the subject, that the mechanical response of masonry is highly nonlinear and the geometry of structures often introduce deep complexities and uncertainties, why different strategies of analysis and different approaches and scales of representation of the mechanical behavior of masonry have been proposed. The authors categorize and discuss the different strategies of analysis and approaches and conclude that each computational solution shows peculiar limitations and a specific area of application, why the choice of the most suitable modeling strategy is a matter of the task [15].

The aim of this paper is thus to carry out a review of the main guidelines within structural robustness of masonry and of the main approaches in the field of computational modelling strategies of masonry. The content and range of the aspects dealt with form a guide for anyone interested in entering this field of study. Even though other authors previously have provided excellent reviews of modeling strategies for the computational analysis of masonry structures and research on progressive collapse and robustness of structures [4, 15], the present review specifically orient towards structural robustness of masonry structures and suitable computational modelling strategies in this context. The paper include:

- A description structural robustness (Section E.2) and recommended guidelines within masonry constructions.
- A description of present computational modelling strategies of masonry (Section E.4) subdivided into into three main categories of approaches.
- The authors' reflections on present and future needs in the field of robustness of masonry structures and suitable computational modelling approaches (Section E.5).

E.2 Structural robustness

The interest of structural robustness began with the progressive collapse incident of Ronan Point in London in 1968 after a gas explosion. The attention on the subject of robustness and safety only became larger with events such as the Murrah building collapse in Oklahoma, 1995, the collapse of the World Trade Center buildings in New York, 2001, and the collapse of the Achimota Melcom Shopping Centre in Acra, 2012 [4].

E.3 Robustness as concept

Defining structural robustness

In the decades after Ronan point robustness of structures was codified in various building codes and researched by various authors, all trying to define robustness in their own way. One common denominator is that robustness is resistance of disproportionate collapse or progressive collapse, which definition also is varying from author to author. The literature study of robustness made by Adam et al. makes an overview of different definitions of progressive and disproportionate collapse and of structural robustness both providing the reader with common understanding of the wordings. The findings of Adam et al. are outlined in below recreated tables 13 and 14.

Table 13: Selected definitions of progressive and disproportionate collapse

Source	Definition
Allen and Schriever	Progressive collapse [...] can be defined as the phenomenon in which local failure is followed by collapse of adjoining members which in turn is followed by further collapse and so on, so that widespread collapse occurs as a result of local failure.
Gross and McGuire	A progressive collapse is characterized by the loss of load-carrying capacity of a relatively small portion of a structure due to an abnormal load which, in turn, triggers a cascade of failure affecting a major portion of the structure.
GSA guidelines	Progressive collapse is a situation where local failure of a primary structural component leads to the collapse of adjoining members which, in turn, leads to additional collapse. Hence, the total damage is disproportionate to the original cause.
ASCE 7-05	Progressive collapse is defined as the spread of an initial local failure from element to element resulting, eventually, in the collapse of an entire structure or a disproportionately large part of it.
Ellingwood	A progressive collapse initiates as a result of local structural damage and develops, in a chain reaction mechanism, into a failure that is disproportionate to the initiating local damage.
Canisius et al.	Progressive collapse, where the initial failure of one or more components results in a series of subsequent failures of components not directly affected by the original action is a mode of failure that can give rise to disproportionate failure.
NISTIR 7396	Progressive collapse—The spread of local damage, from an initiating event, from element to element resulting, eventually, in the collapse of an entire structure or a disproportionately large part of it; also known as disproportionate collapse.
Agarwal and England	Disproportionate collapse results from small damage or a minor action leading to the collapse of a relatively large part of the structure. [...] Progressive collapse is the spread of damage through a chain reaction, for example through neighbouring members or storey by storey. [...] Often progressive collapse is disproportionate but the converse may not be true.
Krauthammer	Progressive collapse is a failure sequence that relates local damage to large scale collapse in a structure.
Starossek and Haberland	Disproportionate collapse. A collapse that is characterized by a pronounced disproportion between a relatively minor event and the ensuing collapse of a major part or the whole of a structure.Progressive collapse. A collapse that commences with the failure of one or a few structural components and then progresses over successively affected other components.
Kokot and Solomos	Progressive collapse of a building can be regarded as the situation where local failure of a primary structural component leads to the collapse of adjoining members and to an overall damage which is disproportionate to the initial cause.
Parisi and Augenti	Progressive collapse [...] is a chain reaction mechanism resulting in a pronounced disproportion in size between a relatively minor triggering event and resulting collapse, that is, between the initial amount of directly damaged elements and the final amount of failed elements.

Table 14: Selected definitions of structural robustness

Source	Definition
GSA guidelines	Robustness–Ability of a structure or structural components to resist damage without premature and/or brittle failure due to events like explosions, impacts,fire or consequences of human error, due to its vigorous strength and toughness.
EC1–Part 1–7	Robustness: The ability of a structure to withstand events like fire, explosions, impact or the consequences of human error, without being damaged to an extent disproportionate to the original cause.
Bontempi et al.	The robustness of a structure, intended as its ability not to suffer disproportionate damages as a result of limited initial failure, is an intrinsic requirement, inherent to the structural system organization.
Agarwal and England	Robustness is [...] the ability of a structure to avoid disproportionate consequences in relation to the initial damage.
Biondini et al.	Structural robustness can be viewed as the ability of the system to suffer an amount of damage not disproportionate with respect to the causes of the damage itself.
Vrouwenvelder	The notion of robustness is that a structure should not be too sensitive to local damage, whatever the source of damage.
JCSS	The robustness of a system is defined as the ratio between the direct risks and the total risks (total risks is equal to the sum of direct and indirect risks), for a specified time frame and considering all relevant exposure events and all relevant damage states for the constituents of the system.
Starossek and Haberland	Robustness. Insensitivity of a structure to initial damage. A structure is robust if an initial damage does not lead to disproportionate collapse.
Fib Model Code 2010	Robustness is a specific aspect of structural safety that refers to the ability of a system subject to accidental or exceptional loadings (such as fire, explosions, impact or consequences of human errors) to sustain local damage to some structural components without experiencing a disproportionate degree of overall distress or collapse.
Brett and Lu	[...] ability of a structure in withstanding an abnormal event involving a localized failure with limited levels of consequences, or simply structural damages.

As table 13 indicates progressive collapse and disproportionate collapse is often used interchangeably although not being the same thing. A progressive collapse describes the behaviour of the structural collapse, where as a disproportionate collapse refers to the size of the collapse in context of the initial cause. Therefore, a collapse can be progressive without being disproportionate and vice versa, but the term does of cause not rule out each other[6].
Likewise, table 14 shows a lack of consensus on the definition of structural robustness. Though, the wordings differ it is broadly agreed that robustness is the ability of the structure to avoid consequences disproportionate to the event causing failure. Adam et al. prolong the description by arguing that the actual robustness of a structure is a threat-dependent property of the entire structural system where it depends on the system's characteristics, strength, ductility, redundancy, continuity, and the type of abnormal loading. The authors underline structural robustness depends mostly on redundancy, which is the structures ability to redistribute loads after a local failure of one or few elements, hereby developing alternative load paths [4].

Designing structural robustness

Robustness of structures is handled by designing structures with the above mentioned system characteristics in the scale that it is needed. The design approaches that exists for designing robust structures differs in codes around the world, but is mostly variations of one or more basis approaches, where the common approaches is Tie-force based design methods, Alternative load path methods, Key element design, and Risk-based methods[6].

Tie-force based design methods

The methods are prescriptive rule based approaches, where the structural robustness indirectly is enhanced by considering the structure to meet robustness requirements through minimum levels of ductility, continuity and tying. Tie-force based design requires the designer to detail the structure such that members are mechanically tied together in accordance with specified requirements. For example in EN 1991 annex A minimum requirements of the capacity of vertical and horizontal ties are stated, to ensure that junctions have the ability to redistribute loads to some extent. Arup(2011) concludes in their literature study that there is a general consensus amongst most of the published literature that tie-force methods provide a minimum level of robustness to structures, but that the level of robustness cannot be quantified. The methods are found suitable for low-risk structures, but that deterministic methods are necessary as a supplement for buildings which are higher-risk. Arup's conclusion is based on several researchers finding tying inadequate in developing sufficient resistance against progressive collapse [6].

Alternative load path methods

The methods are quantitative and direct approaches, where the structure is shown to have adequate resistance against collapse by forming new load transferring mechanisms in the case that a load bearing member should fail. The capability of a structure to adequately redistribute the additional loads is achievable through redundant design by continuity of load bearing elements, ductile junctions, as well as designing statically indeterminant systems. If the residual load carrying capacity in these new transferring mechanisms is insufficient to sustain this additional load those elements will fail and the collapse will propagate [6]. Alternative load path approaches is widely accepted to be based on notional element removal, where the aim is to demonstrate robustness explicitly by assessing the ability of the structure to redistribute the additional loads under codified damage conditions. Adam et al. addresses the concern of some researchers that the approach in practice requires several assumptions and simplifications resulting into a huge number of potential assumption combinations, which can lead to design solutions with different levels of robustness. Within these considerations is among others, whether or not to account for

the source of the local damage and the dynamic effects of the hazard [4].

Key element design

The method is a direct scenario-specific design method, where structural members which failure can activate a progressive collapse are identified and designed to resist accidental loads specified in codes, hereby increasing the likelihood of the structure's survival in case of an accidental event. The key element design approach is recommended in many codes and guidelines, but is in some countries seen a method of last resort when the alternative load path methods are unable to demonstrate sufficient load redistribution ability of the structure [27].

Risk-based methods

Risk-based method is commonly used where the structural design fall outside normal limits and the consequences of a collapse will be severe, where such building classes is specified codes and national building regulations. Systematic risk assessment may draw upon and implement one or more of the above methods of design, since by implementing them the probability of either a hazard happening, damage occurring given a hazard, or extensive global damage given a hazard are reduced [6].

Designing structures to be less vulnerable to progressive collapse requires consideration of the damaged state as consequence of a hazard and to provide the structure with multiple load paths. Best practices will start with a selection of a structural system and provide it with ductile details that are capable of developing large inelastic deformations.
For the vast majority of structures, the design requirements may be prescribed using indirect methods e.g. prescriptive rule based approaches, resulting in robust structures with great capacity to sustain abnormal loading. For larger structures and when it is shown that the minimum tie force required by the indirect method can not be developed, direct analytical methods may be used to determine the design details required through alternative load paths to redistribute load and key elements to resist a specified threat [27].

E.3.1 Masonry specific robustness

The design approaches mentioned above are applicable to any structure and are considered in building codes around the world. Codes normally provide additional specific requirements for different materials and forms of construction in the form of additional detailing rules, as part of indirect design measures. In the decades after the Ronan Point accident a lot of research was made whereas both research and experimental tests up til now mainly has been focusing concrete, steel, and composite structures, practically ignoring masonry structures [4].

The lack of interest of structural robustness of masonry structures up until now combined with the difficulties to form alternative load paths in masonry have let to rather vague guidelines in numerous codes. In table 15 guidelines from selected sources are tabulated hereby highlighting the issue. The sources do broadly agree on the three usable methodologies to construct robust masonry structures, e.g. usage of horizontal, vertical, and peripheral ties, enhancing element strengths and alternative load paths.

Tie force requirements

All the sources in table 15 but GSA suggest using a tie-ing system only the British Standard and the UFC4 provide specific requirements to tie-ing force capacities, whereas the British requirements relies on the building class to be 2A or 2B and the UFC4 requirements relies on the building to be at least in Risk category 2. The British requirements for horizontal and peripheral

Table 15: Selected guidelines of structural robustness of masonry structures

Source	Guidelines	Specifies requirements
NISTIR 7396 [27]	In masonry structures, peripheral horizontal ties should be provided along the whole perimeter within a nominal distance of slab edge, and anchored at reentrant corners. Interior horizontal ties should be provided both ways either uniformly or in strips at regular spacing or in walls in close proximity to the floor or roof. Exterior horizontal ties should be provided from perimeter columns and walls to floor slabs.	no
EC6–Part 1–1 [28]	(2) The structural behaviour under accidental situations should be considered using one of the following methods: - Members designed to resist the effect given in EN 1991-1-7 - The hypothetical removal of essential load bearing members in turn - Use of a tie-ing system - Reducing the risk of the accidental actions.	no
UFC4-023-03 [29]	Provide three horizontal ties; longitudinal, transverse, and peripheral. Vertical ties are required in columns and load-bearing walls. The Alternate Path method, where applicable, to verify that the structure can bridge over removed elements. The Enhanced Local Resistance requirements, where applicable, for framed and load-bearing wall masonry buildings. The structure shall be able to bridge over vertical load-bearing elements that are notionally removed one at a time.	Yes
GSA [30]	Use the Alternate Path method to verify that the structure can meet defined acceptance criteria.	no
BS5628-1 [5]	Peripheral, internal and column wall ties should be provided at each floor level and at roof level, but where the roof is of lightweight construction such ties need to be provided at that level. Vertical ties should extent from roof level to the foundation or to a level at and below which the relevant members of structure are protected	Yes*

**Tie-force requirements depends on the building class*

tie-ing force capacities evolves around a basic tie force $f_t = min(60kN; (20+4\cdot n_s)kN)$, where n_s is the number of stories. The code differentiate between internal and external walls and columns by scaling the basic tie force with a constant either fixed or depending on characteristic dead and live loads, span lengths and story heights. Vertical tie-ing force capacities are stated as the greater of $\frac{(34\cdot A}{8000}\cdot(\frac{h_a}{t})^2)N$ or $100\frac{kN}{m}$ length of wall or per column, with A, h_a, and t being the cross section area in *mm*, the clear column or wall height, and the column or wall thickness. The Department of Defence(UFC4) suggests a general approach named the Load and Resistance Factor Design approach that distinguish between one-way and two-way load bearing systems. Generally, the design tie strength must be greater than or equal to the required tie strength;

$$\phi \cdot R_n \geq R_u$$

The design tie strength is the product of a material specific strength reduction factor, ϕ, and a nominal tie strength R_n. The required tie strength pr. $\frac{kN}{m}$ in the longitudinal or transverse direction is $3\cdot w_F \cdot L_1$, where w_F is the floor load through combination of dead and live loads and L_1 the span length. In figure 125 from UFC4 the L_1, spacing requirements between the ties, and column-wall-areas are schematized for two-way span load bearing wall constructions. L_1 is

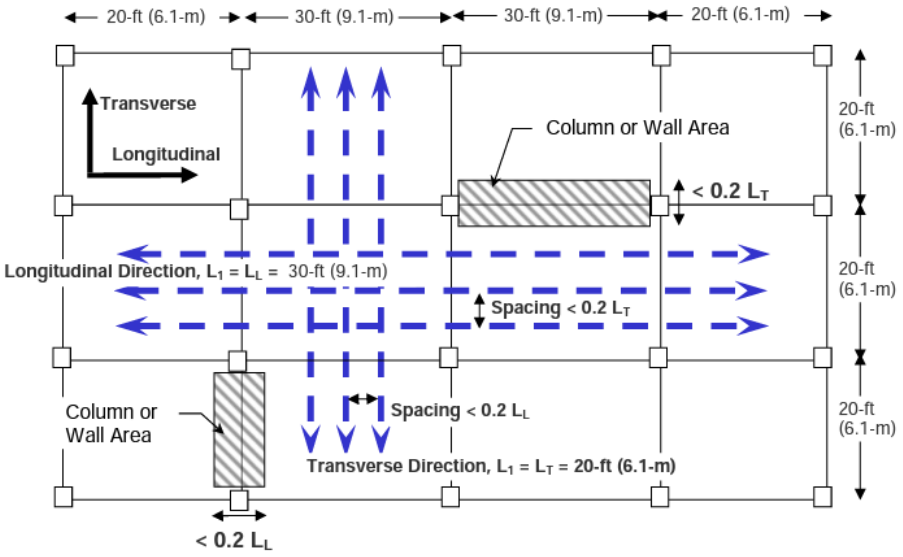

Figure 125: Determination of L_1 and column area for Frame and two-way span Load-bearing wall construction [29]

equal to the one-sided span and the spacing between the ties must not exceed a fifth of the span. In the column or wall area twice the tie force requirements shall be placed in the direction of the tie under consideration. Similar approaches is suggested for peripheral tie force requirements. The vertical tie must have a design strength in tension equal to the largest vertical load received by a column or wall from any one story, using the tributary area and the floor load w_F [5, 29]. The remainder of the sources in table 15 do not mention tie-ing force capacities. The British Standard supports their requirements with a phrase stating 'provide effective anchoring', which Arup(2011) finds very unfortunate. The phrase was reformulated from the 2002 edition where it stated effective horizontal ties what Arup argues to be indisputably more robust than 'effective anchoring', as may be shown from an analysis of the connection details under the horizontal tie forces given in the codes of practice [6].
Arup(2011) and Morton(BDA1985) continuously raises concerns regarding anchorage in masonry. It is argued that a hazard could have the effect of dragging out the individual bricks in which the ties are anchored and refer to a test on a model concrete panel high rise block at the Building Research Establishment where this behaviour was confirmed [31]. The reason of the behaviour is that the capacity of most of the details recommended in BS 5628-1 annex D relies on friction at the block/mortar interface. Two of the recommended details are illustrated in figure 126 and 127 wherefrom the local anchorage issues and friction reliance can be interpreted.

In many cases with ties fastened to masonry the block/mortar interface is limited to the friction of the bed joint why the capacity of such joints will depend on friction and vertical load, and will be heavily influenced by issues such as quality control, workmanship, shrinkage or reduction in bond between the floor, mortar and the wall [6].

Enhanced local resistance

The second common guideline among the tabulated sources in table 15 is designing the member to resist the hazard or enhanced local resistance. Load bearing elements are basically to be designed to resist any imaginable load scenario which reasonably could happen. Both the Eurocode and Department of Defence support the guideline with hazards, requirements and design loads, which acts regardless of material type of the structural element. It is worth noting that

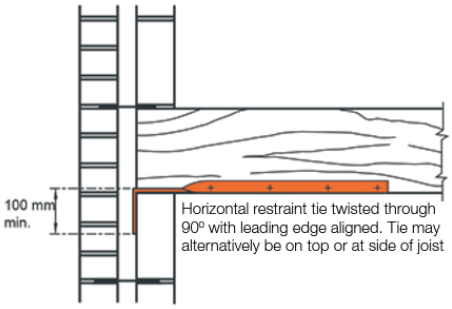

Figure 126: Example of horizontal ties [5]

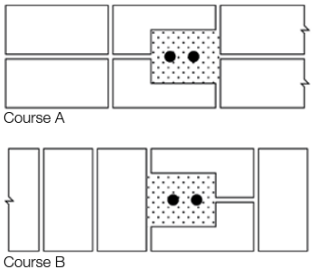

Figure 127: Example of vertical ties

local enhancement is a direct design scenario-specific method, why its main focus is to avoid local failure and not prevent progressive collapse given failure [4].

Alternative load paths

The last common guideline in the quest of designing robust masonry structures is the alternative load path method. As with the local enhanced resistance guideline, alternative load paths are not alone a masonry tool. Of the sources in table 15 the Eurocode and and Department of Defence support support the guideline with requirements of which elements to be notionally removed. The British Standard and General Services Administration relies on requirements of the Eurocode and and Department of Defence, respectively. Successful redistribution of load through alternative load paths within masonry structures relies on mobilisation by compressive strut action, which can have substantial load bearing capacity. Other authors refer to this behaviour as arching action and though figures 128a and 128b schematize the action differently it is to versions of the same, both preventing localized failure from affecting a larger portion of the structure. It is important to stress, that for arching action to be effective, adequate abutments capable of providing sufficient resistance against rotation, lateral and axial movements are necessary [27, 6, 31, 7].

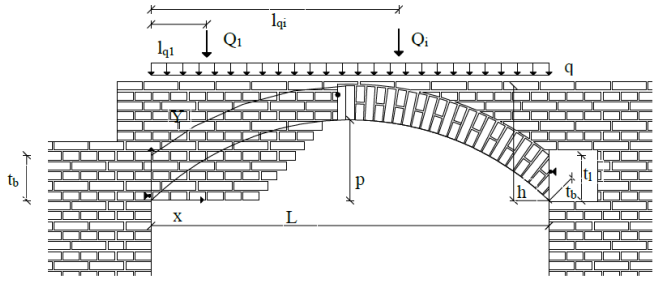

(a) Hidden arch

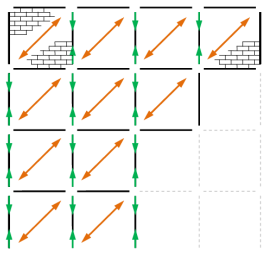

(b) Compressive strut action

Figure 128: Redistribution of load by alternative load paths [6][7]

The mentioned guidelines in table 15 will all provide a structure with some level of robustness. That being said, robustness was in section E.3 defined as the ability of the structure to avoid consequences disproportionate to the event causing failure, and comparing with the robustness outcome of enhanced local resistance the guideline does not provide a structure with such ability. Providing a structure with horizontal and vertical ties will on the other hand give as structure such abilities if the tie-ing details are thoroughly made such that local failure of the anchorages are prevented, though being, as mentioned, heavily influenced by issues such as quality control, workmanship, and shrinkage. Ensuring alternative load paths are arguably the

guideline who fits the robustness definition the best, but is at the same time the more difficult guideline to demonstrate. Intuitively, alternative load paths in masonry can be proved through arching actions, where several authors stress that a great potential of load bearing capacity can be located.

E.3.2 Testing structural robustness

Experimental setups

Robustness as a structural ability is difficult to measure and to experimentally test, but huge advances in the field of progressive collapse has made it possible to improve existing codes and design recommendations and calibrate numerical models. According to Adam et al. most of the experimental tests made to date have mostly been focusing on concrete and steel structures, where failure of one or more columns was simulated and considered threat independent scenarios on four different levels [4]:

a) sub-assemblages usually formed by two beams and one or more columns.

b) frames formed by beams and columns.

c) building structures constructed solely for experimental purposes.

d) actual buildings condemned to demolition.

Common for type a and b is both the prototype size and the types structural elements. The structural assemblages often consist two span beams and one or three columns, whereas the tests simulate the removal of a column often simulated with hydraulic actuators. The behaviour of beams and beam-column joints are studied in order to characterise the resistance mechanisms that could help to hold up a progressive collapse such as flexural, arch, and catenary action. To analyse in detail some researchers use digital image correlation (DIC) to analyse the cracks and strains during different stages of the tests.

Type c experimental test subjects are structures constructed to act as "specimens", wherefrom particularly reliable results can be obtained if care is given to their design, construction, monitoring, data acquisition and treatment of the results. According to Adam et al. the reliability of this method of testing means that the results obtained can be used as a dependable source for calibrating numerical models and proposed measures for codes and design recommendations, but is quite expensive and risky why it is rarely used.

Lastly type d, tests on buildings to be demolished. Some authors have taken advantage of such buildings, in which they have simulated the failure of one or more columns in both steel and concrete structures. In the full scale experiments commented by Adam et al. damage is generally simulated by removing up to four columns either internal or on the perimeter. The structures tend to be sufficiently robust to withstand the simulated damage, where the damage detected after the failures was insignificant with only quite small vertical displacements thanks to the appearance of Vierendeel action-based alternative load paths and contribution of infill wall and external walls. One test showed that the more storeys a building has, the greater its load redistribution capacity after the failure of a column.

Each experimental setup has its own benefits. Local robustness with specific resistance mechanisms and capacities of structural details are most likely to be tested in labs with exact equipment and variable control, and if more variables are introduced and the test subjects are structures constructed to act as "specimens" dependable sources for calibrating numerical models can be achieved. Full scale testing of actual buildings condemned to be demolished

comes with a price of many unknowns and different resistance mechanisms against progressive collapses, but is a great way of testing global robustness of a structure.

Testing masonry structures

Experimental tests of masonry specifically focusing on structural robustness has been a neglected area, but has recently been given attention. In the main part the effect masonry working as a secondary element such as infill walls in concrete frames or masonry panel subjected to blast loads. In any case the experiment is setup as a sub-assemblage making it possible to test in labs and minimize unknown variables.

In progressive collapse analysis if masonry not is primary load bearing element only its weight is are considered and not its stiffness. Kai Qian and Bing Li test the effect of masonry infilled walls on the load resisting capacity of reinforced concrete frames to mitigate progressive collapse and find that ignoring the effects of masonry infilled walls in progressive collapse design may result in substantial inaccuracy in predicting the stiffness, strength, and failure modes to resist progressive collapse [8].

Only a few studies focusing on robustness have been carried out with masonry as the primary structural element. Out-off-plane behaviour of masonry walls subject low-velocity impacts and blast loads is focus of these studies aiming to explore brick masonry's relatively small resistance against such loading types. Adam et al. concludes in their literature research that this subject deserves further investigation to assess and reduce the vulnerability of buildings to catastrophic explosions that frequently occur as a result of gas leaks from building utility service systems [4].

Rising attention on the subject of structural robustness of masonry structures in the field of experimental mechanics have led to some test of sub-assemblages mainly focusing on the structural element subjected to a hazard. This leaves large scale tests on the effects of a hazard in terms of a progressive collapse of masonry structures still unexplored and earlier mentioned substantial load bearing capacities([27, 6, 31, 7]) unproven.

E.4 Computational Modelling Of Masonry

E.4.1 Mechanics Of Masonry

The term unreinforced masonry describes a wide range of material combinations but generally describes a combination of quasi-brittle rock like blocks as the primary constituents. Masonry can be made "dry", that is without any binding agent connecting the blocks, however as this is not used on a significant scale in Denmark, all masonry so forth will be describing a composite material of quasi brittle blocks connected either with Portland based cement mortar, lime mortar or adhesive mortars.

The mechanical behaviour of Masonry is therefore defined by the properties of the blocks and by the mortar as well as the joint interaction of the two. In general, the failure modes of masonry are describable by five different mechanisms as are listed below, and illustrated in figure 129, [15].

(a) Block-mortar interface tensile failure

(b) Block-mortar interface shear sliding failure

(c) Diagonal masonry shear-compression failure

(d) Crushing failure of Masonry blocks

(e) Block and mortar tensile cracking normal to head joints

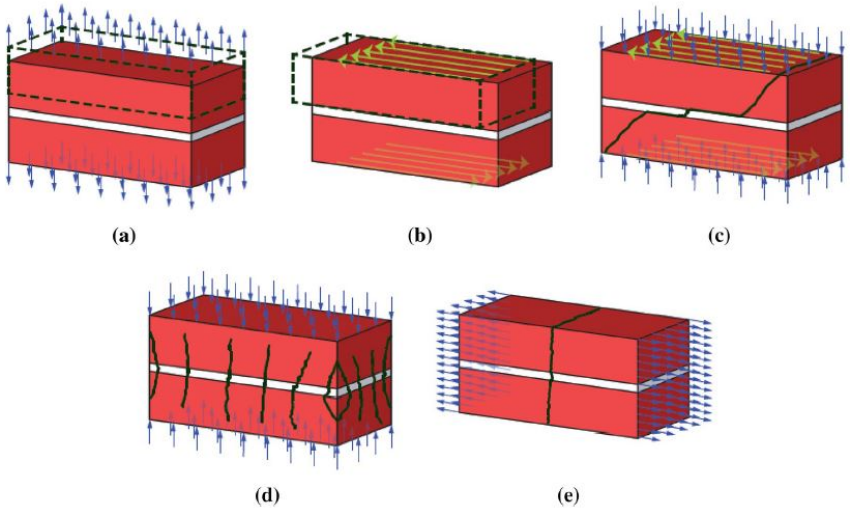

Figure 129: Masonry failure modes [15]

Masonry is, due to the combination of blocks and mortar and the bond pattern of the two an anisotropic and heterogeneous material. The anisotropic characteristics of masonry exists elastically in the sense that the stress-strain relationship differs with the respect to orientation and in regards to strength as the strength properties also differs with respect to orientation. Similarly, there is a significant difference between tensile and compression strengths complicating even further with compressive strength of the blocks being significantly higher. Furthermore, anisotropy is also observed in the brittleness of the material that is the post peak response differs with respect to load orientation as well. This is illustrated in below figure 130, [19] which

shows different failure modes with respect to load inclination. Several things are noteworthy, the failure modes are not equally brittle, as brick failure as seen in the shear failure of mode B1 and the compression crushing failure of mode C are very brittle yet the shear mortar failure modes are somewhat ductile.

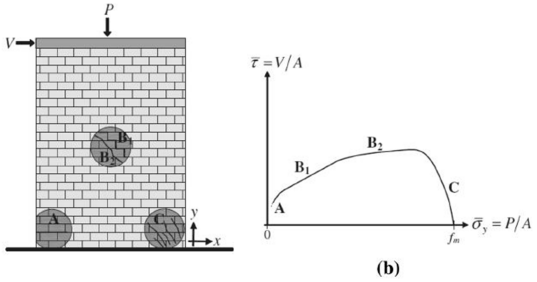

Figure 130: Masonry response with respect to orientation

Masonry as a structural material is therefore highly non-linear and therefore very difficult to computationally characterize. Another aspect of difficulty is the stochastic aspect of the strength and geometry of a specific masonry wall, that is the general unpredictability of the specific strength of masonry and the specific geometry especially for a larger geometry. This is caused by the fact that not all bricks have necessarily the very same strength, and the geometrical layout is very prone to constructional errors such as varying joint thicknesses making it generally very difficult, perhaps folly to predict the accurate structural response of structural masonry.

Computational modelling of unreinforced masonry structures present many difficulties. The structural behaviour of masonry structures is heterogeneous, anisotropic and mostly non-elastic resulting in a highly non-linear mechanical behaviour. These factors complicates the numerical modelling of masonry structures, yet viable approaches exists. In this paper, computational modelling strategies of masonry is coarsely divided into three main categories of approaches which are:

- Continuum deformation based models
- Block based models
- Limit analysis models

E.4.2 Continuum based models

Continuum based models revolves around simplifying the masonry as a continuous media and thereby allowing the application of well established stiffness based finite element procedures and as such, this approach can generally be characterizable as a macro-modelling approach. The inherent issue with this approach is the fact that masonry is not continuous but an assemblage of bricks and mortar. This creates issues with the formulation of the constitutive laws for the computationally continuous masonry, where two main approaches exists [15]:

- Direct approaches, the constitutive equations are formulated and the mechanical properties are subsequently calibrated for instance by experimental means and directly implemented in finite element continuum analysis.

- Homogenization on a structural scale of the masonry by coupling a material scale model of a representative volume of masonry with a global continuum model and either adopting this directly as above, however multi scale methods where the masonry scale model is either corrected adaptively or for each step.

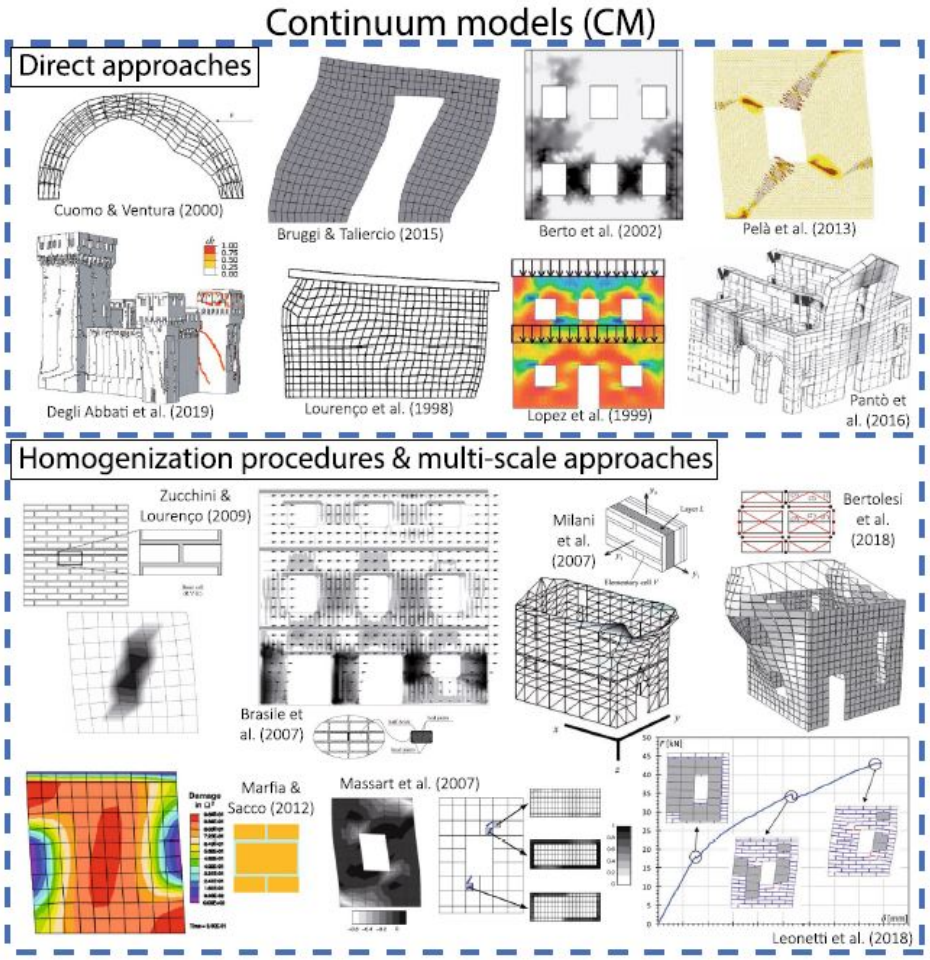

Figure 131: Continua approach results, fig 12. in [15]

Approximating the constitutive behaviour by the approaches shortly outlined above introduces errors however the strength of these approaches lies within the computational efficiency of modern finite element software allowing for very sophisticated models to be formulated.

Direct approaches

The direct approaches requires the characterization of the mechanical behaviour by some approximating general constitutive law and the parameterization of the mechanical properties governing these laws, here several families exists.

- Drastic idealization of the masonry constitutive behavior allowing for simple and elegant however, inaccurate solutions.
- Nonlinear constitutive laws based on either fracture mechanics, damage mechanics or plasticity theory

- Spring based systems, the system is not modelled as a perfect continuum as deformations and non-linearities are centralized in the springs at the interfaces connecting the elements however the structure is discretized as a continuous mesh.

The idealization approaches generally evolves around Heyman's model [32] of masonry as a perfect no-tension material, which circumvents the issue of the troublesome constitutive behaviour of masonry in tension regime and thereby allows for numerically inexpensive solutions, which however are inaccurate due to the fact that masonry does have tension capacity and ultimately results in discrepancies between the modelled failure modes and some experimentally observed tensional failure modes. With this type of simplification a deformation based FE model can be created as done in [33]. The same type of simplification is also applied in a wide range of limit analysis based models and these simplifications were widely used in the era before modern computational ability, whereas now it can serve as a quick preliminary analysis tool.

The second approach, the formulation of nonlinear constitutive laws and implementation into a finite element model of deformable elements based on some nonlinearity model of either plasticity, fracture or damage mechanics is a field thoroughly researched in relation to concrete structures, however when implemented with respect to masonry the multi-level anisotropy as described earlier presents challenges. Especially, phenomena such as block separation, block rotation and frictional sliding are hard to model by continuum constitutive approaches[34]. A way to approach this deficiency, is to introduce interface non-linear springs between the brick finite elements and thereby diverging form the pure continua approach however, fracture, damage and softening of these springs is possible to model. These types of solutions are sound on paper however, difficulties lies within the issue of numerical convergence as sharp non-linearities such as block separation can cause the numerical simulation to bounce back and forth without convergence.

Homogenization Approaches

The family of homogenization approaches can generally be considered an equidistant point between micro and macro modelling. The general procedure is to define the constitutive behaviour by a volume deemed representative and then applying this to a macro sized continuum finite element model. This constitutive model can then by recalibrated during the numerical process, thus allowing for the masonry material complexities to by continuously formulated appropriately as the structure strains. Two main approaches with different complexity levels exist:

- A-priori homogenization
- Step by step homogenization

A-priori homogenization means performing the constitutive homogenization of a representative volume which can approximately characterize the macro behavior of the masonry structure prior to the continuum finite element analysis and then performing the global analysis with the a-priori deduced mechanical parameters. This concept of homogenization was first phrased in 1992 by S. Pietruszczak [35], where he employed the approach of defining the global elastic parameters of a masonry structure by means of a-priori homogenization. Later on, the methodology is extended to also define a strength domain and a homogenized failure surface as done by Milani in [17]. This approach generally provides a strong tool in the application of real

structures, as the computational effort required is not massive making the approach applicable to real-life sized structures.

Step by step homogenization means computing mechanical parameters of the representative volume as the structure progressively strains and fractures and thereby iteratively performing the structural analysis by reiterating the evaluation of the mechanical parameters. This allows for much more complicated models to be formulated and allows to describe non-linearities such as softening, damage, contact effects and frictional sliding not achievable by the a-priori homogenization [15]. The approach is computationally demanding as it requires the global scale model and the material scale model to run in tandem and step by step update the constitutive behaviour, yet the methodology provides strong predictive ability of the masonry response up until very large strains and separation of blocks where the continuum framework lacks. A final point regarding homogenization approaches is that it requires some interpretation of the final predicted failure deformation configuration of the brickwork as it does not fail as a homogeneous continua but by separation of individual blocks and thereby creating inconsistencies between the real failure deformation stage and the modelled one.

E.4.3 Block based models

Block based models is within this paper defined as a family of models where the masonry bricks and the mortar connecting them is modelled separately and thereby avoiding a wide range of issues intrinsic to the continuum approach outlined above. A non-exhaustive list of the advantages to block-based modelling is:

- An-isotropy is implicitly included in the constitutive behaviour as the actual masonry bond is modelled and the mechanical parameters of brick and mortar can be modelled independently of each other.
- Failure modes are clearly identifiable in contrast to continuum approaches
- Out of plane and in-plane loading and their interaction can be modelled

The advantages are therefore many, the only major drawback is the massive computational effort required to execute the models properly, thereby rendering these models most appropriate for academic research and smaller scale models. Within the general philosophy of block-based models lies several sub-approaches. In this paper, two major ones are defined and categorized into the following main approaches:

- Heterogeneous finite element approaches
- Contact-mechanics approaches

Heterogeneous finite element approaches

The heterogeneous finite element approaches is based within the well-known framework of deformable finite elements, but the mesh is created with some elements representing bricks and some representing the mortar contrary to the continuum based models outlined earlier. Within this framework is again two main methods. The first and simplest is the application of zero thickness interface elements representing the mortar within the finite element mesh whereas the second approach is to model the texture of the masonry by means of solid elements with mechanical properties of the brick, and solid elements with mechanical properties of the mortar.

In the interface element approach, the material non-linearity phenomena are most often concentrated in the interface elements corresponding well with the fact that most yielding modes can be attributed to the mortar, see figure 129, which also makes the computational demand less in contrary to having the bricks behave non-linearly as well. The material non-linearities are then handled by nonlinear springs between the solid continuum elements representing the bricks and the interface element allowing for softening effects and frictional sliding to be modelled. A general issue of the stiffness based finite element approaches is the issue of geometrical non-linearities attributed to the separation of blocks resulting in large displacements conflicting with the need of nodal compatibility. A rather complete model, incorporating both material non-linearity by interface elements and geometric non-linearity by kinematics as well as being in 3D is presented in [36] by Mancorini in 2011 adopting the type of elements as illustrated in figure 132.

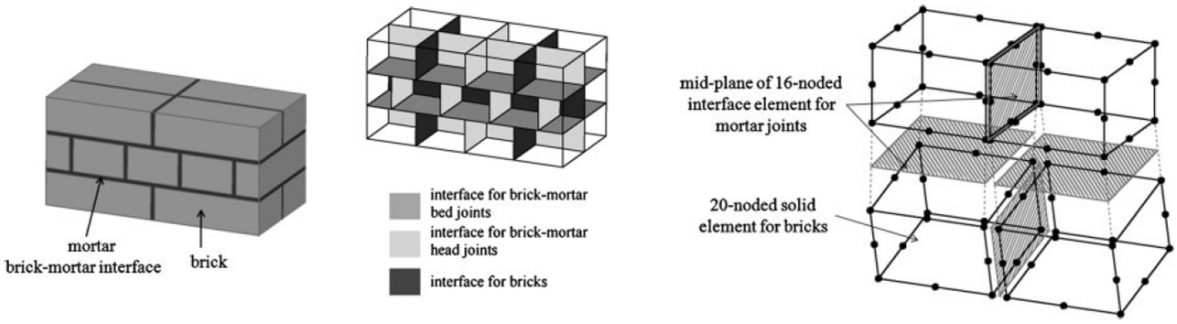

Figure 132: Mancorini FE interface model, fig 1 and 2. in [36]

The other method of representing the brickwork as a heterogeneous finite element assemblage of solid continuum elements is not literally as well presented as the interface approach, yet [37] does a comparative study where the authors create a model with solid element bricks connected with interface elements, solid bricks connected with solid mortar elements, and a combination of the two where the both solid mortar and solid bricks are connected with an interface element - they also put in interface elements vertically within the brick elements to be able to model compressive splitting of the elements. An illustration of the configuration is shown below in below figure 133.

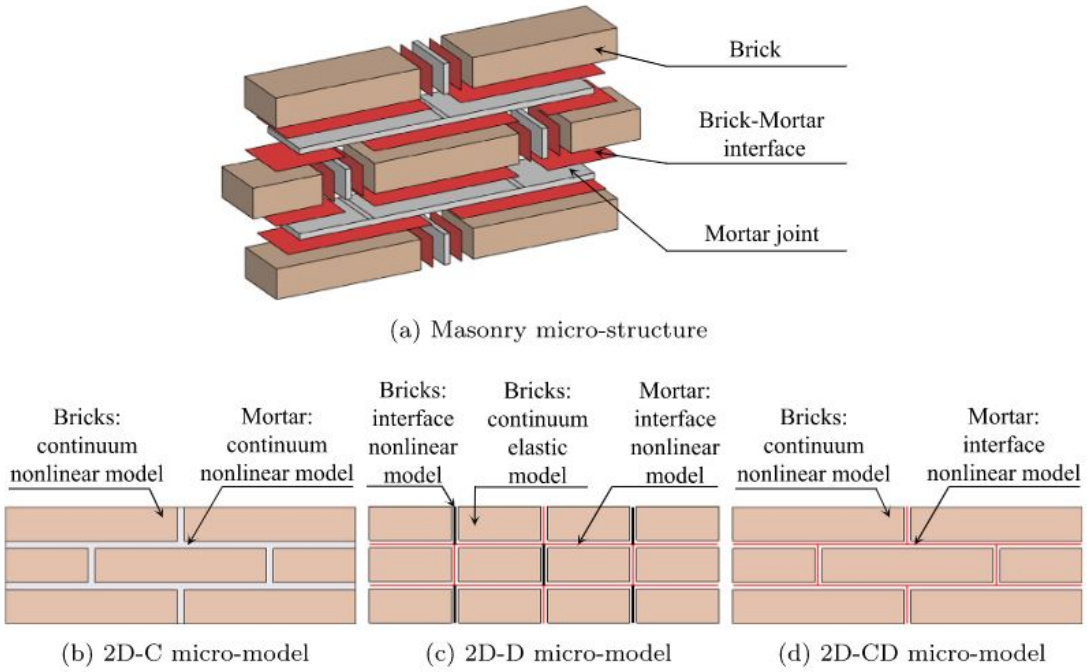

Figure 133: Petracca masonry modelling, fig 1 [37]

The material nonlinearity model is one based on damage mechanics and they eventually conclude that all the three models created replicates well an experiment conducted on a masonry shear wall with the differences being that the interface model and the combined model slightly overestimates shear strength and the solid continuum one slightly conservatively underestimates shear strength.

Contact mechanics

The family of contact models revolves around the concept of contact mechanics which revolves

around the study of rigid or deformable bodies touching each other, where perpendicular normal stress is generated as a consequence of the contact and tangential frictional stresses are subsequently generated. Several approaches exists, but the must widely diffused method - both in academics and in commercial software - is the Discrete Element Method originally developed by P.A. Cundall in 1971. This approach discretises a solid into a finite volume of individual particles, then initializing the simulation each particle is set an initial velocity and for each explicit time step, contacts are generated, subsequent normal and frictional forces are calculated and velocities are calculated by an explicit integration scheme. In below figure 134 is a failure mode of a panel under vertical load by Sarhosis from [38] from a discrete element simulation.

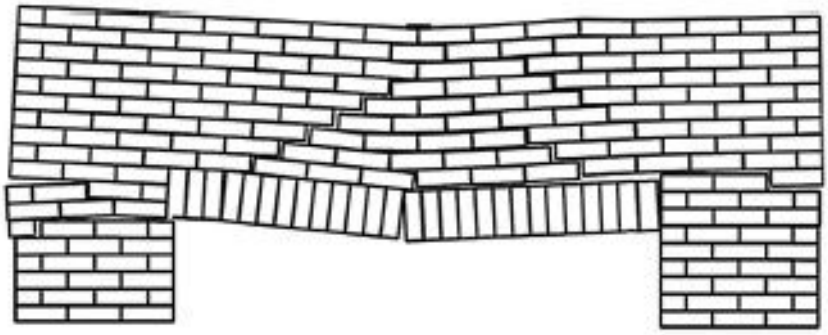

Figure 134: Sarhosis DEM simulation, p.85 in [38]

Relating this method specifically to masonry, the particles are the bricks, and the mortar is simulated by springs generated at contact points with constitutive laws representing the non-linear properties of the mortar and a failure criterion such as the Mohr-Coloumb. This formulation allows most of the masonry non-linear phenomena to be described such as block separation and frictional sliding but it has a hard time simulating compressive crushing of the bricks. The discrete element method is a framework applicable to many fields of study but it excels when tackling masonry mechanics as all the heterogeneities of masonry are implicitly accounted for. A drawback of the discrete element method, is the computational demand of applying it to larger structures and the fact the output of a simulation is the spatial and kinetic configuration of the blocks with little knowledge of the stress state of the structure [38].

E.4.4 Limit analysis models

Limit analysis is fundamentally based around the principles of plastic lower bound and upper bound solutions. These solutions are based upon the extremum principles(lower and upper) which states that, a solution can be obtained without the fulfillment of all three of the basic conditions required for an exact solution: physical, kinematic, and static/dynamic but rather, with only two of them which in practice is very convenient. Combining physical and static/dynamic conditions forms the lower bound solutions and combining the physical and kinematic forms the upper bound solutions wherein each an infinite amount of solutions satisfying the two conditions can be found. The lower bound solutions approach the exact collapse multiplier from below, making them safe solutions whereas the upper bound solutions approach the exact collapse multiplier from above, rendering them generally unsafe unless the practicing engineer is confident in he's abilities.

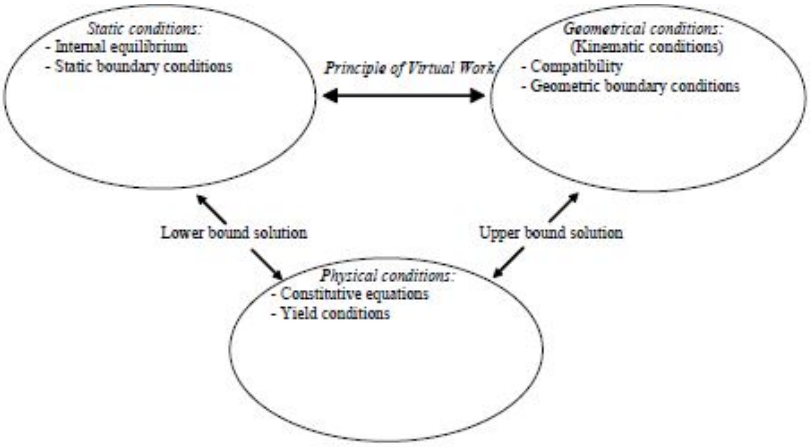

Figure 135: Illustration of basic conditions and their applicability to plastic solutions

Limit analysis solutions has and is still being applied to masonry structures especially in the practical design of masonry structures especially as the solutions with a few simplifications are demonstrable by hand and therefore circumvents many of the difficulties of modelling masonry. Computational numerical models of masonry is however not as widespread as for instance non-linear deformation finite element modelling. The following two subsections give a brief overview of a few approaches to computational limit analysis divided into lower bound and upper bound solutions.

Lower bound solutions

Applying the plastic lower bound theorem to masonry dates back to Heyman [32] where the basic methodology is the assumption of no-tension strength and thereby finding a network of compression only struts within the structure in equilibrium. This simplification yields good results when applied to masonry structures with practically negligible tension strength as for instance historical masonry where any mortar has perished away however, when applied to modern time masonry structures with tensional capacity this assumption halts.

A framework for computational limit analysis utilizing plane strain linear stress finite element is developed by Sloan[1] initially developed for geotechnics, however the framework has been applied to masonry by Sutcliffe [16] and Milani [17] with success. The original framework formulates the structural statics problem as a linear programming optimization problem where the discretized equilibrium acts as equality constraints and a linearized yielding criterion acts as inequality constraints. The framework is therefore generally applicable to many materials as long as they have sufficient deformation capacity for the ultimate stress distribution to realize. This is somewhat an issue for masonry as brittle failure modes are present as shown in figure 129 however if one can ensure that this failure mode - compressive splitting - doesn't occur then the methodology is sound. The mechanical behaviour is controlled within the yielding criterion and this should therefore be formulated with care. The yielding criterion requires some sort homogenization as it needs to be applicable independently of the orientation of the stress field on the brick, a methodology for this has been conducted in [17] where a representative volume element(RVE) using constant stress triangles has been used.

Upper bound solutions

The stress based finite element approach can also be extended to upper bound solutions as demonstrated by both Milani and Sloan allowing rigorous solutions to be found as one can find both an upper and a lower bound and compare. They both use an associative flow rule and a equality matrix is created containing plastic multiplier rates following this associative flow rule

and velocity relations within the discretized field and boundaries. One can then express the energy dissipated in element surfaces and minimizing this returns an upper bound solutions.

Another upper bound approach is the Discontinuity layout optimization. This approach employs the principles of yield line theory and is originally developed for shear yield lines in soil but has also been applied to bending yield lines in concrete slabs. It has also been applied for masonry but only for masonry arches by Gilbert [39] furthermore, a commercial software called LimitState uses discontinuity layout optimization for analysis of masonry arch bridges. The method discretizes a geometry and draws lines between the nodes and then employs an analogy to optimal truss structures to identify kinematically admissible yield lines and subsequently uses an optimization program to minimize the work done for the individual admissible yield line configurations.

As this study aims to quantify how to numerically describe masonry in context of robustness, the primary goal is something to describe deep beam or arching behaviour within shear walls. This means that an upper bound program would have to predict yield lines as a combination of shear and bending yielding while simultaneously accounting for all the anisotropic mechanical parameters, which is troublesome for the reliability of an eventual numerical model.

E.4.5 Discussion of computational approaches in relation to robustness

The choice of computational tool usually comes down to the trade off between speed and the accuracy or complexity required where it is most often preferable to choose the simplest model available with sufficient accuracy to describe the issue. As stated earlier, computational formulations of masonry mechanical behaviour is not easy and the very accurate models especially the nonlinear finite element ones are computationally demanding. As the issue at hand is that of structural robustness and therefore failure modes of large geometries, a fairly efficient and less demanding approach is needed.

Another consideration is what type of result is needed. As outlined in chapter 2, disregarding key element design and the tie-force system as sub-optimal robustness design methodologies, the primary codified approach to structural robustness is alternative load paths and as such, a computational approach that finds alternative stress distributions such as lower bound limit analysis is a fitting tool. This is also what is done in reinforced concrete robustness design with alternative load paths by lower bound limit analysis however, reinforced concrete is more ductile and the ability to plastically redistribute stresses is not refutable whereas for masonry the assumption of freely redistributing stresses must come with more care.

The method of linearly varying stress elements as developed by Sloan [1] and applied to masonry by [16] is chosen as the preferred approach to develop a tool to evaluate robustness of masonry structures by alternative load paths. To reiterate, the method evolves around equilibrium and a homogenized yield rule, one of the RVE homogenization approaches as described in [17] or the one by Lourenco as adopted by [16] can be taken.

The method however has the following disadvantages:

- The method is based on 2D stress state elements and will require altercations to treat 3D stress state problems. This is not strictly needed for alternative load path design but many concrete failure events such as impact and explosion loads are out-of-plane loads and as such are not strictly describable by the 2d lower bound stress elements.

- The testing of robustness will probably include some out of plane load and some dynamic effects which the framework cannot account for.
- The method requires a carefully calibrated homogenized yield model to yield accurate results. Due to the inherent uncertainties and multiple levels of anisotropy this is hard to define for an existing large structure not carefully created in a laboratory.

All these disadvantages are deemed inconsequential when compared with the advantages:

- Simplicity - the method is inherently very simple as there is no need to quantify complex hardening laws or plastic flow rules which keeps computational time down, but also the authors believe it to be advantageous to take the simplest approach required to sufficiently solve a problem. The simplicity also makes the methodology adoptable for practical design purposes.
- There is relatively few mechanical parameters to characterize, this comes as a continuation of the above point but as the yield surface is the only material mechanical law to define there is no need for hardening or plastic flow laws to be formulated and parameterized.
- The method appears to be one of the approaches that can handle the computational demand of a real life sized structural element.
- The concept of limit analysis harmonizes well with the idea of structural robustness where one envisions the structure in the event of failure.

In conclusion, the approach to deemed best for continuation is that of lower bound limit analysis with stress elements as created by [1].

E.5 Conclusions

This paper presents a description of the cornerstones of structural robustness and a review of the main guidelines in the field of the progressive collapse of masonry structures along with a review of the existing numerical modelling strategies.
The development of structural robustness strategies for masonry structures has been shown and concluded to be far behind strategies and guidelines for steel, concrete and composite structures. Only the UFC4 and the British masonry code state specific requirements related to the tie-ing force guideline, which is argued not to fit masonry material behaviour very well, since local and effective Anchorage is hard to obtain in a low tension capacity -if any- material mostly relying on friction. Alternative load paths is argued to be the most fitting robustness strategy, though there is still a long way to go. Experimental tests and numerical studies needs to made to define tools to prove robustness of masonry structures, hereby reducing the uncertainty and unknowns on the subject when building large structures in masonry. Recent experimental tests on masonry have been focusing on element behaviour when subjected to blast and impact loads, which in the field of structural robustness mostly relates to the enhanced local stiffness strategies by trying to describe both capacities of masonry and the force acting on the element. Large scale tests testing the structural consequences of a local failure is needed to verify possible alternative load bearing mechanisms within masonry structures.

Existing numerical modelling strategies divided into three categories has been described and advantages and disadvantages are of each modelling strategy category are pointed out. Focusing on structural robustness the most suitable modelling strategy is discussed and it is concluded that a fairly accurate and less computational demanded approach is needed when trying to describe failure modes of large geometries. The most suitable approach is found to be a lower bound limit analysis where simplicity, familiarity and low computational demand outweighs disadvantages like being 2D based and therefore do not include out-of-plane loads and the reliance on well calibrated homogenized yield model to produce accurate results.